

# **DEVELOPMENT OF VOLTAGE CONTROLLER AND FAULT ANALYSIS OF SELF EXCITED INDUCTION GENERATOR SYSTEM**

**JYOTIRMAYEE DALEI**



**Department of Electrical Engineering  
National Institute of Technology Rourkela  
Rourkela-769008, INDIA  
July 2016**

# **Development of Voltage Controller and Fault Analysis of Self Excited Induction Generator System**

*A thesis submitted to National Institute of Technology Rourkela  
in partial fulfillment of the requirements of the degree of*

**Doctor of Philosophy**

**in**

**Electrical Engineering**

**by**

**Jyotirmayee Dalei**

**Roll no-511EE109**

*Under the supervision of*

**Prof. Kanungo Barada Mohanty**



**Department of Electrical Engineering  
National Institute of Technology Rourkela  
Rourkela-769008, INDIA  
July 2016**



**Kanungo Barada Mohanty**

Associate Professor

04-July-2016

## **Supervisor's Certificate**

This is to certify that the work presented in this thesis entitled “*Development of Voltage Controller and Fault analysis of Self Excited Induction Generator System*” by “*Jyotirmayee Dalei*”, Roll Number 511EE109, is a record of original research carried out by her under my supervision and guidance in partial fulfillment of the requirements of the degree of *Doctor of Philosophy in Electrical Engineering*. Neither this dissertation nor any part of it has been submitted for any degree or diploma to any institute or university in India or abroad.

(Kanungo Barada Mohanty)

*This research work is dedicated to  
My Father Late Sri Dibakar Dalai*



## Declaration of Originality

I, Jyotirmayee Dalei, Roll Number-511EE109 hereby declare that this thesis entitled “*Development of Voltage Controller and Fault Analysis of Self Excited Induction Generator System*” represents my original work carried out as a doctoral student of NIT Rourkela and, to the best of my knowledge, it contains no material previously published or written by another person, nor any material presented for the award of any other degree or diploma of NIT Rourkela or any other institution. Any contribution made to this research by others, with whom I have worked at NIT Rourkela or elsewhere, is explicitly acknowledged in the thesis. Works of other authors cited in this dissertation have been duly acknowledged under the section “References”. I have also submitted my original research records to the scrutiny committee for evaluation of my dissertation.

I am fully aware that in case of any non-compliance detected in future, the Senate of NIT Rourkela may withdraw the degree awarded to me on the basis of the present dissertation.

04-July-2016

NIT Rourkela

Jyotirmayee Dalei

# Acknowledgment

It brings me immense gratification to convey my deep sense of gratitude to my supervisor Prof. K. B. Mohanty for his expert guidance and support throughout my research work. His suggestions and ideas provided the base to my research and inspired me to be a philosopher. This work would not have been completed without his active involvement. I look at him with great respect for his profound knowledge and relentless pursuit for perfection.

I also offer my sincere thanks to Prof. B. Subudhi, Prof. A. K Panda, Prof. K. K Mohapatra and Prof. P. Singh for their constructive suggestions and encouragement. I would also like to express my sincere thanks to Prof. J. K. Satapathy, Head of the Department of Electrical Engineering.

I am really indebted to Prof. A. K. Pradhan, for his very generous help whenever it was needed.

I would like to thank my research colleagues, Mrs. Tulika, Ms. Swarnabala, Mrs. Dipti, Ms. Aditi, Ms. Pragyan, Mr. Kishor, Mr. Aswini, Mr. Rabi, Mr. Vinaya, Mr. Pradeep and Mr. Kailash who are all helped and encouraged me during this period.

My thanks also to staff members of this department for their cooperation during this research work.

It would have been impossible to achieve anything without the blessings of my parents, parents-in-law, uncle-in-law and aunty-in-law. It is not possible to carry out this research without the encouragement of my brother-in-law Mr. Gajapati and Mr. Amulya during the toughest of times. I also express my thanks to my brother Mr. Rajendra, my sister Mrs. Renu and Mrs. Dipti, my brother-in-law Mr. Lambodar, Mr. Kaustava, Mr. Bharata, Mr. Vikram and my sister-in-law Mrs. Sarmistha, Mrs. Ila, Mrs. Poonam, Mrs. Buni and Mrs. Suman.

I am grateful to my husband Dr. K. C. Ray for relieving me and allow me to carry this research and tolerate my negligence during this period. It could not have been possible to achieve this research work without his suggestions, ideas, support, sacrifice and patience. Last but not the least, I can not express my words for my son Krishnesh for his support, patience and who favour a lot to make my dream come true.

04-July-2016

NIT Rourkela

Jyotirmayee Dalei

## Abstract

Increasing fuel cost and attempt to get pollution free environment, renewable sources of energy such as the wind, solar, micro-hydro, tidal wave, and biomass, etc. have grabbed recently the attention of researchers. Among these available energy resources, the use of wind energy is growing rapidly to generate and supply electricity as grid connected or stand-alone mode. To generate electric power from such non-conventional sources, self-excited induction generator (SEIG) is found to be a suitable option for either using in grid connected mode or isolated mode. Selection of SEIG in these areas depends on its advantages such as low cost, less maintenance, and absence of DC excitation. High maintenance and installation costs including transmission losses of conventional power supply to remote or isolated place by means of power grid can be reduced by installing stand-alone wind driven SEIG system at those places. In the year of 1935, self-excitation concept in squirrel cage induction machine with capacitors at their stator terminals was introduced by Basset and Potter. But the problems associated with SEIG are its poor voltage and frequency regulation under load and prime mover speed perturbations which put a limit on the use of SEIG for a long time. By controlling active and reactive power accurately, it is possible to regulate frequency and voltage of SEIG terminal during load and speed perturbations. Various efforts have been put by researchers in developing SEIG voltage and frequency controller but these control schemes demand multiple sensors along with complex electronic circuits. This dissertation presents some studies and development of new voltage controller of the SEIG system for balanced resistive,  $R - L$  and induction motor (IM) load that is used in isolated or remote areas. So in this context, an attempt is taken to develop an optimized voltage controller for SEIG using Generalized Impedance Controller (GIC) with a single closed loop. Stable zones of proportional and integral gains for GIC based SEIG system are computed along with parameter evaluation of the GIC based SEIG system. Further, Particle Swarm Optimization (PSO) technique is used to compute the optimal values of proportional and integral gains within the stable zone. The research work on SEIG system is extended to develop a voltage controller for SEIG with minimum number of sensors to make the system less complex and cost effective. Here, a voltage peak computation technique is developed using Hilbert Transform and computational efficient COordinate Rotation DIgital Computer (CORDIC) which requires only one voltage sensor and processed to control SEIG voltage for GIC based SEIG system. This voltage control scheme is implemented on commercially available TMS320F2812 DSP processor and performed laboratory experiment to study the performance of GIC based SEIG system during load switching. The work of this thesis is not confined only to study an optimal and simple voltage controller for SEIG system but also extended to investigate the fault identification methodologies of

SEIG system. Here, the features of non-stationary SEIG signal with faults are extracted using Hilbert-Huang Transform (HHT). Further, different classifiers such as MultiLayer Perceptron (MLP) neural network, Probabilistic Neural Network (PNN), Support Vector Machine (SVM), and Least Square Support Vector Machine (LS-SVM) are used to identify faults of SEIG system. In this study, it is observed that LS-SVM among above classifiers provides higher classification accuracy of 99.25%.

**Keywords:** Renewable energy; Self-excited induction generator; Generalized impedance controller; Particle swarm optimization technique; Voltage peak computation; Fault detection; Feature extraction and classification methods.

# Contents

<b>Supervisor’s Certificate</b>	<b>ii</b>
<b>Dedication</b>	<b>iii</b>
<b>Declaration</b>	<b>iv</b>
<b>Acknowledgment</b>	<b>v</b>
<b>Abstract</b>	<b>vi</b>
<b>List of Figures</b>	<b>xii</b>
<b>List of Tables</b>	<b>xxii</b>
<b>List of Abbreviations</b>	<b>xxii</b>
<b>List of symbols</b>	<b>xxiv</b>
<b>1 Introduction</b>	<b>1</b>
1.1 Background . . . . .	1
1.2 Motivation of the present work . . . . .	2
1.3 Objective of the present work . . . . .	3
1.4 Overview of the work done and methods . . . . .	3
1.5 Contribution of the thesis . . . . .	5
1.6 Organization of the thesis . . . . .	6
<b>2 Literature survey</b>	<b>7</b>
2.1 Introduction . . . . .	7
2.2 Modeling of SEIG to evaluate dynamic performance . . . . .	7

2.3	Voltage and frequency controller of SEIG . . . . .	9
2.4	Fault analysis of SEIG . . . . .	21
<b>3</b>	<b>Dynamic modeling and performance analysis of wind driven SEIG system</b>	<b>23</b>
3.1	Introduction . . . . .	23
3.2	Modeling of wind turbine . . . . .	24
3.3	Determination of minimum excitation capacitance value for the SEIG . . . . .	26
3.4	Modeling of SEIG . . . . .	29
3.5	Excitation modeling . . . . .	30
3.6	Load modeling . . . . .	31
3.6.1	For resistive load . . . . .	31
3.6.2	For $R - L$ load . . . . .	31
3.6.3	Modeling of induction motor as dynamic load . . . . .	31
3.7	Results and Discussion . . . . .	33
3.7.1	SEIG voltage build-up process at no-load . . . . .	34
3.7.2	Performance of SEIG during different loading condition . . . . .	36
3.8	Summary of the Chapter . . . . .	47
<b>4</b>	<b>Development of an optimized voltage controller for GIC based SEIG system</b>	<b>48</b>
4.1	Introduction . . . . .	48
4.2	Modeling of generalized impedance controller (GIC) . . . . .	49
4.3	Operation of generalized impedance controller (GIC) . . . . .	50
4.3.1	GIC operation while floats across SEIG . . . . .	51
4.3.2	GIC Operation as a capacitor or an inductor . . . . .	51
4.4	Voltage control of GIC based SEIG system . . . . .	53
4.5	Computation of optimal proportional and integral gains within stable zone for controlling SEIG voltage . . . . .	53
4.5.1	Parameters evaluation of GIC based voltage controller of SEIG system . . . . .	54
4.5.2	Derivation to compute stable zone of proportional and integral gains . . . . .	55
4.5.3	Computation of best optimal proportional and integral gains of voltage controlled GIC based SEIG system . . . . .	67
4.6	Results and Discussion . . . . .	74
4.6.1	Transient performance of optimized GIC based SEIG feeding resistive load . . . . .	74
4.6.2	Transient performance of optimized GIC based SEIG system feeding IM load . . . . .	94

4.6.3	Harmonic analysis of optimized GIC based SEIG system . . . . .	106
4.7	Summary of the chapter . . . . .	109
<b>5</b>	<b>GIC based SEIG system using HT and CORDIC</b>	<b>110</b>
5.1	Introduction . . . . .	110
5.2	Voltage control scheme of GIC based SEIG system using the proposed voltage computation technique . . . . .	111
5.2.1	Computation of voltage and frequency of SEIG using HT and CORDIC	111
5.2.2	Implementation of voltage controller of GIC based SEIG system using proposed voltage computation technique . . . . .	119
5.3	Results and Discussion . . . . .	120
5.4	Summary of the chapter . . . . .	126
<b>6</b>	<b>Fault analysis of SEIG system</b>	<b>127</b>
6.1	Introduction . . . . .	127
6.2	Transient performance analysis of SEIG during balanced and unbalanced faults . . . . .	128
6.2.1	Three phase short circuit across SEIG . . . . .	128
6.2.2	Line-to-line fault across SEIG . . . . .	130
6.2.3	Single capacitor opening in capacitor bank . . . . .	131
6.2.4	Single line opening at load . . . . .	132
6.2.5	SEIG electromagnetic torque in various faults taken for investigations	134
6.3	Hilbert-Huang Transform (HHT) . . . . .	134
6.3.1	Empirical Mode Decomposition (EMD) . . . . .	135
6.3.2	Hilbert Transform (HT) . . . . .	137
6.4	Feature Extraction using Hilbert-Huang Transform (HHT) . . . . .	141
6.5	Classification . . . . .	141
6.5.1	Classification using MultiLayer Perceptron (MLP) neural network .	142
6.5.2	Classification using Probabilistic Neural Network (PNN) . . . . .	143
6.5.3	Classification using Support Vector Machine (SVM) . . . . .	145
6.5.4	Classification using Least Square Support Vector Machine (LS-SVM)	154
6.6	Results and Discussion . . . . .	157
6.7	Summary of the chapter . . . . .	160
<b>7</b>	<b>Conclusions and future scope</b>	<b>161</b>
7.1	Conclusions of the thesis . . . . .	161
7.2	Scope for future work . . . . .	163

<b>References</b>	<b>164</b>
<b>Thesis Dissemination</b>	<b>171</b>
<b>Author's Biography</b>	<b>172</b>
<b>Appendix</b>	<b>174</b>



# List of Figures

2.1	Different types of voltage regulating scheme of SEIG . . . . .	9
2.2	Thyristor switched capacitor scheme of VAR compensator . . . . .	10
2.3	Voltage control of SEIG based on Static VAR Compensator (SVC) . . . . .	11
2.4	Schematic diagram of regulated voltage of SEIG using DC load control . . .	13
2.5	Voltage regulation of SEIG using short shunt . . . . .	13
2.6	Voltage regulation of SEIG using long-shunt . . . . .	14
2.7	Representation of STATCOM . . . . .	15
2.8	Control strategy of current controlled based STATCOM to regulate SEIG voltage . . . . .	16
2.9	Schematic diagram of voltage and frequency regulator of SEIG using ELC .	17
2.10	Schematic diagram of voltage and frequency regulator of SEIG using gen- eralized impedance controller . . . . .	17
2.11	Schematic diagram of voltage and frequency regulator of SEIG using solid state regulator . . . . .	18
2.12	Schematic diagram of voltage controller of SEIG using DC load controller .	19
2.13	Schematic diagram of voltage controller of SEIG using wavelet/PSO based embedded system integrated with SEIG and STATCOM . . . . .	20
2.14	Schematic diagram of SSSC based SEIG voltage controller . . . . .	21
3.1	Schematic diagram of a SEIG system . . . . .	24
3.2	Power coefficient ( $C_p$ ) vs tip speed ratio ( $\lambda$ ) . . . . .	25
3.3	Mechanical power vs turbine speed at different wind speeds . . . . .	26
3.4	Per phase equivalent circuit of the self-excited induction generator . . . . .	27
3.5	Simplified representation of the circuit of Figure 3.4 . . . . .	27
3.6	Graph of the identified (black) and approximated (red) magnetizing induc- tances vrs magnetising current . . . . .	34
3.7	Simulation results of wind driven SEIG system at no load: (a) Line voltage of SEIG (b) Peak of the line voltage of SEIG (c) Stator line current of SEIG (d) Capacitor current (e) Frequency of SEIG . . . . .	35

3.8	Experimental set up of SEIG system . . . . .	36
3.9	Experimental waveforms of SEIG stator voltage and current build-up process of SEIG system at no load . . . . .	36
3.10	Simulation results of SEIG with resistive loading: (a) SEIG stator line voltage (b) SEIG stator line current (c) Load current (d) SEIG frequency (e) SEIG active power (f) Reactive power demanded by SEIG . . . . .	37
3.11	Captured experimental waveforms of SEIG stator line voltage and load current during loading condition . . . . .	38
3.12	Simulation results of SEIG with $R - L$ load switching: (a) SEIG active power (b) Reactive power demanded by SEIG (c) Stator peak voltage (d) Stator line current (e) Load current (f) SEIG frequency . . . . .	39
3.13	Simulation results of overloaded SEIG system: (a) SEIG active power (b) Reactive power demanded by SEIG (c) Stator line voltage (d) Load current . . . . .	40
3.14	Experimental waveforms of overloaded SEIG line voltage and load current . . . . .	40
3.15	Simulation results of wind turbine driven SEIG fed IM load system:(a) SEIG active power (b) Reactive power demanded by SEIG (c) Stator line voltage (d) Load current . . . . .	41
3.16	Experimental set up of SEIG fed IM load . . . . .	42
3.17	Experimental waveforms of SEIG fed IM load: SEIG line voltage (top), stator current of IM load (bottom) . . . . .	42
3.18	Simulation results of wind turbine driven SEIG system with wind speed perturbations: (a) Wind speed (b) SEIG rotor speed (c) SEIG peak voltage (d) Active power of SEIG (e) Reactive power demanded by SEIG (f) Load current (g) SEIG frequency . . . . .	44
3.19	Simulation results of wind turbine driven SEIG system with with increase of excitation capacitance: (a) SEIG line voltage (b) SEIG peak voltage (c) Active power of SEIG (d) Reactive power demanded by SEIG (e) SEIG stator line current (f) Load current (g) SEIG frequency . . . . .	46
3.20	Experimental waveforms of SEIG stator voltage (top) and load current (bottom) with increase of excitation capacitance value . . . . .	47
4.1	Schematic diagram of a GIC based SEIG system . . . . .	50
4.2	Phasor diagram of GIC while floating across SEIG . . . . .	51
4.3	Phasor diagram of GIC while operated as capacitor . . . . .	52
4.4	Phasor diagram of GIC while operated as inductor . . . . .	52
4.5	Feedback control system . . . . .	54

4.6	Open loop response of GIC based SEIG system for step change in modulation index . . . . .	55
4.7	Plot of the terms involved in expression (4.33) for $-\frac{1}{k_v} < k_p < \frac{1}{k_v}$ . . . . .	58
4.8	Plot of the terms involved in expression (4.33) for $k_p = \frac{1}{k_v}$ . . . . .	59
4.9	Plot of the terms involved in expression (4.33) for $-\frac{1}{k_v} < k_p$ . . . . .	59
4.10	Regions associated with parameter $a_j$ . . . . .	62
4.11	Analysis of equation (4.33) in the $k_p - z$ plane when $T > 0$ . . . . .	63
4.12	Plot for finding $\alpha$ of the voltage controlled GIC based SEIG system . . . . .	66
4.13	Plot for finding $z$ of the voltage controlled GIC based SEIG system . . . . .	67
4.14	Stable zone of proportional and integral gains for voltage controlled GIC based SEIG system . . . . .	68
4.15	Flow chart to compute the optimum value of $k_p$ and $k_i$ using particle swarm optimization technique . . . . .	70
4.16	Simulation results of PSO to compute optimal gains for GIC based SEIG system for run 1 : (a) Searching value of $k_p$ (b) Searching value of $k_i$ . . . . .	71
4.17	Simulation results of PSO to compute optimal gains for GIC based SEIG system for run 2 : (a) Searching value of $k_p$ (b) Searching value of $k_i$ . . . . .	71
4.18	Simulation results of PSO to compute optimal gains for GIC based SEIG system for run 3 : (a) Searching value of $k_p$ (b) Searching value of $k_i$ . . . . .	71
4.19	Simulation results of SEIG peak voltage under different perturbations for 7 different $k_p$ and $k_i$ : (a) wind speed perturbation (b) Resistive load of 100 $\Omega$ /phase switched on (c) Resistive load of 400 $\Omega$ /phase added . . . . .	73
4.20	Simulation result showing SEIG and GIC voltage waveforms with steady-state value of $\delta$ after switching of GIC at no load . . . . .	75
4.21	Simulation results showing: (a) variation of SEIG active power after GIC switching (b) variation of GIC active power after connection with SEIG . . . . .	75
4.22	Simulation result showing variation of SEIG frequency after switching with GIC . . . . .	75
4.23	Simulation result showing modulation index variation of GIC (no-load) with time . . . . .	76
4.24	Simulation results showing reactive power variation of GIC based SEIG system at wind speed of 9.8 m/s: (a) SEIG (b) GIC (c) Excitation capacitor . . . . .	76
4.25	Simulation result showing variation of SEIG peak voltage after connection with GIC . . . . .	77

4.26	Closed loop simulation results of proposed GIC based SEIG system with loading and wind speed variations: (a) Wind speed variations (input for simulation)(b) Rotor speed of SEIG (c) Stator frequency of SEIG (d) Stator peak voltage of SEIG. . . . .	77
4.27	Simulation result showing variation of SEIG frequency corresponding to wind speed change from 9.8 m/s to 10.8 m/s . . . . .	78
4.28	Simulation result showing variation of SEIG active power corresponds to wind speed change from 9.8 m/s to 10.8 m/s . . . . .	78
4.29	Simulation result showing SEIG and GIC voltage waveforms with steady-state value of $\delta$ in wind speed change from 9.8 m/s to 10.8 m/s. . . . .	79
4.30	Simulation result showing variation of GIC active power corresponding to wind speed change from 9.8 m/s to 10.8 m/s . . . . .	79
4.31	Simulation result showing SEIG peak voltage waveform corresponding to wind speed change from 9.8 m/s to 10.8 m/s . . . . .	79
4.32	Simulation result showing variation of modulation index of GIC with time corresponding to wind speed change from 9.8 m/s to 10m/s. . . . .	80
4.33	Simulation results showing reactive power variation corresponding to wind speed change from 9.8 m/s to 10.8 m/s (a) GIC (b) SEIG (c) Excitation capacitor . . . . .	80
4.34	Simulation result showing variation of SEIG frequency due to switching of 100 $\Omega$ /phase load . . . . .	81
4.35	Simulation results showing active power variation due to switching of 100 $\Omega$ /phase load: (a) load (b) SEIG (c) GIC . . . . .	81
4.36	Simulation result showing SEIG and GIC voltage waveforms with steady-state value of $\delta$ due to switching of 100 $\Omega$ /phase load . . . . .	81
4.37	Simulation result showing variation of modulation index due to switching of 100 $\Omega$ /phase load . . . . .	82
4.38	Simulation result showing SEIG peak voltage waveform due to switching of 100 $\Omega$ /phase load . . . . .	82
4.39	Simulation results showing reactive power variation due to switching of 100 $\Omega$ /phase load: (a) GIC (b) SEIG (c) Excitation capacitor . . . . .	82
4.40	Simulation results showing active power variation due to load switching of 400 $\Omega$ /phase: (a) load (b) SEIG (c) GIC . . . . .	83
4.41	Simulation result showing SEIG and GIC voltage waveforms with steady-state value of $\delta$ due to load switching of 400 $\Omega$ /phase . . . . .	83
4.42	Simulation result showing variation of modulation index of GIC with time corresponding to load switching of 400 $\Omega$ /phase . . . . .	84

4.43	Simulation result showing SEIG peak voltage variation due to load switching of 400 $\Omega$ /phase . . . . .	84
4.44	Simulation results showing reactive power variation due to load switching of 400 $\Omega$ /phase: (a) GIC (b) SEIG (c) Excitation capacitor . . . . .	84
4.45	Simulation result showing variation of SEIG frequency corresponding to increase in wind speed from 10.8 m/s to 11.2 m/s . . . . .	85
4.46	Simulation result showing SEIG and GIC voltage waveforms with steady-state value of $\delta$ corresponding to increase in wind speed from 10.8 m/s to 11.2 m/s . . . . .	85
4.47	Simulation results showing variation of active power corresponding to increase in wind speed from 10.8 m/s to 11.2 m/s: (a) load (b) SEIG (c) GIC .	86
4.48	Simulation result showing variation of modulation index of GIC with time	86
4.49	Simulation result showing SEIG peak voltage variation corresponding to increase in wind speed from 10.8 m/s to 11.2 m/s . . . . .	86
4.50	Simulation results showing reactive power variation corresponding to increase in wind speed from 10.8 m/s to 11.2 m/s: (a) GIC (b) SEIG (c) excitation capacitor . . . . .	86
4.51	Simulation result showing variation of SEIG frequency corresponding to increase in wind speed from 11.2 m/s to 10.9 m/s . . . . .	87
4.52	Simulation result showing SEIG and GIC voltage waveforms with steady-state value of $\delta$ corresponding to decrease wind speed from 11.2 m/s to 10.9 m/s . . . . .	87
4.53	Simulation results showing variation of active power corresponding to decrease in wind speed from 11.2 m/s to 10.9 m/s: (a) load (b) SEIG (c) GIC .	88
4.54	Simulation result showing variation of modulation index of GIC with time corresponding to decrease in wind speed from 11.2 m/s to 10.9 m/s . . . . .	88
4.55	Simulation result showing variation of SEIG peak voltage corresponding to decrease in wind speed from 11.2 m/s to 10.9 m/s . . . . .	88
4.56	Simulation results showing reactive power variation corresponding to increase in wind speed from 11.2 m/s to 10.9 m/s: (a) GIC (b) SEIG (c) excitation capacitor . . . . .	88
4.57	Simulation result showing variation of SEIG frequency corresponding to removal of load at wind speed 10.9 m/s . . . . .	89
4.58	Simulation result showing SEIG and GIC voltage waveforms with steady-state value of $\delta$ corresponding to removal of load at wind speed 10.9 m/s . .	90
4.59	Simulation results showing variation of active power corresponding to removal of load at wind speed 10.9 m/s: (a) load (b) SEIG (c) GIC . . . . .	90

4.60	Simulation result showing variation of modulation index of GIC with time corresponding to removal of load at wind speed 10.9 m/s . . . . .	90
4.61	Simulation result showing variation of SEIG peak voltage corresponding to removal of load at wind speed 10.9 m/s m/s . . . . .	91
4.62	Simulation results showing variation of reactive power corresponding to removal of load at wind speed 10.9 m/s: (a) GIC (b) SEIG (c) excitation capacitor . . . . .	91
4.63	Simulation result showing variation of SEIG frequency corresponding to decrease in wind speed from 10.9 m/s to 10.5 m/s . . . . .	92
4.64	Simulation result showing SEIG and GIC voltage waveforms with steady-state value of $\delta$ corresponding to decrease in wind speed from 10.9 m/s to 10.5 m/s . . . . .	92
4.65	Simulation results showing variation of active power corresponding to decrease in wind speed from 10.9 m/s to 10.5 m/s: (a) load (b) SEIG (c) GIC .	92
4.66	Simulation result showing variation of modulation index of GIC corresponding to decrease in wind speed from 10.9 m/s to 10.5 m/s . . . . .	93
4.67	Simulation result showing variation of SEIG peak voltage corresponding to decrease in wind speed from 10.9 m/s to 10.5 m/s m/s . . . . .	93
4.68	Simulation results showing variation of reactive power corresponding to decrease in wind speed from 10.9 m/s to 10.5 m/s: (a) GIC (b) SEIG (c) Excitation capacitor . . . . .	93
4.69	Closed loop simulation results of stator current and load current waveforms of optimized GIC based SEIG system during different perturbations: (a) Stator line current waveform of of SEIG (b) Load current waveform . . . .	94
4.70	Closed loop simulation results of proposed GIC based SEIG with IM loading and wind speed perturbations: (a) Wind speed (b) Rotor speed of SEIG (c) Stator frequency of SEIG (d) Stator peak voltage of SEIG . . . . .	95
4.71	Simulation result (GIC based SEIG system to feed IM load) showing SEIG frequency variation corresponding to wind speed change from 9.8 m/s to 10.8 m/s . . . . .	96
4.72	Simulation result (GIC based SEIG system to feed IM load) showing variation of SEIG active power corresponds to wind speed change from 9.8 m/s to 10.8 m/s . . . . .	97
4.73	Simulation result (GIC based SEIG system to feed IM load) showing SEIG and GIC voltage waveforms with steady state-value of $\delta$ in wind speed change from 9.8 m/s to 10.8 m/s . . . . .	97



4.74	Simulation result (GIC based SEIG system to feed IM load) showing variation of GIC active power corresponding to wind speed change from 9.8 m/s to 10.8 m/s (GIC based SEIG system to feed IM load) . . . . .	97
4.75	Simulation result (GIC based SEIG system to feed IM load) showing SEIG peak voltage waveform corresponding to wind speed change from 9.8 m/s to 10.8 m/s (GIC based SEIG system to feed IM load) . . . . .	98
4.76	Simulation result (GIC based SEIG system to feed IM load) showing variation of modulation index of GIC with time corresponding to wind speed change from 9.8 m/s to 10.8 m/s . . . . .	98
4.77	Simulation results (GIC based SEIG system to feed IM load) showing reactive power variation corresponding to wind speed change from 9.8 m/s to 10.8 m/s (GIC based SEIG system to feed IM load): (a) GIC (b) SEIG (c) Excitation capacitor . . . . .	98
4.78	Simulation results of speed and torque variation of IM load (mechanical load is zero) connected with GIC based SEIG at 10.8 m/s wind speed: (a) Rotor Speed of IM (b) Electromagnetic torque of IM . . . . .	99
4.79	Simulation result showing SEIG frequency variation with IM load (mechanical load is zero) at 10.8 m/s wind speed . . . . .	99
4.80	Simulation results showing active power variation with IM load (mechanical load is zero) at 10.8 m/s wind speed: (a) SEIG (b) GIC (c) IM load . . . . .	99
4.81	Simulation result showing variation of SEIG peak voltage with IM load (mechanical load is zero) at 10.8 m/s wind speed speed . . . . .	100
4.82	Simulation results showing reactive power variation with IM load (mechanical load is zero) at 10.8 m/s wind speed speed: (a) SEIG (b) IM load (c) Excitation capacitor (d) GIC . . . . .	100
4.83	Simulation results showing speed and torque variation of IM load corresponding to insertion of mechanical load of 4 Nm with 10.8 m/s wind speed: (a) IM speed (b) IM torque . . . . .	101
4.84	Simulation result showing SEIG frequency variation corresponding to IM load (insertion of 4 Nm mechanical load ) with 10.8 m/s wind speed . . . . .	101
4.85	Simulation results showing active power variation corresponding to IM load (insertion of 4 Nm mechanical load ) with 10.8 m/s wind speed . . . . .	101
4.86	Simulation results showing reactive power variation corresponding to IM load (insertion of 4 Nm mechanical load ) with 10.8 m/s wind speed: (a) SEIG (b) IM load (c) excitation capacitor (d) GIC . . . . .	102
4.87	Simulation result showing SEIG frequency variation corresponding to IM load (4 Nm mechanical load ) with 11.2 m/s wind speed . . . . .	102

4.88	Simulation results showing active power variation corresponding to IM load (4 Nm mechanical load) with 11.2 m/s wind speed: (a) SEIG (b) IM load (c) GIC . . . . .	103
4.89	Simulation results showing reactive power variation corresponding to IM load (4 Nm mechanical load ) with 11.2 m/s wind speed: (a) SEIG (b) IM load (c) Excitation capacitor (d) GIC . . . . .	103
4.90	Simulation results showing speed and torque variation of IM load corresponding to wind speed 11.2 m/s (at t=7 s) and 10.9 m/s (at t=8 s): (a) IM speed (b) IM torque . . . . .	104
4.91	Simulation result showing SEIG frequency variation corresponding to wind speed 11.2 m/s (at t=7 s) and 10.9 m/s (at t=8 s) with IM load . . . . .	104
4.92	Simulation results showing active power variation corresponding to wind speed 11.2 m/s (at t=7 s) and 10.9 m/s (at t=8 s) with IM load: (a) SEIG (b) IM load (c) GIC . . . . .	105
4.93	Simulation results showing reactive power variation corresponding to wind speed 11.2 m/s (at t=7 s) and 10.9 m/s (at t=8 s) with IM load: (a) SEIG (b) IM load (c) excitation capacitor (d) GIC . . . . .	105
4.94	Simulation results of SEIG stator current and IM stator current waveforms of GIC based SEIG with IM loading and wind speed perturbations: (a) SEIG stator current (b) stator current of IM load . . . . .	106
4.95	FFT analysis of optimized GIC based SEIG system feeding resistive load: (a) SEIG stator voltage (b) SEIG stator current (c) load voltage (d) load current . . . . .	107
4.96	FFT analysis of optimized GIC based SEIG system feeding IM load: (a) SEIG stator voltage (b) SEIG stator current (c) IM stator voltage (d) IM stator current . . . . .	108
5.1	Block diagram of the conventional peak voltage computation technique . .	112
5.2	Block diagram of the proposed peak voltage computation technique using HT and CORDIC . . . . .	112
5.3	Rotation of vector on a two dimensional plane . . . . .	114
5.4	Rotation of vector on a two dimensional plane performing a series of successive $n$ -rotations . . . . .	115
5.5	Schematic diagram of the proposed GIC based voltage controlled SEIG system using HT and CORDIC algorithm . . . . .	120



5.6	Simulation results to test the proposed amplitude and frequency estimation technique: (a) Voltage signal with varying amplitude and frequency (b) Computed voltage amplitude using proposed technique (c) Computed frequency using proposed technique. . . . .	121
5.7	Simulation result of peak voltage computation of SEIG during speed and load perturbations in closed loop using two different peak computation techniques. . . . .	122
5.8	Schematic diagram of the control circuit to implement the proposed control scheme. . . . .	123
5.9	Experimental set up to implement the proposed technique using TMS320F2812 DSP processor . . . . .	123
5.10	Experimental results (a) Generation of pulses (b) Wave form of line voltage of GIC and SEIG during synchronization of GIC with SEIG (c) Wave form of line voltage of GIC (filtered) and SEIG after synchronization of GIC with SEIG . . . . .	124
5.11	Captured experimental photograph of GIC integration with SEIG using TMS320F2812 DSP processor . . . . .	125
5.12	Experimental waveforms of SEIG line voltage, line current and load line current during GIC and load switching in closed loop using proposed technique. . . . .	126
6.1	Diagram of SEIG system . . . . .	128
6.2	Diagram of SEIG system with three phase short circuit fault . . . . .	129
6.3	Simulation results of SEIG performance for three phase short circuit fault: (a) SEIG voltage waveform (b) SEIG current waveform . . . . .	130
6.4	SEIG re-excitation voltage and current waveforms after three phase short circuit fault clearing and load removal . . . . .	131
6.5	Diagram of SEIG system with line-to-line fault . . . . .	131
6.6	Simulation results of SEIG performance for line-to-line fault: (a) SEIG voltage waveform (b) SEIG current waveform . . . . .	132
6.7	SEIG voltage and current waveforms after clearance of line-to-line fault and load removal . . . . .	132
6.8	SEIG voltage and current waveforms for one capacitor opening . . . . .	133
6.9	SEIG voltage and current waveforms for opening of one phase of load . . . . .	133
6.10	Simulation results of electromagnetic torque developed by SEIG during different faults: (a) Three phase short circuit (b) Line-to-line fault (c) Single capacitor opening (d) Single phase load opening . . . . .	134

6.11	Negative sequence component of SEIG stator voltage (before and after) (a) for three phase short circuit fault (b) for line-to-line fault . . . . .	137
6.12	IMF components of SEIG stator negative sequence voltage (before and after) for three phase short circuit using EMD method . . . . .	137
6.13	IMF components of SEIG stator negative sequence voltage (before and after) for line-to-line fault using EMD method . . . . .	138
6.14	Simulation results for SEIG three phase short circuit detection using HT: (a) First IMF obtained from negative sequence voltage during three phase short circuit (b) instantaneous amplitude response of first IMF (c) instantaneous frequency response of first IMF . . . . .	140
6.15	Simulation results for SEIG line-to-line fault detection using HT: (a) First IMF obtained from negative sequence voltage during line-to-line fault (b) instantaneous amplitude response of first IMF (c) instantaneous frequency response of first IMF . . . . .	140
6.16	Block diagram of a classification process . . . . .	142
6.17	A multilayer perceptron neural network. . . . .	143
6.18	A probabilistic neural network. . . . .	144
6.19	SVM classifier (hard-margin) . . . . .	146
6.20	SVM classifier (soft-margin) . . . . .	150
6.21	Non-linear separation of input and feature space . . . . .	152
6.22	Two mappings in a support vector machine (i) nonlinear mapping from the input space to feature space; (ii) linear mapping from the feature space to output space . . . . .	152
6.23	Flowchart of the proposed technique to classify SEIG faults. . . . .	158
7.1	Root distribution of $\hat{C}_i(\hat{\omega})$ . . . . .	175

# List of Tables

3.1	The parameters of the wind turbine model . . . . .	33
3.2	Parameters of induction machine used as SEIG . . . . .	33
3.3	The constants of the magnetization characteristics of SEIG . . . . .	34
3.4	The parameters of the induction machine used as load . . . . .	41
3.5	Comparison of simulation and experimental results . . . . .	47
4.1	Computed proportional and integral gains of stable zones of GIC based SEIG system . . . . .	67
4.2	Parameters taken to implement PSO algorithm . . . . .	69
4.3	Optimal $k_p$ and $k_i$ gains obtained from PSO for 20 runs . . . . .	72
4.4	Total harmonic distortions comparison optimized GIC based SEIG system feeding resistive load with [1] . . . . .	108
4.5	Total harmonic distortions comparison optimized GIC based SEIG system feeding IM load with [1] . . . . .	108
5.1	Values of the elementary angles $\alpha_i$ for $i = 0$ to 15 . . . . .	115
5.2	Elementary functions using CORDIC algorithm . . . . .	118
6.1	SEIG fault classification results obtained using HHT with LS-SVM for 1st fold. . . . .	159
6.2	Comparison of fault classification results using different classifiers . . . . .	159
6.3	Average classification accuracy obtained over four-fold using four different classifier . . . . .	160

## List of Abbreviations

Abbreviation	Description
SEIG	Self-Excited Induction Generator
VAR	Volt Ampere Reactive
GIC	Generalized Impedance Controller
IGBT	Insulated Gate Bipolar Transistor
PWM	Pulse Width Modulated
VSI	Voltage Source Inverter
ELC	Electronic Load Controller
STATCOM	STATtic synchronous COMpensator
SSSC	Static Synchronous Series Compensator
STFT	Short-Time Fourier Transform (STFT)
DFT	Discrete Fourier Transform
DWT	Discrete Wavelet Transform
PSO	Particle Swarm Optimization
HT	Hilbert Transform
CORDIC	COordinate Rotation DIgital Computer
PI	Proportional and integral
DSP	Digital Signal Processor
ADC	Analog to Digital conversion
DAC	Digital to analog conversion
THD	Total Harmonic Distortion
SC	Short circuit
HHT	Hilbert-Huang-Transform
EMD	Empirical Mode Decomposition
IMF	Intrinsic Mode Functions
MLP	Multilayer Perceptron
PDF	Probability Density Function
MSE	Mean Square Error
PNN	Probabilistic Neural Network
SVM	Support Vector Machine
LS-SVM	Least Square Support Vector Machine
OVO	One vs one
OVA	One vs All

# List of Symbols

Symbol	Description
$\rho$	Density of air
$A$	Exposed area by the wind turbine
$v_\omega$	Wind speed
$C_p$	Power coefficient of the wind turbine
$\beta$	Blade pitch angle
$\lambda$	Tip speed ratio
$r$	Radius of the swept area of the wind turbine
$\omega_T$	Turbine angular speed
$V_g$	Air gap voltage
$F$	Per unit frequency
$V_L$	Terminal voltage
$v$	Per unit speed
$F$	Per unit frequency
$C$	Per phase value of excitation capacitance
$X_c$	Per unit reactance at base frequency
$R_s, R_r, R_L$	Per unit stator resistance, rotor resistance and load resistance, respectively
$X_{ls}, X_{lr}, X_L$	Per unit stator leakage reactance, rotor leakage reactance and load reactance, respectively
$X_m$	Per unit saturated magnetizing reactance
$I_s$	Steady state stator current
$i_{sd}, i_{sq}$	$d$ and $q$ components of SEIG stator currents
$i_{rd}, i_{rq}$	$d$ and $q$ components of SEIG rotor currents
$v_{sd}, v_{sq}$	$d$ and $q$ components of SEIG stator voltages
$v_{rd}, v_{rq}$	$d$ and $q$ components of SEIG rotor voltages
$i_m$	Magnetizing current of SEIG
$T_e$	Electromagnetic torque of SEIG
$T_{drive}$	Mechanical input torque of SEIG
$J$	Moment of inertia of SEIG rotor
$P$	Number of poles of SEIG
$R_{ld}, R_{lq}$	$d$ and $q$ components of load resistances
$L_{ld}$ and $L_{lq}$	$d$ and $q$ components of load inductances
$i_{sdm}$ and $i_{sqm}$	$d$ and $q$ components of stator currents of IM load
$i_{rdm}$ and $i_{rqm}$	$d$ and $q$ components of rotor currents of IM load
$v_{sdm}$ and $v_{sqm}$	$d$ and $q$ components of stator voltages of IM load
$v_{rdm}$ and $v_{rqm}$	$d$ and $q$ components of rotor voltages of IM load

Symbol	Description
$\omega_{mm}$	Mechanical rotor speed of IM load
$R_{sm}$	Stator resistance of IM load
$R_{rm}$	Rotor resistance of IM load
$L_{lsm}$	Stator leakage inductance of IM load
$L_{lrm}$	Rotor leakage inductance of IM load
$L_{mm}$	Unsaturated mutual inductance of IM load
$T_{Lm}$	Load torque applied to IM load
$J_m$	Moment of inertia of IM load
$P_m$	Number of poles of IM load
$\omega_{rm}$	Electrical rotor speed of IM load
$v_m$	SEIG peak voltage
$v_{mref}$	SEIG rated peak voltage
$\varepsilon(t)$	Error voltage
$m$	Modulation index
$V_{ab}, V_{bc}, V_{ca}$	SEIG line voltages
$f_p$	Instantaneous frequency
$x, y$	Initial vector
$x', y'$	Final vector
$\phi$	Rotation angle
$K_n$	Scale factor
$A_n$	Amplification factor
$n$	Number of rotations
$\alpha_i$	Elementary angles
$z_n$	Total accumulated rotation angle
$k_p$	Proportional gain
$k_i$	Integral gain
$S_a, S_b, S_c, \overline{S_a}, \overline{S_b}, \overline{S_c}$	Switching signals
$M_{max}(t)$	Local maxima
$M_{min}(t)$	Local minima
$A(t)$	Mean of the upper and lower envelope
$C_1(t)$	First IMF component
$R(t)$	Residual component
$V_n$	Negative sequence component of voltage
$NI, NH, NJ$	Number of nodes in the input layer, hidden layer, and output layer respectively
$w_{ih}$	Connection weight between the input layer $i$ and hidden layer $h$
$w_{hj}$	Connection weight between the hidden layer $h$ and output layer $j$
$o_i$	output vector of the input layer
$o_j$	output vector of the hidden layer
$w$	weight vector
$b$	Offset or bias term
$D$	Margin
$S_1, S_2$	Support vectors
$F(w)$	Objective function
$\gamma_i$	Lagrange multipliers
$J$	Lagrangian function
$N$	Training examples
$\Psi(x)$	Nonlinear mapping functions
$K$	Kernel function
$\eta$	Classification efficiency

# Chapter 1

## Introduction

### 1.1 Background

In many countries, a significant proportion of the population in the rural and remote area lives without power. Due to remote/isolated location and low population densities, supplying power to these areas by conventional means or by extending grid is too expensive and somewhere difficult. Oil crisis in the year 1970 and hope for the pollution-free environment have taken attraction of the energy researchers to use renewable energy sources such as solar, biomass, wind and micro-hydro for providing power to isolated/remote areas. Among aforesaid available renewable energy sources, wind and micro-hydro are found to be suitable in these areas [1], [2], [3], [4], [5]. According to Indian Wind Energy Association (InWEA), installed capacity of India from wind is 24,759 MW (as on November 2015) and ranked 4th in the world [6]. To generate electric power from such non-conventional sources, self-excited induction generator (SEIG) is found to be a suitable option for either using in grid connected mode or isolated mode [7], [8], [9]. SEIG is selected to be used in isolated or remote areas where accessible of grid supply is not possible by making small-scale power generating system in the range of 0.5 kW to 100 kW [10]. Selection of SEIG in these areas depends on its advantages such as low cost, less maintenance, and absence of DC excitation. High maintenance and installation costs including transmission losses of conventional power supply to remote or isolated place by means of power grid can be reduced by installing stand-alone wind driven SEIG system at those places. In the year of 1935, self-excitation concept in squirrel cage induction machine with capacitors at their stator terminals was introduced by Basset and Potter [1]. For a sufficient rotor speed of an externally driven induction machine, the residual magnetic flux enables to build up a low Electro Motive Force (EMF) across stator of the induction machine. By connecting the appropriate value of capacitor across stator terminals, the process of induced EMF and current in the stator continues to grow. The process of building voltage and current continues until a steady-state condition achieved [11]. But the problem associated with SEIG are its poor

voltage and frequency regulation under load and prime mover speed perturbations which put a limit on the use of SEIG for a long time. By controlling active and reactive power accurately, it is possible to regulate frequency and voltage of SEIG terminal during varied load and prime mover speed. Various efforts have been put by researchers in developing SEIG voltage and frequency controller. Existing control techniques use multiple sensors along with complex electronic circuits that makes SEIG system complex and expensive. Hence, SEIG system demands simple and efficient control techniques with minimum number of sensors to reduce the complexity of the system for regulating voltage and frequency.

Similar to voltage and frequency control issues fault analysis and detection of SEIG system are also very challenging issues in remote and isolated areas. Voltage collapse and de-excitation occurs in SEIG during short circuit fault, line-to-line fault and single phase capacitor opening and these faults develop excessive high torque. Torque pulsation also occurs due to single line opening at SEIG load [12]. Voltage collapse occurs during these cases within 5 to 6 cycles. So conventional protection schemes are not able to identify these faults [13]. In addition to this, it is essential to investigate fault identification methodologies of SEIG system to avoid interruption of power supply and to reduce the risk of shaft failure of SEIG.

## **1.2 Motivation of the present work**

As discussed in the previous section, SEIG system used in isolated/remote areas has significant importance which attracted many researchers to study its voltage control and fault detection scheme. Recently different types of voltage and frequency controller are addressed for SEIG system such as on STatic Synchronous Compensator (STATCOM) [14], Electronic Load Controller (ELC) [15], Generalized Impedance Controller (GIC) [16] and Static Synchronous Series Compensator (SSSC) [1]. All these control schemes are based on sensing either voltage or current which require multiple sensors and complex electronic circuits which make SEIG system complex and expensive. Hence to make voltage control scheme of SEIG system simple, minimum number of sensors preferably a single sensor should be used along with simple electronic system.

Understanding the importance of SEIG, the performance analysis of SEIG during balanced and unbalanced faults should be investigated. Few literatures have reported transient performance analysis during balanced and unbalanced faults of SEIG systems and recently (year 2013) [13], DWT has been used to identify the three phase short circuit fault. However, the faults of SEIG system are non-stationary in nature, thus the selection of mother wavelet in case DWT technique is also a major challenge. Hence an alternative signal



processing technique should be investigated to analyze faults of SEIG system.

### 1.3 Objective of the present work

The specific objectives of the thesis are presented as follows.

- To simulate wind turbine driven SEIG system by taking different types of loads such as resistive load,  $R - L$  load, induction motor (IM) load.
- To conduct laboratory experiments on SEIG system to verify its performance under different conditions without using any controller and to validate the simulation results.
- To propose a new technique to compute SEIG peak voltage using Hilbert transform and COordinate Rotation DIgital Computer (CORDIC).
- To develop voltage controller for SEIG system used in isolated or remote areas.
- To compute optimal values of proportional and integral gains of the voltage controller, using Particle Swarm Optimization (PSO) technique.
- To simulate and to analyze SEIG system performance with the developed controller for wind speed variations, resistive and IM load.
- To implement the proposed control technique using a commercially available TMS320F2812 DSP processor and to conduct experiments on SEIG system to maintain rated voltage during load switching and to validate the simulation results.
- To perform transient analysis for SEIG system by taking different types of faults such as three phase short circuit, line-to-line fault, single line opening at load and single phase capacitor opening.
- To develop efficient signal processing technique for fault analysis of SEIG system.

### 1.4 Overview of the work done and methods

To study control and fault detection scheme for SEIG system it is essential to develop mathematical model of SEIG system. Thus, in the beginning of this thesis, mathematical model of SEIG system is developed. To develop the wind turbine driven SEIG system, a 4.2 kW wind turbine and a 3.7 kW induction machine are taken. Parameters of the induction machine used as SEIG are determined by conducting different tests (d.c resistance test, blocked rotor test and synchronous speed test) in the laboratory. The magnetization characteristic of the SEIG is nonlinear. From synchronous speed test, relation between magnetizing inductance  $L_m$  and magnetizing current  $i_m$  is obtained. There after steady-state and transient analysis of wind driven SEIG system are performed in MATLAB/Simulink environment for performance prediction. Experiments of SEIG system by taking resistive

load, induction motor load and heavy resistive load are also carried out. Experiment is also conducted by increasing capacitance excitation during loading condition to analyze SEIG performance.

As voltage and frequency controller are essential for SEIG system under load and prime mover speed variations, recently different types of voltage and frequency controller addressed for SEIG system such as STATCOM, ELC, GIC and SSSC. These control schemes are based on sensing either voltage or current which require multiple sensors and complex electronic circuits which make SEIG system complex and expensive. Among these control schemes, SEIG system integrated with GIC [16] maintain SEIG voltage and frequency efficiently with three sensors and one single loop using voltage as feedback. But, this voltage control scheme is not addressed the design of optimal proportional and integral gains which make GIC based SEIG system stable. However, determination of optimal proportional and integral gains which also makes the closed loop system stable is a tedious task. Many researchers have reported tuning methods in the ideal case for stabilizing *PID*, but they have not considered delay/dead times of the system. In 2002 Silva *et al.* [17] provided mathematical derivations to characterize the set of proportional, integral and derivative gains that stabilize the first-order plant with time delay. Further, these authors in 2005 [18] extended their work to provide mathematical derivations to characterize the set of proportional and integral gains that stabilize a first-order plant with time delay and in this thesis these mathematical derivations are used to compute stable zone of GIC based SEIG system. The plant (GIC integrated with SEIG) is considered here as a first order due to its step response. Parameters of this plant are also evaluated. Mathematical derivations provided by Silva *et al.* [18] are used to compute stable zones of proportional and integral gains for control voltage of SEIG integrated with GIC. Further optimal values of proportional and integral gains within stable zone are computed using PSO technique. Simulation is carried out to study the performance of an optimized GIC based SEIG system with wind speed variation, resistive and IM load. To show the effectiveness of the proposed technique for a 3.7 kW SEIG system, the computation of total harmonic distortions (THD) is assessed and compared with existing technique.

Generalized impedance controller is being used as voltage and frequency controller for SEIG systems. In this control scheme, the computation of instantaneous peak voltage plays a significant role. In the conventional technique, all the three terminal voltages of SEIG are required to be sensed for peak computation. This conventional approach demands three sensors along with arithmetic functions such as square, sum, and square root. Further, this work has been extended to make voltage controller simple and cost effective. In this context, a new technique is proposed to compute voltage using only one sensor along with Hilbert Transform (HT) and COordinate Rotation DIgital Computer (CORDIC). The pro-

posed technique is implemented on commercially available TMS320F2812 Digital Signal Processor to carry out experiment for GIC based SEIG system.

The work in this thesis is not confined only to study voltage control of SEIG system but also extended to identify SEIG faults. In this context, simulation is performed by taking different types of faults such as three phase short circuit, line-to-line fault, single line opening at load and single phase capacitor opening to perform the transient analysis of SEIG system. Using the mathematical model of SEIG and MATLAB/Simulink, different types of faults are initiated. For each type of fault, SEIG stator voltage signals are sensed and negative sequence component computed as it retains the information under disturbance condition. The Empirical Mode Decomposition (EMD) method is then applied to each negative sequence component for obtaining the intrinsic mode functions (IMFs). First 6 IMFs are selected and then, Hilbert Transform is applied on these IMFs. Further, the features of each IMF such as energy, standard deviation of the amplitude and phase contour are obtained. So, eighteen number of features are selected for each faulty signal. These features are used to study and classify faults of SEIG system by using various classifier methodologies such as MultiLayer Perceptron (MLP) neural network, Probabilistic Neural Network (PNN), Support Vector Machine (SVM), and Least Square Support Vector Machine (LS-SVM). In this study 140 different cases of each type of fault are taken where 40 and 100 cases selected randomly for training and testing of these classifiers methods. To evaluate these methods, the input size of the matrix is reshuffled and given to each classifier. The overall average accuracy obtained using classifiers MLP, PNN, SVM and LS-SVM are 92.75 %, 97 %, 98.25 % and 99.25 %, respectively. This is an obvious to select LS-SVM classifier along with proposed feature extraction methodology which provide the accuracy of 99.25 %.

## 1.5 Contribution of the thesis

With reference to brief work done and methods presented in the previous section, the main contributions of this thesis are highlighted here.

- Review of mathematical model of SEIG and its validation through MATLAB/Simulink simulations and experiments.
- Development of an optimized generalized impedance controller (GIC) for voltage control of SEIG system using particle swarm optimization (PSO).
- Development of simple GIC for voltage control of SEIG system using Hilbert transform (HT) and COordinate Rotation DIGital Computer (CORDIC) with one voltage sensor. This controller is implemented on commercially available DSP processor TMS320F2812 and

laboratory experiment is carried out for SEIG system.

■ A new fault detection and classification scheme for the SEIG system is proposed by exploiting Hilbert-Huang Transform (HHT) and Least Square Support Vector Machine (LS-SVM).

## 1.6 Organization of the thesis

The rest of the thesis is organized as following chapters.

**Chapter 2:** This chapter highlights critical reviews on modeling of SEIG to evaluate dynamic performance, different types of voltage and frequency controller of SEIG, different types of signal processing techniques to process SEIG fault signals.

**Chapter 3:** Dynamic modeling and performance analysis of wind driven SEIG system are the subject matters of this chapter.

**Chapter 4:** This chapter presents the development of an optimized generalized impedance controller (GIC) based SEIG system.

**Chapter 5:** A cost effective controller for GIC based SEIG system using Hilbert Transform and COordinate Rotation DIgital Computer (CORDIC) is presented in this chapter.

**Chapter 6:** The subject matters of this chapter is to propose an efficient methodology to detect the faults of SEIG system.

**Chapter 7:** This chapter concludes the work presented in the thesis by highlighting the limitation and future scope of the work presented in the thesis.

# Chapter 2

## Literature survey

### 2.1 Introduction

In this chapter, the literature survey is covered based on various issues associated with Self Excited Induction Generator (SEIG) and presented here in different subsections. Comparison of various works on SEIG is also presented to highlight the importance of the proposed work in subsequent chapters. Section 2.2 presents the review of work done by different researchers on modeling of SEIG to evaluate its dynamic performance. The major bottlenecks of SEIG are poor voltage and frequency regulation with varied prime mover speed and load. Section 2.3 covers various attempts put by researchers to develop voltage and frequency controller of SEIG. Understanding the importance of SEIG, it is realized that fault signals of SEIG should be analyzed to identify different types of SEIG faults. As the SEIG fault signals are non-stationary in nature, in this context section 2.4 describes the review of different types of signal processing techniques to analyze non-stationary signals.

### 2.2 Modeling of SEIG to evaluate dynamic performance

In this section, literature survey is carried out to discuss suitable existing techniques to analyze the performance of SEIG. Two approaches are available in literature to analyze SEIG; one approach uses per-phase equivalent circuit that includes loop-impedance method and node-admittance method, and another approach uses  $d - q$  axis model.

In literature numerous attempts have been explained to analyze SEIG using the per-phase equivalent circuit. The per-phase equivalent circuit is obtained from a steady-state condition. Literatures [19], [20], [21], [22], [23] have employed loop impedance method to analyse steady state performance of SEIG using per-phase equivalent circuit. In the loop impedance method, the equivalent impedance of the per-phase equivalent circuit is

separated into real and imaginary parts. Then, two simultaneous nonlinear equations are obtained to express frequency and magnetizing reactance of SEIG. The equations are then solved to get values of frequency and magnetizing reactance by using Newton-Raphson technique [22]. Nodal admittance method applied in [24], [25] to analyze steady-state performance of SEIG to the per-phase equivalent circuit. In the nodal admittance method, the equivalent admittance of the per-phase equivalent circuit is separated into real and imaginary parts. The real part of the admittance is expressed by a higher order polynomial of frequency and independent of magnetizing reactance [24]. The imaginary part of the admittance is a nonlinear equation and expressed regarding frequency and magnetizing reactance of SEIG. First frequency is determined from the real part of the equation and then substituted in the imaginary part of the equation to get magnetizing reactance. Obtained values of frequency and magnetizing reactance using either approach are then used to evaluate the steady-state performance of the SEIG with the help of magnetization curve. By using loop impedance and nodal admittance methods, it is possible to evaluate the steady-state performance of SEIG but the common problem with both approaches, require detailed algebraic derivations for the coefficients of the equations. So, both approaches can have chances of human errors and also are time-taking processes. Thus, the previous methods are not suitable, flexible and can applicable only to specific circuit models.

Recently, routines of MATLAB are available to obtain solution of a set of nonlinear equations (for evaluating steady-state performance) have been used by many researchers [26], [27], [28]. Obtaining solutions of these nonlinear equations with available MATLAB routines do not require detailed/explicit algebraic expression does not necessitate to use Newton-Raphson method where the partial derivative of the equations are required. Alolah and Alkanhal [26] solved the nonlinear equations by using classic global optimizers such as  $f_{min}$  and  $constr$  which are numerically based routines available in MATLAB. Haque [27] used  $f_{solve}$  routines available in Optimization Toolbox of MATLAB to solve nonlinear equations. But in both approaches, initial guess of unknown variables are required. Kheldoun used *DIRECT* algorithm [28] to evaluate steady-state performance of SEIG, this algorithm requires only the upper and lower values of unknown variables which are easy to calculate [28]. Genetic algorithm based technique is used by Joshi *et al.* in [29] to evaluate the steady-state performance of SEIG using the per-phase equivalent circuit. Since per-phase equivalent circuit approach is obtained from a steady-state condition, hence not helpful to analyze transient performance of SEIG.

Moreover, to evaluate both steady-state and transient performance of SEIG,  $d - q$  axis model approach which is based on the generalized machine theory have been used by many researchers Elder *et al.* [30], Grantham *et al.*, [31], Natarajan *et al.* [32] Shridhar *et al.* [33], Wang *et al.* [34], Seyoum *et al.* [11], Chatterjee *et al.* [35] and Idjdarene *et al.*[36].

It is reported in these literatures  $d - q$  axis model in stationary frame is suitable to evaluate SEIG performance during speed and load perturbations. It is also reported that SEIG voltage and frequency vary with speed and load perturbations [11]. In this context stationary frame model will be beneficial as it is easily interfaced with power electronic controller [32] which required to develop voltage and frequency controller and its capability for hardware implementation in real time described in next subsection.

## 2.3 Voltage and frequency controller of SEIG

In this section, reviews of work related to voltage and frequency regulation of SEIG developed by many researchers are described and highlighted. Voltage is regulated through reactive power control using shunt and series compensation. The overall classification of voltage regulating scheme of SEIG is presented in Fig. 2.1 [5] and described as follows.

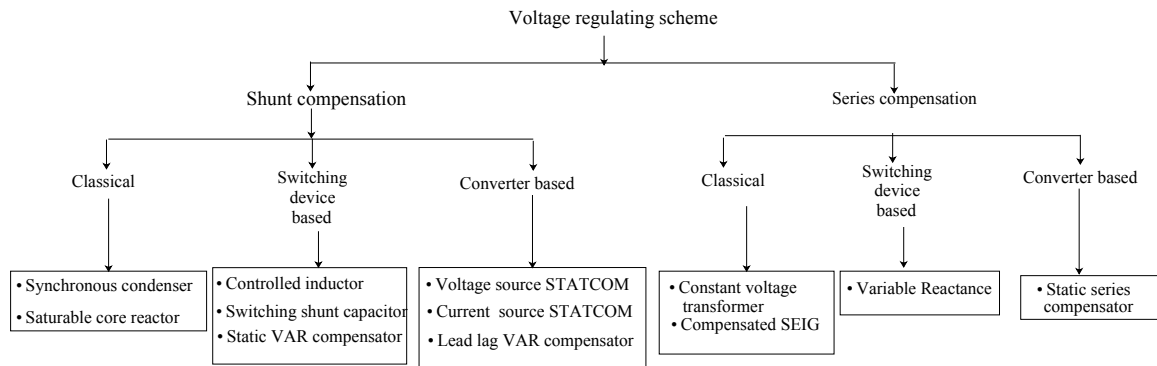


Figure 2.1: Different types of voltage regulating scheme of SEIG

In 1979 Ooi and David [37] suggested use of synchronous condenser to control excitation of SEIG. However, this scheme is very expensive if used in real time and also required maintenance for synchronous condenser and hence never used for SEIG.

Development of solid-state switches is attractive to many researchers. In the recent past numerous attempts have been done to develop low-cost voltage regulating scheme of SEIG by controlling VAR [30]. These studies helped to develop new technique for voltage and frequency controller of SEIG. Conventionally, fixed or, capacitor/inductor bank have been used for VAR compensator, power factor correction and voltage regulation.

Brennen and Abbondanti [38] and Malik and Haque [39] used thyristor controlled reactor (TCR) to develop voltage controller of SEIG. Commonly TCR consists of a fixed capacitor connected in parallel with a thyristor controlled inductor as shown in Fig. 2.2. Here, zero VAR demand makes zero excitation across SEIG. The thyristor switch is closed



so that the inductor cancels the influence of capacitor on SEIG. In case of non zero leading VAR demand, the closing of the switch is delayed by a variable angle (firing angle)  $\alpha$  with respect to peak of the SEIG so that the current across inductor can be decreased. With increasing value of  $\alpha$  ( $0^\circ \leq \alpha \leq 90^\circ$ ), the current across inductor further reduces, which results in increase of VAR for SEIG. For maximum VAR demands, only fixed capacitors are selected. This is possible by keeping firing angle of thyristor at  $90^\circ$  resulting the switch to open and zero current flows across inductor and maximum rated capacitive current flows for excitation. However, the problems associated with this scheme result losses in the inductor along with discontinuous nature of current drawn by the inductor. This injects large amount of harmonic current ( $5^{th}$ ,  $7^{th}$ ) into SEIG.

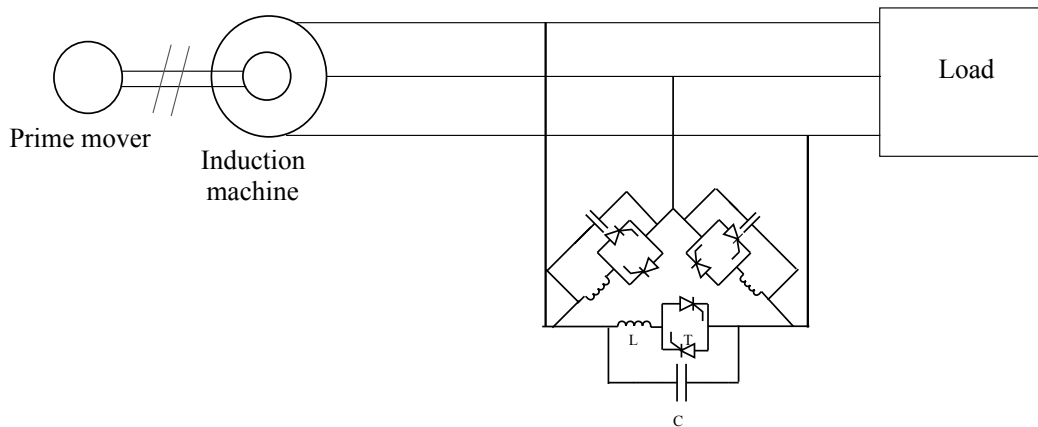


Figure 2.2: Thyristor switched capacitor scheme of VAR compensator

Elder [30] in 1984, attracted by the development of low-cost static VAR compensator, developed voltage control scheme of SEIG using TCR and Thyristor Switched Capacitor (TSC). In TSC scheme, a fixed capacitor bank is sufficient to excite the induction machine and run as SEIG at no load. However, loading and speed perturbation requires variable lagging VAR that generated by switching in additional steps of capacitance. The capacitance used for voltage control purpose are binary weighted to minimize the number of switches required to produce a given range of capacitance. In this scheme, a thyristor is placed in anti-parallel with a diode that results in maximum turn-on and turn-off times in one cycle. To avoid large inrush currents, the thyristor must turn on when the voltage across it is zero. This scheme is simple and cost effective. The presence of flickers on output voltage during load perturbation and the requirement of a large number of electronic switches and capacitors make these methods less attractive for general applications [40].

In 1987 Malik *et al.* [41] suggested terminal voltage of SEIG to be regulated by using excitation capacitor. It has been found that capacitance value required for a loaded machine



is significantly more than the no-load value and also it is affected by load impedance, power factor and machine speed. The maximum output power of SEIG depends on the terminal capacitance and the machine speed. Hence, practically it is not a feasible solution to control voltage. In 1992 Mishra *et al.* [42] developed a voltage regulator for SEIG to maintain voltage irrespective of the nature and amount of load. This voltage regulator contained a fixed value of capacitor bank and a saturable core reactor with appropriate feedback. This scheme regulates voltage by controlling current in the saturable core reactor. The demerits of this voltage scheme are involvement of large size and heavier weight of inductor.

In 2003, Tarek Ahmed *et al.* [43] proposed a new algorithm for evaluating the steady performance analysis of the three phases SEIG driven by a variable speed prime mover for stand-alone independent power supply. This scheme contains a closed loop (with *PI* controller) static VAR compensator composed of TCR in parallel with TSC to regulate terminal voltage as depicted in Fig. 2.3. In this technique, reactive power control possible but active power control is not possible. The problems with this scheme are sluggish response, high switching transients and injecting current harmonics into the bus.

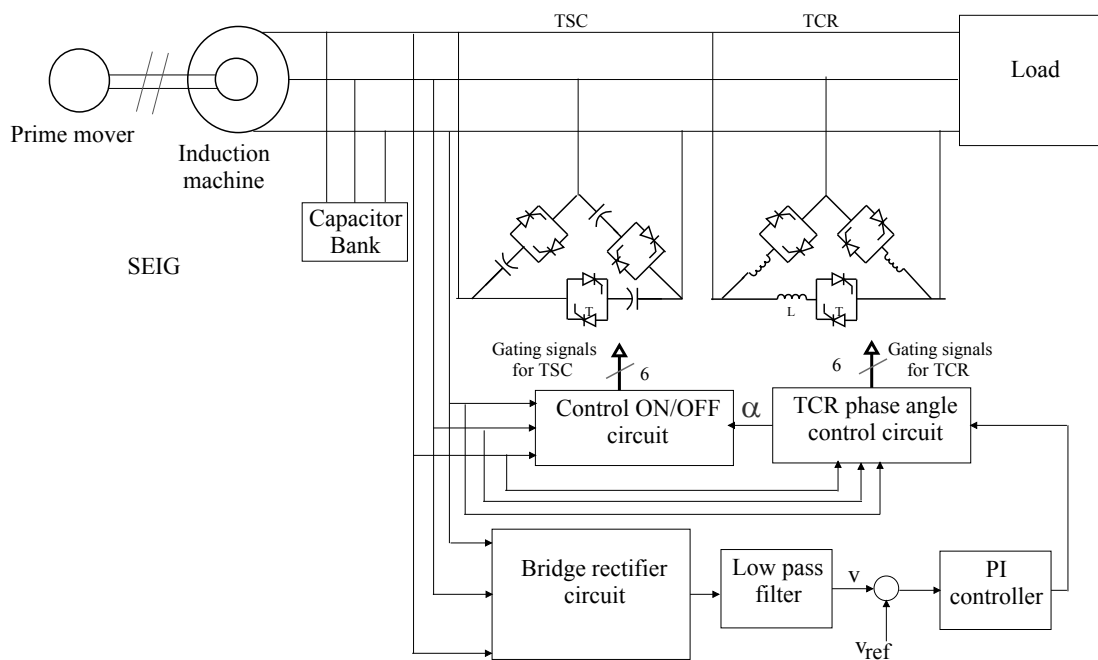


Figure 2.3: Voltage control of SEIG based on Static VAR Compensator (SVC)

SEIG voltage control is possible [30] by using naturally commutated converters,. This scheme uses AC/DC full wave 6-pulse bridge converter with single dc reactor. Naturally commutated converters can provide leading VAR (or drawing lagging VAR) which is required by SEIG. The VAR demanded by SEIG can be met by continuously adjusting

the trigger angle. The only disadvantage of this technique is that trigger angle lies between  $87^\circ$ - $90^\circ$  and for angles less than  $87^\circ$  large DC flows in the converter. This scheme also injects harmonics to SEIG terminals. Though a portion of this amount is filtered by excitation capacitor, still distortion occurs in SEIG voltage especially with light load [44]. Hence, this technique is not preferred to control SEIG voltage.

Lead-lag VAR compensators have been proposed by numerous researchers to obtain better VAR controlling capability in both lead and lag regions. Two common types of lead-lag VAR controllers are available; (i) Current source type lead-lag VAR compensator (ii) Voltage source type lead-lag VAR compensator.

Muljadi and Lipo [45] used a series connected pulse width modulated voltage source inverter with battery bank to control SEIG voltage and frequency. Disadvantage of this scheme is at lower SEIG speed, low-frequency harmonic distortions appear.

Khan [46] suggested a scheme using inductively loaded current controlled solid-state lead-lag VAR compensator in parallel with excitation capacitor. For triggered angle between  $90^\circ$ - $270^\circ$ , the compensator produce an equivalent capacitive effect at SEIG. Hence, self-excitation occurs and improves voltage regulation under wide input and load power variations. This compensator acts as a lag VAR source during low SEIG rotor speed and over load case. It acts as a lag VAR sink during high SEIG rotor speed and light load case. Though this scheme reported that could use for both micro-hydro and wind driven SEIG. But, there is chances of failure of this scheme for a heavy load at high SEIG rotor speed.

Hamid *et al.* [47] suggested a voltage regulating scheme using current type converter based STATCOM (CTC-STATCOM). In this scheme the converter is connected across the excitation capacitor of SEIG, which provides leading or lagging current depending on the load. Poor current sensitivity is a limitation of this scheme.

B Singh *et al.* [48] suggested a voltage regulating scheme using STATic synchronous CONDenser (STATCON). In this scheme,  $d - q$  axes stationary frame is used. This scheme consists fast power devices IGBTs. STATCON is nothing but a three-phase IGBT based current controlled voltage source inverter (CC-VSI) and an electrolytic capacitor at its DC side. STATCON is connected across the excitation capacitor and provides leading or lagging current, as SEIG required to maintain voltage with variation to load.

Marra and Pomilio, [49] in 1999 suggested a regulated voltage constant frequency scheme for SEIG using voltage source pulse width modulation bi-directional inverter and chopper. The PWM converter operates in this scheme as a VAR compensator with constant fundamental frequency and regulated voltage. In this scheme, two types of configuration are described one for DC load control and other for AC load control. Fig. 2.4 shows the schematic diagram of the regulated voltage of SEIG using DC load control. Here, the DC controllable load consists a resistance  $R_{dc}$  and switch  $S$ . Hysteresis control is used to

generate the pulse of switch  $S$ . Similarly for AC load voltage control AC load controller comprises of a three-phase delta connected resistive load where each branch is SCR controlled. In this configuration,  $V_{DC}$  is taken as one input of  $PI$  controller to produce SCR drive reference. In this scheme, SEIG voltage is regulated by keeping modulation index constant. This technique is simple but uses an extra switch that increases the cost of the system and also appears harmonic current in the DC capacitor.

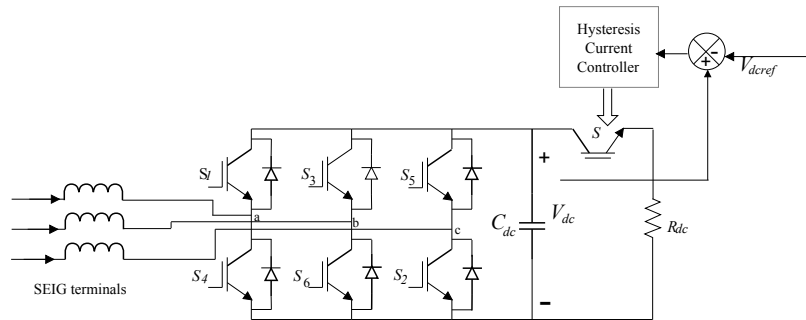


Figure 2.4: Schematic diagram of regulated voltage of SEIG using DC load control

Shridhar *et al.* [33] proposed a voltage regulating scheme of SEIG using short shunt. Fig. 2.5 shows voltage regulating scheme of SEIG using short-shunt. Series capacitors have zero contribution during no-load condition. As the load connects with SEIG system, the extra reactive power is injected into SEIG by inserting series capacitors. Selection of suitable value of series capacitance is essential.

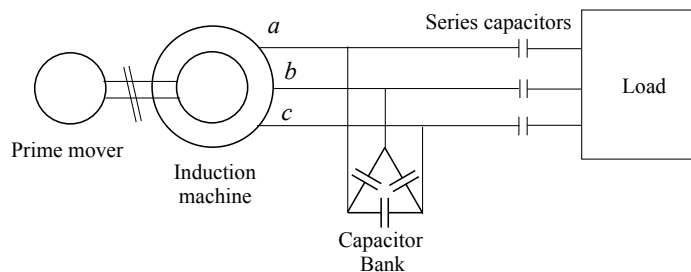


Figure 2.5: Voltage regulation of SEIG using short shunt

Wang and Lee [50] proposed a voltage regulating scheme of SEIG using both long shunt and short shunt to feed an induction motor (IM) load. The short-shunt configuration of SEIG system is already presented in Fig. 2.5. Series capacitors are connected between SEIG and IM load in this configuration. Series capacitance and impedance of IM load produce low-frequency oscillation of higher magnitude in IM currents, speed, torque. Low

frequency oscillation limit the IM speed to around half of its rated and sometimes will be responsible for subsynchronous resonance (SSR). Fig. 2.6 shows voltage regulating scheme of SEIG using long-shunt. For long shunt configuration, at no load both shunt and series capacitor contribute. However, higher values of shunt and series capacitance are needed for this configuration. Though, these schemes are simple and cost effective but result in unstable behavior while feeding IM load. S Singh *et al.* [51] suggested that using damping resistors across series capacitors low-frequency oscillation remove from the SEIG-IM system. Due to this chances of SSR occurrence also avoided and IM run successfully. But if the damping resistor is not selected properly, it results in voltage collapse for over damping and oscillations does not die out. B Singh *et al.* [52] suggested that by selecting a suitable value of the series capacitor in the short shunt configuration of SEIG system, IM operates safely. But if the selection is not correct SSR appears in SEIG IM system.

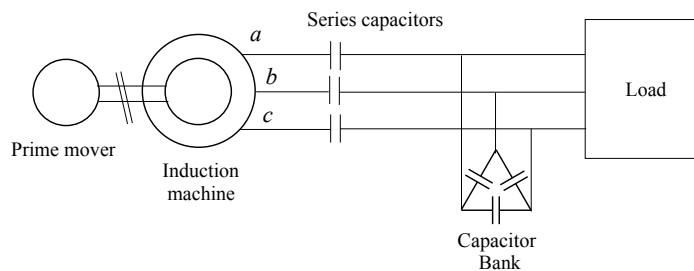


Figure 2.6: Voltage regulation of SEIG using long-shunt

Wekhnde *et al.* [53] presented an experimental studies of STATCON based SEIG which is suitable for variable speed, constant voltage operation. The transient and steady-state response of the system are good for only first two or three cycles. Active power control limited to furnishing only the losses in the generator system is a limitation of this scheme.

Kuo *et al.* [54] proposed a voltage regulating scheme of SEIG using STATic synchronous COMPensator (STATCOM). To develop SEIG in this scheme, synchronous rotating reference frame based on  $d - q$  axis model is used. STATCOM is nothing but a three-phase IGBT based current-controlled voltage source inverter (CC-VSI). CC-VSI consists six IGBT switches with anti-parallel diodes as shown in Fig. 2.7. The controlled lagging or leading currents injected by CC-VSI. The control strategy of this scheme is shown in Fig. 2.8, same with control strategy presented in [48]. This control scheme is based on source current control, employs two  $PI$  controller to generate reference source currents. Sensed DC voltage  $V_{dc}$  and reference DC voltage  $V_{dcref}$  are compared and error passed to one  $PI$  controller. The output of this  $PI$  controller is  $i_{smd}^*$ .  $i_{smd}^*$  maintains DC link voltage by charging or discharging of DC link capacitor,. SEIG peak voltage  $v_m$  and corresponding reference voltage  $v_{mref}$  are compared and error passed to the second  $PI$  controller. The out-

put of this *PI* controller is  $i_{smq}^*$ , responsible for maintaining SEIG peak voltage. In-phase reference source currents ( $i_{sad}^*$ ,  $i_{sbd}^*$ ,  $i_{scd}^*$ ) are computed by multiplying unit templates ( $u_a$ ,  $u_b$ ,  $u_c$ ) with  $i_{smd}^*$ . Unit amplitude templates ( $u_a$ ,  $u_b$ ,  $u_c$ ) are computed by dividing instantaneous voltages with peak voltage. Quadrature reference source currents ( $i_{saq}^*$ ,  $i_{sbq}^*$ ,  $i_{scq}^*$ ) are computed by multiplying quadrature current templates ( $w_a$ ,  $w_b$ ,  $w_c$ ) with  $i_{smq}^*$ . Finally, the reference source currents ( $i_{sa}^*$ ,  $i_{sb}^*$  and  $i_{sc}^*$ ) are computed by adding in-phase reference source currents and quadrature reference source currents. The reference source currents are compared with the sensed source currents ( $i_{sa}$ ,  $i_{sb}$  and  $i_{sc}$ ). Obtained error current signals are amplified and compared with the triangular carrier wave to get switching functions  $S_a$ ,  $S_b$ , and  $S_c$  of VSI for providing gate signals to IGBT. This voltage control scheme deals with both linear and non-linear load. This scheme provides fast response and able to operate at a high switching frequency. But this scheme involves huge computation along with two *PI* controller and this scheme is silent about SEIG frequency.

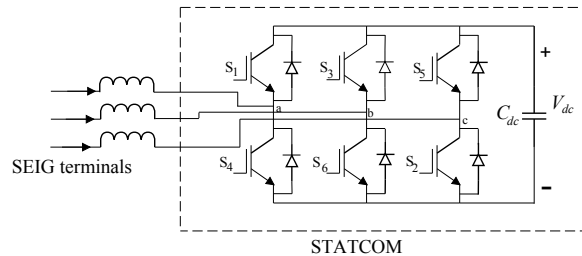


Figure 2.7: Representation of STATCOM

Lopes *et al.* in 2006, [55] proposed a voltage and frequency regulator by a reduced rating voltage source inverter (VSI). In this scheme, by connecting a shunt connected VSI and a controllable dump load across excitation capacitor SEIG is able to regulate voltage and frequency. The VSI provides active power to the load when the power generated by SEIG is insufficient. Control strategy developed in this scheme not only takes care of the charge/discharge of the battery but also maintains SEIG rated voltage. When prime mover speed increases, imbalance of active power occurs, and SEIG frequency rises above the rated value. To Maintain SEIG frequency, available excess active power stored in the battery bank and VSI absorbs that active power. But when the battery bank is fully charged or when the power through the VSI exceeds its rated value, dump load draws available excess active power. Similarly, VSI injects active power when the SEIG frequency decreases due to increase of load or reduction of wind speed. Limitation of this scheme is the involvement of dump load.

B Singh *et al.* [56] proposed an electronic load controller (ELC) for SEIG to regulate

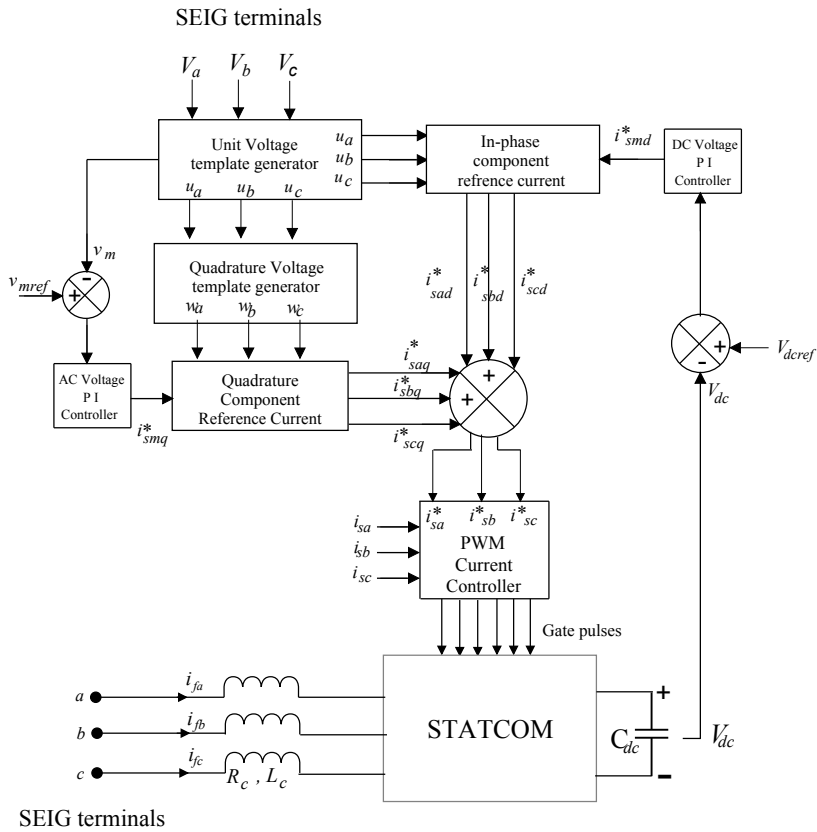


Figure 2.8: Control strategy of current controlled based STATCOM to regulate SEIG voltage

voltage and frequency as presented in Fig. 2.9. This type of regulator is suitable for low-power rating (less than 50 kW), uncontrolled hydro power unit. Here, for maintaining constant output power of SEIG with variation to consumer load, controllable dump loads are connected as described in [49]. Three-phase ELC comprises of a three-phase uncontrolled rectifier, filtering capacitor, chopper, and dump load. For low power applications, a single phase ELC is used where a three-phase rectifier replaced by single-phase rectifier. Other components are same but with different ratings and an IGBT is used for chopper. The efficiency of the system is low because of dump load so unattractive.

Perumal *et al.* [16] proposed voltage and frequency regulator of SEIG using generalized impedance controller (GIC) suitable for wind turbine driven SEIG. Control scheme of GIC based SEIG system is presented in Fig. 2.10. GIC is nothing but a pulse-width modulated (PWM) bidirectional voltage source inverter (VSI) with a bank of battery connected at its DC bus and reactor  $X_c$  connected across AC bus. GIC operates as a variable impedance across SEIG. In this scheme, SEIG peak voltage and rated peak are compared, and error passed to the *PI* controller. The output of *PI* controller (modulation index) is multiplied

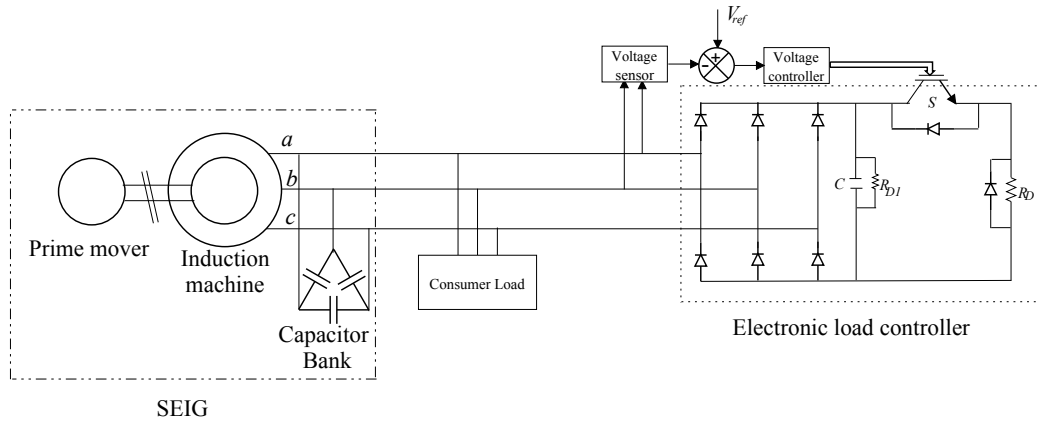


Figure 2.9: Schematic diagram of voltage and frequency regulator of SEIG using ELC

with sine wave of unit amplitude and reference frequency, and then compared with carrier wave to obtain switching signals  $S_a, S_b, S_c, \bar{S}_a, \bar{S}_b, \bar{S}_c$  of VSI for providing gate drives to IGBTs. SEIG voltage is regulated by updating modulation index of VSI and phase angle  $\delta$  between fundamental component of inverter output voltage and SEIG terminal voltage. Here, SEIG terminal frequency follows GIC frequency that is set at 50 Hz. Correction: The advantages of this control scheme are simplicity and requirement of three voltage sensors along with one PI controller.

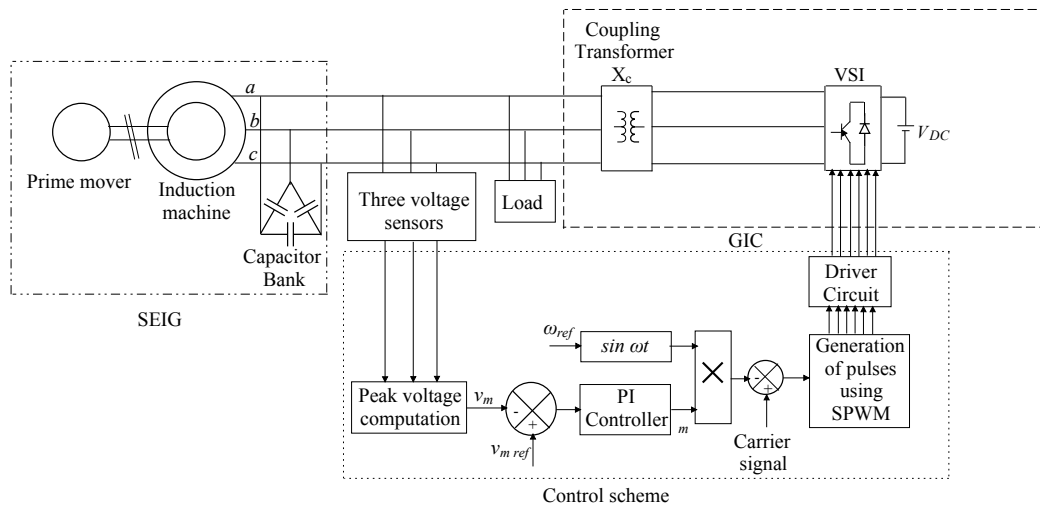


Figure 2.10: Schematic diagram of voltage and frequency regulator of SEIG using generalized impedance controller

B Singh and Kasal [57] proposed solid state voltage and frequency regulator which is suitable for wind turbine driven SEIG. The schematic diagram of the controller is shown



in Fig. 2.11. The controller comprises three-phase IGBT based voltage source converter along with a battery at its DC link. Unit amplitude templates ( $u_a, u_b, u_c$ ) are computed by dividing instantaneous voltages with peak voltage. Quadrature components ( $w_a, w_b, w_c$ ) are  $90^\circ$  leading to corresponding ( $u_a, u_b, u_c$ ). Two *PI* controllers are used in this voltage and frequency control scheme. Peak voltage of the SEIG and rated SEIG peak voltage are compared and error passed to *PI* voltage controller. Output of this *PI* controller is  $i_{smq}^*$ . Similarly, SEIG terminal frequency and rated frequency are compared and error passed to *PI* frequency controller. Output of this *PI* controller is  $P_c$ . By dividing difference of filtered load power and  $P_c$  with SEIG peak amplitude,  $i_{smd}^*$  is computed. Active or, in-phase reference source currents ( $i_{sad}^*, i_{sbd}^*, i_{scd}^*$ ) are computed by multiplying ( $u_a, u_b, u_c$ ) with  $i_{smd}^*$ . Reactive or, quadrature reference source currents ( $i_{saq}^*, i_{sbq}^*, i_{scq}^*$ ) are computed by multiplying quadrature current templates ( $w_a, w_b, w_c$ ) with  $i_{smq}^*$ . Reference source currents are generated from reactive reference source currents (responsible to control voltage) and active reference source currents (responsible to control frequency). Reference source currents and sensed source currents are responsible to generate gate pulses. This control scheme is disadvantageous owing to its huge computational burden for generating reference source current and use of two *PI* controllers.

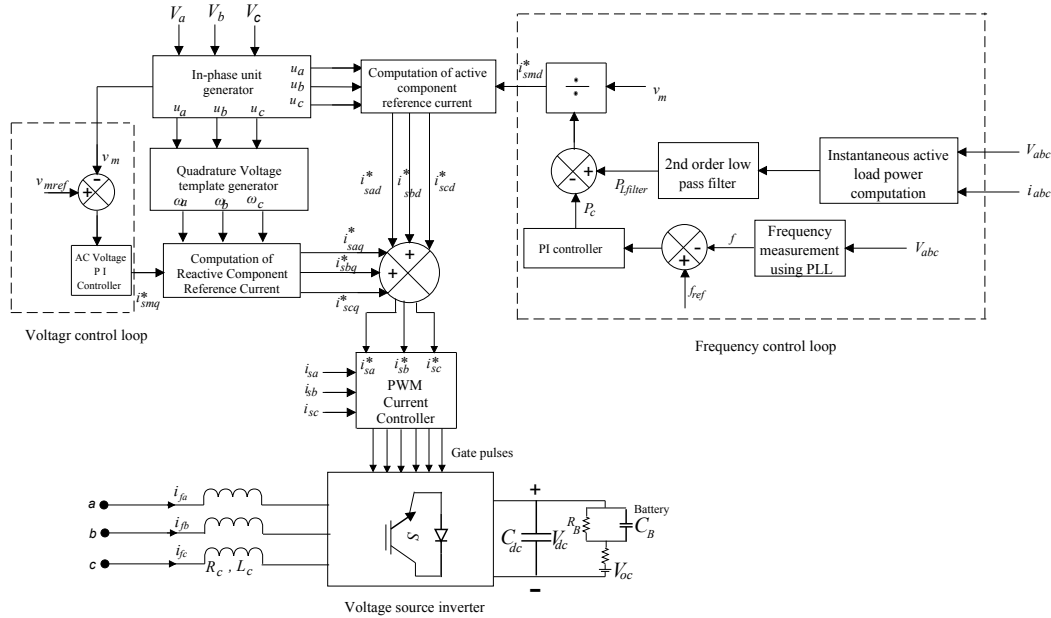


Figure 2.11: Schematic diagram of voltage and frequency regulator of SEIG using solid state regulator

Kasal *et al.* [58] developed STATCOM based voltage regulator to control SEIG peak voltage. Here, a dynamic load is connected across SEIG and control scheme verified exper-



imentally by using DSP processor.

Palwalia and Singh [59] proposed DSP based fuzzy voltage and frequency regulator for self-excited induction generator. This scheme used an equal time ratio control AC chopper controllable load. The consumer load and SEIG controller are connected in parallel across SEIG. The SEIG total power is the sum of consumer load power and dump load power. Dump power of this scheme controlled through IGBTs. When  $R$  load connected to SEIG, transfers of power from dump load to consumer load occur and load seen by SEIG behaves as constant. The limitation of this scheme is the proper design of dump load and wasted of power in dump load makes the voltage regulating scheme unattractive.

Youssef [9] proposed voltage and frequency regulator of SEIG as shown in Fig. 2.12 using pulse width modulation converter with variable DC-link voltage. In this scheme extra switch is absent, and SEIG voltage maintains with variation to load and speed perturbations by updating modulation index. In this way, this is different from [49]. Proper selection of  $R_{dc}$  is essential, this is one limitation of this scheme. The presence of  $R_{dc}$  is another disadvantage of this scheme as power wasted unnecessarily.

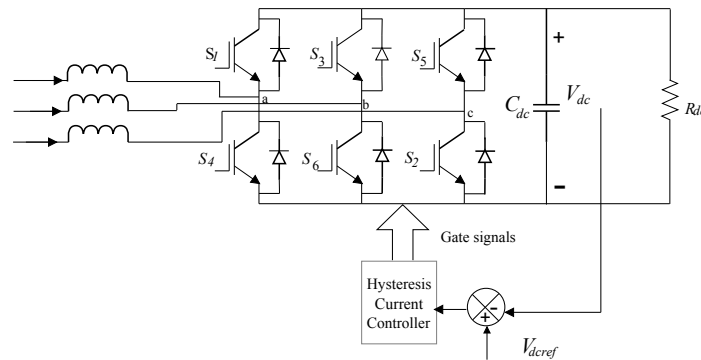


Figure 2.12: Schematic diagram of voltage controller of SEIG using DC load controller

Geng *et al.* suggested [60] a direct voltage control (DVC) scheme to control voltage and frequency of SEIG. This scheme consists a  $PI$  controller, lead-lag corrector and a feed-forward compensator. To validate this DVC scheme resistive-inductive and non-linear load used. Lead-lag corrector is used to extend the stability margin. Voltage harmonics are obtained in this scheme due to the cross-coupling matrix, to alleviate these harmonics feed-forward compensator is used.

Lu *et al.* [61] proposed a voltage regulating scheme of STATCOM based SEIG by combining Discrete Wavelet Transform (DWT) and particle swarm optimization (PSO) technique as presented in Fig. 2.13. Here, two different types of induction machines (i) copper rotor induction motor (CRIM) (ii) conventional aluminum rotor induction motor (ARIM) are used as SEIG. Transient appears in SEIG system due to load connection, which is de-

tected by using DWT. Load connection across SEIG demands adjustment of reactive power to maintain SEIG voltage that is computed by using PSO. Commonly in STATCOM based SEIG, reference source currents are generated from  $i_{smd}^*$  and  $i_{smq}^*$ . In this scheme,  $i_{smq}^*$  is computed by dividing SEIG terminal voltage with net reactance ( $X_{ctotal} - X_c$ ). PSO VAR estimator unit provides estimated reactance capacitance  $X_{ctotal}$  after load connection and  $X_c$  is the reactance of excitation capacitance required to develop rated SEIG voltage. Authors have presented experimental results employing 16-bit digital signal controllers using dsPIC33F family. The demerits of this control strategy are requirement of six number of sensors, three for sensing currents to detect load transient and three to compute SEIG peak voltage for computing VAR estimation using PSO.

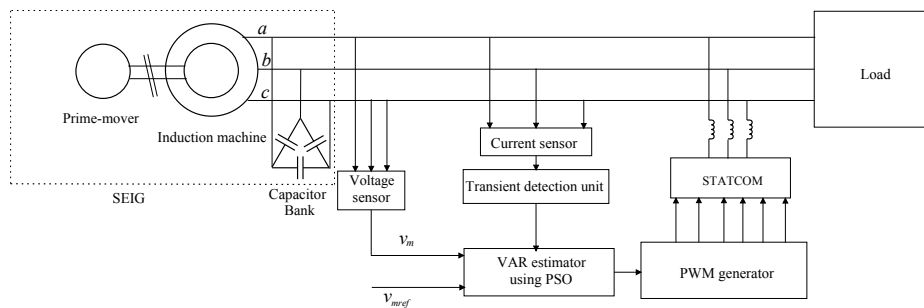


Figure 2.13: Schematic diagram of voltage controller of SEIG using wavelet/PSO based embedded system integrated with SEIG and STATCOM

Chauhan *et al.* [1] developed a voltage scheme of SEIG using Static Synchronous Series Compensator (SSSC) for different types of load such as resistive-inductive ( $R - L$ ), resistive-capacitive ( $R - C$ ) and dynamic motor loads. Schematic diagram of SSSC based SEIG is shown in Fig. 2.14, where SSSC consists CC-VSI, DC link battery and ripple LC filter. This scheme has only one  $PI$  controller that is responsible for generating reference supply current. Peak of the load voltage  $v_m$  is calculated to inject compensating voltage that is required to maintain voltage. So  $v_m$  and  $v_{mref}$  are compared and error sends as input to  $PI$  controller. The output of the  $PI$  controller is peak of the reference current  $i_{mref}$ , which is responsible for maintaining the load voltage by controlling reactive power. The in-phase current templates ( $u_a, u_b, u_c$ ) are computed from line currents ( $i_{sa}, i_{sb}, i_{sc}$ ) and quadrature current templates ( $w_a, w_b, w_c$ ) are computed from in-phase current templates. Reference supply currents ( $i_{sa}^*, i_{sb}^*$  and  $i_{sc}^*$ ) are generated by multiplying  $i_{mref}$  with ( $w_a, w_b, w_c$ ). Finally, reference supply currents and SEIG currents are two inputs to hysteresis current controller for generating gate signals. SSSC behaves as an inductor when the injected voltage is in quadrature leads to the line current. SSSC behaves as a capacitor when the injected voltage is in quadrature lags to the line current. This scheme is valid to regulate SEIG voltage only

and not applicable to regulate SEIG frequency.

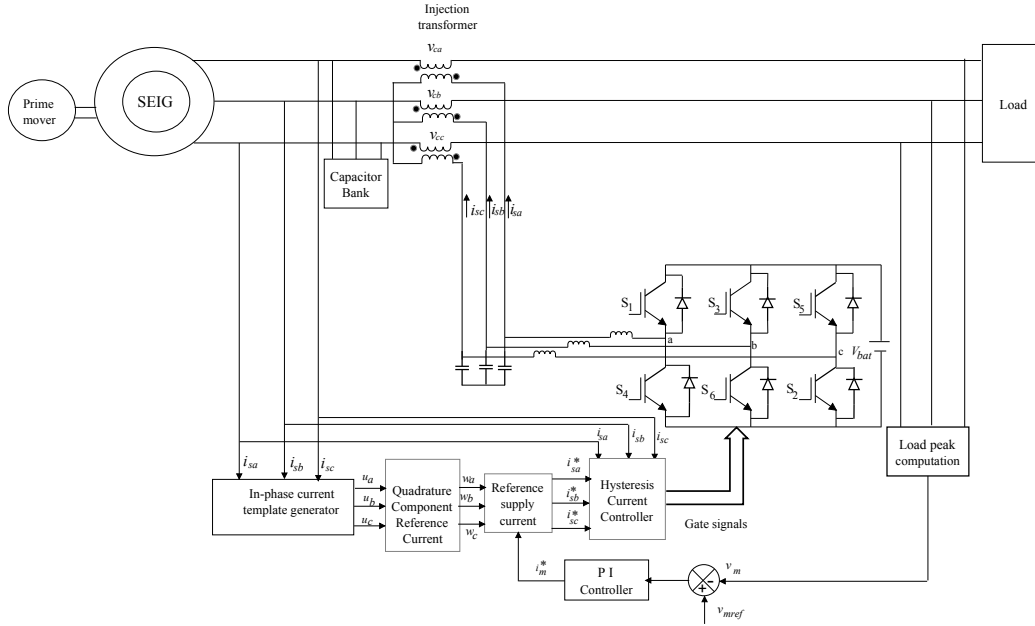


Figure 2.14: Schematic diagram of SSSC based SEIG voltage controller

Deraz and Kader [62] presented a control strategy by connecting current controlled voltage source inverter (CC-VSI) with electronic load controller across consumer load to regulate the voltage of SEIG. To generate reference source currents, two fuzzy logic PI controllers are used.

Hence, from the above review, it is observed that Perumal *et al.* [16] present a simple control scheme for SEIG. To control voltage SEIG is integrated with GIC where three voltage sensors used to control SEIG voltage. Hence, selected in this thesis and extended the work further to develop a voltage control scheme using optimal proportional and integral gains within stable zones along with one voltage sensor.

## 2.4 Fault analysis of SEIG

Due to the importance of SEIG, it is felt that performance analysis of SEIG during balanced and unbalanced faults should be studied. Furthermore, fault detection in SEIG and classification of those faults of SEIG are also challenging issues. Very few literatures are available related to transient performance analysis of SEIG during faults. Jain *et al.* [12] presented transient performance analysis of SEIG during balanced and unbalanced faults using  $d-q$  axis in stationary reference frame. Authors reported [12] that voltage collapse and de-excitation occurs in SEIG, during three phase short circuit, line-to-line fault, sin-

gle line opening and single phase capacitor opening. Excessive high torque and sustained vibration torque occurs during these cases. Excessive high torque and sustained vibration torque are extremely dangerous for SEIG leading to increased maintenance cost and risk of shaft failure. Iyer *et al.* [13], presented time taken to re-excite the SEIG depends upon saturation level, excitation capacitance, discharge time, type of fault and duration of fault. In [13], authors also reported that the re-excitation time is more compared to pre-fault excitation time. If the fault is detected and cleared before the excitation decays to zero, time takes to re-excite the SEIG reduces.

So, it is a challenging issue to select an effective signal processing technique that can provide information from these nonlinear and non-stationary signals. In literature number of signal processing techniques are suggested. Discrete Fourier transform (DFT) is one of the fast technique to provide frequency information only but does not provide any information regarding the time occurrence of frequency components [63]. Hence, this technique is restricted to as an alternative to stationary signals only. The use of Short-Time Fourier Transform (STFT) with a constant window for all frequencies present in the signal (especially for non-stationary signals) [64] is used as an alternative to Discrete Fourier Transform (DFT). It provides constant resolution for all frequencies for the whole signal. By using a wide window, it is possible to analyze low-frequency components (good frequency resolution) but not able to get good time resolution. To get good time resolution, narrow window is essential. So STFT provides good resolution either in time or frequency domain depending on the size of window. The wavelet transform is addressed in literature after that to avoid the constant window problem of STFT. The WT uses shorter windows at high frequency and wider windows for low frequency. Hence, WT is capable of monitoring closely the features of non-stationary signals. Iyer *et al.* [13] used Discrete Wavelet Transform (DWT) for fault detection of SEIG system. However, wavelet transform analysis results depend on selection of the mother wavelet [65].

Recently Hilbert-Huang Transform (HHT) has grabbed the attention of researchers to analyze non-stationary signals [66] using empirical mode decomposition (EMD) and Hilbert transform (HT) [67]. EMD is a self-adaptive signal processing technique. The basis of this technique is on the local characteristics time of a signal. EMD decomposes the signal into a collection of oscillating components known intrinsic mode functions (IMFs) using a shifting procedure. IMFs work as the basis function that are computed by the signal itself [68]. Hence, HHT is used in this thesis for fault analysis of SEIG system.

The following chapters present the details of work done and contributions of the thesis.

# Chapter 3

## Dynamic modeling and performance analysis of wind driven SEIG system

### 3.1 Introduction

Currently to meet the never-ending electrical energy demand, researchers are giving more emphasize on renewable energy sources such as the wind, solar, small hydro and biogas. Out of the available renewable energy sources, wind power is clean and abundantly available in vast areas like mountain, on the shore, offshore, remote and isolated areas. Due to lower cost, rugged construction and maintenance-free operation induction generators are found to be an excellent option for wind power plants [69]. Induction generator requires an adequate amount of reactive power which must be provided externally to set up the magnetic field needed to convert the available mechanical power at its shaft into electrical power [70]. Reactive power can be supplied to the induction generator by connecting it to with grid, and this mode is called a grid-tied mode. Alternatively, by connecting appropriate value of capacitor bank, reactive power can be supplied to the induction generator. Such mode is called an isolated or stand-alone mode, and the generator is called Self-Excited Induction Generator (SEIG). Prime mover for the SEIG may be a wind turbine or, micro-hydro turbine. In this chapter the prime mover considered is a wind turbine. Steady state and transient analysis of such wind turbine driven SEIG system are beneficial for design and performance prediction of the SEIG system.

This chapter presents the step-by-step development of models for different units of the SEIG with the steady-state and transient analysis for performance prediction and design of excitation capacitor. Various types of load can be connected with SEIG. In this chapter resistive,  $R-L$  and induction motor (IM) load are connected to SEIG.

Section 3.2 describes modeling of the wind turbine. Section 3.3 presents the ana-

lytical determination of minimum excitation capacitance required for SEIG followed by dynamic modeling of SEIG in section 3.4. Excitation modeling is given in section 3.5 followed by modeling of different types of load in section 3.6. Induction motor as a dynamic load on SEIG is also modeled in the section 3.6.3. Section 3.7 presents the simulation and experimental results of the SEIG system. Summary of the chapter is presented in section 3.8.

## 3.2 Modeling of wind turbine

Fig. 3.1 shows schematic diagram of a SEIG system, where the prime mover is a wind turbine. Wind turbine driven SEIG system is used in isolated areas where an extension of the grid is not feasible. The wind turbine employed in these areas is up to 100 kW rating and called a small wind turbine. The wind turbine converts the kinetic energy available in the wind into mechanical energy. The power available in the wind is given by the time-rate of kinetic energy of the flowing air mass and expressed as follows.

$$P_{\omega} = 0.5\rho Av_{\omega}^3 \quad (3.1)$$

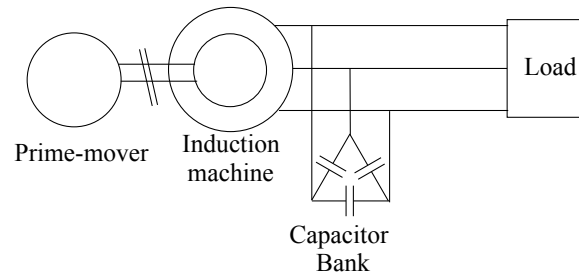


Figure 3.1: Schematic diagram of a SEIG system

The wind turbine does not capture the total power available in the wind. The amount of power captured by the wind turbine is given as follows.

$$P_t = 0.5C_p\rho Av_{\omega}^3 \quad (3.2)$$

where  $\rho$ , is the density of air (generally  $1.21 \text{ kg/m}^3$ ).  $A$  is the exposed area by the wind turbine in  $\text{m}^2$ .  $v_{\omega}$  is the wind speed in  $\text{m/s}$ . ( $C_p = \frac{P_t}{P_{\omega}}$ ) is the power coefficient of the wind turbine. Theoretical maximum value of  $C_p$  is (0.59) [71] given by Betz limit but in commercial turbines (maximum value approximately 0.46).  $C_p$  is expressed as a function

of the tip speed ratio ( $\lambda$ ) and blade pitch angle ( $\beta$ ), given by equation (3.3) [72].

$$C_p(\lambda, \beta) = 0.5176 \left( \frac{116}{\lambda_i} - 0.4\beta - 5 \right) e^{-\frac{21}{\lambda_i}} + 0.00068\lambda \quad (3.3)$$

where

$$\frac{1}{\lambda_i} = \frac{1}{\lambda + 0.08\beta} - \frac{0.035}{\beta^3 + 1} \quad (3.4)$$

Tip speed ratio is expressed as

$$\lambda = \frac{\omega_T r}{v_\omega} \quad (3.5)$$

where,  $r$  is the radius of the swept area of the wind turbine in m.  $\omega_T$  is the turbine angular speed in rad/s. For the wind turbine of 4.2 kW with pitch angle,  $\beta = 0^\circ$  the  $C_p$  versus  $\lambda$  has the shape shown in Fig. 3.2. For a fixed pitch wind turbine, the  $C_p$  versus  $\lambda$  curve is same for different wind speed and has same maximum value  $C_{pmax}$  for the optimum value  $\lambda_{opt}$  for each wind speed as depicted in the Fig. 3.2.

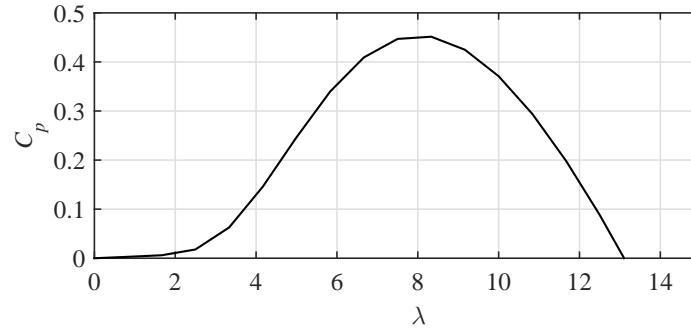


Figure 3.2: Power coefficient ( $C_p$ ) vs tip speed ratio ( $\lambda$ )

Mechanical power versus turbine speed plot for this type of fixed turbine is shown in Fig. 3.3. The maximum power extracted by the turbine and the turbine speed at which the maximum power occurs increase with the increase in the wind speed. To generate electrical power from wind, wind turbine is connected to a generator. As mentioned, for isolated areas SEIG is the suitable option for generating electrical power from wind. But SEIG needs an appropriate value of capacitance for excitation. Minimum capacitance value required for SEIG at no load is derived in the next section.

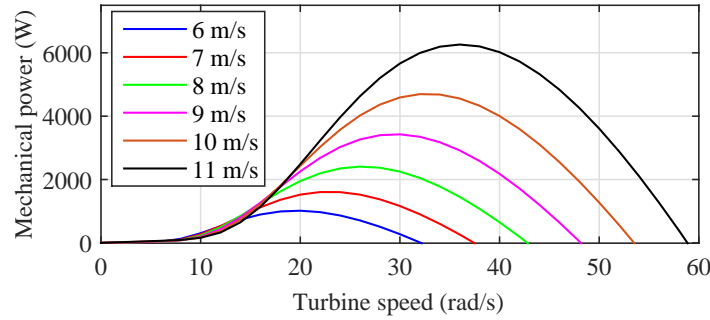


Figure 3.3: Mechanical power vs turbine speed at different wind speeds

### 3.3 Determination of minimum excitation capacitance value for the SEIG

For determining minimum capacitance value, the per-phase equivalent circuit of three-phase SEIG with  $R-L$  load and an excitation capacitor is shown in Fig. 3.4. All the variables and parameter values of Fig. 3.4, are expressed in per unit (p.u) for convenience of analysis. Fig. 3.5 is the simplified representation of the circuit of Fig. 3.4 and the total impedance of the circuit is represented by  $Z_t$ .

where,

$$Z_t = Z_s + (Z_L || Z_c) + (Z_m || Z_r).$$

$$Z_s = \frac{R_s}{F} + jX_{ls}, Z_L = \frac{R_L}{F} + jX_L, Z_c = \frac{-jX_c}{F^2}, Z_m = jX_m \text{ and } Z_r = \frac{R_r}{F-v} + jX_{lr}.$$

$\frac{V_g}{F}$  is the ratio of air gap voltage to frequency, which depends on the magnetic flux and hence magnetizing reactance.

$\frac{V_t}{F}$  is the ratio of terminal voltage to frequency.

$F, v$  are p.u frequency and p.u speed of SEIG, respectively.

$C, X_c$  are per phase value of excitation capacitance and its p.u reactance ( at base frequency).

$R_s, R_r, R_L$  are p.u stator resistance, rotor resistance and load resistance, respectively.

$X_{ls}, X_{lr}, X_L$  are p.u stator leakage reactance, rotor leakage reactance and load reactance, respectively.

$X_m$  is p.u saturated magnetizing reactance.

By applying loop analysis to the circuit in Fig. 3.5 at steady state, the expression obtained is

$$I_s Z_t = 0 \quad (3.6)$$



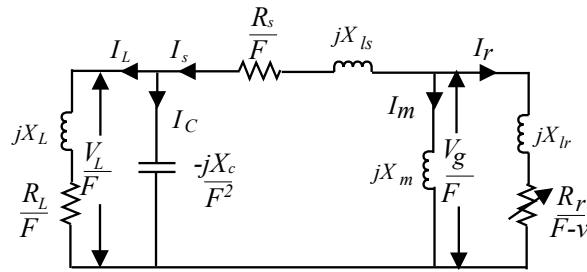


Figure 3.4: Per phase equivalent circuit of the self-excited induction generator

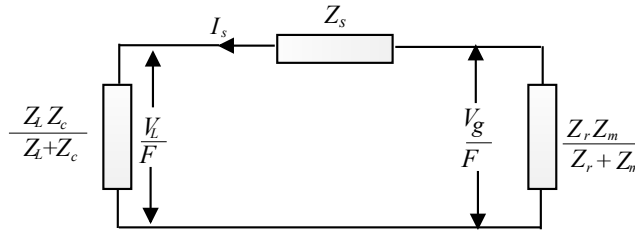


Figure 3.5: Simplified representation of the circuit of Figure 3.4

where  $I_s$  is the steady state stator current. The self-excitation process of SEIG requires that the current in the loop,  $I_s$  in equation (3.6) is not zero. So at, steady state

$$Z_t = 0 \quad (3.7)$$

$$\frac{Z_L Z_c}{Z_L + Z_c} + Z_s + \frac{Z_r Z_m}{Z_r + Z_m} = 0 \quad (3.8)$$

$$\frac{Z_L Z_c}{Z_L + Z_c} = -\left(Z_s + \frac{Z_r Z_m}{Z_r + Z_m}\right) \quad (3.9)$$

$$\frac{Z_c}{1 + \left(\frac{Z_c}{Z_L}\right)} = -\left(Z_s + \frac{Z_r Z_m}{Z_r + Z_m}\right) \quad (3.10)$$

At no load  $Z_L = \infty$ . Hence,

$$Z_c = -\left(Z_s + \frac{Z_r Z_m}{Z_r + Z_m}\right) \quad (3.11)$$

$$Z_c(Z_r + Z_m) + Z_s(Z_r + Z_m) + Z_r Z_m = 0 \quad (3.12)$$

Substituting the impedances by circuit parameters in equation (3.12) and rearranging the terms, provides following expression.

$$\begin{aligned} \frac{-jX_c}{F^2} \left( \frac{R_r}{F - v} + j(X_{lr} + X_m) \right) + jX_m \left( \frac{R_r}{F - v} + jX_{lr} + \frac{R_s}{F} + jX_{ls} \right) \\ + \left( \frac{R_r}{F - v} + jX_{lr} \right) \left( \frac{R_s}{F} + jX_{ls} \right) = 0 \end{aligned} \quad (3.13)$$

$$\begin{aligned} \frac{-jX_c R_r}{F^2(F-\nu)} + \frac{X_c}{F^2}(X_{lr} + X_m) + jX_m \left( \frac{R_r}{F-\nu} + \frac{R_s}{F} \right) - X_m(X_{lr} + X_{ls}) \\ + \frac{R_r}{F-\nu} \frac{R_s}{F} - X_{lr}X_{ls} + j \left( \frac{R_r}{F-\nu}X_{ls} + \frac{R_s}{F}X_{lr} \right) = 0 \end{aligned} \quad (3.14)$$

$C_{min}$  is determined by equating the imaginary part of the (3.14) to zero, and computed as follows.

$$\frac{-X_c R_r}{F^2(F-\nu)} + X_m \left( \frac{R_r}{F-\nu} + \frac{R_s}{F} \right) + \left( \frac{R_r}{F-\nu}X_{ls} + \frac{R_s}{F}X_{lr} \right) = 0 \quad (3.15)$$

By considering ( $X_{ls} = X_{lr}$ ), equation (3.15) is simplified as follows.

$$-X_c \left( \frac{R_r}{F^2(F-\nu)} \right) + X_m \left( \frac{R_r}{F-\nu} + \frac{R_s}{F} \right) + \left( \frac{R_r}{F-\nu} + \frac{R_s}{F} \right) X_{ls} = 0 \quad (3.16)$$

$$-X_c \left( \frac{R_r}{F^2(F-\nu)} \right) + (X_m + X_{ls}) \left( \frac{R_r}{F-\nu} + \frac{R_s}{F} \right) = 0 \quad (3.17)$$

$$-X_c \left( \frac{R_r}{F^2(F-\nu)} \right) = -(X_m + X_{ls}) \left( \frac{R_r}{F-\nu} + \frac{R_s}{F} \right) = 0 \quad (3.18)$$

$$X_c = (X_m + X_{ls}) \left( \frac{R_r}{F-\nu} + \frac{R_s}{F} \right) \frac{F^2(F-\nu)}{R_r} \quad (3.19)$$

Malik and Mazi [41] computed the ratio  $\frac{F}{\nu}$  with minimum capacitance value for induction machine at no load taking different speeds. It is reported that the ratio  $\frac{F}{\nu} \approx 1$ . So, it is concluded that during no-load conditions of SEIG, the machine slip is almost zero and the  $pu$  frequency of the generated voltage is almost equal to the  $pu$  rotor speed [41]. Based on this, here taken,  $F \approx \nu$  and  $F - \nu \approx 0$ . These values are substituted in equation (3.19) and  $X_{cmax}$  or,  $C_{min}$  can be obtained as follows.

$$X_{cmax} \approx (X_{ls} + X_m) \nu^2 \quad (3.20)$$

$$C_{min} = \frac{1}{\omega(X_{ls} + X_m) \nu^2} \quad (3.21)$$

From the above equation, it is concluded that minimum excitation capacitance  $C_{min}$  required for SEIG during no load condition varies inversely as sum of leakage reactance and magnetizing reactance and also the rotor speed of the SEIG. To validate the developed expression, the calculated capacitance value is used in simulation and experiment on the SEIG. Next section describes the mathematical representation of the SEIG using the  $d - q$  axis stationary reference frame.

### 3.4 Modeling of SEIG

As described in section 2.2, SEIG performance can be analyzed using per-phase equivalent circuit approach and  $d - q$  axis model based on the generalized machine theory. Per-phase equivalent circuit approach involves the loop impedance method and the nodal admittance method. Steady-state performance of SEIG can be evaluated using per-phase equivalent circuit approach, but it has limitations to analyze the transient phenomenon [34]. To analyze the dynamic performance of SEIG under different types of loading condition, in this section the  $d - q$  axis stationary frame model of induction machine [73] is presented. Using  $d - q$  components of the stator and rotor currents  $i_{sd}$ ,  $i_{sq}$ ,  $i_{rd}$  and  $i_{rq}$  as state variables, electrical dynamics of the SEIG is represented by state-space model as given in equations (3.22)-(3.25) [35].

$$\frac{di_{sd}}{dt} = \frac{1}{(L_s L_r - L_m^2)} [\omega_r L_m^2 i_{sq} - L_r r_s i_{sd} + \omega_r L_m L_r i_{rq} + L_m r_r i_{rd} + L_r v_{sd}] \quad (3.22)$$

$$\frac{di_{sq}}{dt} = \frac{1}{(L_s L_r - L_m^2)} [-L_s r_s i_{sq} - \omega_r L_m^2 i_{sd} + L_m r_r i_{rq} - \omega_r L_m L_r i_{rd} + L_r v_{sq}] \quad (3.23)$$

$$\frac{di_{rd}}{dt} = \frac{1}{(L_s L_r - L_m^2)} [\omega_r L_m L_s i_{sq} + r_s L_m i_{sd} - \omega_r L_s L_r i_{rq} - r_r L_s i_{rd} + L_m v_{sd}] \quad (3.24)$$

$$\frac{di_{rq}}{dt} = \frac{1}{(L_s L_r - L_m^2)} [r_s L_m i_{sq} + \omega_r L_m L_s i_{sd} - L_s r_r i_{rq} + \omega_r L_s L_r i_{rd} - L_m v_{sq}] \quad (3.25)$$

where,

$$L_s = L_{ls} + L_m \quad (3.26)$$

$$L_r = L_{lr} + L_m \quad (3.27)$$

In equations (3.22)-(3.25), subscripts  $v$  and  $i$  are for instantaneous voltage and current. Subscripts  $d$  and  $q$  are for the direct and quadrature axes. Subscripts  $s$  and  $r$  are for the stator and rotor variables. Subscript  $l$  is for leakage component. Subscript  $m$  is for magnetizing component. Subscript  $L$  is for inductance. Subscript  $r$  is for resistance. Subscript  $\omega_r$  is for electrical rotor speed of SEIG. Magnetizing current  $i_m$  is determined from  $i_{sd}$ ,  $i_{sq}$ ,  $i_{rd}$  and  $i_{rq}$  using the expression (3.28) [35].

$$i_m = \sqrt{(i_{sd} + i_{rd})^2 + (i_{sq} + i_{rq})^2} \quad (3.28)$$

As the magnetization characteristic of SEIG is nonlinear, magnetizing inductance  $L_m$  varies with magnetizing current  $i_m$ . From synchronous speed test, relation between magnetizing

inductance  $L_m$  and magnetizing current  $i_m$  are obtained and expressed as

$$L_m = f(i_m) \quad (3.29)$$

The electromagnetic torque  $T_e$  of SEIG is given by equation (3.30) [35].

$$T_e = \left(\frac{3}{2}\right) \left(\frac{P}{2}\right) L_m [i_{sq}i_{rd} - i_{sd}i_{rq}] \quad (3.30)$$

The torque balance equation of the SEIG is

$$T_{drive} = T_e + J \left(\frac{2}{P}\right) \frac{d\omega_r}{dt} \quad (3.31)$$

where,  $T_{drive}$  is the mechanical input torque of SEIG.  $J$  is the moment of inertia of rotor.  $P$  is the number of poles of SEIG, respectively. The torque balance gives speed dynamic equation

$$\frac{d\omega_r}{dt} = \frac{P}{2J} (T_{drive} - T_e) \quad (3.32)$$

Capacitor being one major part of SEIG, the excitation modeling for SEIG system is described in the next section.

### 3.5 Excitation modeling

The excitation system dynamics are described using  $d - q$  components of stator voltage ( $v_{sd}$  and  $v_{sq}$ ) as state variables, as given in equations (3.33)-(3.34).

$$\frac{dv_{sd}}{dt} = \frac{i_{ed}}{C_{ed}} \quad (3.33)$$

$$\frac{dv_{sq}}{dt} = \frac{i_{eq}}{C_{eq}} \quad (3.34)$$

Three-phase SEIG voltages and currents are transformed from  $a - b - c$  to  $d - q$  stationary reference frame and vice-versa [73], using equations (3.35) and (3.36).

$$\begin{bmatrix} v_a \\ v_b \\ v_c \end{bmatrix} = \begin{bmatrix} 0 & 1 \\ -\frac{\sqrt{3}}{2} & -\frac{1}{2} \\ \frac{\sqrt{3}}{2} & -\frac{1}{2} \end{bmatrix} \begin{bmatrix} v_{sd} \\ v_{sq} \end{bmatrix} \quad (3.35)$$

$$\begin{bmatrix} v_{sd} \\ v_{sq} \end{bmatrix} = \begin{bmatrix} 0 & -\frac{1}{\sqrt{3}} & \frac{1}{\sqrt{3}} \\ 1 & 0 & 0 \end{bmatrix} \begin{bmatrix} v_a \\ v_b \\ v_c \end{bmatrix} \quad (3.36)$$

The value of minimum capacitor required for voltage build up of SEIG as determined from (3.21) is substituted in the equations (3.33) and (3.34). The  $d - q$  modeling of different types of load are described in the next section.

## 3.6 Load modeling

Different types of load such as  $R$ ,  $R - L$  and induction motor (IM) load are normally connected to the wind turbine driven SEIG system. To get the performance of complete system, modeling of only wind turbine and SEIG are not sufficient. Additionally, modeling of loads is also essential. These are presented in the subsequent subsections.

### 3.6.1 For resistive load

The  $d$  and  $q$  axes current equations for the balanced  $R$  load connected to SEIG are given as

$$i_{ld} = \frac{v_{sd}}{R_{ld}} \quad (3.37)$$

$$i_{lq} = \frac{v_{sq}}{R_{lq}} \quad (3.38)$$

where  $R_{ld}$  and  $R_{lq}$  are  $d$  and  $q$  components of load resistances

### 3.6.2 For $R - L$ load

The  $d$  and  $q$  axes current equations for the balanced  $R - L$  load connected to SEIG are expressed as

$$\frac{di_{ld}}{dt} = \frac{v_{sd}}{L_{ld}} - i_{ld} \frac{R_{ld}}{L_{ld}} \quad (3.39)$$

$$\frac{di_{lq}}{dt} = \frac{v_{sq}}{L_{lq}} - i_{lq} \frac{R_{lq}}{L_{lq}} \quad (3.40)$$

where  $L_{ld}$  and  $L_{lq}$  are  $d$  and  $q$  components of load inductances.

### 3.6.3 Modeling of induction motor as dynamic load

Three phase induction motor (IM) is often used as a dynamic load on SEIG. The  $d - q$  model of symmetrical three phase squirrel cage IM in the current state-space form [74], is

given by

$$\frac{d}{dt}[i_{mM}] = [L_{mM}]^{-1}([v_{mM}] - [r_{mM}][i_{mM}] - \omega_{mm}[G_{mM}][i_{mM}]) \quad (3.41)$$

where,

$$\begin{aligned} [v_{mM}] &= [v_{sdm} \ v_{sqm} \ v_{rdm} \ v_{rqm}]^T \\ [i_{mM}] &= [i_{sdm} \ i_{sqm} \ i_{rdm} \ i_{rqm}]^T \\ [r_{mM}] &= \text{diag}[R_{sm} \ R_{sm} \ R_{rm} \ R_{rm}] \\ [L_{mM}] &= \begin{bmatrix} L_{lsm} + L_{mm} & 0 & L_{mm} & 0 \\ 0 & L_{lsm} + L_{mm} & 0 & L_{mm} \\ L_{mm} & 0 & L_{lrm} + L_{mm} & 0 \\ 0 & L_{mm} & 0 & L_{lrm} + L_{mm} \end{bmatrix} \\ [G_{mM}] &= \begin{bmatrix} 0 & 0 & 0 & 0 \\ 0 & 0 & 0 & 0 \\ L_{mm} & 0 & L_{lrm} + L_{mm} & 0 \\ 0 & -L_{mm} & 0 & -L_{lrm} + L_{mm} \end{bmatrix} \end{aligned}$$

where,

$i_{sdm}$  and  $i_{sqm}$ , are  $d$  and  $q$  components of stator currents of IM load, respectively.

$i_{rdm}$  and  $i_{rqm}$ , are  $d$  and  $q$  components of rotor currents of IM load, respectively.

$v_{sdm}$ ,  $v_{sqm}$ , are  $d$  and  $q$  components stator voltages of IM load, respectively.

$v_{rdm}$  and  $v_{rqm}$  are  $d$  and  $q$  components rotor voltages of IM load, respectively.

$\omega_{mm}$  is mechanical rotor speed of IM load.

$R_{sm}$  is stator resistance of IM load.

$R_{rm}$  is rotor resistance of IM load.

$L_{lsm}$  is stator leakage inductance of IM load.

$L_{lrm}$  is rotor leakage inductance of IM load.

$L_{mm}$  is unsaturated mutual inductance of IM load.

The developed electromagnetic torque and torque balance equations of the IM load, are given as [74]

$$T_{em} = \left( \frac{3P_m}{4} \right) (L_{mm})(i_{sqm}i_{rdm} - i_{sdm}i_{rqm}) \quad (3.42)$$

$$T_{em} = T_{Lm} + J_m \frac{d\omega_{mm}}{dt} \quad (3.43)$$

$$\frac{d\omega_{mm}}{dt} = \frac{1}{J_m}(T_{em} - T_{Lm}) \quad (3.44)$$

where,  $T_{Lm}$  is load torque applied to IM load,  $J_m$  is moment of inertia of IM load,  $\omega_{rm}$  is electrical rotor speed of IM load and  $P_m$  is number of poles of IM load.

### 3.7 Results and Discussion

To develop the wind turbine driven SEIG system, a 4.2 kW wind turbine and a 3.7 kW induction machine are taken and simulated in MATLAB/Simulink environment. Parameters of the wind turbine model are given in Table 3.1 and available in [75].

Table 3.1: The parameters of the wind turbine model

Rated power capacity	4.2 kW
Blade diameter	4.9 m
Swept area	19 m <sup>2</sup>
Number of blades	3

Parameters of the induction machine used as SEIG are measured by conducting different tests (d.c resistance test, blocked rotor test and synchronous speed test) in the laboratory. The parameters of the 3.7 kW, 415 V, 7.5 A, 50 Hz, 1500 r.p.m SEIG obtained from experiments are given in Table 3.2.

Table 3.2: Parameters of induction machine used as SEIG

$R_s$	$R_r$	$X_{ls}$	$X_{lr}$	$X_m$	$J$
7.34Ω	5.64Ω	6.7Ω	6.7Ω	157 Ω	0.16 kg/m <sup>2</sup>

The magnetization characteristic of the SEIG is nonlinear. From the synchronous speed test, the relation between magnetizing inductance  $L_m$  and magnetizing current  $i_m$  is obtained and represented in the form of a polynomial [76]. A fifth-degree polynomial is taken in this thesis and given as:

$$L_m = a_5 i_m^5 + a_4 i_m^4 + a_3 i_m^3 + a_2 i_m^2 + a_1 i_m + a_0 \quad (3.45)$$

where  $a_5, a_4, \dots$  and  $a_0$  are constants obtained through curve fitting with experimentally, corresponding characteristics given in Fig. 3.6. The value of these constants are given in Table 3.3.

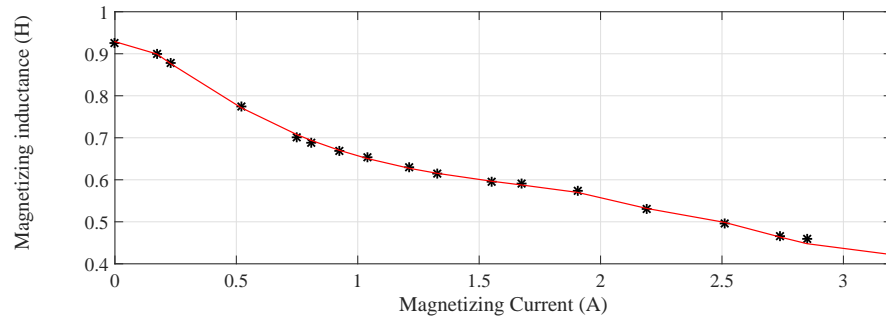


Figure 3.6: Graph of the identified (black) and approximated (red) magnetizing inductances vrs magnetising current

Table 3.3: The constants of the magnetization characteristics of SEIG

$a_5$	$a_4$	$a_3$	$a_2$	$a_1$	$a_0$
-0.0038	0.0576	-0.304	0.713	-0.853	1.043

### 3.7.1 SEIG voltage build-up process at no-load

Simulation of wind driven SEIG system is carried out in MATLAB/Simulink environment. To simulate the wind turbine driven SEIG system, 4.2 kW wind turbine (taking data given in Table 3.1) is connected with the 3.7 kW SEIG (taking data given in Table 3.2) through a gear box. The speed ratio  $N_1 : N_2$  of gear box for this work is taken (1:3). Minimum value of capacitance for the SEIG system at no load is calculated using the developed expression (3.21).  $C_{min}$  is 19  $\mu\text{F}$  but capacitance value selected is more than this  $C_{min}$  value. Capacitance value selected for the SEIG system in this work is 21.5  $\mu\text{F}$ . For wind speed of 9.8 m/s SEIG r.m.s voltage developed is 415 V corresponding to peak voltage of 586.8 V. Stator peak line current is 6.9 A. Simulation results of wind turbine driven SEIG system at no load are shown in Fig. 3.7. SEIG line voltage and peak SEIG line voltage during no-load are presented in Fig. 3.7 (a) and (b), respectively. It is observed that SEIG voltage increases from zero voltage and settles to rated peak voltage 586.8 V at  $t=0.55$  s. Fig. 3.7 (c) shows SEIG stator current increases from zero A to 6.9 A. SEIG frequency at no-load is presented in Fig. 3.7 (d). It is observed that SEIG frequency reaches to 50 Hz at  $t=0.55$  s, as soon as SEIG voltage achieves steady-state rated value.

Fig. 3.8 shows the experimental set up of SEIG system. Captured experimental waveforms of SEIG during no load condition at 1500 r.p.m are depicted in Fig. 3.9. The Fig. 3.9 has two windows. In the top window the top figure represents SEIG stator line



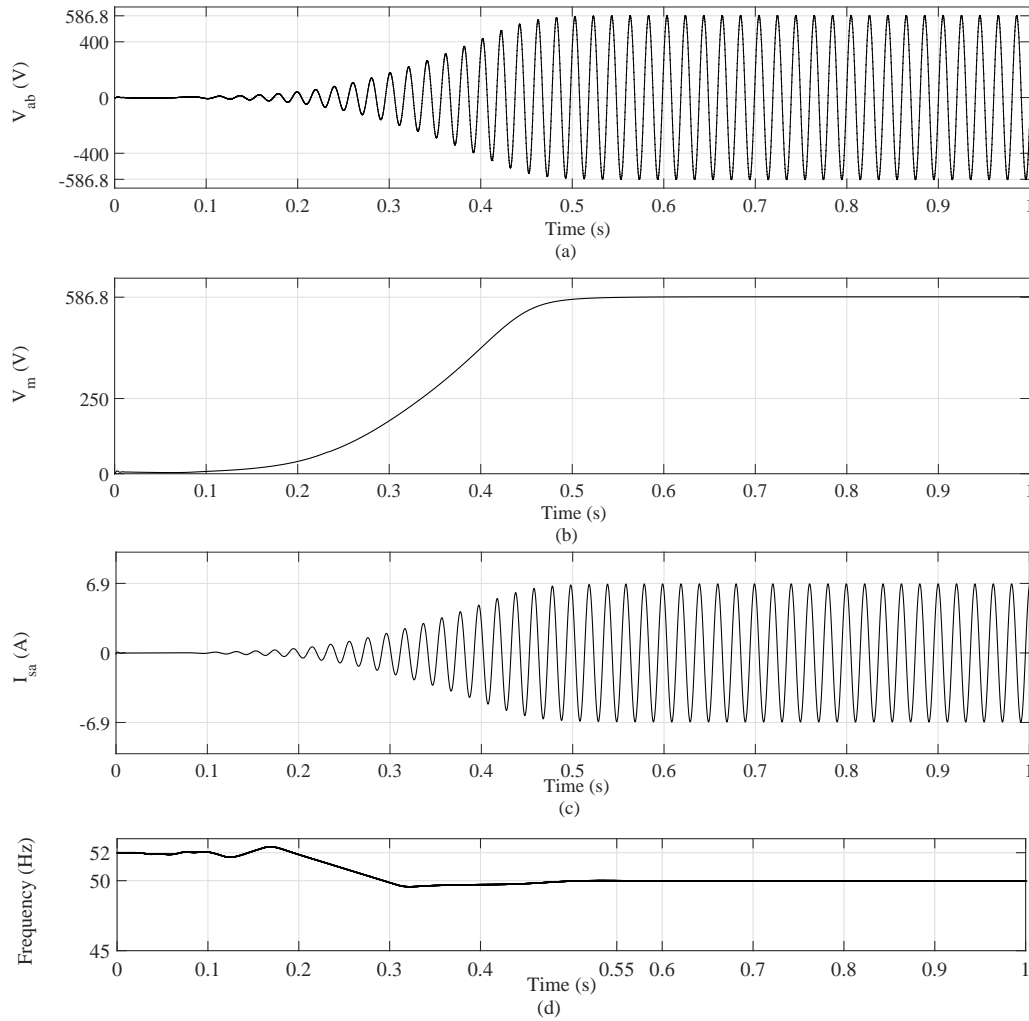


Figure 3.7: Simulation results of wind driven SEIG system at no load: (a) Line voltage of SEIG (b) Peak of the line voltage of SEIG (c) Stator line current of SEIG (d) Capacitor current (e) Frequency of SEIG

voltage and the bottom figure represents SEIG stator line current. The bottom window of Fig. 3.9 represents the zoomed version of top window. The scale for stator line voltage is 400 V/div and stator current 10 A/div. It is observed from the bottom window of Fig. 3.9 that peak of the SEIG line voltage between phase ‘a’ and ‘b’ at no load is 590 V and stator peak line current of phase ‘a’ 6.5 A. Captured experimental results of no-load SEIG stator voltage and stator current are close to the simulation results of no-load SEIG stator voltage and stator current.



Figure 3.8: Experimental set up of SEIG system

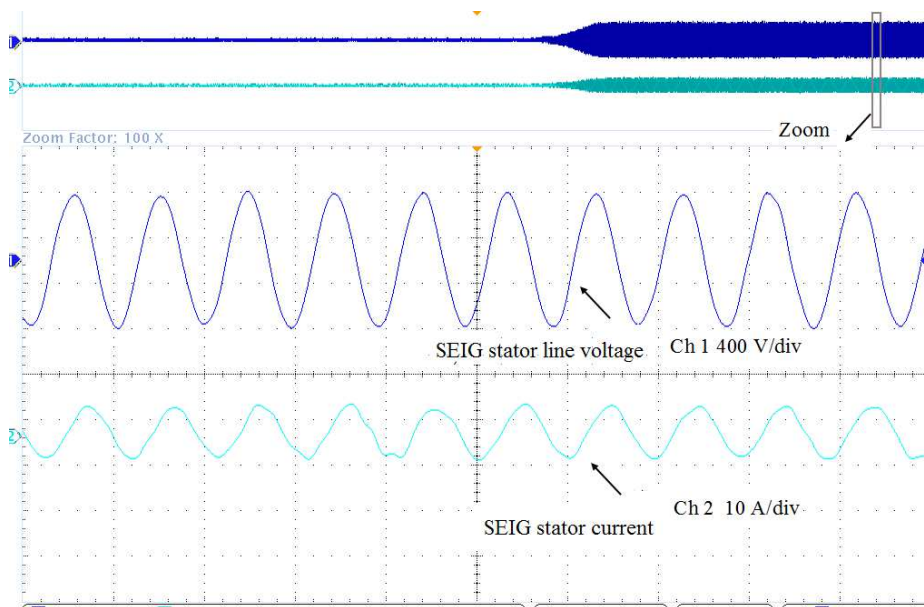


Figure 3.9: Experimental waveforms of SEIG stator voltage and current build-up process of SEIG system at no load

### 3.7.2 Performance of SEIG during different loading condition

Successful voltage build-up process of SEIG can only allow to connect a load to it. The load is connected with SEIG, after the successful development of rated voltage. The performance of wind driven SEIG system under the different types of load and wind speed perturbations are described in the subsequent subsections.

### (a) Performance of wind turbine driven SEIG system during resistive loading condition

To observe the performance of SEIG during loading condition, a star connected resistive load of  $100 \Omega/\text{phase}$  is connected with SEIG at  $t=1$  s for the simulation. Resistive load draws active power from the SEIG, which causes voltage drop across stator impedance. As a consequence SEIG terminal voltage reduces causing the reduction of reactive power. Finally terminal voltage settles at a value below the rated voltage. Fig. 3.10 depicts the simulation results of SEIG system with a  $100 \Omega/\text{phase}$  load. Fig. 3.10 (a), shows that at  $t=1$  s, the peak SEIG line voltage decreases from rated peak of  $586.8$  V to  $469$  V. Fig. 3.10 (b) shows SEIG stator line current decreases from  $6.8$  A to  $5.8$  A. Load current is shown by Fig. 3.10 (c) which increases from  $0$  to  $2.9$  A at  $t=1$  s and settles at  $2.7$  A. SEIG frequency decreases from  $50$  Hz to  $46.69$  Hz as presented in Fig. 3.10 (d). Fig. 3.10 (e) shows that active power drawn at no-load condition is zero W and at  $t=1$  s, after connecting the load, active power of SEIG changes and settles at  $-1100$  W. The sign convention being active power associated with the generator is negative. Fig. 3.10 (f) shows that the reactive power demanded by SEIG at no load is  $-3490$  VAR. The sign convention being reactive power associated with SEIG is negative. After resistive loading, due to decrease in terminal voltage reactive power changed from  $-3490$  VAR and settles at  $-2084$  VAR.

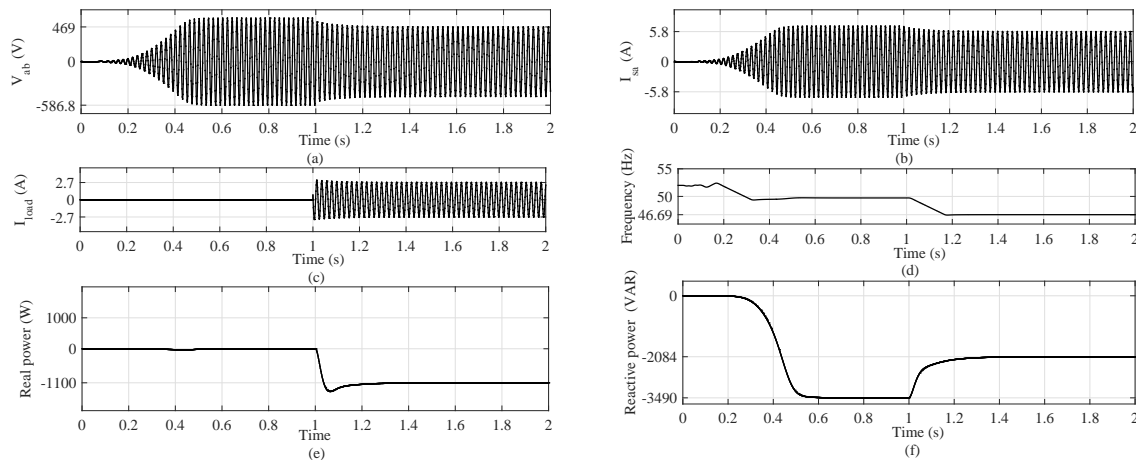


Figure 3.10: Simulation results of SEIG with resistive loading: (a) SEIG stator line voltage (b) SEIG stator line current (c) Load current (d) SEIG frequency (e) SEIG active power (f) Reactive power demanded by SEIG

By taking the same resistive load, the experiment is conducted. Corresponding results are shown in Fig. 3.11. Fig. 3.11 has two windows, bottom window is the zoomed version of top window. Each window contains waveforms of SEIG line voltage between phase ‘a’

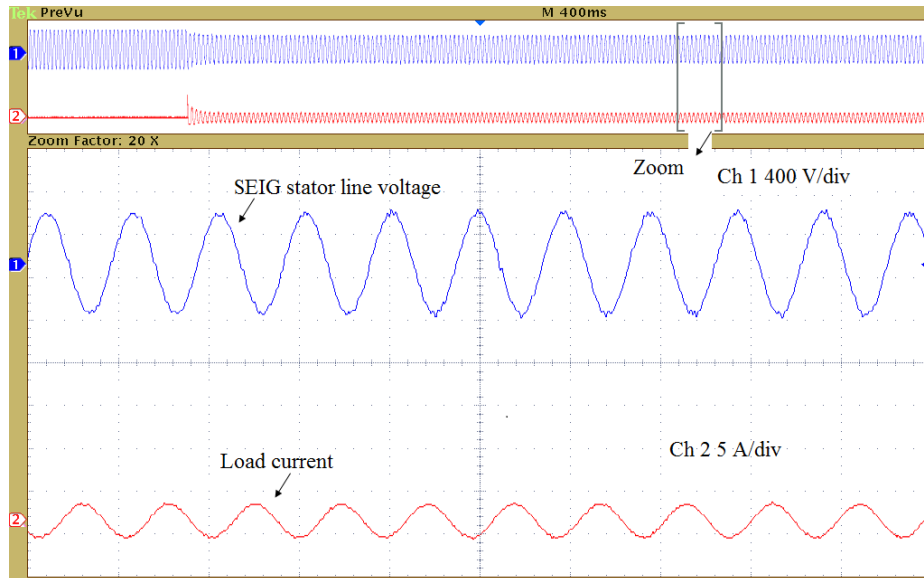


Figure 3.11: Captured experimental waveforms of SEIG stator line voltage and load current during loading condition

and 'b', and line current of phase 'a' of star connected load. Scale for stator line voltage is 400 V/div and load current 5 A/div. It is observed from the Fig. 3.11 that SEIG peak voltage decreases from rated voltage 586.8 V to 464 V due to load connection and load current increases from 0 A to 2.5 A. Experimental SEIG voltage and load current obtained are close to the simulation results. Close agreement between simulation and experimental results depicts the validation of the transient model.

#### (b) Performance of wind turbine driven SEIG system during $R-L$ loading condition

The performance of SEIG during  $R-L$  load switching is studied by connecting a  $R-L$  load of 0.9 power factor,  $Z = 100 + j48.42 \Omega/\text{phase}$  to SEIG at  $t=1$  s. In this type of loading, SEIG provides only active power to the load, and excitation capacitor provides reactive power to the load. Fig. 3.12 (a) shows that active power from SEIG changes from zero W at no-load to -270 W at steady-state after loading. Fig. 3.12 (b) shows that reactive power demanded by SEIG changes from -3490 VAR before loading to -508 VAR after loading due to decrease in terminal voltage. Reduced reactive power to the machine causes further reduction in SEIG terminal voltage. During this loading condition SEIG stator voltage is reduced from rated peak voltage 586.8 V to 257.2 V as seen in Fig. 3.12 (c). SEIG stator peak line current reduces from 6.9 A before loading to 2.57 A after loading, as seen from Fig. 3.12 (d). Peak load current increases from 0 to 1.31 A after loading as evident from Fig. 3.12 (e). SEIG frequency reduces from 50 Hz before loading to 47.52 Hz after loading,

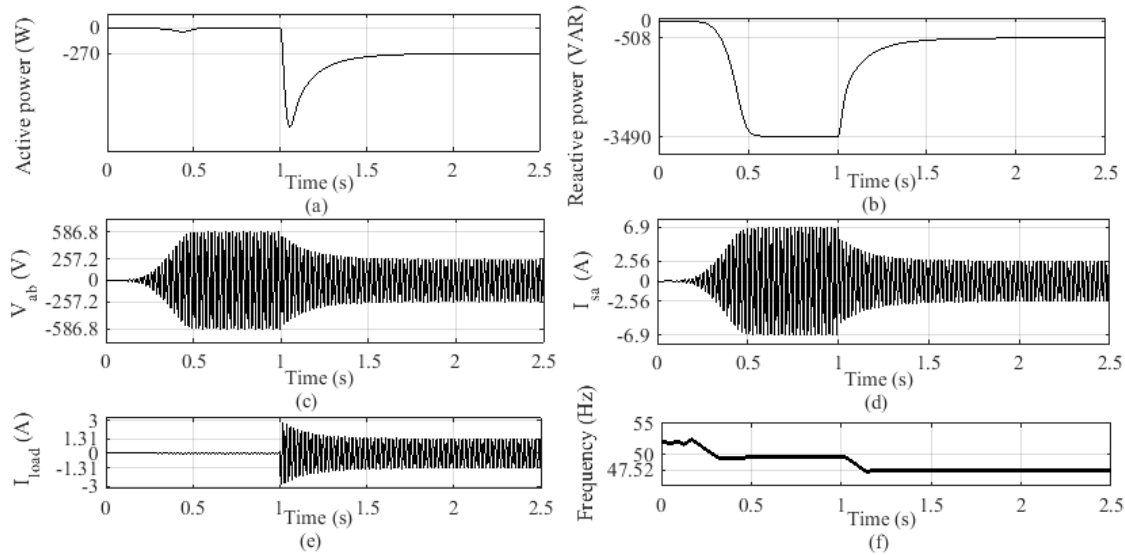


Figure 3.12: Simulation results of SEIG with  $R-L$  load switching: (a) SEIG active power (b) Reactive power demanded by SEIG (c) Stator peak voltage (d) Stator line current (e) Load current (f) SEIG frequency

as observed from Fig. 3.12 (f). If SEIG is overloaded, then excitation fails and voltage collapses, as described in the next subsection.

### (c) Performance of wind turbine driven SEIG system during insertion of overload

The SEIG is operated initially on no-load to develop rated voltage of 415 V r.m.s or, 586.8 V peak. A three phase balanced star connected  $R-L$  load at 0.9 power factor given by  $Z = 50 + 24.21 \Omega/\text{phase}$  is inserted at SEIG terminals. Fig. 3.13 (a) shows that active power from SEIG changes from no-load value of zero to peak transient value of about -1460 W but finally changes to steady-state value of zero. Fig. 3.13 (b) shows that reactive power demanded by SEIG has a no-load value of -3490 VAR before loading which settles at zero after loading. The amount of active and reactive power demanded by the load are more which leads to the SEIG voltage collapse as presented in Fig. 3.13 (c). It is observed that the peak voltage of SEIG decreases from no-load value of 586.8 V to zero after loading. Load current increases from zero (no-load value) to peak value of 5 A during transient period after loading, which finally collapses to zero as shown in Fig. 3.13 (d) due to voltage collapse. Fig. 3.14 shows the experimental results during overload of SEIG. In Fig. 3.14, top window depicts the waveforms of SEIG line voltage and load current, while bottom window shows the zoomed version of top window. Scale taken for stator line voltage is 400 V/div and load current 5 A/div. It is observed from Fig. 3.14 that due to the connection of over load, SEIG voltage collapses to zero. This voltage collapse occurred because of high

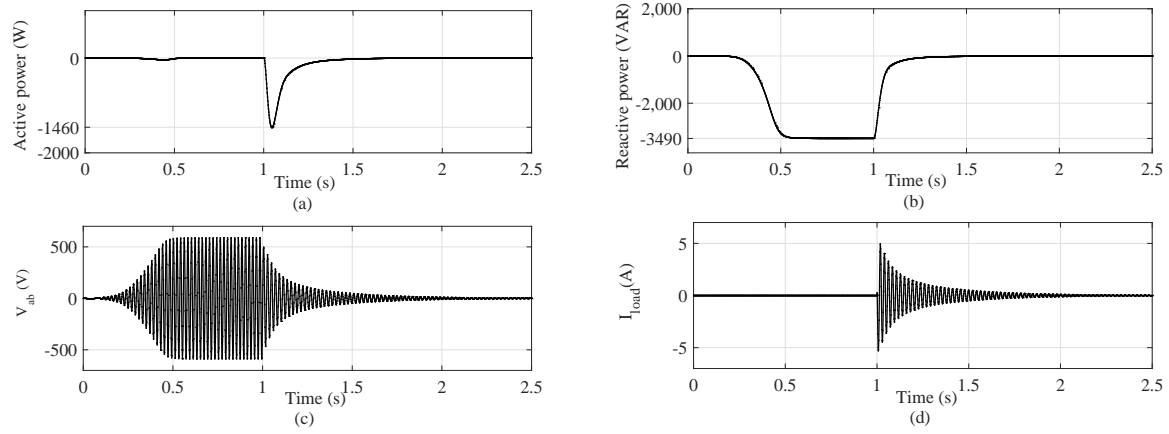


Figure 3.13: Simulation results of overloaded SEIG system: (a) SEIG active power (b) Reactive power demanded by SEIG (c) Stator line voltage (d) Load current

starting load current of approximately 7.5 A. The performance of SEIG feeding induction motor (IM) load is described in the next subsection.

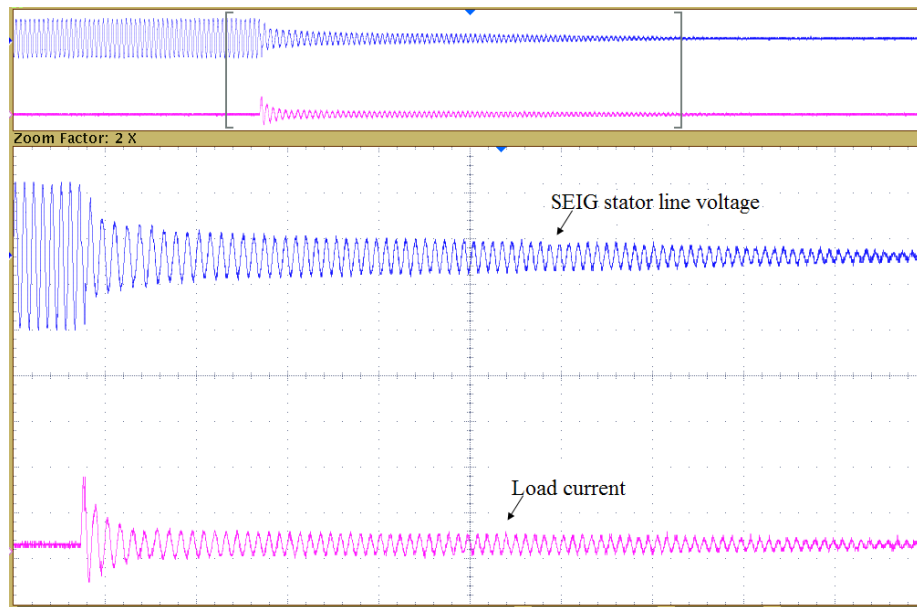


Figure 3.14: Experimental waveforms of overloaded SEIG line voltage and load current

#### (d) Performance of wind driven SEIG system feeding induction motor load

An induction motor (IM) is connected with the wind turbine driven SEIG to observe the performance of SEIG. The specifications of the IM taken as a load are: 1.5 kW, 415 V, 3.2

A, 50 Hz, 1500 r.p.m, delta connected. Its parameters are given in Table 3.4.

Table 3.4: The parameters of the induction machine used as load

$R_{sm}$	$R_{rm}$	$X_{lsm}$	$X_{lrm}$	$X_{mm}$	$J_m$
0.0832 p.u	0.0853 p.u	0.1101 p.u	0.1101 p.u	1.83 p.u	0.0205 p.u kg/m <sup>2</sup>

Fig. 3.15 (a) shows that active power of SEIG changes from no-load value of zero to peak transient value of -828 W after loading but finally settles at zero. Fig. 3.15 (b) shows that the reactive power demanded by SEIG changes from no-load value of -3490 VAR to zero after loading. SEIG stator line voltage has a no-load peak value of 586.8 V which collapses to zero, after loading as seen from Fig. 3.15 (c). The IM stator current increases from zero to peak value of 4.5 A during the transient period after loading, but collapses to zero at steady-state as shown in Fig. 3.15 (d). All of the above occur because of the voltage collapse of SEIG.

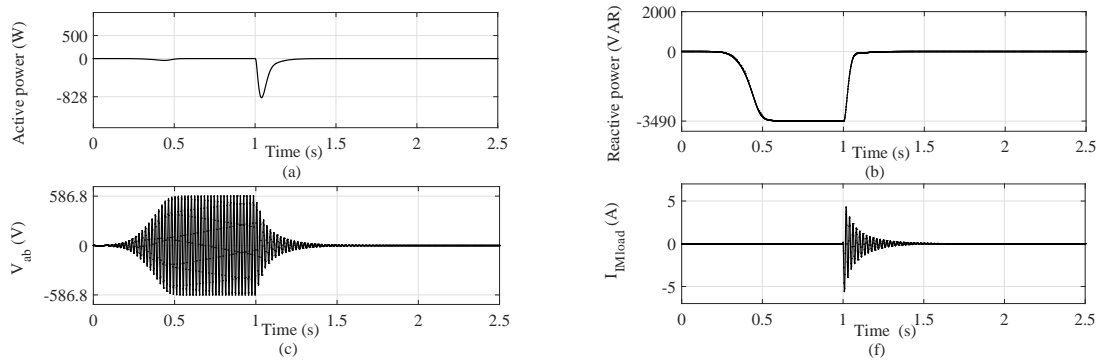


Figure 3.15: Simulation results of wind turbine driven SEIG fed IM load system:(a) SEIG active power (b) Reactive power demanded by SEIG (c) Stator line voltage (d) Load current

Fig. 3.16 shows the experimental set up of SEIG fed IM load system. Fig. 3.17 shows the experimental waveforms of the SEIG fed IM system. SEIG line voltage collapse is shown by Fig. 3.17 (top) and IM stator line current transient is shown by Fig. 3.17 (bottom). Fig. 3.17 (bottom) shows that initially high starting peak current of 8.5 A is drawn by IM load. Due to this starting transient of IM load SEIG voltage collapse occurred, and IM is not able to run smoothly.



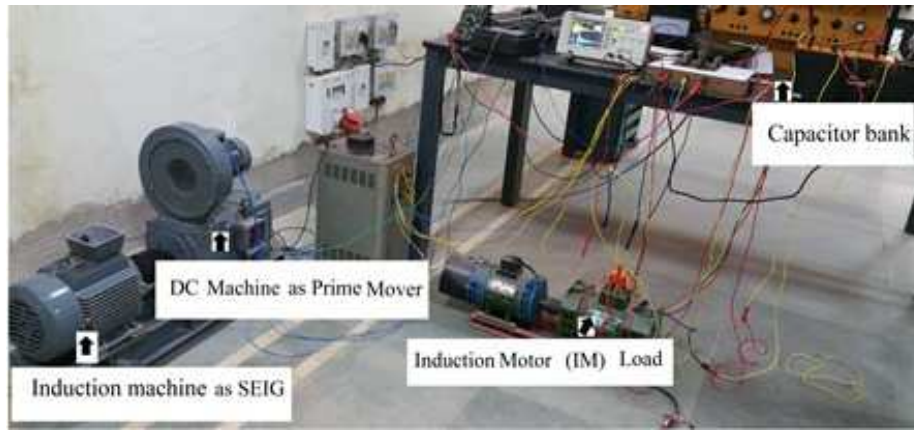


Figure 3.16: Experimental set up of SEIG fed IM load

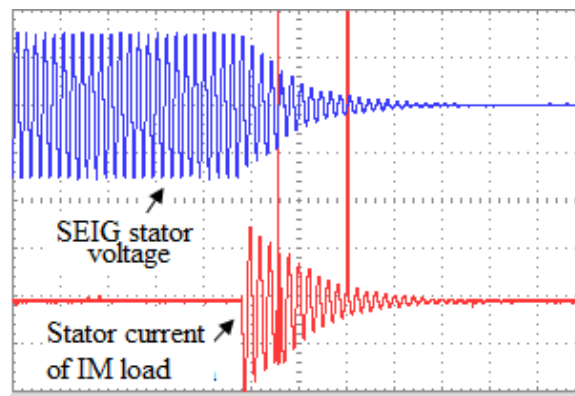


Figure 3.17: Experimental waveforms of SEIG fed IM load: SEIG line voltage (top), stator current of IM load (bottom)

#### (e) Performance of wind driven SEIG system with wind perturbations

As already described, for wind speed of 9.8 m/s with an excitation capacitance of 21.5  $\mu\text{F}$ , SEIG develops rated peak line voltage of 586.8 V. When resistive load of 100  $\Omega$ /phase is connected to SEIG, its terminal voltage decreases to 469 V. To study the performance of wind turbine driven SEIG system with wind perturbations for the same load, the speed of the wind is increased from 9.8 m/s to 10 m/s at  $t=2.5$  s, then decreased to 9.2 m/s at  $t=3.5$  s and at  $t=4.5$  s increased to 11 m/s. The above-mentioned profile of the wind speed, considered for the simulation, is shown in Fig. 3.18 (a). Variations of SEIG rotor speed with respect to wind speed variations, is shown in Fig. 3.18 (b). Load of 100  $\Omega$ /phase is connected at  $t=1$  s. Corresponding to this loading, SEIG rotor speed decreased from 157 rad/s to 156.1 rad/s, as observed in Fig. 3.18 (b). It is observed that SEIG speed and hence stator voltage increased for increasing wind speed and decreased with decreasing



wind speed. At  $t= 2.5$  s, when wind speed increased from 9.8 m/s to 10 m/s, rotor speed increased from 156.1 rad/s to 159.2 rad/s. At  $t=3.5$  s, when wind speed decreased to 9.2 m/s, corresponding to that rotor speed decreased to 147 rad/s. At  $t=4.5$  s, when speed increased to 11 m/s, corresponding to that rotor speed increased to 175 rad/s. At  $t=1$  s, due to loading SEIG peak voltage reduces from 586.8 V to 469 V as observed in Fig. 3.18 (c). At  $t= 2.5$  s, due to increase in rotor speed, peak voltage increases to 506 V. At  $t=3.5$  s, due to decrease in wind and rotor speed, peak voltage reduces to 291.4 V. At  $t=4.5$  s, peak SEIG voltage increases to 606 V. Fig. 3.18 (d) shows the active power of SEIG. Active power changed from no load value zero to -1100 W after loading at  $t= 1$  s. When the wind speed increased to 10 m/s at  $t=2.5$  s, corresponding to that active power changed to -1281 W indicating an increase in magnitude of active power output. At  $t=3.5$  s, when wind speed decreased to 9.2 m/s, corresponding to that SEIG active power changed to -430 W indicating a decrease in magnitude of power output. At  $t=4.5$  s, when wind speed increased to 11 m/s, corresponding to that active power changed to -1840 W, indicating an increase in magnitude of power output. Fig. 3.18 (e) shows the reactive power demanded by SEIG. At  $t=1$  s, SEIG voltage reduces due to loading. So, reactive power changed from -3490 VAR to -2084 VAR, indicating a decrease in magnitude. At  $t=2.5$  s, when wind speed increased to 10 m/s and stator voltage increased, reactive power changed to -2474 VAR, indicating an increase in magnitude. At  $t=3.5$  s, when wind speed decreased to 9.2 m/s, reactive power changed to -759.4 VAR indicating a drop in magnitude. At  $t=4.5$  s, when wind speed increased to 11 m/s, SEIG voltage increased and corresponding to that reactive power changed to -3899 VAR, indicating an increase in magnitude. The reason behind these variations being active power increased with increasing wind speed and decreased for decreasing wind speed. The amount of active power output of SEIG, rotor speed, stator voltage and magnitude of VAR increased or decreased corresponding to that. Fig. 3.18 (f) shows the load current of SEIG under wind speed perturbations. Peak value of load current increases from 0 to 3 A at  $t=1$  s and reaches to a steady-state peak value of 2.7 A. At  $t=2.5$  s, wind speed increased and due to that SEIG voltage increased. So peak value of load current also increased to 2.9 A. At  $t=3.5$  s, due to decrease in wind speed, SEIG peak voltage decreases. So peak value of load current decreases from 2.9 A and settles at a steady-state peak value of 1.68 A. At  $t=4.5$  s, load current increases with wind speed and SEIG voltage reaches to the steady-state peak value of 3.5 A. Frequency of SEIG is shown by Fig. 3.18 (g). Due to connection of load at  $t=1$  s, SEIG frequency decreases from 50 Hz to 46.69 Hz. At  $t=2.5$  s wind speed increases, so SEIG frequency increases from 46.69 Hz to 47 Hz. At  $t=3.5$  s wind speed decreases, so SEIG frequency decreases from 47 Hz to 45 Hz. Increase of wind speed at  $t=4.5$  s, increases SEIG frequency from 45 Hz to 53 Hz.

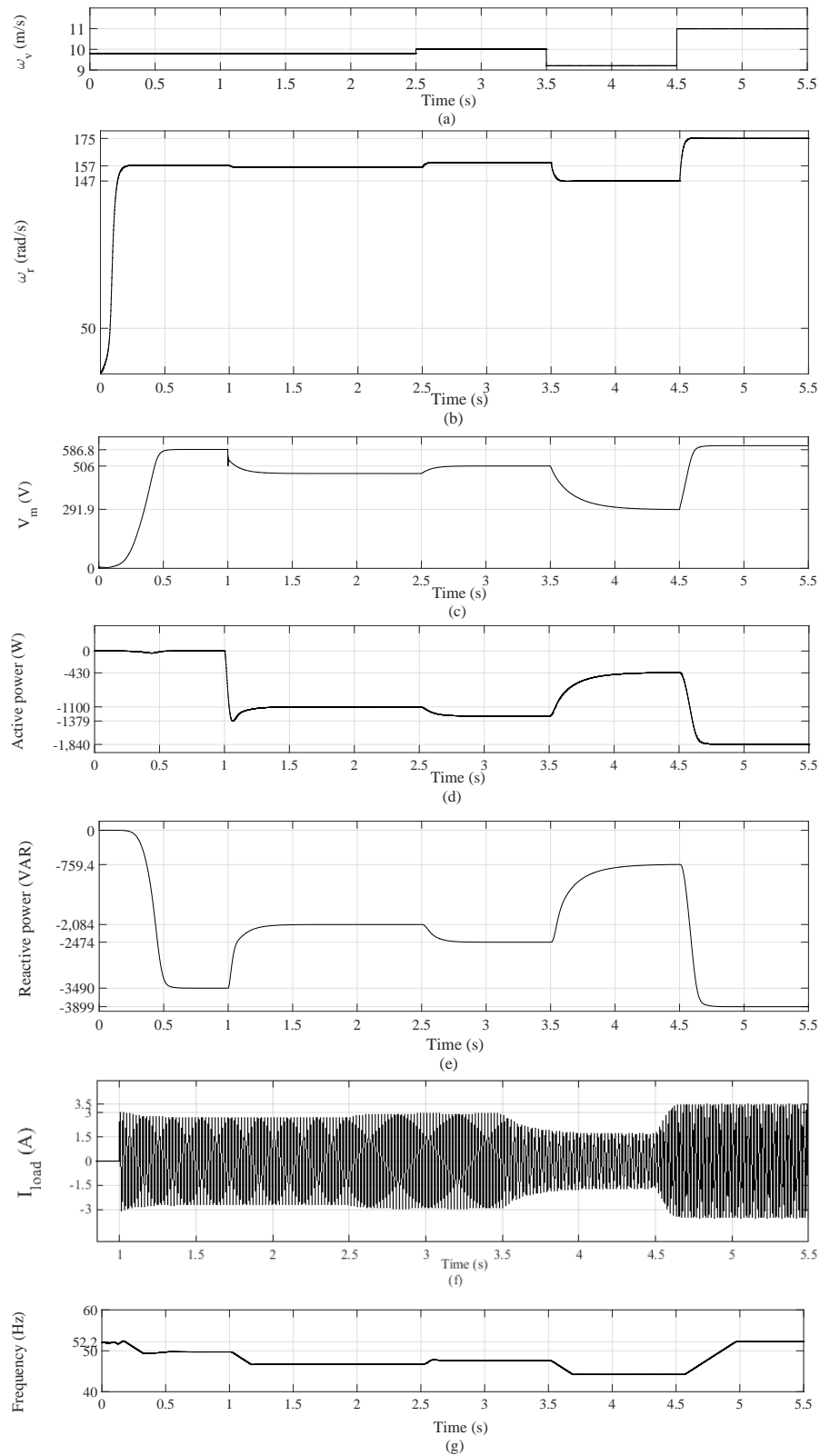


Figure 3.18: Simulation results of wind turbine driven SEIG system with wind speed perturbations: (a) Wind speed (b) SEIG rotor speed (c) SEIG peak voltage (d) Active power of SEIG (e) Reactive power demanded by SEIG (f) Load current (g) SEIG frequency

### (f) Performance of wind driven SEIG system with variation of excitation capacitance

To observe the performance of wind turbine driven SEIG system with variation of excitation capacitance, a variable capacitor is connected across SEIG. For the fixed prime mover speed, peak SEIG terminal voltage of 586.8 V is developed by connecting the capacitor bank with 21.5  $\mu\text{F}$  capacitance value per phase. As already discussed, load connection of 100  $\Omega$ /phase with SEIG, decreased the SEIG peak voltage to 469 V. It is understood, by adjusting the excitation capacitance, SEIG voltage can be compensated. At  $t=2.5$  s excitation capacitance value is increased by 7  $\mu\text{F}$ / phase. Fig. 3.19 (a) shows the waveform of SEIG stator voltage, whose peak value increased from 469 V to 564 V due to capacitance increase at  $t=2.5$  s. Peak stator voltage profile is shown in Fig. 3.19 (b). Fig. 3.19 (c) shows the active power from the SEIG which increased from no load value of zero to -1100 W due to load connection at  $t=1$  s. Due to increase in capacitance at  $t= 2.5$  s and subsequent increase in voltage, active power changed to -1522 W indicating an increase in magnitude. Fig. 3.19 (d) shows the reactive power demanded by SEIG changed from -2084 VAR to -3790 VAR indicating an increase in magnitude, due to voltage increase. Fig. 3.19 (e) shows the SEIG stator line current. Due to load connection at  $t=1$  s, SEIG stator line current peak value reduced from 6.9 A to 5.8 A. Due to increase in capacitance at  $t=2.5$  s, SEIG stator line current peak value increased from 5.8 A to 8.5 A. Fig. 3.19 (f) shows the SEIG load current after loading at  $t=1$  s, SEIG load current peak value increases from 0 to 2.9 A at steady-state. Due to increase in capacitance at  $t=2.5$  s, SEIG load current peak value increases from 2.9 A to 3.18 A. Fig. 3.19 (g) shows the SEIG stator frequency. SEIG stator frequency is reduced from 50 Hz to 46.3 Hz. Due to increase in capacitance at  $t=2.5$  s, SEIG stator frequency remains unchanged.

Fig. 3.20 shows the experimental waveforms of SEIG stator line voltage and load current with the increase of excitation capacitance value. Top window of Fig. 3.20 presents SEIG stator line voltage and load current. Zoomed version of top window is shown in bottom window. It is observed from the Fig. 3.20 that due to load connection SEIG voltage reduces from rated peak voltage of 590 V voltage to 464 V and load current peak value changes from 0 A to 2.5 A. Due to increase in capacitance of 7  $\mu\text{F}$  SEIG voltage changes from 464 V to 560 V and load current increases from 2.5 A to 3 A. The capacitance excitation is increased by taking the value available in the laboratory.

These peak voltages and peak currents obtained from the experiment are in very close agreement with corresponding values obtained from simulation, as evident from Table 3.5.

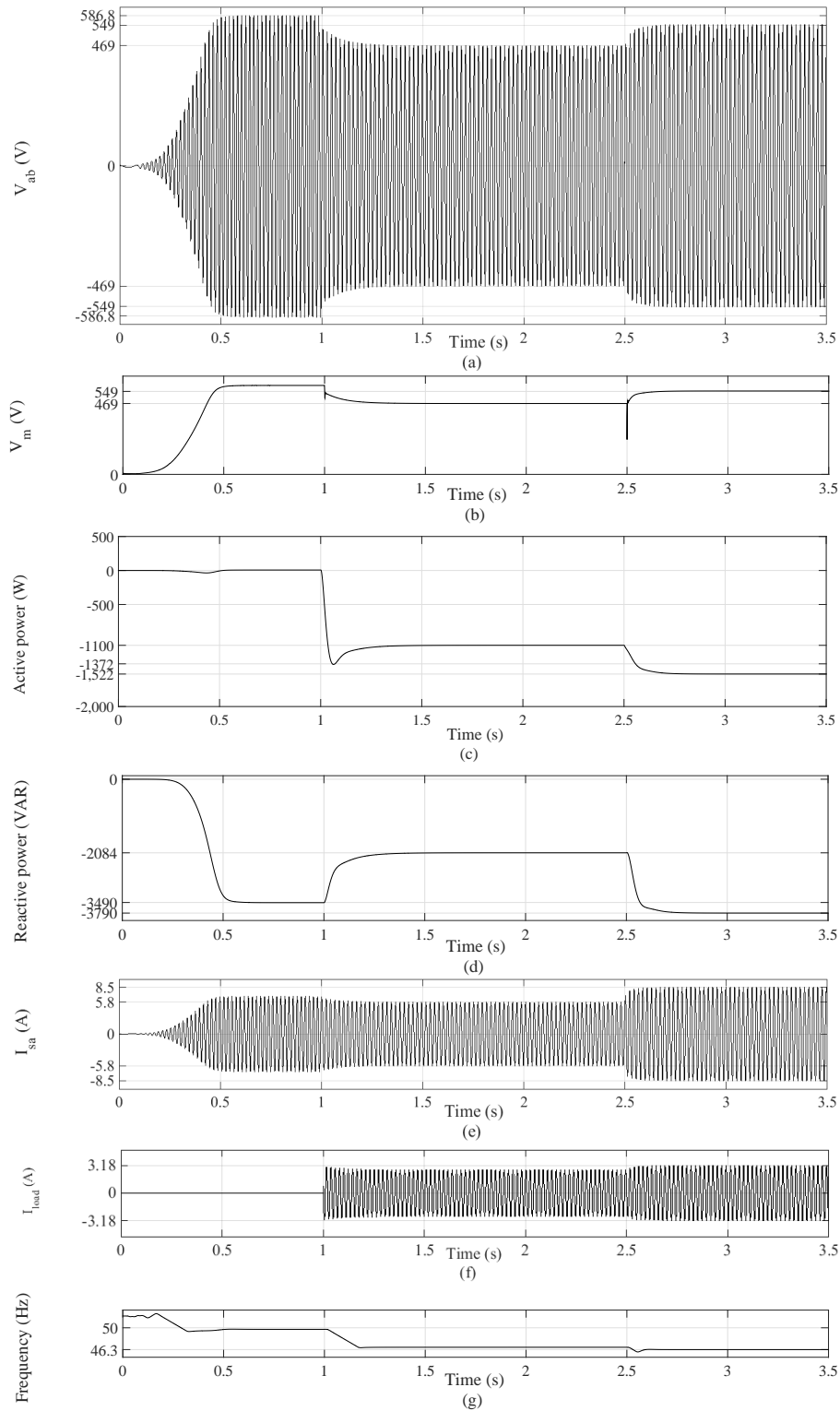


Figure 3.19: Simulation results of wind turbine driven SEIG system with with increase of excitation capacitance: (a) SEIG line voltage (b) SEIG peak voltage (c) Active power of SEIG (d) Reactive power demanded by SEIG (e) SEIG stator line current (f) Load current (g) SEIG frequency

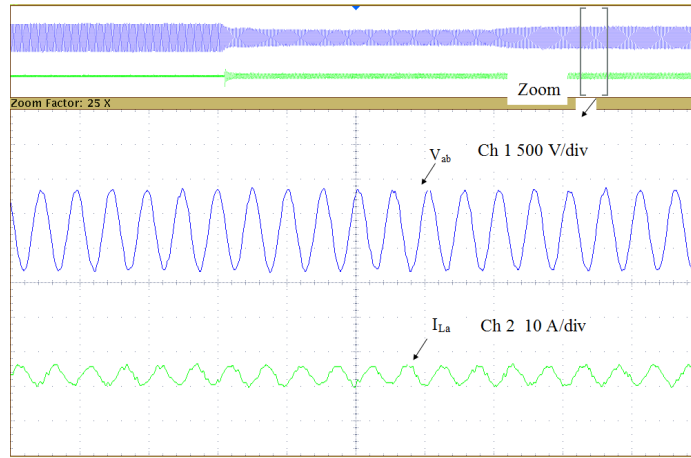


Figure 3.20: Experimental waveforms of SEIG stator voltage (top) and load current (bottom) with increase of excitation capacitance value

Table 3.5: Comparison of simulation and experimental results

Case	Simulation value						Experimental value					
	$V_{ab}$ (V)		$I_{sa}$ (A)		$I_{load}$ (A)		$V_{ab}$ (V)		$I_{sa}$ (A)		$I_{load}$ (A)	
	Initial	Final	Initial	Final	Initial	Final	Initial	Final	Initial	Final	Initial	Final
No load	0	586.8	0	6.9	0	0	0	590	0	6.5	0	0
with 100	586.8	469	6.9	5.8	0	2.9	590	464	6.5	5.6	0	2.5
Over load	586.8	0	6.9	0	0	0	590	0	6.5	0	0	0
IM load	586.8	0	6.9	0	0	0	590	0	6.5	0	0	0
Increase of C	469	564	5.8	8.5	2.9	3.18	464	560	5.6	8	2.5	3

### 3.8 Summary of the Chapter

An analytical expression for the minimum value of capacitance required to develop SEIG rated voltage and frequency is derived. Mathematical model of wind turbine driven SEIG system is reviewed. Simulation of developed wind driven SEIG model is carried out in MATLAB/Simulink environment. The performance of wind turbine driven SEIG system taking different types of load such as resistive load,  $R-L$  load, induction motor (IM) load is discussed. Simulation and experimental results of SEIG system with resistive load, heavy load and IM load are presented and compared. It is observed that SEIG excitation fails with overload and IM load. Simulation results of SEIG system with wind variations are also discussed and presented. Voltage can be compensated to some extent by increasing the excitation capacitance value. Simulation and experimental results of SEIG system with capacitance variation are presented, discussed and compared. It is observed that SEIG voltage and frequency vary with load, prime mover speed and excitation capacitance. Hence, SEIG demands voltage and frequency controller to maintain SEIG voltage and frequency.

# Chapter 4

## Development of an optimized voltage controller for GIC based SEIG system

### 4.1 Introduction

As discussed in previous chapter, voltage and frequency of SEIG are changed with load and prime mover speed. So SEIG demands voltage and frequency controller to maintain its terminal voltage and frequency during load and prime mover speed perturbations. Fixed value capacitors in parallel with saturable core reactor are used for controlling the terminal voltage of SEIG [42]. However, this scheme involves discrete steps and large size inductors. Voltage is also regulated using static VAR compensator (SVC) [43]. This scheme composed of TCR in parallel with TSC. However, the problem with this scheme are sluggish response, high switching transients and injecting current harmonics into the bus. Innovation of power electronic switches, digital signal processors and enriched control algorithm enabled researchers to use STAtic COMpensator (STATCOM) for improving performance of SEIG [48], [58], [16], [9], [59]. All these control schemes are based on sensing either voltage or current which demand multiple sensors and complex electronic circuits which make SEIG system complex and expensive. Among all, control scheme proposed by Perumal *et al.* [16] to regulate SEIG voltage and frequency is simple. This control scheme consists three sensors along with a single loop where voltage is used as feedback. But this voltage control scheme is not addressed the design of optimal proportional and integral gains which make GIC based SEIG system stable. However, determination of optimal proportional and integral gains which also makes the closed loop system stable is a tedious task. Most of the literature have reported tuning methods in the ideal case for stabilizing *PID*. But these tuning methods have not considered delay/dead time of the system. In 2002 Silva *et al.* [17] provided mathematical derivations to characterize the set of proportional, integral and derivative gains that stabilize the first-order plant with time delay.

Further these authors in 2005 [18] extended their work to provide mathematical derivations to characterize the set of proportional and integral gains that stabilize a first-order plant with time delay and in this chapter these mathematical derivations are used to compute proportional and integral gains. The plant (GIC integrated with SEIG) is considered here as a first order due to its step response. Parameters of the plant are evaluated and then mathematical derivations provided by Silva *et al.* [18] used to compute stable zones of proportional and integral gains for controlling voltage of SEIG integrated with GIC. Further, optimal values of proportional and integral gains within stable zone are computed using PSO technique. Performance of optimized GIC based SEIG system by taking resistive and IM load under varied wind speed is studied in MATLAB/Simulink environment.

In this chapter modeling of GIC and its operation are described in section 4.2 and 4.3, respectively. Section 4.4 describes voltage control scheme of GIC based SEIG system followed by section 4.5 which describes computation of optimal proportional and integral gains of GIC based SEIG system to regulate voltage. Section 4.6 describes performance of optimized GIC based SEIG system by taking resistive and IM load under varied wind speed followed by chapter summary.

## 4.2 Modeling of generalized impedance controller (GIC)

Generalized impedance controller (GIC) is a pulse width modulated (PWM) voltage source inverter (VSI) with a bank of battery connected to its DC bus and a coupling transformer having reactance  $X_c$  connected at its AC bus that are highlighted in Fig. 4.1 for SEIG system. The output voltage of GIC [16] is expressed as

$$\begin{bmatrix} v_{invaN} \\ v_{invbN} \\ v_{invcN} \end{bmatrix} = \frac{V_{DC}}{3} \begin{bmatrix} 2 & -1 & -1 \\ -1 & 2 & -1 \\ -1 & -1 & 2 \end{bmatrix} \begin{bmatrix} S_a \\ S_b \\ S_c \end{bmatrix} \quad (4.1)$$

where  $v_{invaN}$ ,  $v_{invbN}$  and  $v_{invcN}$  are the instantaneous output voltages of  $a$ ,  $b$  and  $c$  phases of the inverter, respectively.  $V_{DC}$  is the DC voltage.  $S_a$ ,  $S_b$  and  $S_c$  are the switching function of the three legs of the voltage source inverter. When  $S_a = 1$ ,  $S_1$  (the upper switch of phase-a limb) is on.  $S_4$  (the lower switch of phase-a limb) is on when  $S_a = 0$ . Similarly, when  $S_b = 1$ ,  $S_3$  (the upper switch of phase-b limb) is on.  $S_6$  (the lower switch of phase-b limb) is on when  $S_b = 0$ . For  $S_c = 1$ ,  $S_5$  (the upper switch of phase-c limb) is on.  $S_2$  (the lower switch of phase-c limb) is on when  $S_c = 0$ . The state equation of instantaneous current injected into the point of common coupling (PCC) by the VSI is given by equation (4.2).

$$\begin{bmatrix} pi_{GICa} \\ pi_{GICb} \\ pi_{GICc} \end{bmatrix} = \frac{R_c}{L_c} \begin{bmatrix} -1 & 0 & 0 \\ 0 & -1 & 0 \\ 0 & 0 & -1 \end{bmatrix} \begin{bmatrix} i_{GICa} \\ i_{GICb} \\ i_{GICc} \end{bmatrix} + \frac{1}{L_c} \begin{bmatrix} v_{aN} - v_{invaN} \\ v_{bN} - v_{invbN} \\ v_{cN} - v_{invcN} \end{bmatrix} \quad (4.2)$$

where  $R_c$  and  $L_c$  are resistance and inductance of coupling transformer, respectively.  $v_{aN}$ ,  $v_{bN}$  and  $v_{cN}$  are the instantaneous terminal phase voltages of SEIG.  $i_{GICa}$ ,  $i_{GICb}$  and  $i_{GICc}$  are the instantaneous currents of  $a, b$  and  $c$  phases of GIC.  $pi_{GICa}$ ,  $pi_{GICb}$  and  $pi_{GICc}$  are the rate of change of  $i_{GICa}$ ,  $i_{GICb}$  and  $i_{GICc}$ , respectively. The next subsection describes the operation of GIC.

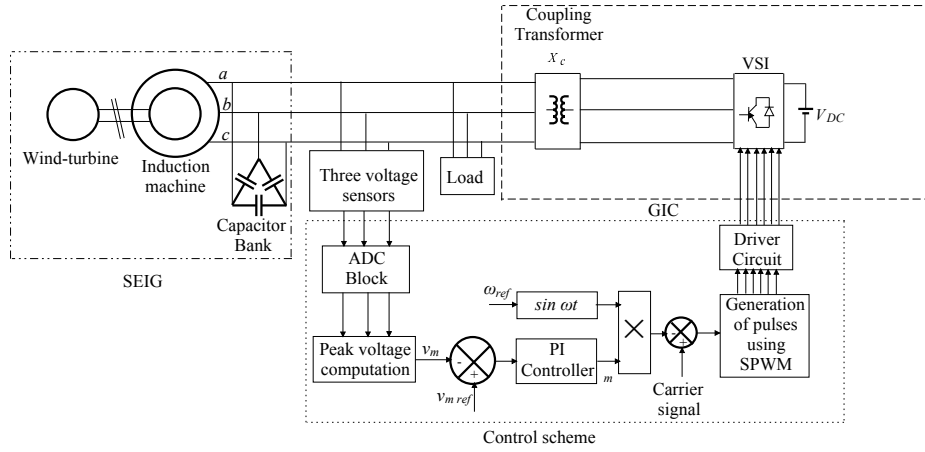


Figure 4.1: Schematic diagram of a GIC based SEIG system

### 4.3 Operation of generalized impedance controller (GIC)

The GIC is connected with the SEIG at PCC in such a manner that no exchange of active power and reactive power between them occurs. The expressions given in [77] for GIC active power  $P$  and reactive power  $Q$  are reproduced as follows.

$$P = v^2 \frac{r_1}{X_c} \sin \delta \quad (4.3)$$

$$Q = v^2 \frac{1 - r_1 \cos \delta}{X_c} \quad (4.4)$$

$$r_1 = \frac{v_{inv}}{v} \quad (4.5)$$



$$v_{inv} = \frac{k_1 m V_{DC}}{\sqrt{2}} \quad (4.6)$$

where  $v$  is the fundamental voltage of SEIG.

$v_{inv}$  is the fundamental voltage of GIC.

$r_1$  is the ratio of the GIC and SEIG fundamental voltages.

$\delta$  is the phase angle between the GIC and SEIG fundamental voltages.

$m$  is the modulation index of the inverter.

and  $k_1$  is the turns ratio of coupling transformer.

Substituting  $r_1 = 1$  in (4.5) and using it in (4.6), the expression for critical value of  $m$  is derived as,

$$m_{critical} = \frac{\sqrt{2}v}{k_1 V_{DC}} \quad (4.7)$$

As already described, to connect GIC with SEIG at PCC, exchange of active and reactive power between SEIG and GIC should be zero. So, to connect GIC with SEIG, relative phase angle  $\delta$  and modulation index are set at  $0^\circ$  and  $m_{critical}$ , respectively. The operation of GIC with various values of  $r_1$  and phase angle  $\delta = 0^\circ$  are presented in next subsection.

### 4.3.1 GIC operation while floats across SEIG

When the voltage magnitude ratio between fundamental component of the GIC and the SEIG output voltages, *i.e.*,  $r_1 = 1$  and the relative phase angle between them  $\delta = 0^\circ$ , during these conditions no exchange of active and reactive power occurs between them. During this condition, the value of modulation index  $m$ , is called critical value of modulation index  $m_{crit}$ . The phasor diagram corresponding to this operating condition is shown in Fig. 4.2.

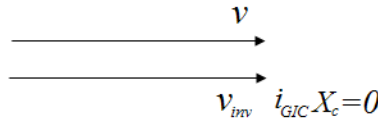


Figure 4.2: Phasor diagram of GIC while floating across SEIG

### 4.3.2 GIC Operation as a capacitor or an inductor

When the relative phase angle *i.e.*,  $\delta$  between fundamental components of GIC output voltage ( $v_{inv}$ ) and the SEIG terminal voltage ( $v$ ) be zero, GIC operated as a pure VAR compensator. Corresponding to this condition, the current  $i_{GIC}$  drawing is always either  $90^\circ$  leading or lagging with respect to the potential difference between  $v_{inv}$  and  $v$ . This occurs

because of the coupling transformer connecting between the SEIG and GIC terminals. Due to presence of switching losses small active power flows into the GIC which are too small compared to reactive power into GIC so neglected.

When the magnitude of the fundamental component of GIC ( $v_{inv}$ ) is higher than that of SEIG ( $v$ ), GIC provides reactive power to the SEIG. In this case the voltage ratio *i.e.*,  $r_1 > 1$  and GIC operated as a pure capacitor. Phasor diagram corresponding to this condition is shown in Fig. 4.3. Current value  $i_{GIC}$  is obtained from the voltage difference between  $v_{inv}$  and  $v$  and the coupling reactance  $X_c$ . Corresponding to this condition the current leads the voltage by  $90^\circ$ .

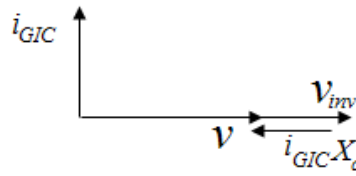


Figure 4.3: Phasor diagram of GIC while operated as capacitor

When the magnitude of the fundamental component of GIC ( $v_{inv}$ ) is lower than that of SEIG ( $v$ ), GIC absorbs reactive power from the SEIG. In this case the voltage ratio *i.e.*,  $r_1 < 1$  and GIC operated as a pure inductor. Phasor diagram corresponding to this condition is shown in Fig. 4.4. Current value  $i_{GIC}$  is obtained from the voltage difference between  $v$  and  $v_{inv}$  and the coupling reactance  $X_c$ . Corresponding to this condition the current lags the voltage by  $90^\circ$ . GIC with DC battery bank can provide or absorb reactive power according to the

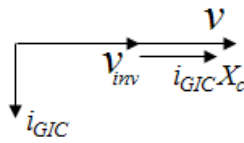


Figure 4.4: Phasor diagram of GIC while operated as inductor

amplitude of GIC fundamental voltage as mentioned in the above discussion and the phasor diagrams presented in Fig. 4.2, Fig. 4.3 and Fig. 4.4. Variation of the fundamental component of GIC voltage is achieved by varying the GIC modulation index,  $m$ . Next section describes how modulation index varies with respect to SEIG voltage.

## 4.4 Voltage control of GIC based SEIG system

Fig. 4.1 shows the schematic diagram of GIC based voltage controlled SEIG system. The peak voltage of SEIG is compared with the peak reference voltage and the error passed through the *PI* controller as shown in Fig. 4.1. The output of the *PI* controller is the modulation index, ( $m$ ). The *PI* controller is considered for maintaining terminal voltage, because of its simplicity, good performance, fast response and zero steady-state error. The *PI* controller is described by

$$y(t) = k_p \varepsilon(t) + k_i \int_0^t \varepsilon(t) dt \quad (4.8)$$

where  $y(t) = m$ .  $\varepsilon(t)$  is the error voltage *i.e.*, difference between  $v_{mref}(t)$  and  $v_m(t)$ .  $v_{mref}(t)$  is the SEIG rated peak voltage.  $v_m(t)$  is the computed peak voltage of SEIG.  $k_p$  and  $k_i$  are the optimized proportional gain and integral gain of the *PI* controller, respectively.

The *PI* controller maintains the terminal voltage of SEIG at the rated value. The output of *PI* controller is multiplied with sine wave of unit amplitude and reference frequency, and then compared with carrier wave to obtain switching signals  $S_a, S_b, S_c, \overline{S}_a, \overline{S}_b, \overline{S}_c$  of VSI for providing gate drives to IGBTs. But determination of proportional and integral gains of *PI* optimally which also makes the closed loop system stable is a tedious task which covered in next section.

## 4.5 Computation of optimal proportional and integral gains within stable zone for controlling SEIG voltage

Various methods have been developed and reported in the literature over last four decades regarding setting the parameters of *P*, *PI*, and *PID* controllers [17]. Out of these, few methods are developed on characterizing the dynamic response of the plant to be controlled with a first-order model including time delay. Moreover most of these tuning methods though provides satisfactory results, but not gives any information regarding about all stabilizing *PID* controllers with dead time remains unknown. In 2002 Silva *et al.* in [17] provided complete solution to the problem of characterizing the set of all *PID* gains that stabilize a given first-order plant with time delay. Further these authors in 2005 [18] extended their work to provide mathematical derivations to characterize the set of proportional and integral gains that stabilize a first-order plant with time delay. Mathematical derivations provided by Silva *et al.* are reproduced in the following subsection and used to compute stable zones of proportional and integral gains for controlling voltage of SEIG integrated with GIC. Next subsection describes the evaluation of parameters of GIC based voltage controller of SEIG

system.

### 4.5.1 Parameters evaluation of GIC based voltage controller of SEIG system

The GIC based SEIG system is the plant and taken here as a single input single output feedback control system as shown in Fig. 4.5.  $v_m$  is the output voltage of the plant and  $L(s)$  is the controller. The type of the controller considered here is *PI* and represented in following equation.

$$L(s) = k_p + \frac{k_i}{s} \quad (4.9)$$

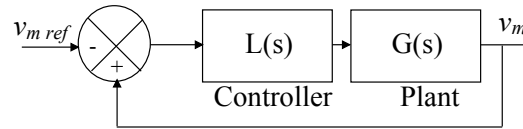


Figure 4.5: Feedback control system

The plant considered here is a first order due to its step response [17] and mathematically represented by as follows.

$$G(s) = \frac{k_v}{1 + sT} e^{-\tau s} \quad (4.10)$$

where  $k_v$  represents the open-loop steady-state gain,  $T$  represents the time constant and  $\tau$  represents the time delay of the plant. These parameters are determined as shown in the Fig. 4.6 graphically. The value of steady-state gain  $k_v$  is evaluated by applying a step change in the modulation index,  $m$  to the plant. At  $t=0.8$  s, modulation index,  $m$  is changed from 0.7 to 0.8 as shown in Fig. 4.6 (a) and corresponding to this change in modulation index,  $m$ ,  $v_m$  changed from 598 V to 664 V as shown in Fig. 4.6 (b).  $k_v$  is evaluates as follows.

$$k_v = \frac{\Delta v_m}{\Delta m} \quad (4.11)$$

Fig. 4.6 (c) is the zoomed version of Fig. 4.6 (b). The parameters  $\tau$  and  $T$  for the plant are evaluated using the time interval between points  $M$  &  $N$  and  $N$  &  $O$ , respectively.  $M$  is the onset of the step change.  $N$  is the intercept of the tangent to the step response having the largest slope with the horizontal axis.  $O$  is the time when the step response has reached to  $0.63 k_v$ . The parameters computed from Fig. 4.6 (b) and Fig. 4.6 (c) of the taken GIC based SEIG system are:  $k_v = 660$ ,  $\tau = 0.004$  and  $T = 0.018$ .

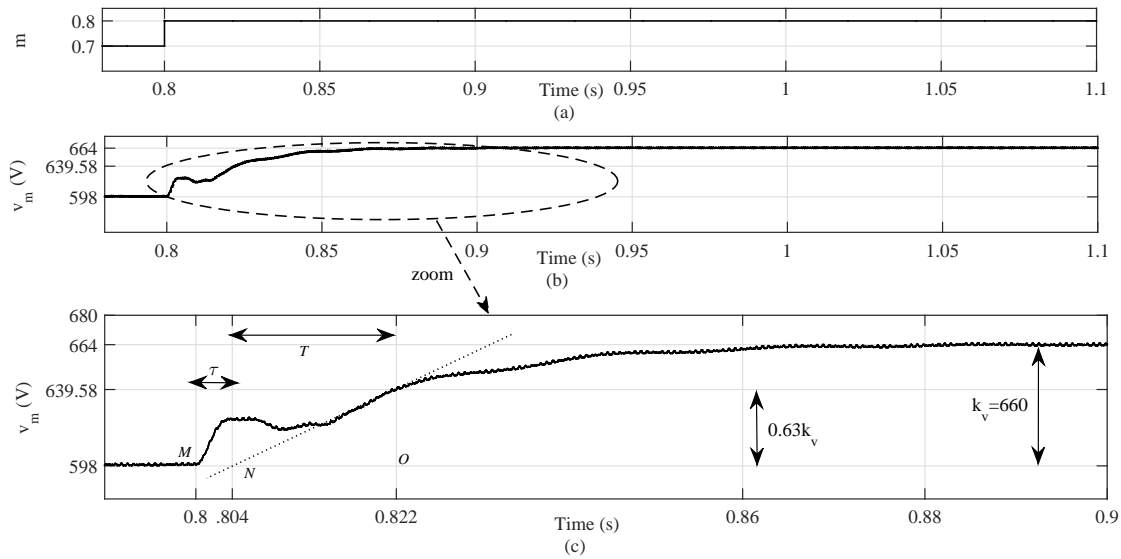


Figure 4.6: Open loop response of GIC based SEIG system for step change in modulation index

The next subsection is reproduced the mathematical expressions [18] to compute stable zone of proportional and integral gains of a first order system with time delay which makes the closed-loop system stable.

## 4.5.2 Derivation to compute stable zone of proportional and integral gains

When the time delay ( $\tau$ ) of the plant model as shown in Fig. 4.5 is zero, then the characteristics equation of the closed-loop system becomes

$$C(s) = Ts^2 + (k_vk_p + 1)s + k_vk_i \quad (4.12)$$

From the characteristic equation (4.12), it is observed that the closed-loop for a delay-free system becomes stable if

$$k_vk_i > 0, k_vk_p + 1 > 0, T > 0 \quad (4.13)$$

or

$$k_vk_i < 0, k_vk_p + 1 < 0, T < 0 \quad (4.14)$$

For an open loop system, if  $T > 0$  means the system is stable in open loop. However, if  $T < 0$  means the system is unstable in open loop. The conditions presented in (4.13) is true for open loop stable plant. However, expression (4.14) is true for open loop unstable

plant. Further, to access the closed loop stability of the delay-free system the following two conditions are presented by assuming positive steady-state gain  $k_v$  and given as follows.

$$k_p > \frac{-1}{k_v}, k_i > 0 \text{ (open-loop stable plant, i.e, } T > 0 \text{ )} \quad (4.15)$$

$$k_p < \frac{-1}{k_v}, k_i < 0 \text{ (open-loop unstable plant, i.e, } T < 0 \text{ )} \quad (4.16)$$

For computation of stable zones of an open loop stable delay-free plant, expression (4.15) is used. Similarly, expression (4.16) is applicable to compute the stable zones for delay-free open loop unstable plant. However, computed steady-state gain, delay and time constant of the plant (GIC based SEIG) are:  $k_v = 660$ ,  $\tau = 0.004$  and  $T = 0.018$ . Since GIC based SEIG is a time delay first order open loop stable system, stable zone presented in (4.15) is not applicable. Stable zone computation of proportional ( $k_p$ ) and integral ( $k_i$ ) gains of open loop stable time delay plant which makes the closed loop stable are described as follows.

The characteristic equation of the time delay system is given as follows.

$$C(s) = (k_v k_i + k_v k_p s) e^{-\tau s} + (1 + Ts)s \quad (4.17)$$

To compute the stability of the closed-loop system, it is essential that all the roots of the expression (4.17) lie in the open left hand plane (LHP). Due to the presence of the exponential term  $e^{-\tau s}$ , the number of roots of the expression (4.17) are infinite, so tedious task to check stability. So to solve this problem a quasi-polynomial  $C^*(s)$  is constructed by multiplying a term  $e^{\tau s}$  with  $C(s)$  and given as follows.

$$C^*(s) = e^{\tau s} C(s) = k_v k_i + k_v k_p s + (1 + Ts) s e^{\tau s} \quad (4.18)$$

By substituting  $s = j\omega$  in expression (4.18) and there after separating real and imaginary parts following expressions are obtained

$$C^*(j\omega) = C_r(\omega) + jC_i(\omega) \quad (4.19)$$

where

$$C_r(\omega) = k_v k_i - \omega \sin(\tau\omega) - T\omega^2 \cos(\tau\omega) \quad (4.20)$$

$$C_i(\omega) = \omega [k_v k_p + \cos(\tau\omega) - T\omega \sin(\tau\omega)] \quad (4.21)$$

Since  $k_v > 0$  and  $\tau > 0$  then it is observed from expressions (4.20) and (4.21) that the gain  $k_i$  only affects the  $C_i(\omega)$  whereas the gain  $k_p$  affects the imaginary part of the  $C^*(j\omega)$ . To compute the stabilizing gains ( $k_p$ ,  $k_i$ ) further, the variables of the expressions (4.20) and

(4.21) are changed by substituting  $\tau\omega = z$  and rewritten as follows.

$$C_r(z) = k_v k_i - \frac{z}{\tau} \sin(z) - T \frac{z^2}{\tau^2} \cos(z) \quad (4.22)$$

$$C_r(z) = k_v \left[ k_i - \frac{z}{k_v \tau} \sin(z) - T \frac{z^2}{k_v \tau^2} \cos(z) \right] \quad (4.23)$$

$$C_r(z) = k_v \left[ k_i - \frac{z}{k_v \tau} \left( \sin(z) + \frac{T}{\tau} z \cos(z) \right) \right] \quad (4.24)$$

$$C_r(z) = k_v [k_i - a(z)] \quad (4.25)$$

where,

$$a(z) = \frac{z}{k_v \tau} \left[ \sin(z) + \frac{T}{\tau} z \cos(z) \right] \quad (4.26)$$

$$C_i(z) = \frac{z}{\tau} \left[ k_v k_p + \cos(z) - \frac{T}{\tau} z \sin(z) \right] \quad (4.27)$$

Based on the Theorem 5.5 [18] presented in Appendix A, to confirm the stability of the quasi-polynomial  $C^*(s)$  two conditions must be satisfied which are given as follows.

**Step 1:** For some  $\omega_o$  in the range  $(-\infty, \infty)$

$$E(\omega_o) = C'_i(\omega_o)C_r(\omega_o) - C_i(\omega_o)C'_r(\omega_o) > 0 \quad (4.28)$$

For  $\omega_o = 0$ , value of  $z_o = \tau\omega_o = 0$ . These values are substituted in equations (4.25) and (4.27) and provides,  $C_r(z_o) = k_v k_i$  and  $C_i(z_o) = 0$ . Further, derivative of  $C_r(z_o)$ , *i.e.*,  $C'_r(z_o) = 0$ . Derivative of the expression (4.27) is expressed as follows.

$$C'_i(z) = \frac{k_v k_p}{\tau} + \left( \frac{1}{\tau} - \frac{T}{\tau^2} z^2 \right) \cos(z) - \left( \frac{1}{\tau} z + \frac{2T}{\tau^2} z \right) \sin(z) \quad (4.29)$$

Substituting  $z_o = 0$  in expression (4.29), value of  $C'_i(z_o)$  becomes  $\frac{(k_v k_p + 1)}{\tau}$ . Values of  $C_r(z_o)$ ,  $C'_r(z_o)$ ,  $C_i(z_o)$  and  $C'_i(z_o)$  are substituted in expression (4.28) which provides expression (4.30).

$$E(z_o) = \left( \frac{k_v k_p + 1}{\tau} \right) (k_v k_i) \quad (4.30)$$

Since  $k_v > 0$  and  $\tau > 0$ , if  $k_i > 0$  and  $k_p > -\frac{1}{k_v}$ , then only  $E(z_o) > 0$ .

**Step 2:** Next the interlacing of the roots  $C_r(z)$  and  $C_i(z)$  are checked. The roots of  $C_i(z)$  are

computed from expression (4.27) by equating with zero and expressed as follows.

$$\frac{z}{\tau} \left[ k_v k_p + \cos(z) - \frac{T}{\tau} z \sin(z) \right] = 0 \quad (4.31)$$

From (4.31), the following two expression are obtained.

$$z = 0 \quad (4.32)$$

$$k_v k_p + \cos(z) - \frac{T}{\tau} z \sin z = 0 \quad (4.33)$$

From expression (4.32), it is observed that one root of the  $C_i(z)$  *i.e.*,  $z_0 = 0$ . It is difficult to compute the other roots of the  $C_i(z)$  from expression (4.33). So expression (4.33) provides analytically the other roots of  $C_i(z)$ . The terms involved in the expression (4.33) are plotted in a graph. To obtain the nature of the solutions graphically from the plot, three different cases are considered. In each case the positive roots of the expression (4.33) are denoted by  $z_j$ , where  $j = 1, 2, \dots$ , arranged in increasing order of magnitude.

**Case 1:**  $\left( -\frac{1}{k_v} < k_p < \frac{1}{k_v} \right)$ , Corresponding to this case, two plots *i.e.*, (i)  $\frac{Tz}{\tau}$  vs  $z$  and (ii)  $\frac{k_v k_p + \cos(z)}{\sin(z)}$  vs  $z$  are depicted in Fig. 4.7. The points  $(z_1, z_2, z_3, \dots)$  are determined from the intersection between these two plots as seen in Fig. 4.7.

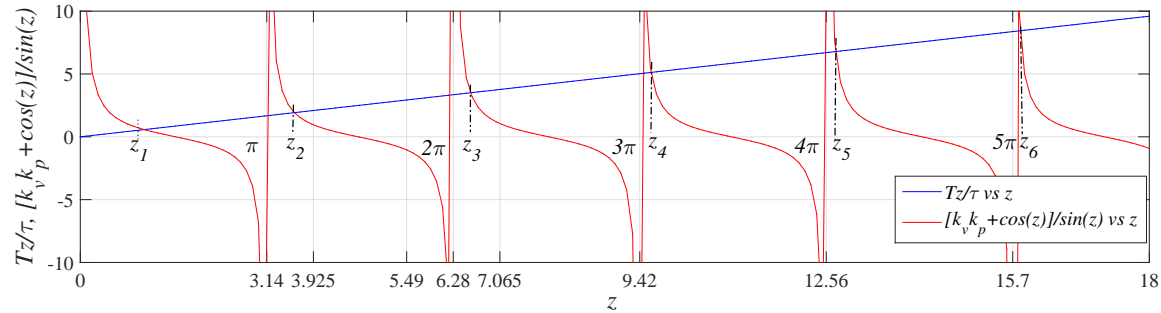


Figure 4.7: Plot of the terms involved in expression (4.33) for  $-\frac{1}{k_v} < k_p < \frac{1}{k_v}$

**Case 2:**  $\left( k_p = \frac{1}{k_v} \right)$ , Corresponding to this case, two plots *i.e.*, (i)  $\frac{Tz \sin(z)}{\tau}$  vs  $z$  and (ii)  $k_v k_p + \cos(z)$  vs  $z$  are presented in Fig. 4.8. The points  $(z_1, z_2, z_3, \dots)$  are determined from the intersection between these two plots as seen in Fig. 4.8.

**Case 3:**  $\left( \frac{1}{k_v} < k_p \right)$ , Corresponding to this case, Fig. 4.9 (a) and Fig. 4.9 (b) represent two plots *i.e.*, (i)  $\frac{Tz}{\tau}$  vs  $z$  and (ii)  $\frac{k_v k_p + \cos(z)}{\sin(z)}$  vs  $z$  by taking two different conditions. The Fig. 4.9



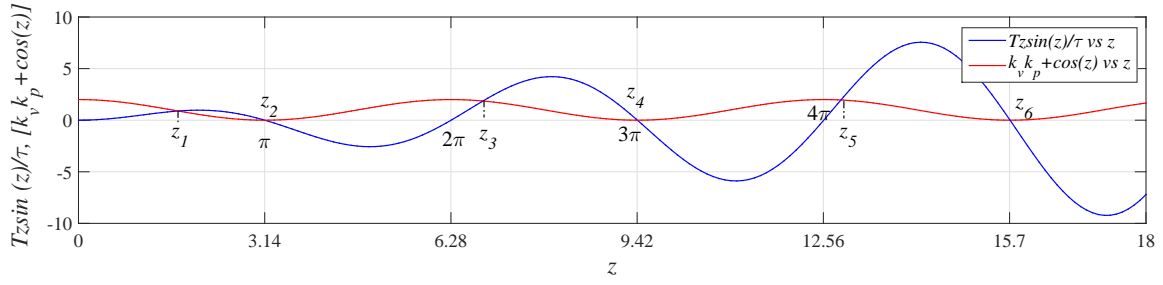


Figure 4.8: Plot of the terms involved in expression (4.33) for  $k_p = \frac{1}{k_v}$

(a) corresponds to the condition where  $\frac{1}{k_v} < k_p < k_u$ , and  $k_u$  is the largest value so that the plot of  $\frac{k_v k_p + \cos(z)}{\sin(z)}$  vs  $z$  intersects the line  $\frac{Tz}{\tau}$  vs  $z$  twice in the interval  $(0, \pi)$ . The Fig. 4.9 (b) corresponds to the condition where  $k_p \geq k_u$ . The plot  $\frac{k_v k_p + \cos(z)}{\sin(z)}$  vs  $z$  is not intersecting the plot  $\frac{Tz}{\tau}$  vs  $z$  twice in the interval  $(0, \pi)$ .

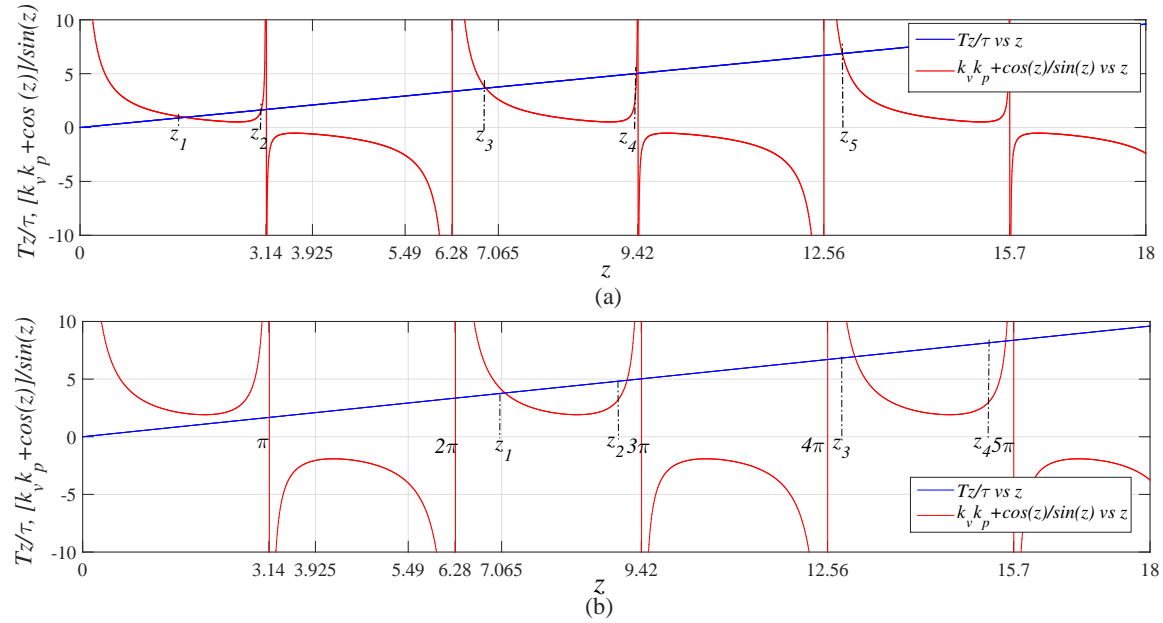


Figure 4.9: Plot of the terms involved in expression (4.33) for  $-\frac{1}{k_v} < k_p$

To determine analytically roots of  $C_i(z)$  three different cases are considered as mentioned above and presented in Fig. 4.7, Fig. 4.8 and Fig. 4.9. The closed loop system is stable for real roots only. To know the natures of the roots of  $C_i(z)$  the results of Theorem 5.6 [18] presented in Appendix A are used here. Based on the Theorem 5.6 a new quasi-polynomial  $C^*(s_1)$  is constructed by changing the variables *i.e.*,  $s = \frac{s_1}{\tau}$  in polynomial  $C^*(s)$

of expression (4.18) and given as follows.

$$C^*(s_1) = k_v k_i + \frac{k_v k_p s_1}{\tau} + \left(1 + \frac{T s_1}{\tau}\right) \frac{s_1}{\tau} e^{s_1} \quad (4.34)$$

The highest powers of  $s_1$  and  $e^{s_1}$  in the expression (4.34) are denoted by  $M_1$  and  $N_1$ , respectively. From the expression (4.34), value of  $M_1 = 2$  and  $N_1 = 1$ . Further, a constant  $\eta_1$  is selected so that value of  $\sin(\eta_1) \neq 0$ . For  $\eta_1 = \frac{\pi}{4}$ , there are three real roots, including a root at origin in the interval  $[0, 2\pi - \frac{\pi}{4}]$  for the above three cases (Fig. 4.7, Fig. 4.8 and Fig. 4.9 (a)), where  $\frac{-1}{k_v} < k_p < \frac{1}{k_u}$ . However, in Fig. 4.9 (b) for the interval  $[0, 2\pi - \frac{\pi}{4}]$  where  $k_p \geq k_u$  there is only one real root, *i.e.* at origin. As the expression of  $C_i(z)$  is an odd function of  $z$ . So, obviously for the interval  $[-(2\pi - \frac{\pi}{4}), 2\pi - \frac{\pi}{4}]$  there are five real roots including root at origin. Also, Fig. 4.7, Fig. 4.8 and Fig. 4.9 (a) have one real root available for the interval  $[2\pi - \frac{\pi}{4}, 2\pi + \frac{\pi}{4}]$ . Hence, all total six real roots are present including a root at origin of the expression for the interval  $[-2\pi + \frac{\pi}{4}, 2\pi + \frac{\pi}{4}]$ . So, based on the Theorem 5.6, for  $\eta_1 = \frac{\pi}{4}$ , in the intervals  $[-2l_1\pi + \eta_1, 2l_1\pi + \eta_1]$ , *i.e.*,  $[-2\pi + \frac{\pi}{4}, 2\pi + \frac{\pi}{4}]$  (for  $l_1 = 1$ )  $C_i(z)$ , consists exactly  $4l_1N_1 + M_1 =$  six ( $l_0 = 1$ ) number of real roots for the range  $\frac{-1}{k_v} < k_p < \frac{1}{k_u}$ . Moreover, it is concluded that  $C_i(z)$  has only real roots for the interval  $\frac{-1}{k_v} < k_p < \frac{1}{k_u}$ . All the roots of  $C_i(z)$  are not real for the range  $k_p > \frac{1}{k_u}$  as not satisfy the criteria present in the Theorem 5.6. So closed loop is stable only for range  $\frac{-1}{k_v} < k_p < \frac{1}{k_u}$ .

Next step is evaluating  $C_r(z)$  corresponding to the roots of  $C_i(z)$ . To get the initial value of  $C_r(z_0)$ , in the expression (4.25),  $z_0 = 0$  is substituted and expressed as follows.

$$C_r(z_0) = k_v [k_i - a(0)] = k_v k_i \quad [\text{As, } a(0)=0] \quad (4.35)$$

Values of  $z_j$  are substituted in the expression (4.25) to evaluate other values of  $C_r(z)$ , where  $j = 1, 2, 3, \dots$

$$C_r(z_j) = k_v [k_i - a(j)] \quad (4.36)$$

Interlacing the roots of  $C_r(z)$  and  $C_i(z)$  is equivalent to  $C_r(z_0) > 0$  (since  $k_i > 0$  as mentioned in step 1),  $C_r(z_1) < 0$ ,  $C_r(z_2) > 0$ ,  $C_r(z_3) < 0$  and so on. Using these values and the expressions (4.35) and (4.36), the following expression is obtained.

$$\begin{aligned}
 C_r(z_0) > 0 &\Rightarrow k_i > 0 \\
 C_r(z_1) < 0 &\Rightarrow k_i < a_1 \\
 C_r(z_2) > 0 &\Rightarrow k_i > a_2 \\
 C_r(z_3) < 0 &\Rightarrow k_i < a_3 \\
 C_r(z_4) > 0 &\Rightarrow k_i > a_4 \\
 &\cdot \\
 &\cdot \\
 &\cdot
 \end{aligned} \tag{4.37}$$

In the expression (4.37), the bounds  $a_j$  are expressed by

$$a_j \triangleq a(z_j) \quad \text{where } j = 1, 2, 3, \dots \tag{4.38}$$

From expression (4.38), it is observed that the odd bounds (*i.e.*,  $a_1, a_3, \dots$ ) to be strictly positive in order to get a feasible range for the gain  $k_i$ . It is observed from Fig. 4.7, Fig. 4.8 and Fig. 4.9 (a) that for  $k_p \in (-\frac{1}{k_v}, k_u)$  the roots of equation (4.33) corresponding to odd values of  $j$  satisfy the following properties:  $z_1 \in (0, \pi)$ ,  $z_3 \in (2\pi, 3\pi)$ ,  $z_5 \in (4\pi, 5\pi)$ , and so on, *i.e.*,  $z_j \in ((j-1)\pi, j\pi)$ . So in these cases the roots of (4.33) corresponding to odd values of  $j$  are either in the first quadrant or in the second quadrant. Thus,

$$\sin(z_j) > 0 \text{ for odd values of } j.$$

The values of  $a_j$  is already defined in (4.26) and expressed by

$$a_j = \frac{z_j}{k_v \tau} \left[ \sin(z_j) + \frac{T}{\tau} z_j \cos(z_j) \right]$$

Thus for  $z_j \neq l\pi$ , where  $l = 0, 1, 2, \dots$ ,  $a_j$  is expressed by

$$a_j = \frac{z_j}{k_v \tau} \left[ \sin(z_j) + \frac{k_v k_p + \cos(z_j)}{\sin(z_j)} \cos(z_j) \right] \tag{4.39}$$

Finally,

$$a_j = \frac{z_j}{k_v \tau} \left[ \frac{1 + k_v k_p \cos(z_j)}{\sin(z_j)} \right] \tag{4.40}$$

From the above expression, it is observed that if  $z_j \neq l\pi$ , then the parameter  $a_j$  is positive if and only if

$$\begin{aligned}
 \sin(z_j) > 0 \text{ and } 1 + k_v k_p \cos(z_j) > 0 \text{ or} \\
 \sin(z_j) < 0 \text{ and } 1 + k_v k_p \cos(z_j) < 0
 \end{aligned}$$

and negative otherwise. The  $k_p - z$  plane is represented in Fig. 4.10. The Fig. 4.10 shows the different regions according to the the value of the parameter  $a_j$ . In the Fig. 4.10, plus (+) sign corresponds to those regions where  $a_j > 0$  and minus sign (-) corresponds to those regions where  $a_j < 0$ . In Fig. 4.10 the dashed line represents the function

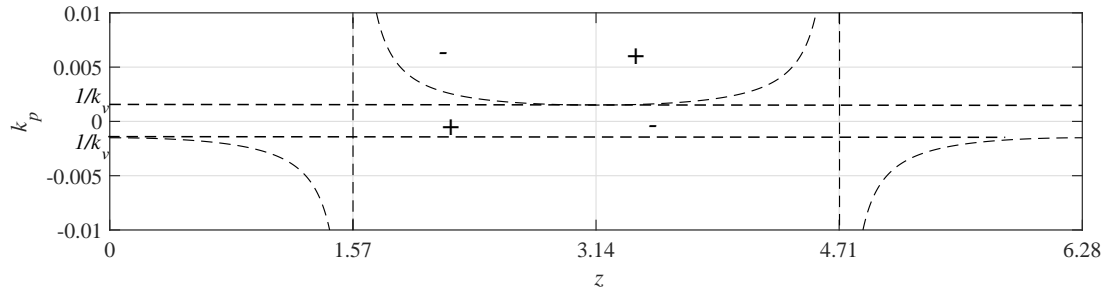


Figure 4.10: Regions associated with parameter  $a_j$

$$1 + k_v k_p \cos(z) = 0$$

or it is rewritten as follows.

$$k_p = -\frac{1}{k_v \cos(z)}$$

Since the function shown in Fig. 4.10 is periodic, the plot repeats itself.

Next objective is plotting the solutions of the expression (4.33) in the  $k_p - z$  plane. It is already derived that the solutions of the expression (4.33) are the nonzero roots of the imaginary part  $C_i(z)$ . The equation (4.33) is rewritten as

$$k_p = \frac{1}{k_v} \left[ \frac{T}{\tau} z \sin(z) - \cos(z) \right] \quad (4.41)$$

Fig. 4.11 shows the plot of the expression (4.41) along with the regions depicted in Fig. 4.10. The intersection of expression (4.41) with the curve  $1 + k_v k_p \cos(z) = 0$  occurs at five values of the parameter  $z$ , *i.e.*,  $0$ ,  $\alpha_1$ ,  $\pi$ ,  $\alpha_2$ , and  $2\pi$ . So each of these values will satisfy the relationship given as follows.

$$\frac{-1}{\cos(z)} = \left[ \frac{T}{\tau} z \sin(z) - \cos(z) \right] \quad (4.42)$$

If the values of  $z \neq l\pi$ , then the expression (4.42) is simplified as,

$$\tan(z) = -\frac{T}{\tau} z \quad (4.43)$$

The solution of the above equation occurs at  $\alpha_1$  and  $\alpha_2$ .

For equation (4.41),  $z_1(k_p)$  and  $z_2(k_p)$  are two positive real roots corresponding to  $k_p$ , and arranged in ascending order of magnitude. From Fig. 4.11, it is observed that for  $k_p \in \left(-\frac{1}{k_v}, -\frac{1}{k_v \cos(\alpha_1)}\right) - \left\{\frac{1}{k_v}\right\}$ , *i.e.*, excluding  $\frac{1}{k_v}$  from this interval then,  
 $a_1 = a(z_1(k_p)) > 0$  and  $a_2 = a(z_2(k_p)) < 0$ .

For  $k_p = \frac{1}{k_v}$ , from Fig. 4.11, it is concluded that  $a_1 = a(z_1(k_p)) > 0$ . Since  $z_2 = \pi$ , Fig. 4.11 or expression (4.40) cannot be used to determine the sign of  $a(z_2(k_p))$ . Using the original

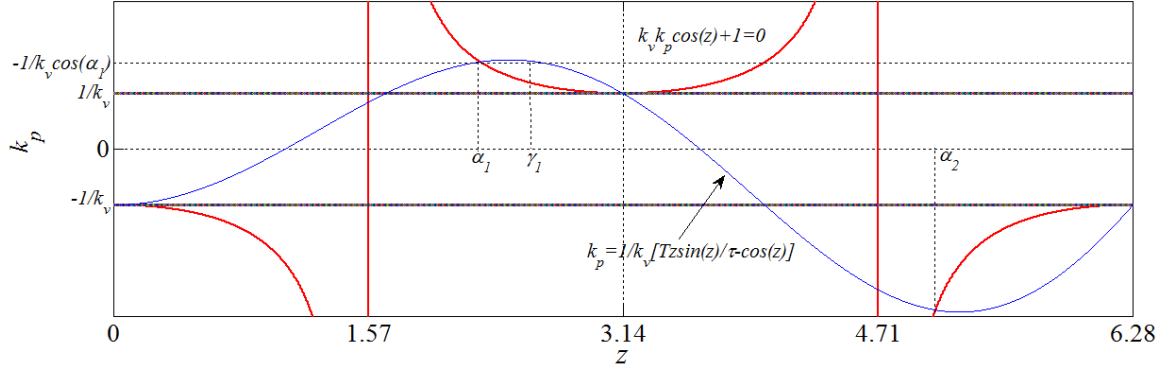


Figure 4.11: Analysis of equation (4.33) in the  $k_p - z$  plane when  $T > 0$

expression of  $a(z)$  as presented in (4.26), the value of  $a_2 = a(z_2(k_p)) < 0$ . From Fig. 4.11, it is observed that for  $k_p > -\frac{1}{k_v \cos(\alpha_1)}$ ,  $a_1 = a(z_1(k_p)) < 0$  and  $a_2 = a(z_2(k_p)) < 0$ . Thus it is concluded that  $a_1 > 0$  if and only if  $k_p < -\frac{1}{k_v \cos(\alpha_1)}$ . Since  $\alpha_1$  satisfies the relationship  $\tan(\alpha_1) = -\frac{T}{L}\alpha_1$ . Thus it is written as,

$$\cos(\alpha_1) = -\frac{1}{\sqrt{1 + \frac{T^2}{L^2}\alpha_1^2}}$$

Therefore,

$$-\frac{1}{k_v \cos(\alpha_1)} = \frac{T}{k_v \tau} \sqrt{\alpha_1^2 + \frac{\tau^2}{T^2}}$$

So from the above discussion, it is occluded that

$$\text{if } -\frac{1}{k_v} < k_p < \frac{T}{k_v \tau} \sqrt{\alpha_1^2 + \frac{\tau^2}{T^2}} \text{ then } a_1 > 0, a_2 < 0.$$

It is observed from Fig. 4.11 that this upper bound on  $k_p$  is less than  $k_u$ , which in this figure corresponds to the maximum of the function

$$k_p = \frac{1}{k_v} \left[ \frac{T}{\tau} z \sin(z) - \cos(z) \right],$$

in the interval  $z \in [0, \pi]$ . As already explained, this is one necessary requirement for inter-lacing. The same approach is used and observed that

$$\text{if } -\frac{1}{k_v} < k_p < \frac{T}{k_v \tau} \sqrt{\alpha_3^2 + \frac{\tau^2}{T^2}} \text{ then } a_3 > 0, a_4 < 0$$

$$\text{if } -\frac{1}{k_v} < k_p < \frac{T}{k_v \tau} \sqrt{\alpha_5^2 + \frac{\tau^2}{T^2}} \text{ then } a_5 > 0, a_6 < 0$$

⋮  
⋮  
⋮

where  $\alpha_j$  is the solution of the following expression.

$$\tan(\alpha) = -\frac{T}{\tau}\alpha \quad \left( \text{in the interval } \left( \left( j - \frac{1}{2} \right) \pi, j\pi \right) \right) \quad (4.44)$$

It is observed from Fig. 4.7, Fig. 4.8, Fig. 4.9 a, the odd roots of expression (4.33), *i.e.*,  $z_j$  where  $j = 1, 3, 5, \dots$ , are getting closer to  $(j - 1)\pi$  as  $j$  increases. So it can be expressed by

$$\lim_{j \rightarrow \infty} \cos(z_j) = 1$$

Furthermore, as the *cosine* function is monotonically decreasing between  $(j - 1)\pi$  and  $j\pi$  for odd values  $j$ , thus it is expressed as

$$\cos(z_1) < \cos(z_3) < \cos(z_5) < \dots \quad (4.45)$$

To develop the stabilizing algorithm for computing proportional and integral gains still some analysis is required and described here, later used in developing the algorithm.

Expression (4.26) is further simplified and written as follows.

$$k_v \tau a_j = z_j \sin(z_j) + \frac{T}{\tau} z_j^2 \cos(z_j) \quad (4.46)$$

After multiplying  $\frac{T}{\tau}$  on both sides of the equation (4.47), the following expression obtained.

$$T k_v a_j = \frac{T}{\tau} z_j \sin(z_j) + \frac{T^2}{\tau^2} z_j^2 \cos(z_j) \quad (4.47)$$

Expression (4.33) is used to further simplify expression (4.47). From expression (4.33), value of  $\frac{T}{\tau} z_j \sin(z_j) = k_v k_p + \cos(z)$  is substituted in (4.47) and provides following expression.

$$T k_v a_j = k_v k_p + \cos(z_j) + \frac{T^2}{\tau^2} z_j^2 \cos(z_j) \quad (4.48)$$

The above expression is simplified further,

$$T k_v a_j - k_v k_p = \cos(z_j) \left( 1 + \frac{T^2}{\tau^2} z_j^2 \right) \quad (4.49)$$

If the values of  $z_j$ , where  $j = 1, 3, 5, \dots$  are arranged in increasing order of magnitude, *i.e.*,  $z_j < z_{j+2}$ , so for odd values of  $j$

$$1 + \frac{T^2}{\tau^2} z_j^2 < 1 + \frac{T^2}{\tau^2} z_{j+2}^2 \quad (4.50)$$

Using expression (4.45) for odd values of  $j$  it can be written that

$$\cos(z_j) < \cos(z_{j+2}) \quad (4.51)$$

Since  $\cos(z_j) > 0$ , expression (4.50) provides the following expression

$$\left( 1 + \frac{T^2}{\tau^2} z_j^2 \right) \cos(z_{j+2}) < \left( 1 + \frac{T^2}{\tau^2} z_{j+2}^2 \right) \cos(z_{j+2}) \quad (4.52)$$

As  $1 + \frac{T^2}{\tau^2}z_j^2 > 0$ , using equation (4.51) the following expression is developed

$$\left(1 + \frac{T^2}{\tau^2}z_j^2\right) \cos(z_j) < \left(1 + \frac{T^2}{\tau^2}z_{j+2}^2\right) \cos(z_{j+2}) \quad (4.53)$$

Using the expression (4.52) and (4.53), the following expression is obtained

$$\left(1 + \frac{T^2}{\tau^2}z_j^2\right) \cos(z_j) < \left(1 + \frac{T^2}{\tau^2}z_{j+2}^2\right) \cos(z_{j+2}) \quad (4.54)$$

Using (4.49), the following expression is developed

$$\begin{aligned} \Rightarrow Tk_v a_j - k_v k_p &< Tk_v a_{j+2} - k_v k_p \\ \Rightarrow a_j &< a_{j+2} \end{aligned} \quad (4.55)$$

So finally it is concluded that for a fixed value of  $k_p$  inside the range  $\frac{-1}{k_v} < k_p < \frac{T}{k_v \tau} \sqrt{\alpha_1^2 + \frac{\tau^2}{T^2}}$ , where  $\alpha_1$  is the solution of  $\tan(\alpha) = -\frac{T}{\tau}\alpha$ ;  $\alpha \in (\frac{\pi}{2}, \pi)$  and the range of  $k_i$  are computed such that the closed-loop system is stable. The range of  $k_i$  is  $0 < k_i < \min_x \{a_j\}$  and the range depends on the bounds  $a_j$  corresponding to odd values of  $j$ . However, if  $\cos(z_1) > 0$ , then the bound  $a_1$  is the minimum of all the odd bounds, and the range of stabilizing  $k_i$  is given by  $0 < k_i < a_1$ . If this does not occur, then the condition of  $\cos(z_1) > 0$  is checked and the value of  $a_3$  is less than all the other bounds  $a_j$  for  $j = 5, 7, 9, \dots$ . The range of stabilizing  $k_i$  is defined by  $0 < k_i < \min\{a_1, a_3\}$ . Since for odd values of  $j$ ,  $\lim_{j \rightarrow \infty} \cos(z_j) = 1$ , it is obvious that  $\cos(z_j) > 0, \forall j$  (for all)  $\geq N$ , where  $N$  is some finite integer. The above discussed procedure, for computing stabilizing gains  $(k_p, k_i)$  which makes the closed loop system stable is highlighted in the following algorithm.

**Algorithm for computing stabilizing control parameters  $(k_p, k_i)$  of a time delay system.**

1. Initialize  $k_p = \frac{-1}{k_v}$ ,  $\Delta k_p = \frac{1}{N+1} \left( \frac{T}{k_v \tau} \sqrt{\alpha_1^2 + \frac{\tau^2}{T^2}} + \frac{1}{k_v} \right)$  and  $j = 1$ , where  $N$  is the desired number of points.
2. Value of  $k_p$  is increased, using  $k_p = k_p + \Delta k_p$ .
3. If value of  $k_p < k_{pmax}$  then go to the next step, Otherwise terminate the algorithm, where  $k_{pmax} = \left( \frac{T}{k_v \tau} \sqrt{\alpha_1^2 + \frac{\tau^2}{T^2}} \right)$ .
4. Roots of the equation  $k_v k_p + \cos(z) - \frac{T}{\tau} z \sin(z) = 0$  are determined.
5. The parameter  $a(z)$  is determined using  $a(z) = \frac{z}{k_v \tau} [\sin(z) + \frac{T}{\tau} z \cos(z)]$ .

6. If  $\cos(z_j) > 0$  then go to next step. Otherwise,  $j = j + 2$  and go to step 4.
7. If Lower and upper bounds are evaluated using  $0 < k_i < \min(a_l)$ , where  $l = 1, 3, 5, \dots, j$ .
8. Go to step 2.

To compute the gains  $(k_p, k_i)$  of the voltage controlled GIC based SEIG system, above algorithm is used so that the closed system becomes stable. To implement the algorithm for GIC based SEIG system computation of  $\alpha$  is essential and  $\alpha$  is computed using the expression (4.44) and corresponding plots are shown in Fig. 4.12. It is observed from this figure that intersection of the two plots *i.e.*,  $(\tan(\alpha) \text{ vs } \alpha)$  and  $-\frac{T}{\tau}\alpha \text{ vs } \alpha$  provides the value of  $\alpha = 1.7008$  (in the interval  $(\frac{\pi}{2}, \pi)$ ). Step 1 and 2 of the above algorithm is used to compute initial  $k_p$  value (-0.00151) and incremental  $\Delta k_p$  value (0.00062). Then using step 3 of the above algorithm  $k_{pmax}$  is computed. The computed  $k_{pmax}$  value for the GIC based SEIG system is 0.0116. Since the initial value of  $k_p$  is less than  $k_{pmax}$ , then  $z$  is computed. Computation of  $z$  is shown in Fig. 4.13. It is observed from Fig. 4.13 that value of  $z_1$  is 0.2909, since  $\cos(z_1) > 0$ , according to step 6, it is not necessary to increase  $j$ . Finally  $k_1$  is computed using step 7 and computed value is 0.1639. The same procedure is used to compute proportional and integral gains (stabilizing zones) for voltage controlled GIC based SEIG system using the above algorithm. Computed values of proportional and integral gains are given in Table 4.1. Plot obtained by taking gains  $k_p$  and  $k_i$  is shown in the Fig. 4.14.

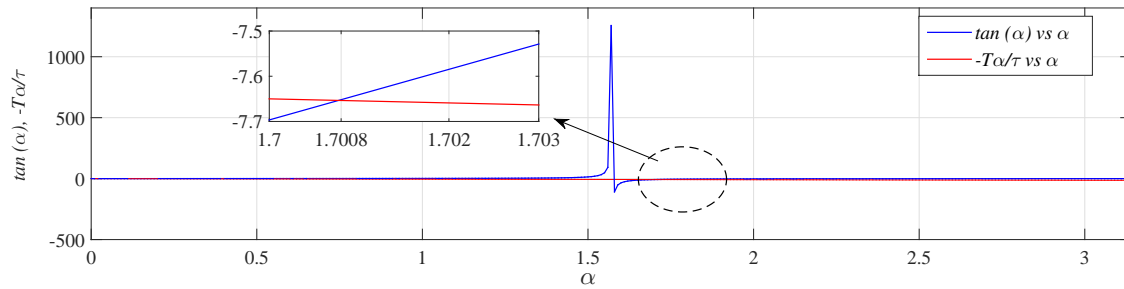


Figure 4.12: Plot for finding  $\alpha$  of the voltage controlled GIC based SEIG system

Computation of stable zones of GIC based SEIG system using the above algorithm is not enough. Next objective is to determine the optimum value of proportional and integral gains within stable zone. It is decided by the constraints minimum overshoot, rise time, settling time and steady state error. To resolve this problem Particle Swarm Optimization (PSO) technique is used. PSO and its implementation on GIC based SEIG system are described in the next subsection.



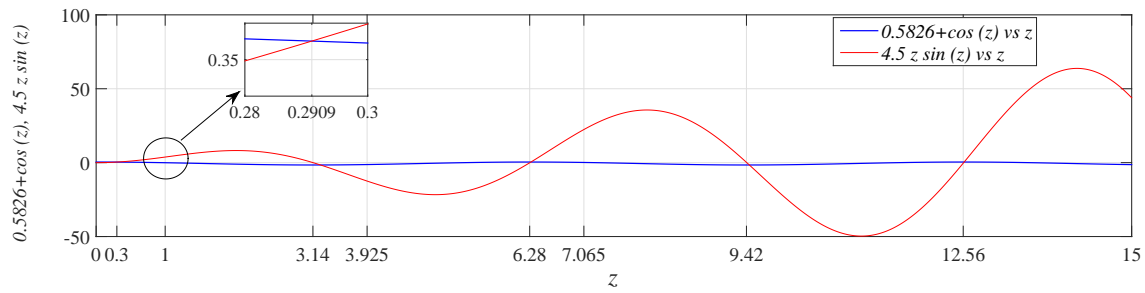


Figure 4.13: Plot for finding  $z$  of the voltage controlled GIC based SEIG system

Table 4.1: Computed proportional and integral gains of stable zones of GIC based SEIG system

$\alpha$	$k_p$	$z_1$	$k_i$
1.7008	-0.00088	0.2909	0.1639
	-0.00028	0.409	0.3223
	0.00032	0.5023	0.4671
	0.00092	0.5829	0.6032
	0.0015	0.6556	0.7229
	0.0021	0.7231	0.8469
	0.0027	0.786	0.9531
	0.0033	0.8475	1.0478
	0.0039	0.9065	1.13
	0.0045	0.9638	1.1994
	0.0051	1.02	1.253
	0.0057	1.076	1.291
	0.0063	1.131	1.312
	0.0069	1.187	1.3122
	0.0075	1.244	1.289
	0.0081	1.299	1.242
0.0087	1.357	1.164	
0.0093	1.418	1.048	
0.0099	1.482	0.8885	
0.0105	1.5497	0.6712	

### 4.5.3 Computation of best optimal proportional and integral gains of voltage controlled GIC based SEIG system

Various techniques such as quadratic programming, and dynamic programming are reported in the literature to address optimization problem [78]. However, computational intelligence based techniques [78] such as Genetic Algorithm (GA) and PSO are widely used for optimization problems. GA technique is based on three main operators such as selection, cross over and mutation. The demerits of GA are: (i) involves with a large number of parameters so computation time more to solve optimization problem, (ii) suitable fitness function may converge optimization problems towards local optima rather than the global optimum of

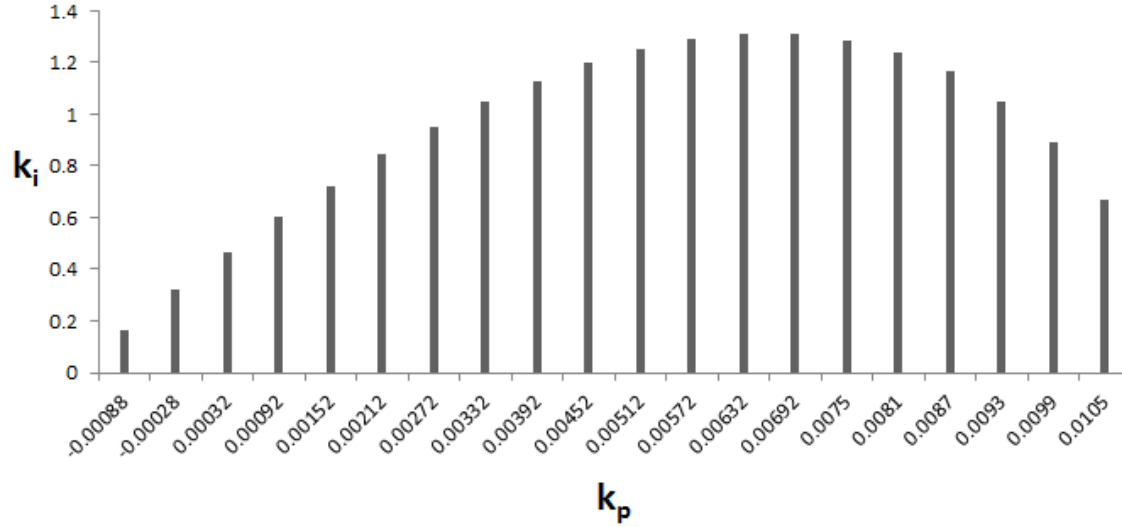


Figure 4.14: Stable zone of proportional and integral gains for voltage controlled GIC based SEIG system

the problem. To address these problems PSO is first introduced by Kennedy and Eberhart [79]. This technique is inspired by the social behavior of organisms in a bird flock or, fish school [80]. Recently particle swarm optimization has been applied to design an optimal *PI* controller for various applications [81], [79], [82]. Merits of PSO are: (i) easy to implement (ii) every particle remember its own previous best value as well as the neighborhood best, therefore it's memory is more capable than GA (iii) based on information provide by most successful particle, all the particles are improving themselves where as in GA, worse solutions discarded and good are selected. Hence, PSO is selected in this chapter to determine optimal proportional ( $k_p$ ) and integral ( $k_i$ ) gains for voltage controlled GIC based SEIG system. Here, to determine the optimal  $k_p$  and  $k_i$  gains following steps of PSO are used. Maximum and minimum value of each  $k_p$  and  $k_i$  gains in PSO are set by maximum and minimum values, respectively of the stable zone computed in previous subsection.

**Algorithm for computing optimal proportional and integral gains to control voltage of GIC based SEIG using PSO technique**

1. Initialization: Initialize number of particles in the population  $S$ , maximum generation number  $gen_{max}$ , weighting co-efficient  $c_1$  and  $c_2$ , weights  $w_{max}$  and  $w_{min}$ . After initialization, randomly generate the initial particles  $s_i$  ( $i = 1, 2, \dots, S$ ) which indicate the possible solutions of  $k_p$  and  $k_i$  value (between minimum and maximum values obtained from stable zone).

2. Objective function computation: Objective function is determined by setting randomly generated  $k_p$  and  $k_i$  in the GIC based SEIG system. The objective function considered in this optimization problem is

$$J_{ISE}(k_p, k_i) = \int_0^t (\Delta V_m)^2 dt \quad (4.56)$$

3. Searching point evaluation: Compare each particle computation value ( $s_i$ ), with its  $pbest_i$ . The best value among the  $pbest_i$  is  $gbest$ . Here  $s_i$  is  $k_p$  and  $k_i$ .
4. Updating of the searching point: The current position of each particle is updated using the following expressions.

$$v_i^{m+1} = wv_i^m + c_1 \times rand_1 \times (pbest_i - s_i^m) + c_2 \times rand_2 \times (gbest - s_i^m) \quad (4.57)$$

$$w = w_{max} - \left[ \frac{w_{max} - w_{min}}{gen_{max}} \times gen \right] \quad (4.58)$$

$$s_i^{m+1} = s_i^m + v_i^{m+1} \quad (4.59)$$

5. Checking of termination condition: When the number of iteration reaches the maximum value, or a better optimum solution obtained, the search is terminated. The controller gains corresponding to  $gbest$ , i.e.,  $k_{p(gbest)}$  and  $k_{i(gbest)}$  are then determined. Otherwise, the process continues, and the loop goes back to step 2.

Flow chart of the PSO algorithm is shown in Fig. 4.15. For computing optimal proportional and integral gains within stable zone, the parameters taken here to implement PSO are given in 4.2.

Table 4.2: Parameters taken to implement PSO algorithm

$S$	$w_{max}$	$w_{min}$	$c_1$	$c_2$	$gen_{max}$
8	0.9	0.4	2	2	60

The developed model has run for 20 times. Fig. 4.16 (a) and (b) show the optimal proportional ( $k_p$ ) and integral ( $k_i$ ) gains obtained using PSO technique for run 1 and are 0.0077 and 0.4564, respectively. Similarly Fig. 4.17 (a) and (b) show the optimal  $k_p$  and  $k_i$  gains obtained using PSO technique for run 2 and are 0.0083 and 0.757, respectively. Obtained optimal  $k_p$  and  $k_i$  gains for run 3 are 0.0078 and 0.973, respectively and shown in Fig. 4.18.

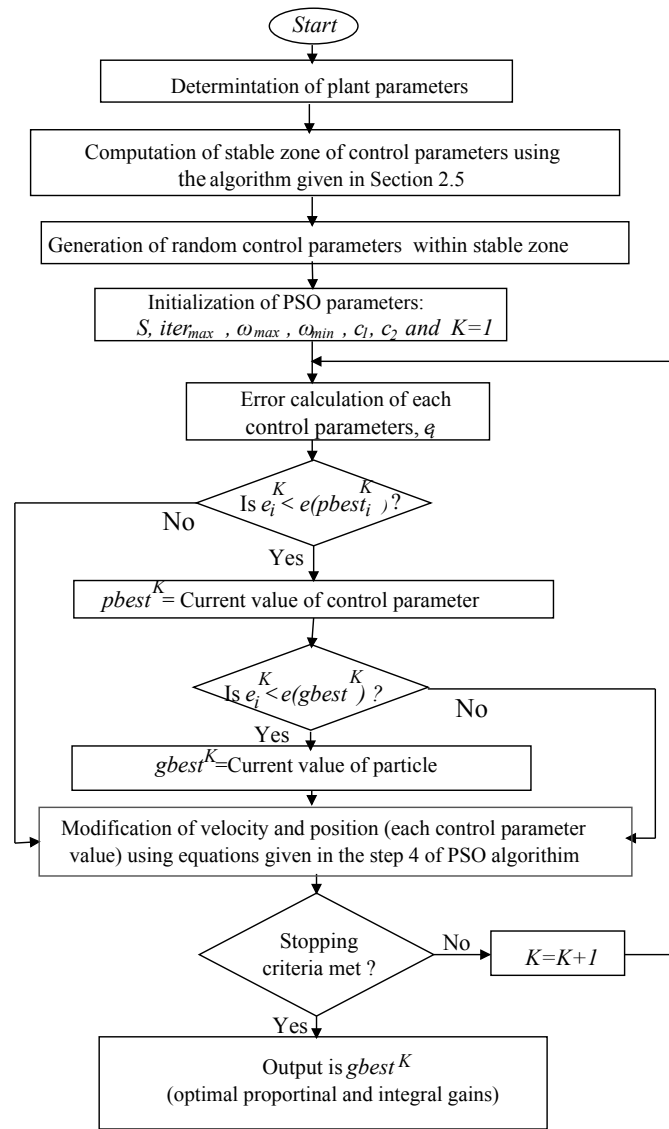


Figure 4.15: Flow chart to compute the optimum value of  $k_p$  and  $k_i$  using particle swarm optimization technique

To show the effectiveness of the proposed algorithm, transient behaviour of SEIG stator peak voltage is studied by taking optimal values obtained from first 7 runs (given in Table 4.3) under three perturbations. Perturbations considered are: increase in wind speed from 9.8 m/s to 10.8 m/s at  $t=2$  s; switching on of resistive load of 100  $\Omega$ /phase at  $t=3$  s; switching on of resistive load of 400  $\Omega$ /phase (total resistive load becomes 80  $\Omega$ /phase) at  $t=4.5$  s. Fig. 4.19 (a) shows the peak voltage  $v_m$  obtained for 7 different  $k_p$  and  $k_i$  under wind speed perturbations at  $t=2$  s. Corresponding peak overshoot and undershoot obtained for 7 different  $k_p$  and  $k_i$  are 1.94 % and 2.31 %, respectively. Transient part of voltage for each case disappears within 8 cycles and achieved steady-state rated peak voltage of 586.8

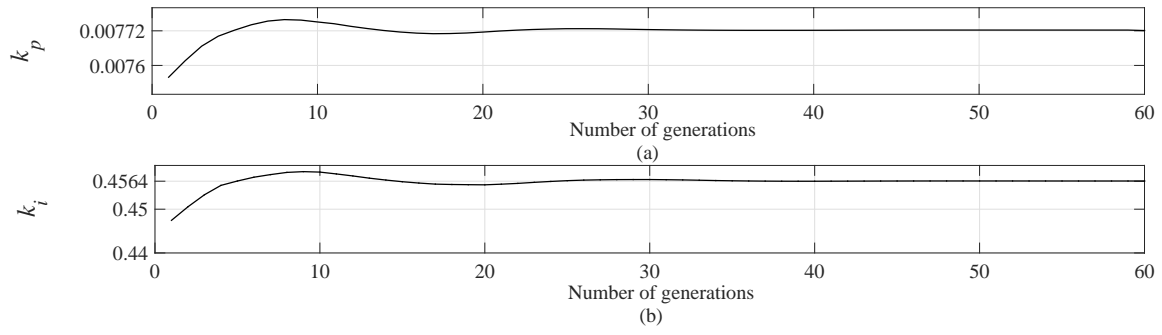


Figure 4.16: Simulation results of PSO to compute optimal gains for GIC based SEIG system for run 1 : (a) Searching value of  $k_p$  (b) Searching value of  $k_i$

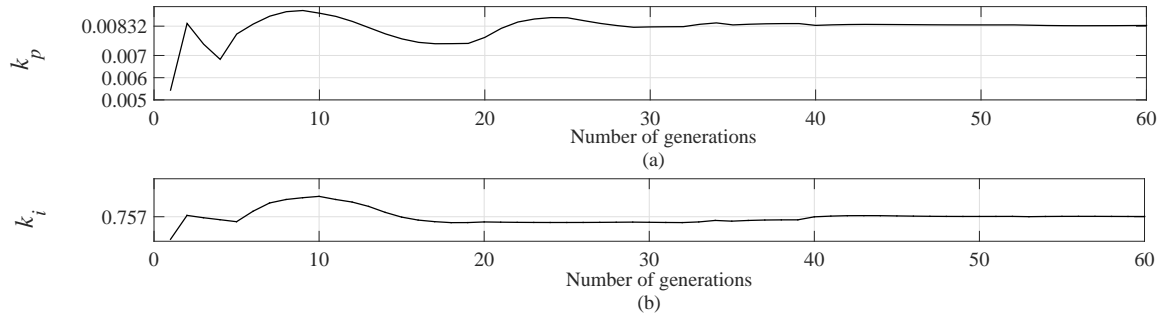


Figure 4.17: Simulation results of PSO to compute optimal gains for GIC based SEIG system for run 2 : (a) Searching value of  $k_p$  (b) Searching value of  $k_i$

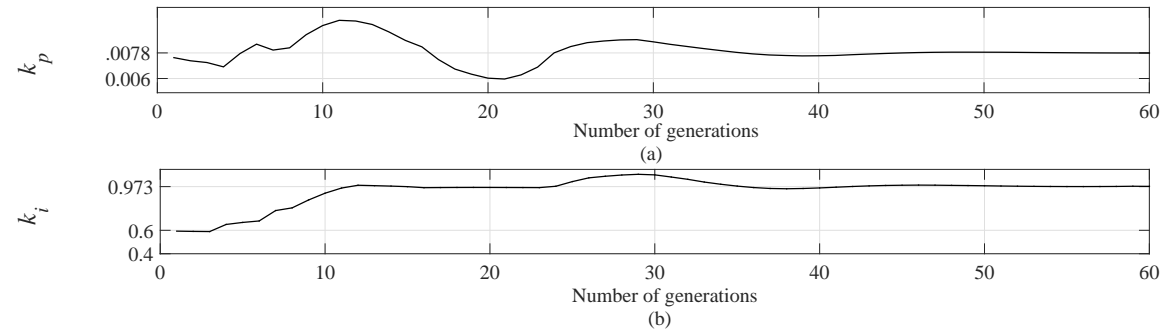


Figure 4.18: Simulation results of PSO to compute optimal gains for GIC based SEIG system for run 3 : (a) Searching value of  $k_p$  (b) Searching value of  $k_i$

V. There is no significant difference appears from each voltage waveform. Fig. 4.19 (b) shows the peak voltage  $v_m$  obtained for 7 different  $k_p$  and  $k_i$  under load switching of 100  $\Omega$ /phase at  $t=3$  s. Corresponding peak overshoot obtained for 7 different  $k_p$  and  $k_i$  are within 3.13 % as seen in Fig. 4.19 (b). Transient parts of voltage for each case disappears within 5

Table 4.3: Optimal  $k_p$  and  $k_i$  gains obtained from PSO for 20 runs

Run	$k_p$	$k_i$
1	0.0077	0.4564
2	0.0083	0.757
3	0.0078	0.973
4	.0082	0.762
5	0.009	0.734
6	0.0065	0.592
7	0.0081	0.795
8	0.0089	0.681
9	0.0075	0.881
10	0.0076	0.915
11	0.008	0.79
12	0.0077	0.902
13	0.0073	0.943
14	0.0069	0.965
15	0.0088	0.691
16	0.0085	0.721
17	0.0064	0.921
18	0.0063	0.891
19	0.0072	0.852
20	0.0082	0.755

cycles and achieved steady-state rated peak voltage of 586.8 V. The results obtained here are almost similar and no significant difference appears. Fig. 4.19 (c) shows the peak voltage  $v_m$  obtained for 7 different  $k_p$  and  $k_i$  under load switching of 400  $\Omega$ /phase at  $t=4.5$  s. It is observed that steady state achieved for all 7 cases within 4 cycles and achieved steady-state rated peak voltage of 586.8 V. Best optimal value from 20 run is decided from the minimum value of objective function. Corresponding to this, the best optimal gains are  $k_p=0.0083$  and  $k_i =0.757$ . Next section describes simulation results in detail of the voltage controlled GIC based SEIG system using the best optimal gains so that the closed loop system stable under varied wind speed and load.

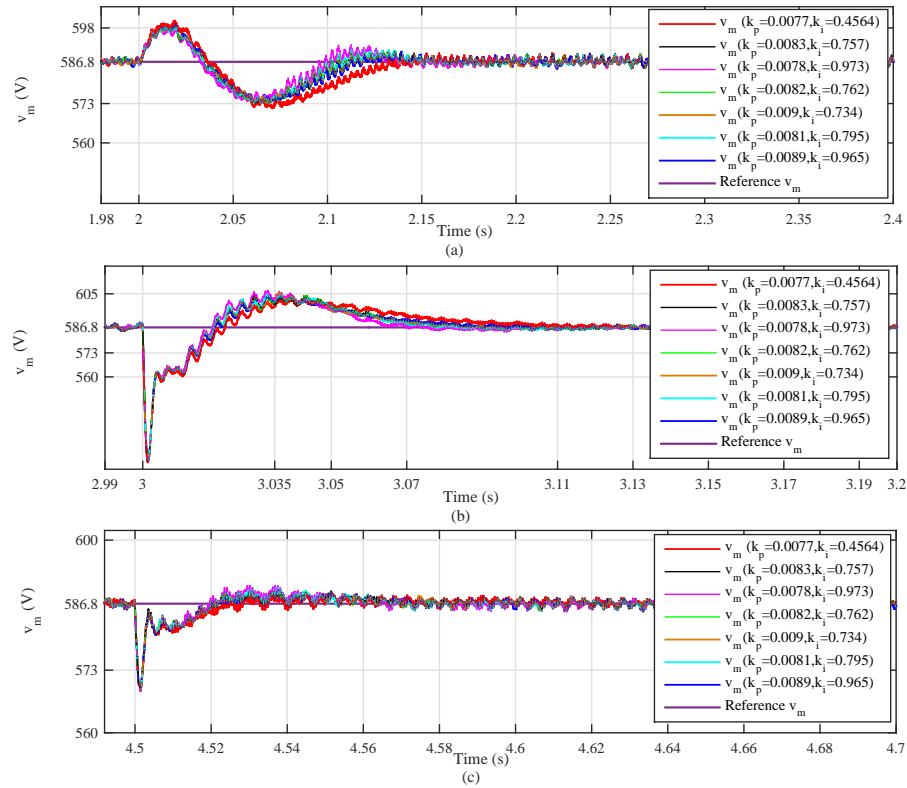


Figure 4.19: Simulation results of SEIG peak voltage under different perturbations for 7 different  $k_p$  and  $k_i$ : (a) wind speed perturbation (b) Resistive load of 100  $\Omega$ /phase switched on (c) Resistive load of 400  $\Omega$ /phase added

## 4.6 Results and Discussion

It is already discussed in section 4.5 that how to select the optimal gains of  $PI$  to make GIC based SEIG system optimized and stable. To study the performance of optimized GIC based SEIG system under different types of load (resistive and IM load) with varied wind speed, simulation is carried out in MATLAB/Simulink environment. Simulation results are described in the subsequent subsections.

### 4.6.1 Transient performance of optimized GIC based SEIG feeding resistive load

Initially, at  $t=0$  s, to develop the rated SEIG voltage, a wind speed of 9.8 m/s is selected for the simulation. To show the effectiveness of the proposed control scheme the perturbations considered by taking resistive ( $R$ ) load are as follows.

1. Switching of GIC at  $t=1$  s,
2. Wind speed increased from 9.8 m/s to 10.8 m/s at  $t=2$  s,
3. Switching of balanced three-phase resistive load of 100  $\Omega$ /phase at  $t=3$  s,
4. Switching of resistive load of 400  $\Omega$ /phase at  $t=4.5$  s,
5. Wind speed increased from 10.8 m/s to 11.2 m/s at  $t=5$  s,
6. Wind speed decreased from 11.2 m/s to 10.9 m/s at  $t=6$  s,
7. Removal of balanced three-phase resistive load of 100  $\Omega$ /phase at  $t=7$  s, and
8. Wind speed decreased from 10.9 m/s to 10.5 m/s at  $t=8$  s.

To maintain rated voltage and frequency of SEIG, GIC is connected across the SEIG terminal in such a manner that GIC and SEIG output voltages have the same fundamental frequency and voltage. GIC is connected across the SEIG, at  $t=1$  s, to synchronize voltage and frequency with SEIG. As described in the section 4.3, GIC is connected with the SEIG at the point of common coupling in such a manner that no exchange of active and reactive power occurs between them at steady-state. To set this condition, the phase angle between GIC and SEIG fundamental voltages should be zero. Fig. 4.20 shows the steady-state waveform of SEIG line voltage and GIC line voltage. It is observed, switching of GIC makes angle  $\delta = 0^\circ$  between GIC and SEIG stator line voltages due to synchronization at no load. Fig. 4.21 (a) and (b) are showing variation of SEIG and GIC active power respectively, during this GIC switching. It is observed from Fig. 4.21 (a) that after GIC is connected at  $t=1$  s,



active power of SEIG reaches to peak of -1780 W at  $t=1.03$  s and comes to zero W at  $t=1.17$  s. Similarly, Fig. 4.21 (b) shows that active power of GIC reaches to peak of 1780 W at  $t=1.03$  s and comes to zero W at  $t=1.17$  s. It is observed from both the figures that exchange of active power between SEIG and GIC becomes zero at the steady-state. Thus frequency of SEIG matches with GIC frequency which is set at 50 Hz. Fig. 4.22 shows the variation of frequency due to GIC connection. It is observed that at  $t=1.21$  s SEIG frequency becomes 50 Hz.

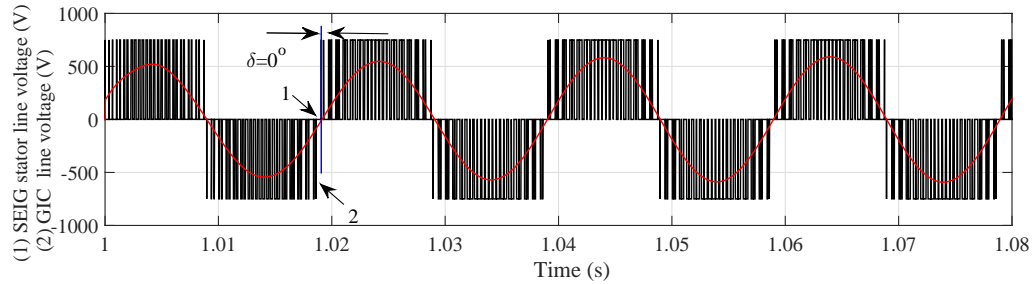


Figure 4.20: Simulation result showing SEIG and GIC voltage waveforms with steady-state value of  $\delta$  after switching of GIC at no load

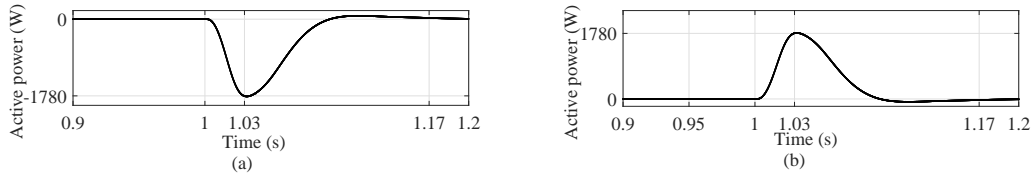


Figure 4.21: Simulation results showing: (a) variation of SEIG active power after GIC switching (b) variation of GIC active power after connection with SEIG

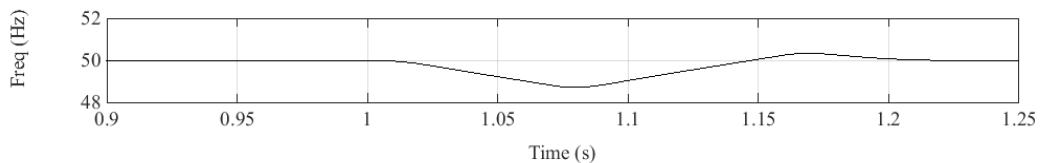


Figure 4.22: Simulation result showing variation of SEIG frequency after switching with GIC

Similarly, reactive power exchange between GIC and SEIG is also zero at the critical value of modulation index,  $m$ . Fig. 4.23 shows the variation of modulation index versus time, where it is observed that the critical value of modulation index,  $m$  0.73. Corresponding to GIC switching, reactive power variation across SEIG, GIC and excitation capacitor are shown in Fig. 4.24 (a), (b) and (c). Reactive power drawn by SEIG before connection of GIC is 3490 VAR as seen in Fig. 4.24 (a). Due to GIC connection SEIG reactive power changes to -2200 VAR at  $t=1.03$  s and comes again to -3490 VAR at  $t=1.15$  s. As observed from Fig. 4.24 (b), reactive power of GIC changes from zero to 906 VAR at  $t=1.03$  s and comes to zero at  $t=1.15$  s. Fig. 4.24 (c) shows reactive power provided by capacitor before GIC connection is 3490 VAR. Due to GIC connection at  $t=1.03$  s reactive power of capacitor changes from 3490 VAR to 3100 VAR and comes to 3490 var at  $t=1.15$  s. Steady-state achieved at  $t=1.15$  s, no exchange of reactive power between SEIG and GIC occurs at this instant, implying that fundamental component of SEIG voltage and GIC output voltage are equal in magnitude and phase. Fig. 4.25 shows variation of SEIG stator peak voltage due to GIC connection and it is observed that SEIG maintains stator peak voltage rated value of 586.8 V at steady-state.

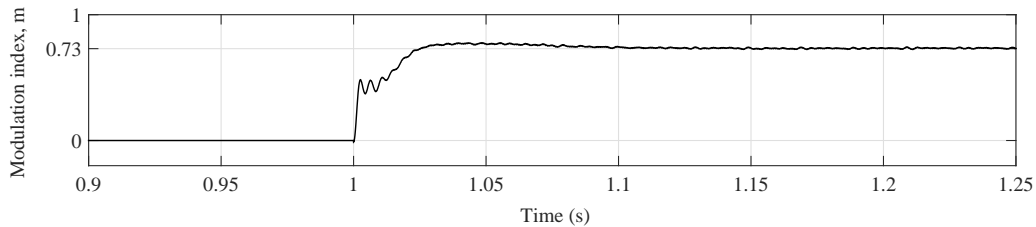


Figure 4.23: Simulation result showing modulation index variation of GIC (no-load) with time

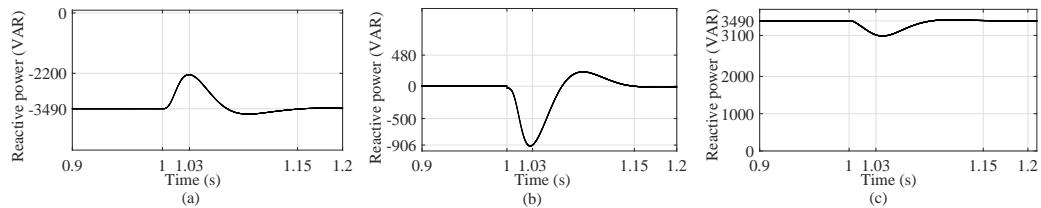


Figure 4.24: Simulation results showing reactive power variation of GIC based SEIG system at wind speed of 9.8 m/s: (a) SEIG (b) GIC (c) Excitation capacitor

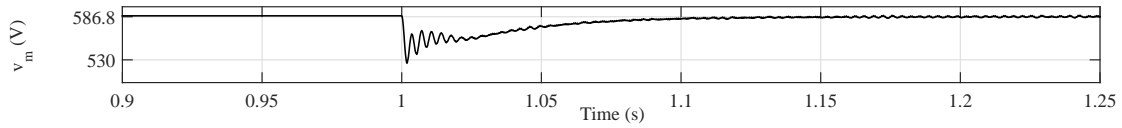


Figure 4.25: Simulation result showing variation of SEIG peak voltage after connection with GIC

Simulation results for variation of the wind speed and load mentioned in the beginning of this subsection are shown in Fig. 4.26. Fig. 4.26 (a) shows the wind speed variation considered as input for simulation, and Fig. 4.26 (b) shows the SEIG rotor speed corresponding to this variation. Fig. 4.26 (c) shows frequency of SEIG controlled in open loop manner by GIC, corresponding to this wind speed and load perturbations. Fig. 4.26 (d) shows SEIG stator peak voltage when controlled in closed loop manner by GIC, corresponding to this wind speed and load perturbations. Detail of Fig. 4.26 are described in subsequent paragraphs.

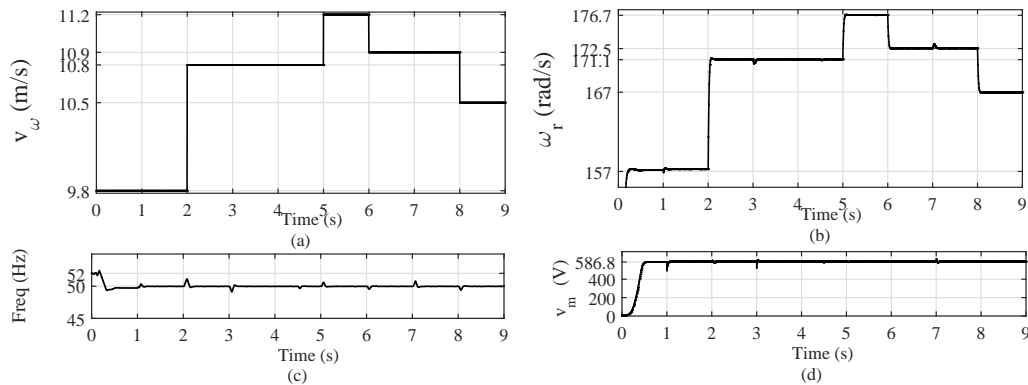


Figure 4.26: Closed loop simulation results of proposed GIC based SEIG system with loading and wind speed variations: (a) Wind speed variations (input for simulation)(b) Rotor speed of SEIG (c) Stator frequency of SEIG (d) Stator peak voltage of SEIG.

At  $t=0$  s, wind speed is 9.8 m/s. Corresponding to 9.8 m/s wind speed, rotor speed of SEIG is 157 rad/s. At  $t=1$  s GIC is connected and that does not cause any change in SEIG rotor speed. When the wind speed changes to 10.8 m/s, 11.2 m/s, 10.9 m/s and 10.5 m/s at  $t=2$  s,  $t=5$  s,  $t=6$  s and  $t=8$  s, in that order, as shown in Fig. 4.26 (a), corresponding to these variations, rotor speed changes to 171.1 rad/s, 176.7 rad/s, 172.5 rad/s and 167 rad/s, respectively. Due to switching of loads at  $t=3$  s,  $t=4.5$  s and  $t=7$  s, negligible notches occur in the rotor speed as shown in Fig. 4.26 (b). This proves healthy functioning of GIC. This SEIG system does not use closed loop frequency control. However, frequency is controlled

by GIC in open loop manner. Due to wind speed variations and load variations, frequency has notches and spikes on the set value of 50 Hz, as evident from Fig. 4.26 (c).

At  $t=2$  s, wind speed changes to 10.8 m/s, and corresponding to this variation, rotor speed changes to 171.7 rad/s. It is observed from Fig. 4.27 that SEIG terminal frequency decreases due to availability of excess active power. Fig. 4.28 shows active power of SEIG changes from zero to -2375 W. Fig. 4.29 shows the new steady-state value of angle  $\delta$  becomes  $-14.4^\circ$ , from the previous value of zero. Increase wind speed leads to increase of  $\delta$  in negative direction. Hence, GIC absorbs active power of 2375 W from SEIG. Fig. 4.30 shows the active power of GIC changes from zero to 2375 W. Following the above frequency transient, the angle  $\delta$  and active power flow in GIC reach the steady-state and finally SEIG frequency becomes equal to the GIC frequency. SEIG frequency is maintained at its rated value without any frequency feedback. This occurs due to excess power absorbed by the GIC during the transient period. As observed in Fig. 4.29, the GIC line voltage lags SEIG stator line voltage by  $\delta = -14.4^\circ$ . Since,  $\delta < 0^\circ$  the GIC acts as an equivalent resistance and this power is stored in DC link battery. Due to active power drawn by GIC, SEIG terminal voltage deviates from the rated value of 586.8 V as shown in Fig. 4.31.

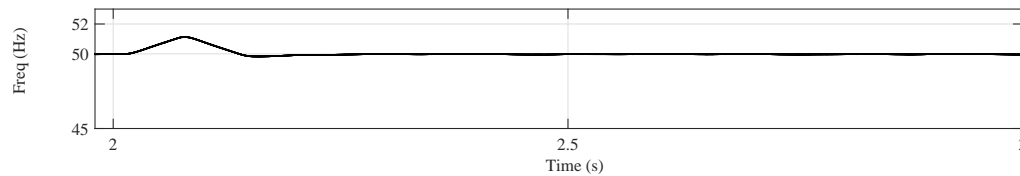


Figure 4.27: Simulation result showing variation of SEIG frequency corresponding to wind speed change from 9.8 m/s to 10.8 m/s

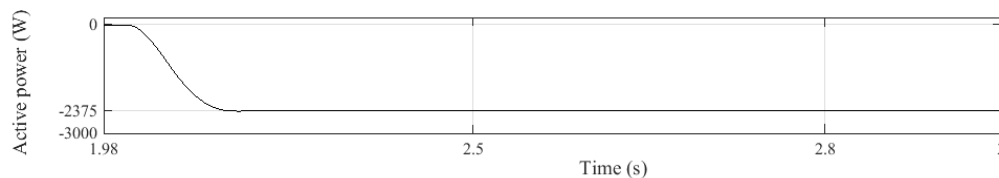


Figure 4.28: Simulation result showing variation of SEIG active power corresponds to wind speed change from 9.8 m/s to 10.8 m/s

But SEIG-GIC operate in closed loop with voltage as feedback, and the  $PI$  updates its output, *i.e.*, modulation index,  $m$  value from 0.73 to 0.83 as presented in Fig. 4.32. The wind speed perturbation taken at  $t=2$  s, makes the fundamental component of GIC output voltage

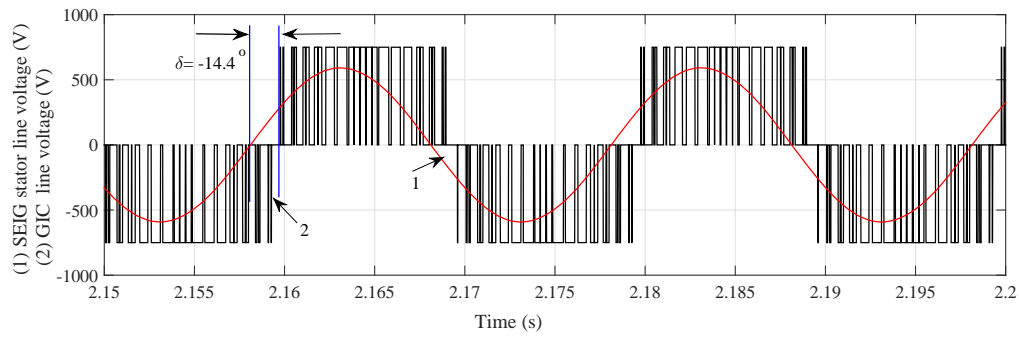


Figure 4.29: Simulation result showing SEIG and GIC voltage waveforms with steady-state value of  $\delta$  in wind speed change from 9.8 m/s to 10.8 m/s.

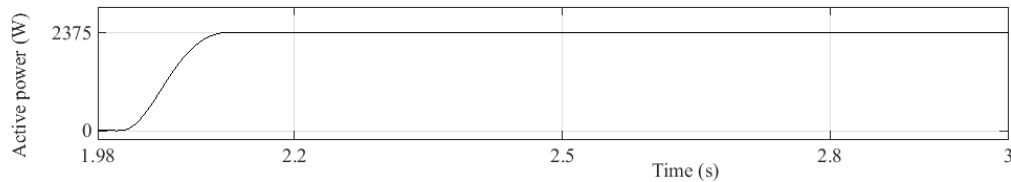


Figure 4.30: Simulation result showing variation of GIC active power corresponding to wind speed change from 9.8 m/s to 10.8 m/s

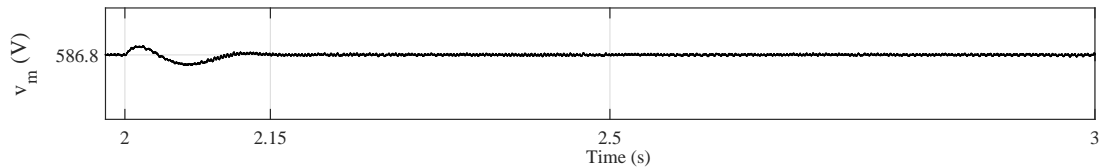


Figure 4.31: Simulation result showing SEIG peak voltage waveform corresponding to wind speed change from 9.8 m/s to 10.8 m/s

more than the fundamental component of SEIG stator line voltage (since  $m$  is more than critical value). Hence, GIC acts as an equivalent capacitor and supplies additional leading reactive power of the order of 705 VAR as shown in Fig. 4.33 (a). Fig. 4.33 (b) shows that steady-state reactive power of SEIG corresponding to this wind perturbation is - 4195 VAR. However, as shown in Fig. 4.33 (c), excitation capacitor provides 3490 VAR in steady-state. Under steady-state,  $\delta$  remains at the same value to maintain the power balance across PCC. The GIC acts as an equivalent parallel combination of resistance and capacitance from time  $t=2$  s to next transient period  $t=3$  s.

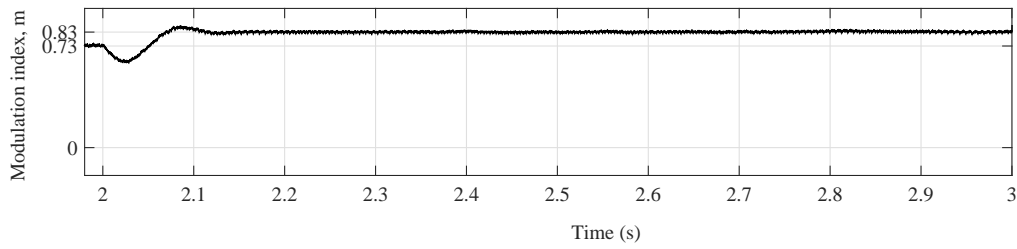


Figure 4.32: Simulation result showing variation of modulation index of GIC with time corresponding to wind speed change from 9.8 m/s to 10m/s.

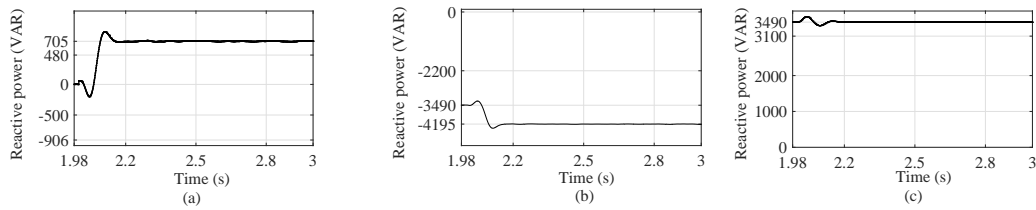


Figure 4.33: Simulation results showing reactive power variation corresponding to wind speed change from 9.8 m/s to 10.8 m/s (a) GIC (b) SEIG (c) Excitation capacitor

At time  $t=3$  s, resistive load of  $100 \Omega/\text{phase}$  is switched on across the SEIG terminals, corresponding to this, SEIG terminal frequency decreases for a moment as shown in Fig. 4.34 due to active power absorbed by the load. Fig. 4.35 (a), (b) and (c) are showing active power variation of load, SEIG and GIC. Fig. 4.35 (a) shows that active power absorbed by this load is 1746 W. As a result angle  $\delta$  between SEIG and GIC voltages increases in positive direction. Fig. 4.36 shows the new steady-state value of angle  $\delta$  becomes  $-7.2^\circ$  from the previous value of  $-14.4^\circ$ . Moreover active power provided by SEIG as shown in Fig. 4.35 (b) is  $-2375$  W and absorbed by load is 1746 W and rest active power of order of 629 W absorbed by GIC (previous value 2375 W at no load) as shown in Fig. 4.35 (c). To maintain power balance due to adding resistive load, the GIC absorbs only 629 W from SEIG (So now equivalent resistance has increased) for matching SEIG frequency with GIC frequency. The GIC based SEIG system is operated in closed loop to make SEIG voltage constant,  $PI$  updates its output *i.e.* modulation index,  $m = 0.81$  as shown in Fig. 4.37. Since modulation index,  $m$  is more than that of critical modulation index,  $m$  value so here GIC output voltage is more than SEIG voltage (as described in section 4.3 value of  $r_1 > 0$ ). Fig. 4.38 shows the SEIG peak voltage variation due to switching of  $100 \Omega/\text{phase}$  load. It is observed that SEIG peak reaches to 602 V and comes back to rated value of 586.8 V. Reactive power variation of GIC, SEIG and excitation capacitor, due to the switching of  $100 \Omega/\text{phase}$  load are presented in Fig. 4.39 (a), (b) and (c). Hence, the GIC still acts as an

equivalent capacitor and it supplies additional reactive power of the order of 705 VAR. During this period VAR drawn from the excitation capacitor remains unchanged (3490 VAR). So from the above discussion it is observed that GIC still operates as an equivalent parallel combination of resistance and capacitance.

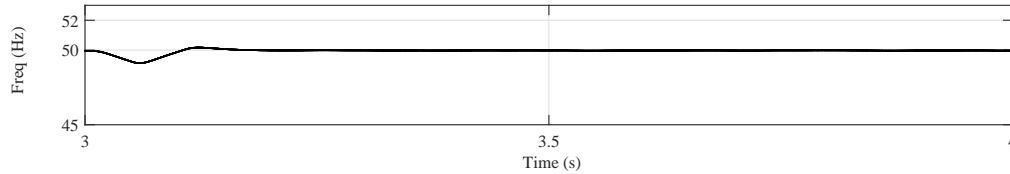


Figure 4.34: Simulation result showing variation of SEIG frequency due to switching of 100  $\Omega$ /phase load

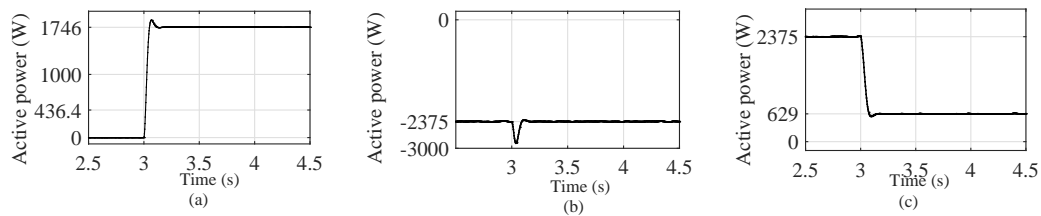


Figure 4.35: Simulation results showing active power variation due to switching of 100  $\Omega$ /phase load: (a) load (b) SEIG (c) GIC

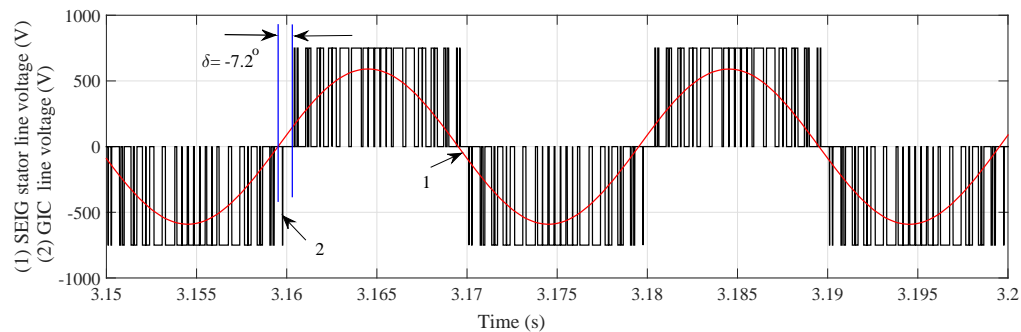


Figure 4.36: Simulation result showing SEIG and GIC voltage waveforms with steady-state value of  $\delta$  due to switching of 100  $\Omega$ /phase load

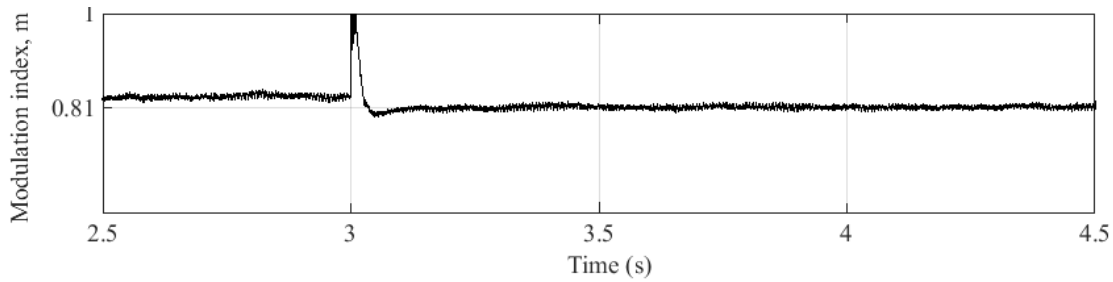


Figure 4.37: Simulation result showing variation of modulation index due to switching of  $100 \Omega/\text{phase}$  load

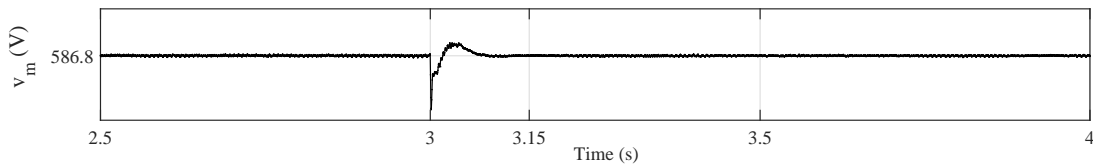


Figure 4.38: Simulation result showing SEIG peak voltage waveform due to switching of  $100 \Omega/\text{phase}$  load

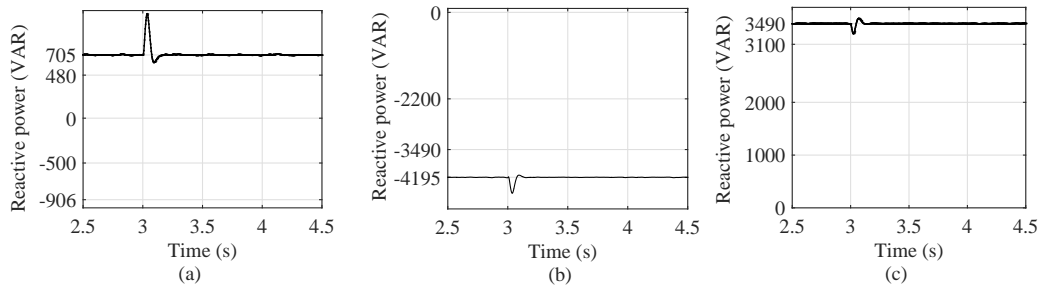


Figure 4.39: Simulation results showing reactive power variation due to switching of  $100 \Omega/\text{phase}$  load: (a) GIC (b) SEIG (c) Excitation capacitor

At time  $t=4.5$  s,  $R$  load of  $400 \Omega/\text{phase}$  is added so net load across SEIG becomes  $80 \Omega/\text{phase}$ . This load perturbation leads to momentary fall in SEIG terminal frequency due to active power drawn by load from the SEIG. Fig. 4.40 (a), (b) and (c) are showing the active power variation of net  $R$  load, SEIG and GIC. It is observed that active power drawn by load is  $2182$  W and active power provided by SEIG is  $-2375$  W. To meet the load requirement  $\delta$  rises in the positive direction. Fig. 4.41 shows the new steady-state value of angle  $\delta$  becomes  $-4.5^\circ$  from the previous value of  $-7.2^\circ$ . Hence GIC further rejects active power and settles at  $192.7$  W till SEIG frequency matches with GIC frequency. Hence, the resistance offered by GIC increases further. As the SEIG-GIC system operated in a closed



loop voltage as feedback, the output of *PI* controller updated its modulation index,  $m$  value like the previous case and settles at 0.83 as presented in Fig. 4.42. In this case also GIC fundamental component of output voltage is more than that of SEIG voltage but the voltage ratio is approximately same with the previous case. Fig. 4.43 shows the SEIG peak voltage variation, it is observed that corresponds to this load switching, SEIG reaches to 570 V and comes back to the rated value of 586.8 V at 4.58 s. Fig. 4.44 (a), (b) and (c) are showing variation of reactive power corresponding to this load switching. Fig. 4.44 (a) shows that steady-state reactive power supplied by GIC is 705 VAR. Fig. 4.44 (b) shows that steady-state reactive power VAR provided by SEIG is -4195 VAR same with previous case. Fig. 4.44 (c) shows that steady-state reactive power VAR provided by excitation capacitor is 3490 VAR same with previous case. During this transient period GIC still operated as an equivalent parallel combination of resistance and capacitance.

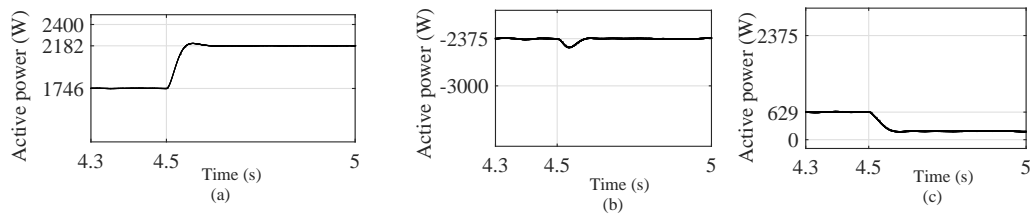


Figure 4.40: Simulation results showing active power variation due to load switching of 400  $\Omega$ /phase: (a) load (b) SEIG (c) GIC

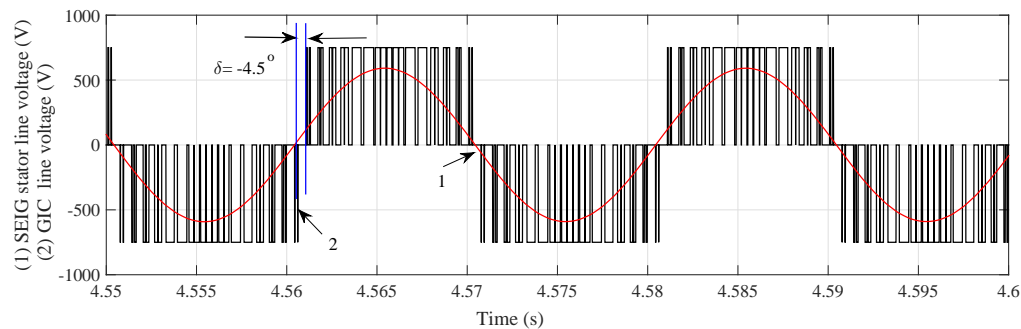


Figure 4.41: Simulation result showing SEIG and GIC voltage waveforms with steady-state value of  $\delta$  due to load switching of 400  $\Omega$ /phase

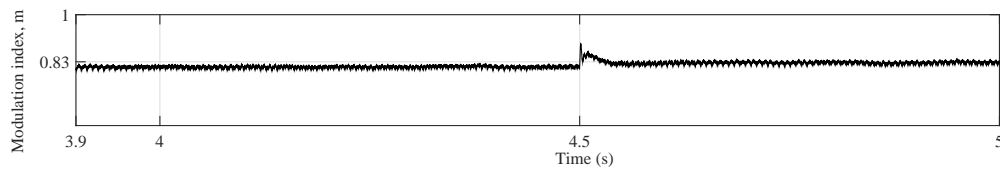


Figure 4.42: Simulation result showing variation of modulation index of GIC with time corresponding to load switching of 400  $\Omega$ /phase

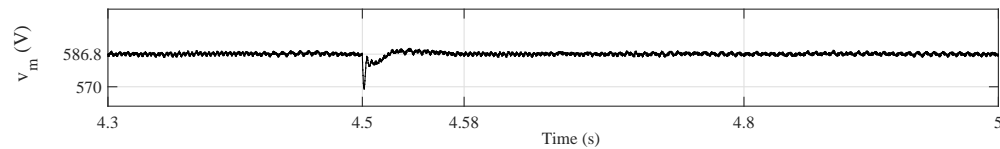


Figure 4.43: Simulation result showing SEIG peak voltage variation due to load switching of 400  $\Omega$ /phase

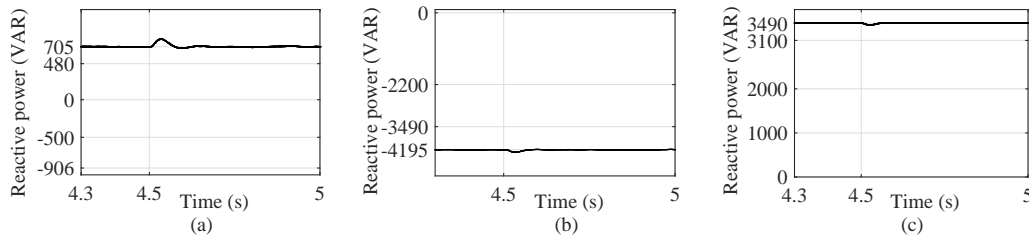


Figure 4.44: Simulation results showing reactive power variation due to load switching of 400  $\Omega$ /phase: (a) GIC (b) SEIG (c) Excitation capacitor

At  $t=5$  s, wind speed changes from 10.8 m/s to 11.2 m/s, and corresponding to this variation, rotor speed changes to 176.7 rad/s. Hence, momentary rise of SEIG frequency appears at  $t=5$  s due to availability of excess active power and after that SEIG frequency follows GIC frequency and comes back to 50 Hz as seen in Fig. 4.45. Due to this perturbation  $\delta$  increases in negative direction. Fig. 4.46 shows the new steady-state value of angle  $\delta$  becomes  $-7.2^\circ$  from the previous value of  $-4.5^\circ$ . Fig. 4.47 (a), (b) and (c) are showing active power variation of load, SEIG and GIC respectively. Corresponding to increase in wind speed from 10.8 m/s to 11.2 m/s, active power supplied by SEIG changes from -2375 to -3405 W. Out of this load absorbs 2182 W and GIC absorbs 1223 W to maintain active power balance.

During this perturbation,  $PI$  updated its output, *i.e.*, modulation index,  $m$  value from 0.83 to 0.86 as presented in Fig. 4.48. In this case also GIC fundamental component of output voltage is more than that of SEIG voltage. Fig. 4.49 shows the SEIG peak volt-

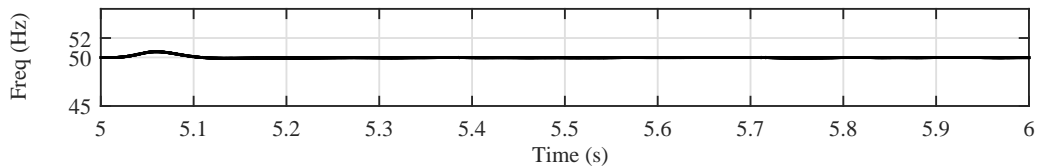


Figure 4.45: Simulation result showing variation of SEIG frequency corresponding to increase in wind speed from 10.8 m/s to 11.2 m/s

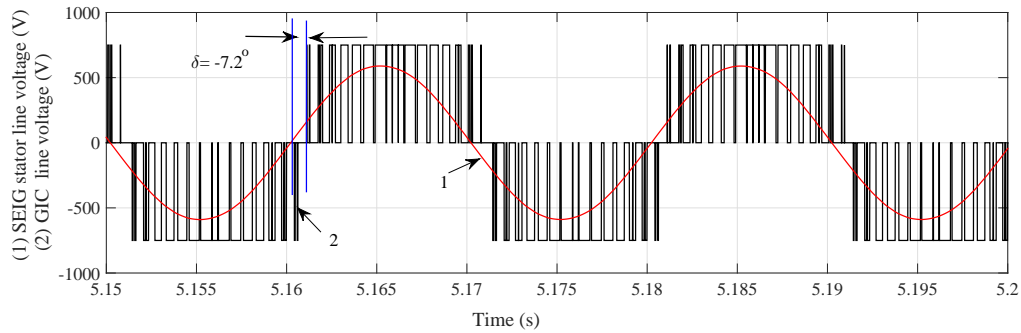


Figure 4.46: Simulation result showing SEIG and GIC voltage waveforms with steady-state value of  $\delta$  corresponding to increase in wind speed from 10.8 m/s to 11.2 m/s

age variation, it is observed that corresponding to this wind perturbation, SEIG reaches to 591.2 V and comes back to the rated value of 586.8 V at 5.16 s. Fig. 4.50 (a), (b) and (c) are showing variation of reactive power of GIC, SEIG and excitation capacitor corresponding to increase in wind speed from 10.8 m/s to 11.2 m/s. During this perturbation, at steady-state GIC supplies 1034 VAR, SEIG demands -4524 VAR and excitation capacitor provides 3490 VAR (same with previous case). During this transient period GIC operates as an equivalent parallel combination of resistance and capacitance.

At  $t=6$  s, wind speed changes from 11.2 m/s to 10.9 m/s, and corresponding to this variation, rotor speed changes from 176.7 rad/s to 172.5 rad/s. Hence, momentary decrease of SEIG frequency appears at  $t=6$  s, with decreased wind speed and after that SEIG frequency follows GIC frequency and comes back to 50 Hz as presented in Fig. 4.51. Corresponding to this wind speed change, Fig. 4.52 shows the new steady-state value of angle  $\delta$  becomes  $-6.21^\circ$  from the previous value of  $-7.2^\circ$ . Fig. 4.53 (a), (b) and (c) are showing active power variation of load, SEIG and GIC respectively. Corresponding to decrease in wind speed from 11.2 m/s to 10.9 m/s, active power supplied by SEIG changes from -3405 W to -2633 W. Load absorbs 2182 W and GIC absorbs 452 W to maintain active power balance.

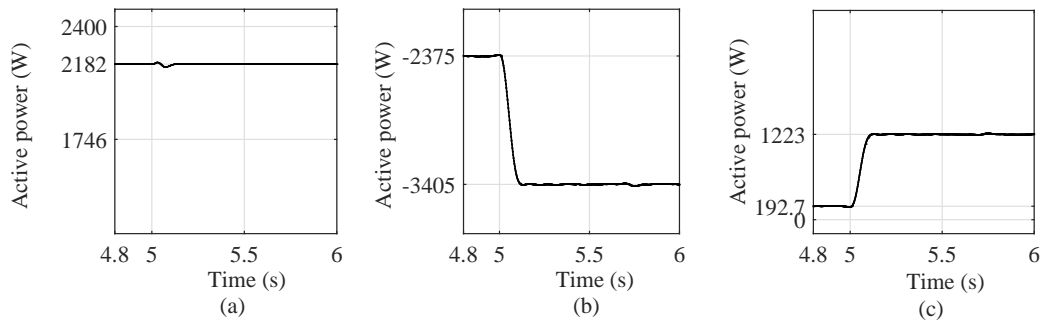


Figure 4.47: Simulation results showing variation of active power corresponding to increase in wind speed from 10.8 m/s to 11.2 m/s: (a) load (b) SEIG (c) GIC

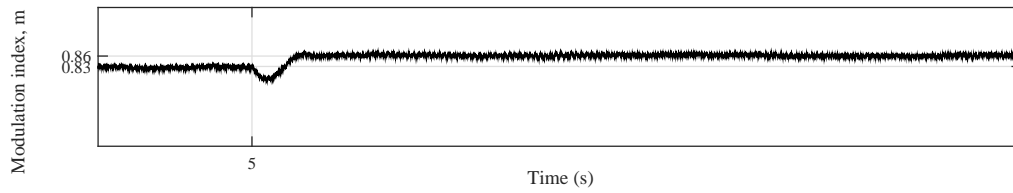


Figure 4.48: Simulation result showing variation of modulation index of GIC with time

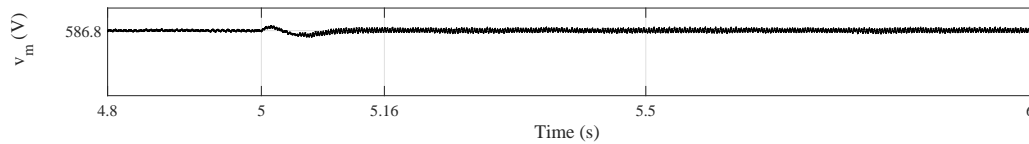


Figure 4.49: Simulation result showing SEIG peak voltage variation corresponding to increase in wind speed from 10.8 m/s to 11.2 m/s

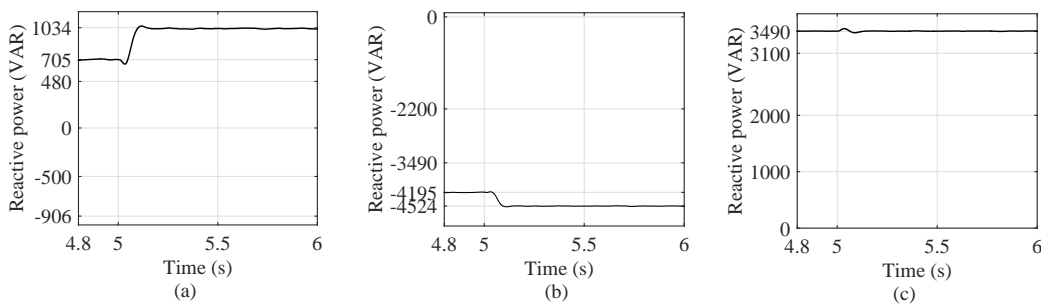


Figure 4.50: Simulation results showing reactive power variation corresponding to increase in wind speed from 10.8 m/s to 11.2 m/s: (a) GIC (b) SEIG (c) excitation capacitor

During this perturbation,  $PI$  updated its output, *i.e.*, modulation index,  $m$  value from 0.86 to 0.83 as presented in Fig. 4.54. In this case also GIC fundamental component

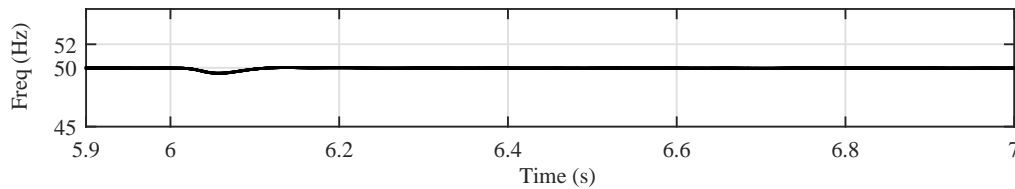


Figure 4.51: Simulation result showing variation of SEIG frequency corresponding to increase in wind speed from 11.2 m/s to 10.9 m/s

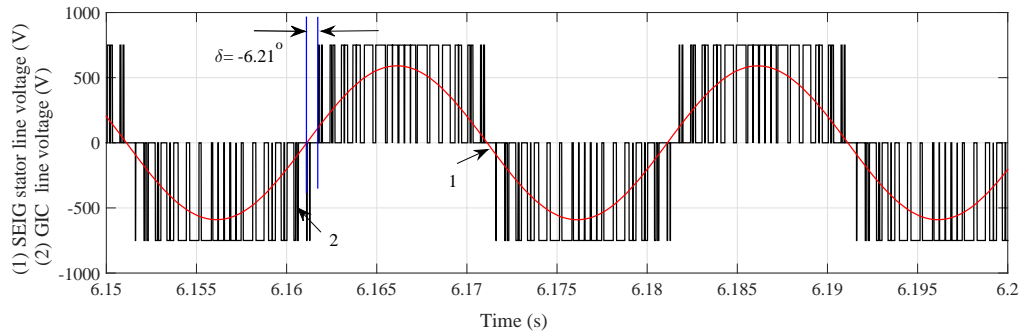


Figure 4.52: Simulation result showing SEIG and GIC voltage waveforms with steady-state value of  $\delta$  corresponding to decrease wind speed from 11.2 m/s to 10.9 m/s

of output voltage is more than that of SEIG voltage. Fig. 4.55 shows the SEIG peak voltage variation corresponding to this wind speed perturbation. It is observed that SEIG peak voltage comes to rated voltage at  $t=6.12$  s. Fig. 4.56 (a), (b) and (c) are showing variation of reactive power of GIC, SEIG and excitation capacitor corresponds to increase in wind speed from 11.2 m/s to 10.9 m/s. During this perturbation GIC supplies 778 VAR, SEIG demands -4268 VAR and excitation capacitor provides 3490 VAR (same with previous case). During this transient period GIC operates as an equivalent parallel combination of resistance and capacitance.

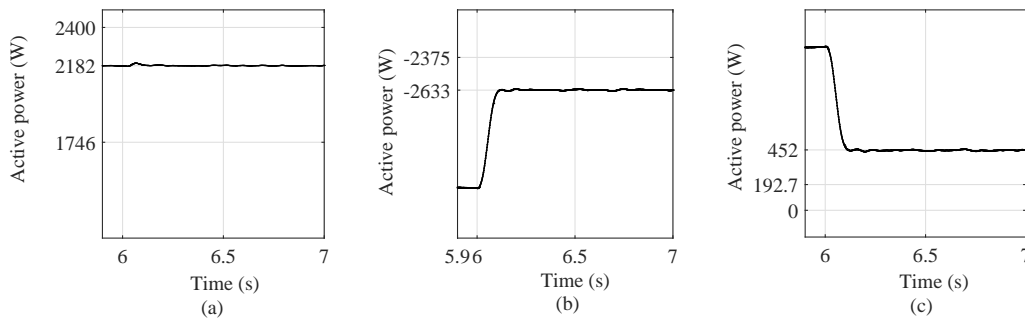


Figure 4.53: Simulation results showing variation of active power corresponding to decrease in wind speed from 11.2 m/s to 10.9 m/s: (a) load (b) SEIG (c) GIC

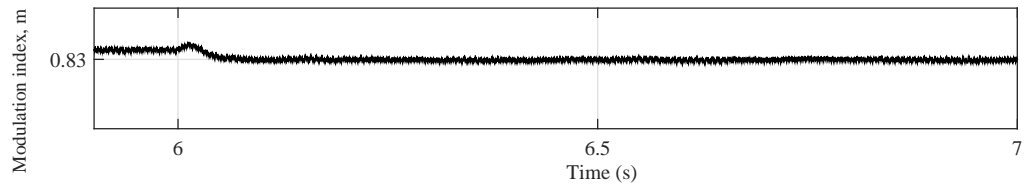


Figure 4.54: Simulation result showing variation of modulation index of GIC with time corresponding to decrease in wind speed from 11.2 m/s to 10.9 m/s

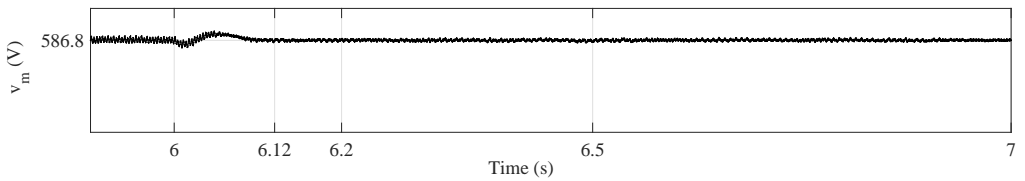


Figure 4.55: Simulation result showing variation of SEIG peak voltage corresponding to decrease in wind speed from 11.2 m/s to 10.9 m/s

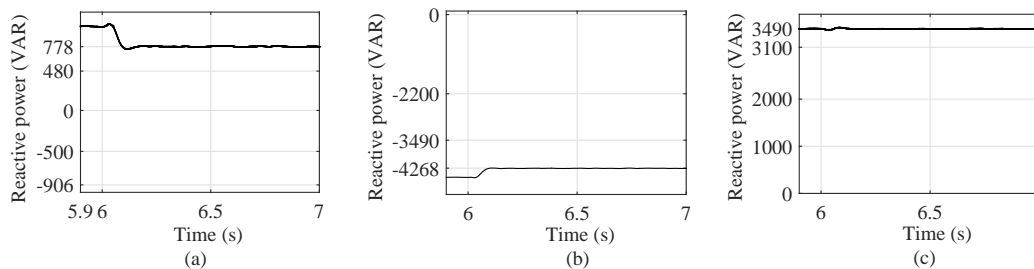


Figure 4.56: Simulation results showing reactive power variation corresponding to increase in wind speed from 11.2 m/s to 10.9 m/s: (a) GIC (b) SEIG (c) excitation capacitor

At  $t=7$  s, resistive load  $100 \Omega/\text{phase}$  is removed from the SEIG terminals which leads to momentary rise in SEIG terminal frequency and after that SEIG frequency follows GIC frequency and comes back to  $50$  Hz as shown in Fig. 4.57. Corresponds to this load change, Fig. 4.58 shows the new steady-state value of angle  $\delta$  becomes  $-14.76^\circ$  from the previous value of  $-6.21^\circ$ . Fig. 4.59 (a), (b) and (c) are showing active power variation of load, SEIG and GIC corresponds to removal of load at wind speed of  $10.9$  m/s. During this perturbation active power supplied by SEIG is  $-2633$  W (same with previous case due to same wind speed). Active power drawn by load is decreased from  $2182$  W to  $436.4$  W (due to removal of load). Active power absorbed by GIC increases from  $452$  W to  $2197$  W (which is more than the previous case) to maintain active power balance. Corresponding to this load perturbation, the output of  $PI$  controller updated its modulation index,  $m$  from  $0.83$  to  $0.84$  as presented in Fig. 4.60. In this case also GIC fundamental component of output voltage is more than that of SEIG voltage. Fig. 4.61 shows SEIG peak voltage changes from rated value of  $586.8$  V to  $613$  V and comes back to rated value at  $7.13$  s. Fig. 4.62 (a), (b) and (c) are showing variation of reactive power of GIC, SEIG and excitation capacitor corresponds to removal of load at wind speed  $10.9$  m/s. During this perturbation GIC supplies  $778$  VAR. SEIG requires about  $4270$  VAR during this transient period. Excitation capacitor supplies  $3490$  VAR (there is no change in the VAR provided by excitation capacitor). During this transient period GIC still operated as an equivalent parallel combination of resistance and capacitance.

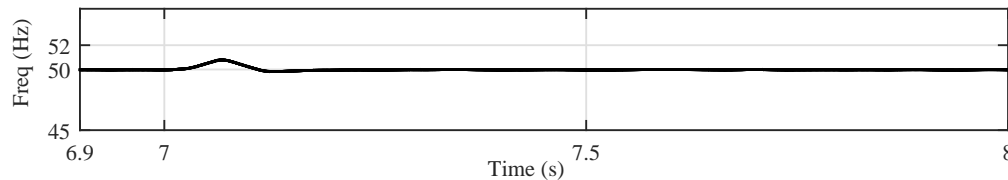


Figure 4.57: Simulation result showing variation of SEIG frequency corresponding to removal of load at wind speed  $10.9$  m/s

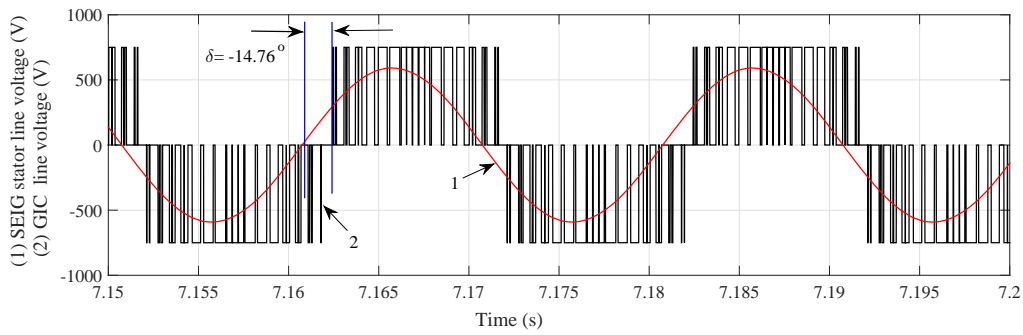


Figure 4.58: Simulation result showing SEIG and GIC voltage waveforms with steady-state value of  $\delta$  corresponding to removal of load at wind speed 10.9 m/s

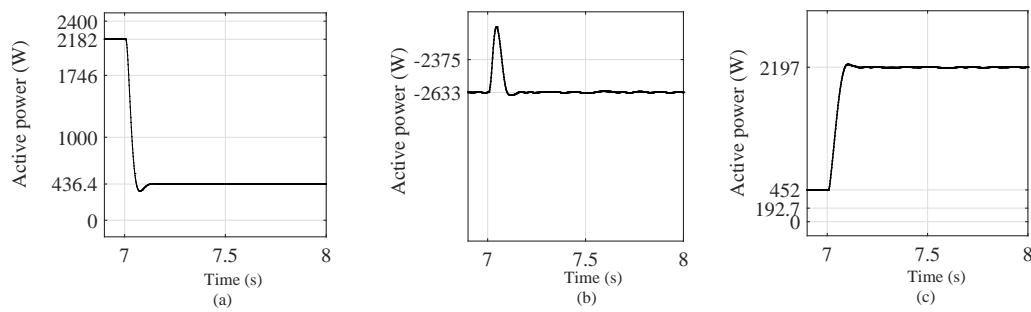


Figure 4.59: Simulation results showing variation of active power corresponding to removal of load at wind speed 10.9 m/s: (a) load (b) SEIG (c) GIC

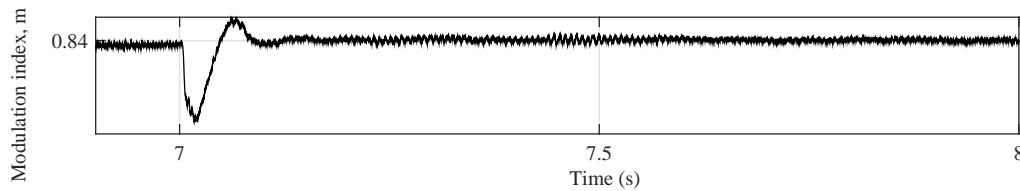


Figure 4.60: Simulation result showing variation of modulation index of GIC with time corresponding to removal of load at wind speed 10.9 m/s

At  $t=8$  s, wind speed changes from 10.9 m/s to 10.5 m/s and corresponding to this variation, SEIG rotor speed decreases to 167 rad/s. Hence, momentary decrease of SEIG frequency appears at  $t=8$  s, with decreased wind speed and after that SEIG frequency follows GIC frequency and comes back to 50 Hz as presented in Fig. 4.63. Corresponding to this wind speed change, Fig. 4.64 shows the new steady state value of angle  $\delta$  becomes  $-8.1^\circ$  from the previous value of  $-14.76^\circ$ . Fig. 4.65 (a), (b) and (c) are showing active power variation of load, SEIG and GIC respectively. Corresponds to decrease in wind speed from



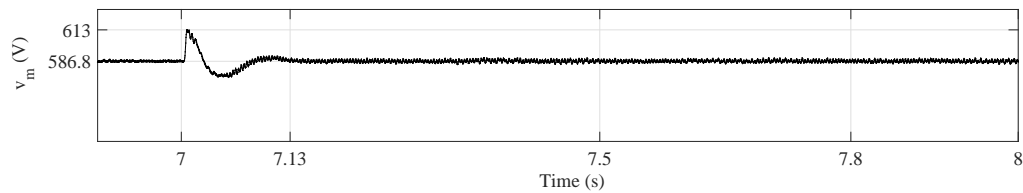


Figure 4.61: Simulation result showing variation of SEIG peak voltage corresponding to removal of load at wind speed 10.9 m/s

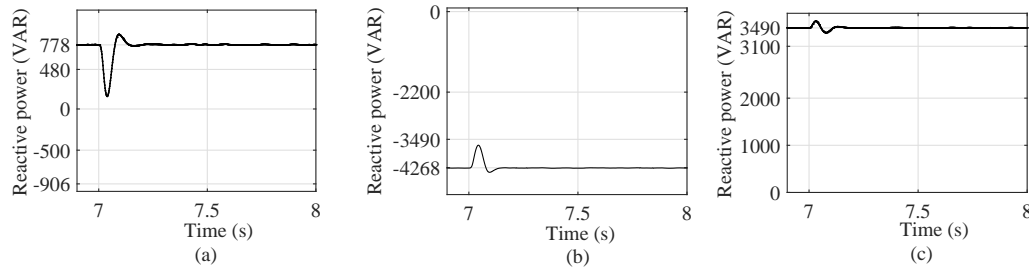


Figure 4.62: Simulation results showing variation of reactive power corresponding to removal of load at wind speed 10.9 m/s: (a) GIC (b) SEIG (c) excitation capacitor

10.9 m/s to 10.5 m/s, active power supplied by SEIG changes from -2633 W to -1612 W. Active power drawn by load is 436.4 W. Active power absorbed by GIC changes from 2197 W to 1165 W to maintain active power balance. During this perturbation  $PI$  updated its output *i.e.*, modulation index,  $m$  value from 0.84 to 0.77 as shown in Fig. 4.66. In this case also GIC fundamental component of output voltage is more than that of SEIG voltage. Fig. 4.67 shows variation of SEIG peak voltage. It is observed that SEIG peak reaches to 594.6 V and comes to rated value of 586.8 V at 8.15 s. Fig. 4.68 (a), (b) and (c) are showing variation of reactive power of GIC, SEIG and excitation capacitor corresponding to decrease of wind speed from 10.9 m/s to 10.5 m/s. During this perturbation period SEIG requires 3976 VAR. GIC supplies of the order of 480 VAR. Excitation capacitor supplies 3490 VAR (there is no change in the VAR provided by excitation capacitor). During this transient period GIC still operates as an equivalent parallel combination of resistance and capacitance.

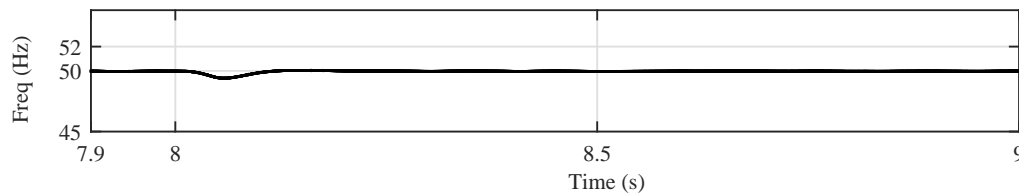


Figure 4.63: Simulation result showing variation of SEIG frequency corresponding to decrease in wind speed from 10.9 m/s to 10.5 m/s

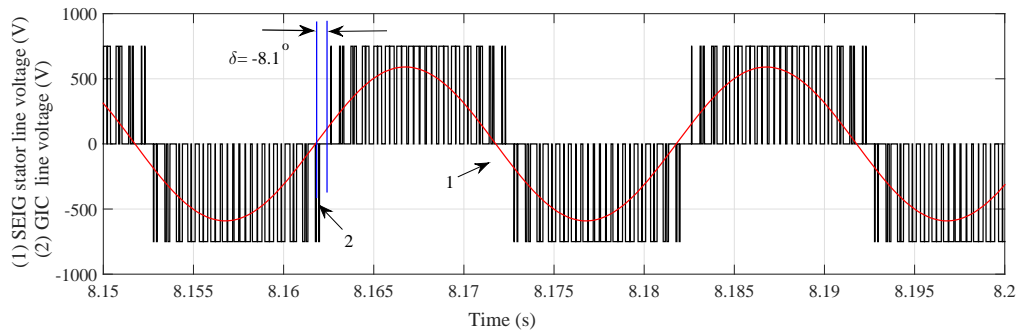


Figure 4.64: Simulation result showing SEIG and GIC voltage waveforms with steady-state value of  $\delta$  corresponding to decrease in wind speed from 10.9 m/s to 10.5 m/s

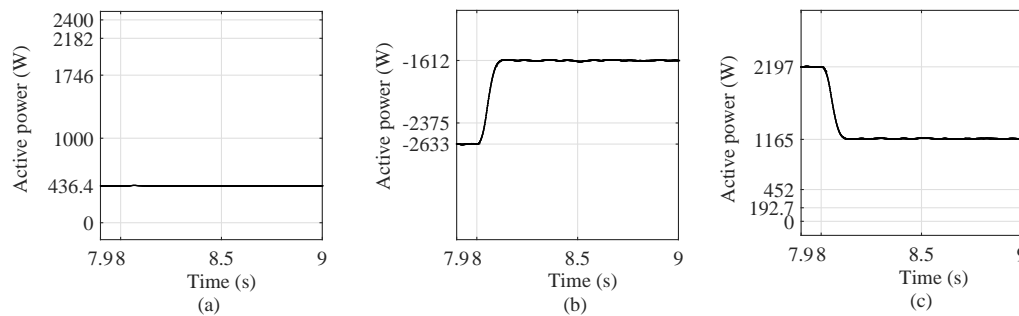


Figure 4.65: Simulation results showing variation of active power corresponding to decrease in wind speed from 10.9 m/s to 10.5 m/s: (a) load (b) SEIG (c) GIC

Fig. 4.69 (a) shows the stator line current waveform. At wind speed of 9.8 m/s and corresponding stator peak voltage of 586.8 V, stator peak current is 6.8 A. At  $t=1$  s, due to switching of GIC, stator peak current remains same. At  $t=2$  s, wind speed increased to 10.8 m/s thus increasing the mechanical power input and active power output of the generator. As the stator voltage of SEIG remains constant due to closed loop voltage control by GIC, the stator current increased to 9.45 A. At  $t=3$  s and 4.5 s, switching of loads of 100  $\Omega$ /phase and 400  $\Omega$ /phase, respectively do not have any effect on stator line current except spike due

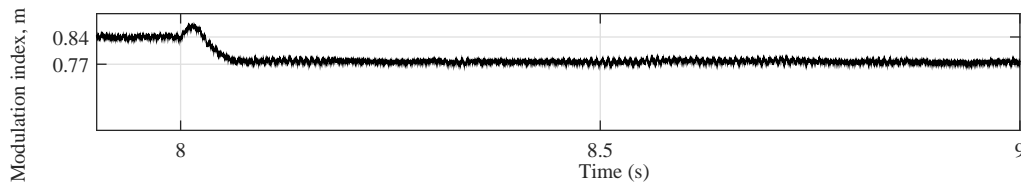


Figure 4.66: Simulation result showing variation of modulation index of GIC corresponding to decrease in wind speed from 10.9 m/s to 10.5 m/s

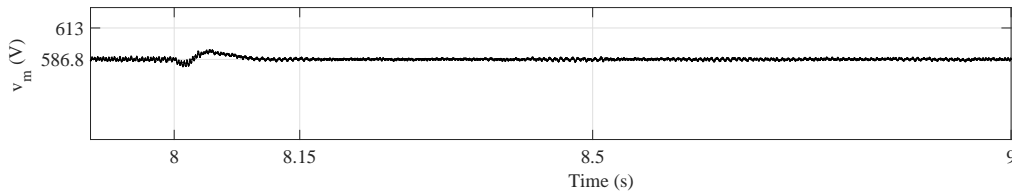


Figure 4.67: Simulation result showing variation of SEIG peak voltage corresponding to decrease in wind speed from 10.9 m/s to 10.5 m/s

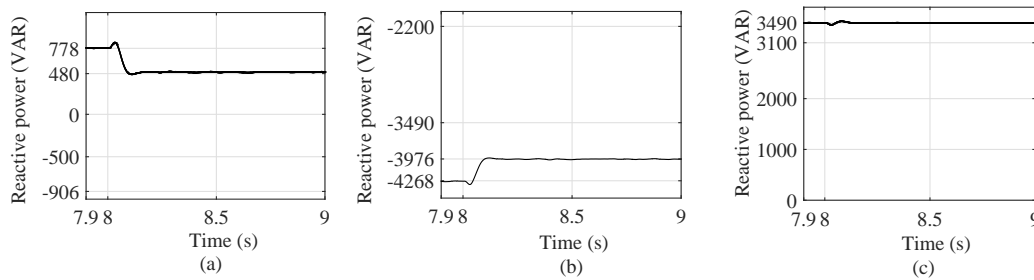


Figure 4.68: Simulation results showing variation of reactive power corresponding to decrease in wind speed from 10.9 m/s to 10.5 m/s: (a) GIC (b) SEIG (c) Excitation capacitor

to healthy functioning of GIC. At  $t=5$  s, wind speed increased to 11.2 m/s thus increasing the mechanical power input and active power output of the generator. As the stator voltage of SEIG remains constant due to closed loop voltage control by GIC, the stator current increased to 11.07 A. The stator peak current decreases from 11.07 A to 9.81 A, due to decrease of wind speed to 10.9 m/s at  $t=6$  s. At  $t=7$  s, load is removed so only a spike occurs and stator current maintains its previous value. At  $t=8$  s, wind speed reduces to 10.5 m/s so mechanical power input and active power output of SEIG decreases. As the stator voltage of SEIG remains constant due to closed loop voltage control by GIC, the stator current decreased from 9.81 A to 8.35 A.

Fig. 4.69 (b) shows the load current waveform. First load is switched on at  $t=3$  s. Till then load current was zero. At  $t=3$  s due to switching of load of  $100 \Omega/\text{phase}$ , load peak

current increase from zero to 3.38 A. At  $t=4.5$  s, due to switching of load of  $400 \Omega/\text{phase}$ , net load decreases to  $80 \Omega/\text{phase}$ . Corresponding to this, load peak current increases from 3.38 A to 4.23 A. At  $t=7$  s,  $100 \Omega/\text{phase}$  load is removed from SEIG so load current reduced from 4.23 A to 0.85 A. After that there is no load change. So load peak current remains constant at 0.85 A. The variation in SEIG stator current with wind speed variation is taken care by GIC and load current not affected by stator current changes.

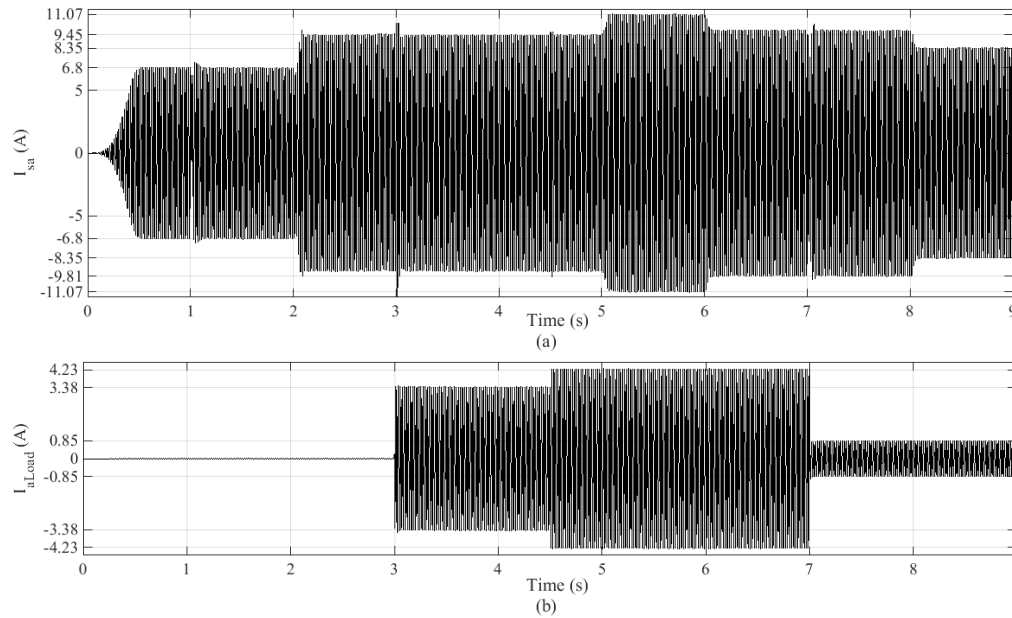


Figure 4.69: Closed loop simulation results of stator current and load current waveforms of optimized GIC based SEIG system during different perturbations: (a) Stator line current waveform of of SEIG (b) Load current waveform

#### 4.6.2 Transient performance of optimized GIC based SEIG system feeding IM load

As the results presented and discussed in the chapter 3, SEIG is not able to operate IM load successfully. So, a closed loop control is essential. Initially at  $t=0$  s, a wind speed of 9.8 m/s is selected in the simulation to develop the rated SEIG voltage. To show the effectiveness of the proposed closed loop control technique and to run smoothly IM load with SEIG, the perturbations considered are as follows.

1. Switching of GIC at  $t=1$  s,
2. Wind speed increased from 9.8 m/s to 10.8 m/s at  $t=2$  s,

3. Switching of IM load at  $t=3$  s with zero mechanical load,
4. Mechanical load of 4 Nm is applied to IM at  $t=5$  s,
5. Wind speed increased from 10.8 m/s to 11.2 m/s at  $t=6$  s,
6. Mechanical load is removed from IM at  $t=7$  s and
7. Wind speed decreased from 11.2 m/s to 10.9 m/s at  $t=8$  s.

Simulation results for variation of wind speed and IM load mentioned in the beginning of this subsection are shown in Fig. 4.70. Fig. 4.70 (a) shows wind speed variation considered as input for simulation, Fig. 4.70 (b) shows the SEIG rotor speed corresponding to this variation. Fig. 4.70 (c) shows frequency of SEIG controlled in open loop manner by GIC, corresponding to this wind speed and load perturbations. Fig. 4.70 (d) shows SEIG stator peak voltage when controlled in closed loop manner by GIC, corresponding to this wind speed and load perturbations. Detail of Fig. 4.70 are described in subsequent paragraphs. As discussed in the previous subsection 4.6.1, GIC is connected with SEIG at  $t=1$  s. GIC is connected with the SEIG at the point of common coupling in such a manner that no exchange of active power and reactive power occurs between them at steady state.

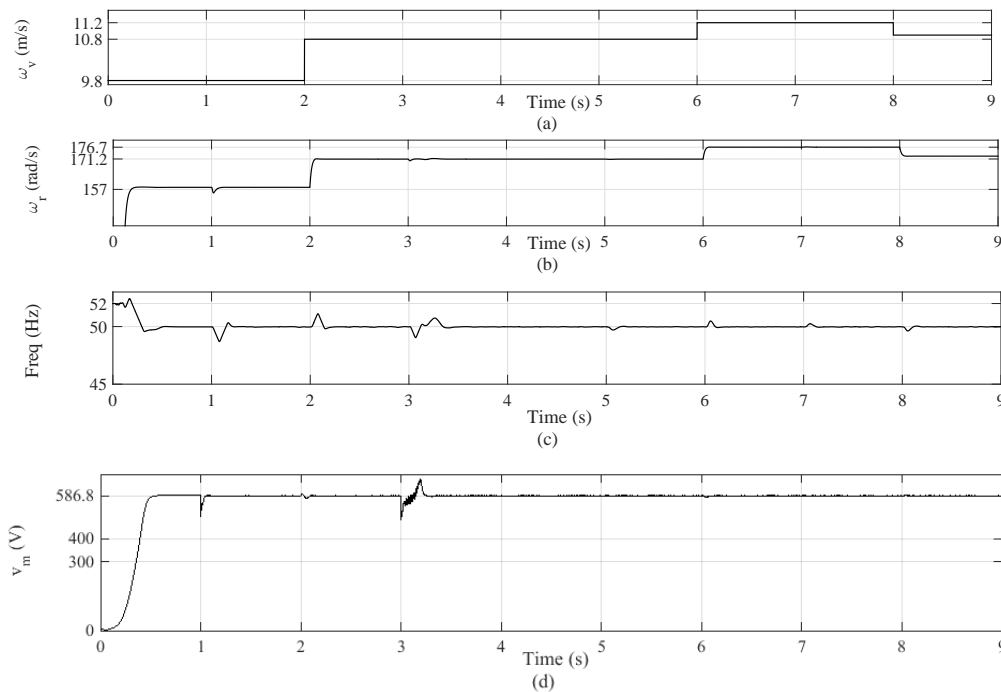


Figure 4.70: Closed loop simulation results of proposed GIC based SEIG with IM loading and wind speed perturbations: (a) Wind speed (b) Rotor speed of SEIG (c) Stator frequency of SEIG (d) Stator peak voltage of SEIG

At  $t=2$  s, wind speed changes to 10.8 m/s, and corresponding to this variation, rotor speed changes to 171.7 rad/s. It is observed from Fig. 4.71 that SEIG terminal frequency increases due to availability of excess active power. Fig. 4.72 shows active power of SEIG changes from zero to -2375 W. Fig. 4.73 shows the new steady-state value of angle  $\delta$  becomes  $-14.4^\circ$ , from the previous value of zero. Wind speed increase leads to increase of  $\delta$  in negative direction. Hence, GIC absorbs active power of 2375 W from SEIG. Fig. 4.74 shows the active power of GIC changes from zero to 2375 W. Following the above frequency transient, the angle  $\delta$  and active power flow in GIC reach the steady-state and finally SEIG frequency becomes equal to the GIC frequency. SEIG frequency is maintained at its rated value without any frequency feedback. This occurs due to excess power absorbed by the GIC during the transient period. As observed in Fig. 4.73, the GIC line voltage lags SEIG stator line voltage by  $\delta = -14.4^\circ$ . Since,  $\delta < 0^\circ$  the GIC acts as an equivalent resistance and this power is stored in DC link battery. Due to active power drawn by GIC, SEIG terminal voltage deviates from the rated value of 586.8 V as shown in Fig. 4.75. But SEIG-GIC operate in closed loop with voltage as feedback, and the  $PI$  updates its output, *i.e.*, modulation index,  $m$  value from 0.73 to 0.83 as presented in Fig. 4.76. The wind speed perturbation taken at  $t=2$  s, makes the fundamental component of GIC output voltage more than the fundamental component of SEIG stator line voltage (since  $m$  is more than critical value). Hence, GIC acts as an equivalent capacitor and supplies additional leading reactive power of the order of 705 VAR as shown in Fig. 4.77 (a). Fig. 4.77 (b) shows that steady-state reactive power of SEIG corresponding to this wind perturbation is -4195 VAR. However, as shown in Fig. 4.77 (c), excitation capacitor provides 3490 VAR in steady state. Under steady-state,  $\delta$  remains at the same value to maintain the power balance across PCC. The GIC acts as an equivalent parallel combination of resistance and capacitance from time  $t=2$  s to next transient period  $t=3$  s.

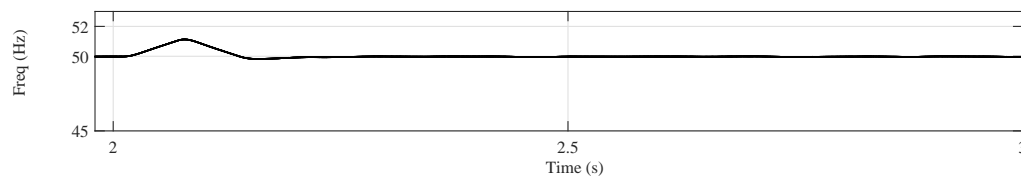


Figure 4.71: Simulation result (GIC based SEIG system to feed IM load) showing SEIG frequency variation corresponding to wind speed change from 9.8 m/s to 10.8 m/s

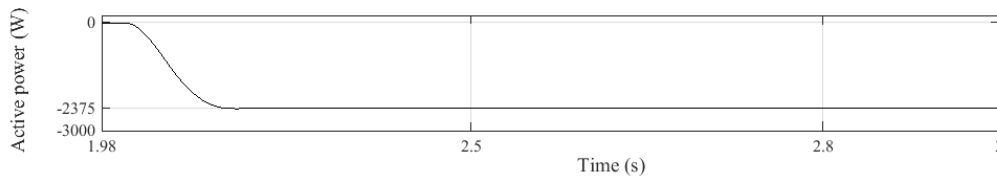


Figure 4.72: Simulation result (GIC based SEIG system to feed IM load) showing variation of SEIG active power corresponds to wind speed change from 9.8 m/s to 10.8 m/s

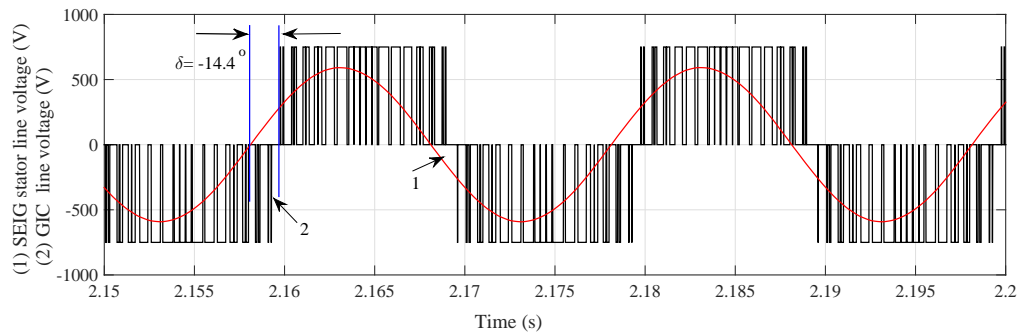


Figure 4.73: Simulation result (GIC based SEIG system to feed IM load) showing SEIG and GIC voltage waveforms with steady state-value of  $\delta$  in wind speed change from 9.8 m/s to 10.8 m/s

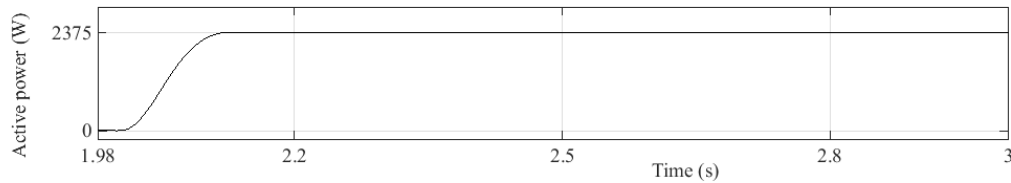


Figure 4.74: Simulation result (GIC based SEIG system to feed IM load) showing variation of GIC active power corresponding to wind speed change from 9.8 m/s to 10.8 m/s (GIC based SEIG system to feed IM load)

At  $t=3$  s, IM is connected to SEIG with no mechanical load, IM attained the rated speed of 157 rad/s at  $t=3.36$  s after the successful starting as seen from Fig. 4.78 (a). The electromagnetic torque of IM is also showing appreciable starting transients that are settled at  $t=3.36$  s as observed from Fig. 4.78 (b). Fig. 4.79 shows SEIG frequency variation with IM load (mechanical load is zero) at 10.8 m/s wind speed. As seen from this figure SEIG frequency reaches to 50 Hz at  $t=3.36$  s. Fig. 4.80 (a), (b) and (c) are showing active power variation of SEIG, IM load and GIC corresponding to this IM load switching. As seen from Fig. 4.80 (a) that steady-state active power provided

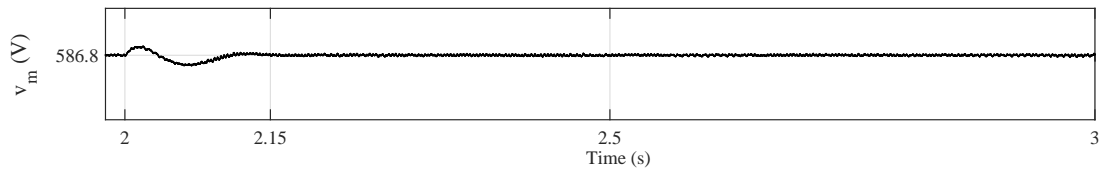


Figure 4.75: Simulation result (GIC based SEIG system to feed IM load) showing SEIG peak voltage waveform corresponding to wind speed change from 9.8 m/s to 10.8 m/s (GIC based SEIG system to feed IM load)

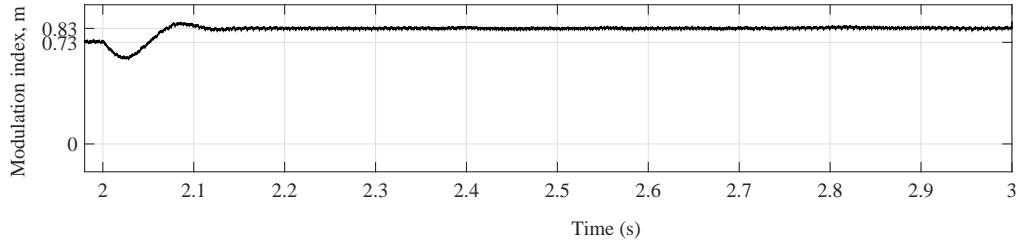


Figure 4.76: Simulation result (GIC based SEIG system to feed IM load) showing variation of modulation index of GIC with time corresponding to wind speed change from 9.8 m/s to 10.8 m/s

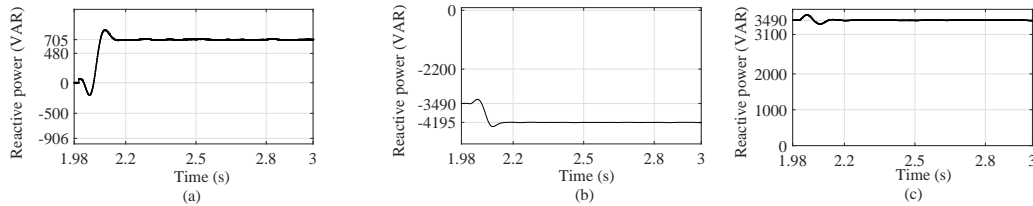


Figure 4.77: Simulation results (GIC based SEIG system to feed IM load) showing reactive power variation corresponding to wind speed change from 9.8 m/s to 10.8 m/s (GIC based SEIG system to feed IM load): (a) GIC (b) SEIG (c) Excitation capacitor

by SEIG is of the order of -2375 W. Fig. 4.80 (b) shows that since IM load is operated with no mechanical load so, active power absorbed by it zero at steady-state. Hence, to maintain active power balance GIC absorbed 2375 W (for maintaining SEIG frequency) as observed in Fig. 4.80 (c). During this transient period GIC offers same resistance to the SEIG system like the previous period. The PI controller updates its output *i.e.*, modulation index,  $m$  to 0.89. SEIG peak voltage comes to rated voltage of 586.8 at 3.29 s, as seen in Fig. 4.81. During this period as discussed in the previous section modulation index is more than critical modulation index value so line voltage of output of GIC is more than stator line voltage of SEIG. Fig. 4.82 (a) shows that during this perturbation VAR demanded by SEIG



is of the order -4194. Fig. 4.82 (b) shows that the VAR demanded by IM load is -753.3 VAR. Total VAR required by SEIG and IM load is provided by capacitor and GIC. It is observed from Fig. 4.82 (c) that capacitor supplies 3490 VAR during this period. Fig. 4.82 (d) shows that the VAR supplied by GIC is 1457.3 VAR.

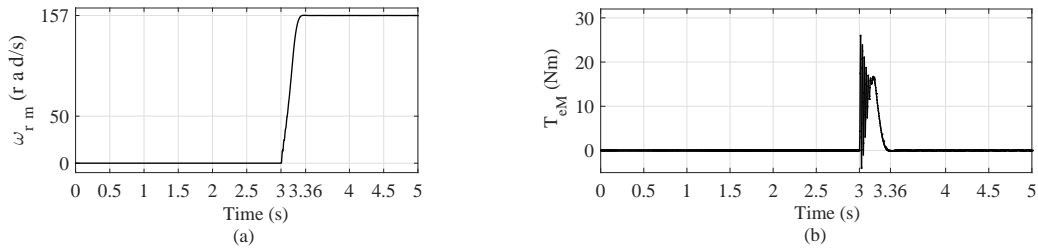


Figure 4.78: Simulation results of speed and torque variation of IM load (mechanical load is zero) connected with GIC based SEIG at 10.8 m/s wind speed: (a) Rotor Speed of IM (b) Electromagnetic torque of IM

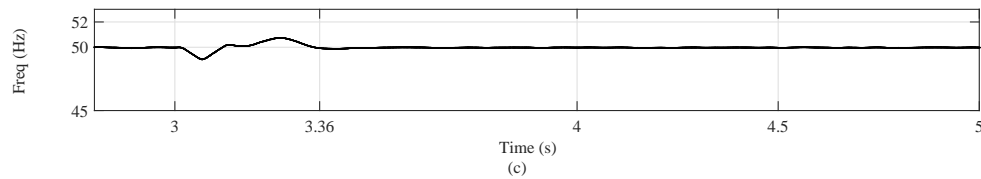


Figure 4.79: Simulation result showing SEIG frequency variation with IM load (mechanical load is zero) at 10.8 m/s wind speed

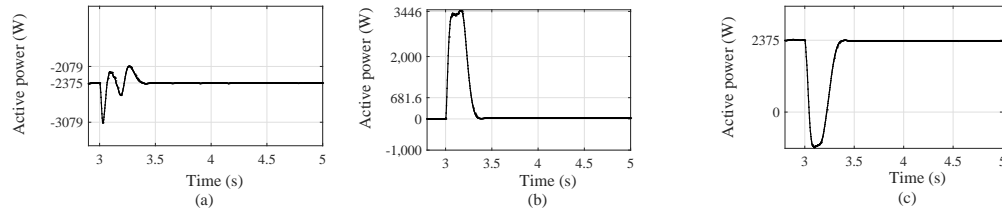


Figure 4.80: Simulation results showing active power variation with IM load (mechanical load is zero) at 10.8 m/s wind speed: (a) SEIG (b) GIC (c) IM load

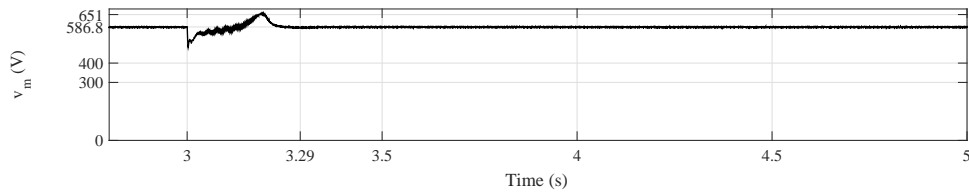


Figure 4.81: Simulation result showing variation of SEIG peak voltage with IM load (mechanical load is zero) at 10.8 m/s wind speed speed

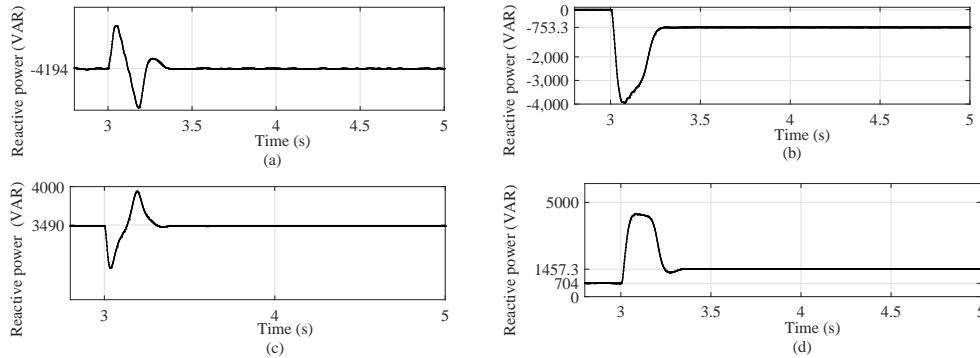


Figure 4.82: Simulation results showing reactive power variation with IM load (mechanical load is zero) at 10.8 m/s wind speed speed: (a) SEIG (b) IM load (c) Excitation capacitor (d) GIC

At  $t=5$  s, mechanical load of 4 Nm is applied to the IM load. Corresponding to this, the speed of IM decreased to 149.2 rad/s as seen from Fig. 4.83 (a) and electromagnetic torque increased to 4 Nm as observed from Fig. 4.83 (b). SEIG terminal frequency falls for a moment and comes back to 50 Hz at  $t=5.16$  s as observed in Fig. 4.84, till active power provided by SEIG matches with active power absorbed by GIC and IM load. Fig. 4.85 (a) shows that active power provided by SEIG is -2375 W. Fig. 4.85 (b) shows that active power absorbed by IM load is of the order of 681.6. Fig. 4.85 (c) shows that active power absorbed by GIC is 1697.4 W to maintain power balance for maintaining SEIG frequency at 50 Hz. During this perturbation GIC operates as a resistance. Since the SEIG-GIC system operates in closed loop by updating output of *PI*, SEIG peak voltage comes to rated voltage of 586.8. Fig. 4.86 (a) and (b) show that reactive power required by SEIG and IM load are -4194 VAR and -753.3 VAR, respectively. It is observed from Fig. 4.86 (c) and (d) that excitation capacitor and GIC supply approximately same amount of VAR as provided in the previous case. The GIC acts as an equivalent parallel combination of resistance and capacitance from time  $t=5$  s to next transient period  $t=6$  s.

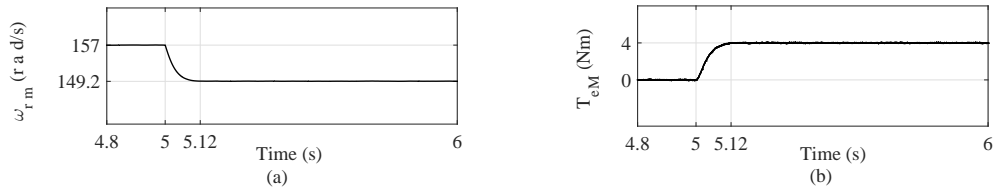


Figure 4.83: Simulation results showing speed and torque variation of IM load corresponding to insertion of mechanical load of 4 Nm with 10.8 m/s wind speed: (a) IM speed (b) IM torque

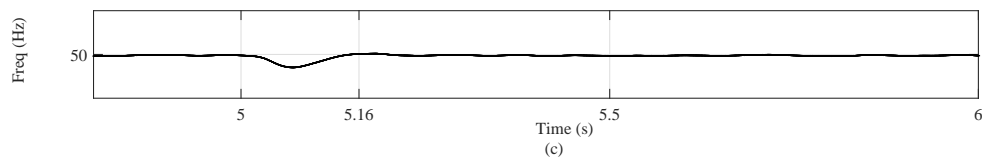


Figure 4.84: Simulation result showing SEIG frequency variation corresponding to IM load (insertion of 4 Nm mechanical load) with 10.8 m/s wind speed

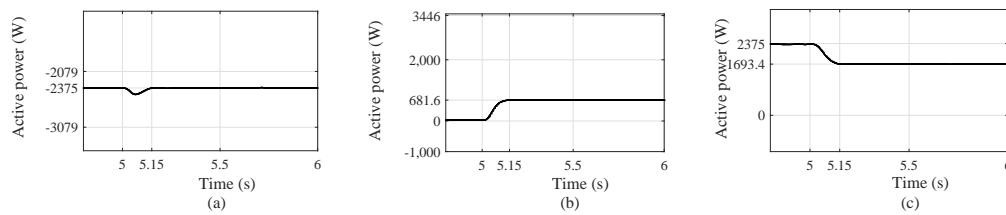


Figure 4.85: Simulation results showing active power variation corresponding to IM load (insertion of 4 Nm mechanical load) with 10.8 m/s wind speed

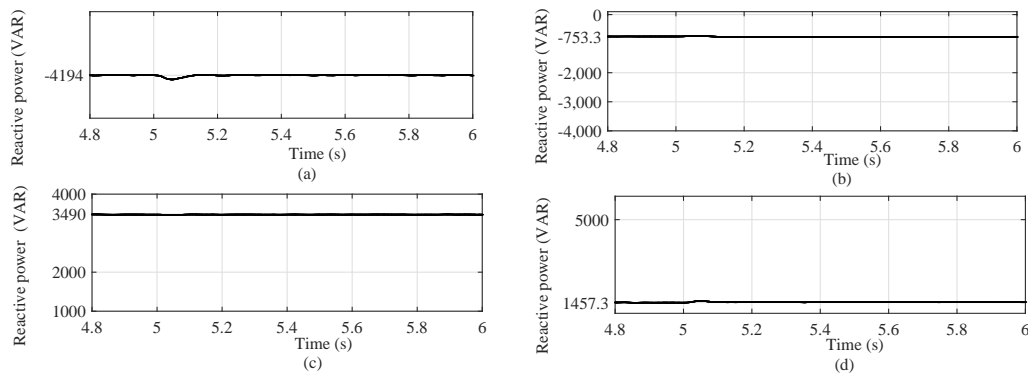


Figure 4.86: Simulation results showing reactive power variation corresponding to IM load (insertion of 4 Nm mechanical load ) with 10.8 m/s wind speed: (a) SEIG (b) IM load (c) excitation capacitor (d) GIC

At  $t=6$  s, due to increase in wind speed from 10.8 m/s to 11.2 m/s, SEIG rotor speed increased from 171.2 rad/s to 176.6 rad/s. As a result SEIG terminal frequency rises for a moment and comes back to 50 Hz at  $t=6.12$  s. IM load rotor speed and torque are same with previous case as there is no change in mechanical load occurs. Fig. 4.88 (a) shows that active power provided by SEIG changes from -2375 W to -3407 W. Fig. 4.88 (b) shows that active power absorbed by IM load is 681.6 W. Fig. 4.88 (c) shows that active power absorbed by GIC changes from 1693.4 W to 2725.4 W. When balance of active power occurs SEIG frequency comes to 50 Hz. During this perturbation GIC operates as a resistance. As voltage is used as a feed back,  $PI$  updates its output and peak of SEIG comes to rated voltage of 586.8 V. Fig. 4.88 (a) shows that reactive power required by SEIG changes from -4194 VAR to -4524 VAR. Fig. 4.88 (b) shows that reactive power required by IM load is -753.3 VAR. Fig. 4.88 (c) shows that VAR supplied by excitation capacitor is 3490 VAR. Fig. 4.88 (d) shows that VAR supplied by GIC changes from 1453 VAR to 1800 VAR. The GIC acts as an equivalent parallel combination of resistance and capacitance from time  $t=6$  s to next transient period  $t=7$  s.

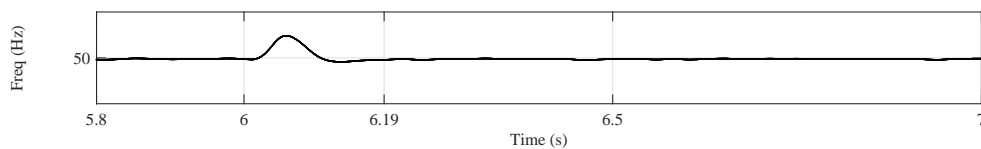


Figure 4.87: Simulation result showing SEIG frequency variation corresponding to IM load (4 Nm mechanical load ) with 11.2 m/s wind speed

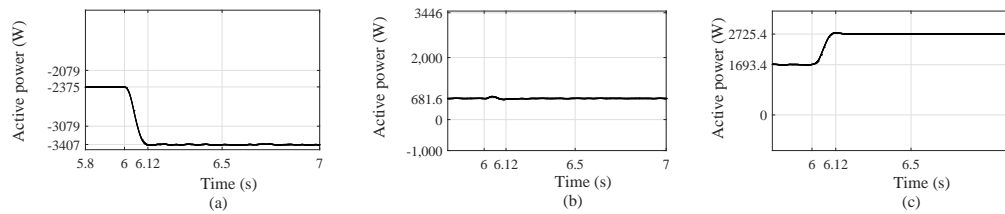


Figure 4.88: Simulation results showing active power variation corresponding to IM load (4 Nm mechanical load) with 11.2 m/s wind speed: (a) SEIG (b) IM load (c) GIC

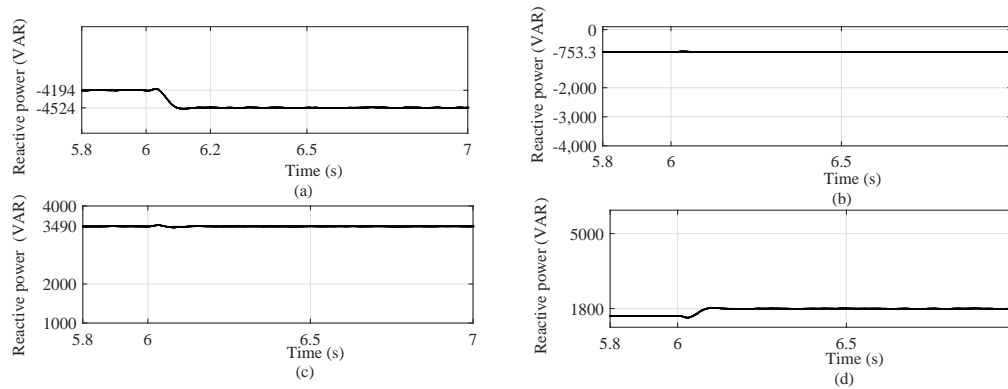


Figure 4.89: Simulation results showing reactive power variation corresponding to IM load (4 Nm mechanical load) with 11.2 m/s wind speed: (a) SEIG (b) IM load (c) Excitation capacitor (d) GIC

At  $t=7$  s, mechanical load of IM load is removed. It is observed from Fig. 4.90 (a) that, corresponding to this IM speed increases from 149.2 rad/s to 157 rad/s. Fig. 4.90 (b) shows electromagnetic torque decreased from 4 Nm to zero at  $t=7.12$  s. Removal of mechanical load results momentary rises in SEIG frequency and brings the frequency to 50 Hz at  $t=7.13$  s as seen in Fig. 4.91. Fig. 4.92 (a) shows that active power provided by SEIG is -3407 W. Fig. 4.92 (b) shows that active power absorbed by IM load decreases from 681.6 W to zero W due to removal of mechanical load across IM. Fig. 4.92 (c) shows that active power absorbed by GIC changes from 2725.4 W to 3407 W. When balance of active power occurs SEIG frequency comes to 50 Hz. During this perturbation GIC operates as a resistance. As voltage is used as a feed back,  $PI$  updates its output and peak of SEIG comes to rated voltage of 586.8 V. Fig. 4.93 (a) shows that reactive power required by SEIG changes from -4194 VAR to -4524 VAR. Fig. 4.93 (b) shows that reactive power required by IM load is -753.3 VAR. Fig. 4.93 (c) shows that VAR supplied by excitation capacitor is 3490 VAR. Fig. 4.93 (d) shows that VAR supplied by GIC changes from 1453 VAR to 1800 VAR. The GIC acts as an equivalent parallel combination of resistance and capacitance from time  $t=7$  s to next transient period  $t=8$  s.

At  $t=8$  s, wind speed decreased from 11.2 m/s to 10.9 m/s, corresponding to that SEIG rotor speed decreased from 176.7 rad/s to 172.5 rad/s. As a result momentary falls in SEIG terminal frequency occurred and comes to 50 Hz at  $t=8.12$  s as seen in Fig. 4.91. Fig. 4.92 (a) shows that active power provided by SEIG changes from -3407 W to -2634 W. Fig. 4.92 (b) shows that active power absorbed by IM load is zero W due to no mechanical load across IM. Fig. 4.92 (c) shows that active power absorbed by GIC changes from 3407 W to 2634 W. When balance of active power occurs SEIG frequency comes to 50 Hz. During this perturbation GIC operates as a resistance. As voltage is used as a feed back,  $PI$  updates its output and peak of SEIG comes to rated voltage of 586.8 V. Fig. 4.93 (a) shows that reactive power required by SEIG changes from -4524 VAR to -4276 VAR. Fig. 4.93 (b) shows that reactive power required by IM load is -753.3 VAR. Fig. 4.93 (c) shows that VAR supplied by excitation capacitor is 3490 VAR. Fig. 4.93 (d) shows that VAR supplied by GIC changes from 1800 VAR to 1539 VAR. The GIC acts as an equivalent parallel combination of resistance and capacitance from time  $t=8$  s to  $t=9$  s.

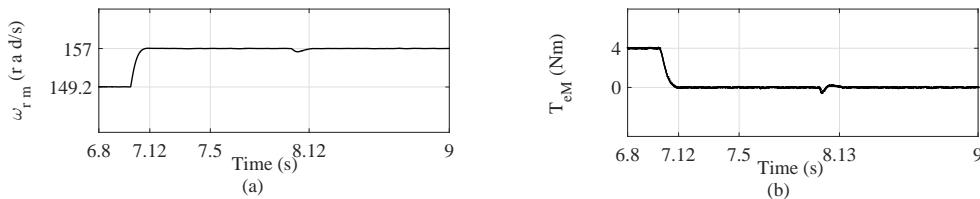


Figure 4.90: Simulation results showing speed and torque variation of IM load corresponding to wind speed 11.2 m/s (at  $t=7$  s) and 10.9 m/s (at  $t=8$  s): (a) IM speed (b) IM torque

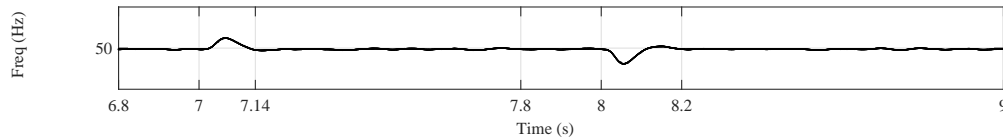


Figure 4.91: Simulation result showing SEIG frequency variation corresponding to wind speed 11.2 m/s (at  $t=7$  s) and 10.9 m/s (at  $t=8$  s) with IM load

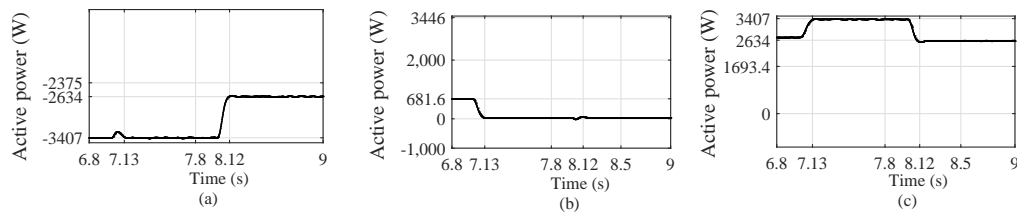


Figure 4.92: Simulation results showing active power variation corresponding to wind speed 11.2 m/s (at  $t=7$  s) and 10.9 m/s (at  $t=8$  s) with IM load: (a) SEIG (b) IM load (c) GIC

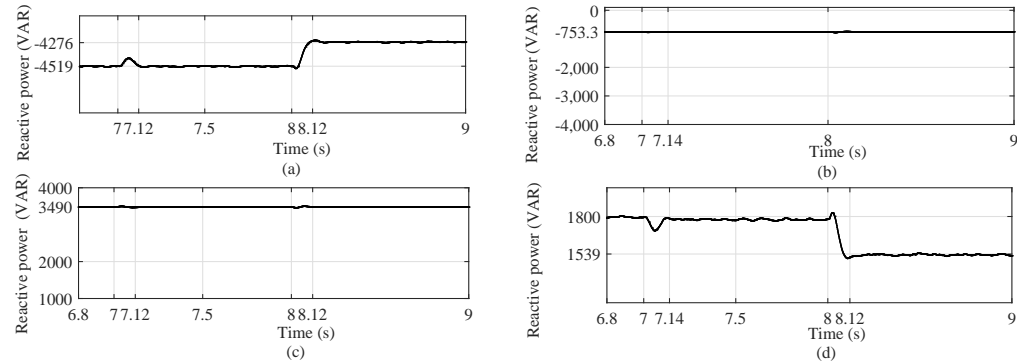


Figure 4.93: Simulation results showing reactive power variation corresponding to wind speed 11.2 m/s (at  $t=7$  s) and 10.9 m/s (at  $t=8$  s) with IM load: (a) SEIG (b) IM load (c) excitation capacitor (d) GIC

Stator current waveform of SEIG for the above simulation study is shown in Fig. 4.94 (a). At wind speed of 9.8 m/s and corresponding stator peak voltage of 586.8 V, stator peak current is 6.8 A. At  $t=1$  s, due to switching of the GIC, stator peak current is 6.8 A. At  $t=2$  s, wind speed increased from 9.8 m/s to 10.8 m/s thus increasing the mechanical power input and active power output of the generator. As the stator voltage of SEIG remains constant due to closed loop voltage control by GIC, the stator peak current increases from 6.8 A to 9.3 A. At  $t=3$  s and 4.5 s, switching of IM load with zero mechanical load and 4 Nm, respectively do not have any effect on stator line current due to healthy functioning of GIC. At  $t=6$  s, wind speed increased from 10.8 m/s to 11.2 m/s thus increasing the mechanical power input and active power output of SEIG. Corresponding to this, stator peak current increases from 9.3 A to 11 A. At  $t=7$  s, mechanical load of IM load is removed, do not have any effect on stator line current due to healthy functioning of GIC. At  $t=8$  s, wind speed decreased from 11.2 m/s to 10.9 m/s so stator current should also decrease from 11 A to 9.8 A.

Fig. 4.94 (b) shows the stator current of IM load. IM load is switched on at  $t=3$  s. Till

then stator current of IM was zero. At  $t=3$  s, due to switching of IM load peak of stator line current of IM increased from zero to 1.45 A. At  $t=5$  s, mechanical load of 4 Nm is applied across IM load due to this peak of stator line current of IM load increased from 1.45 A to 1.98 A. At  $t=7$  s, mechanical load is removed from IM load so stator current of IM load decreased to 1.45 A. After that there is no mechanical load change across IM load. So stator peak current of IM load remains constant at 1.48 A. The variation in SEIG stator current with wind speed variations is taken care by GIC and stator current of IM load is not affected by SEIG stator current changes.

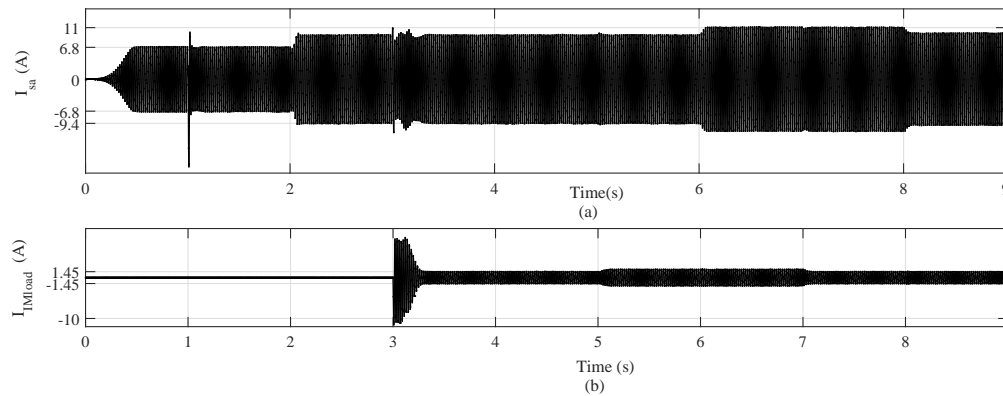


Figure 4.94: Simulation results of SEIG stator current and IM stator current waveforms of GIC based SEIG with IM loading and wind speed perturbations: (a) SEIG stator current (b) stator current of IM load

It is observed from the above simulation results that peak voltage amplitude and terminal frequency of SEIG maintains its rated value (using the computed optimal gains). It is possible due to integration of GIC with SEIG by maintaining active power balance without frequency feedback and by maintaining reactive power using voltage as feedback.

### 4.6.3 Harmonic analysis of optimized GIC based SEIG system

The performance of the optimized GIC based SEIG system is assessed through harmonic analysis. Total harmonic distortion (THD) of voltages and currents at both generator and load side are computed. Harmonic spectrum of SEIG stator voltage, stator current and load current of 2 kW are shown in Fig. 4.95 (a), (b), (c) and (d), respectively. Fig. 4.95 (a) and (b) show that THD of SEIG stator voltage and currents are 0.12% and 0.23%, respectively. Fig. 4.95 (c) and (d) show that THD of the resistive load voltage and current are 0.12% and 0.12%, respectively. Harmonic spectrum of SEIG stator voltage, stator current and IM stator voltage and IM stator current are shown in Fig. 4.96 (a), (b), (c) and (d), respectively.



Fig. 4.96 (a) and (b) show that THD of SEIG stator voltage and currents are 0.17% and 0.14%, respectively. Fig. 4.96 (c) and (d) show that THD of the IM stator voltage and stator current at no load condition are 0.2% and 0.15%, respectively. The THD value of these range are well below the limit of 5%, provided in the standard IEEE519. To show the effectiveness of the optimized GIC based SEIG system feeding  $R$  load and IM load, obtained THD values are compared with [1] and presented in Table 4.4 and Table 4.5, respectively .

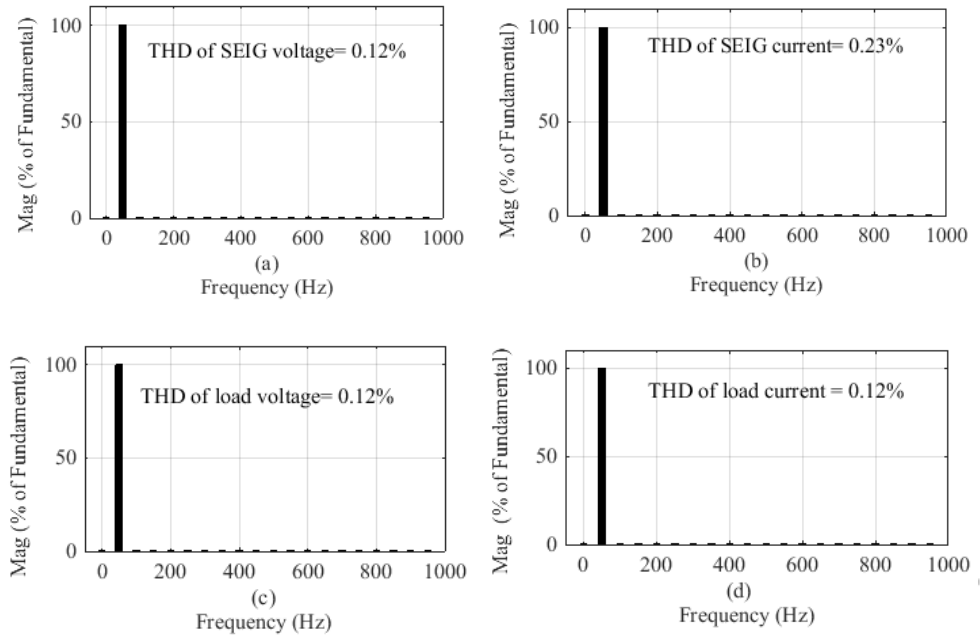


Figure 4.95: FFT analysis of optimized GIC based SEIG system feeding resistive load: (a) SEIG stator voltage (b) SEIG stator current (c) load voltage (d) load current

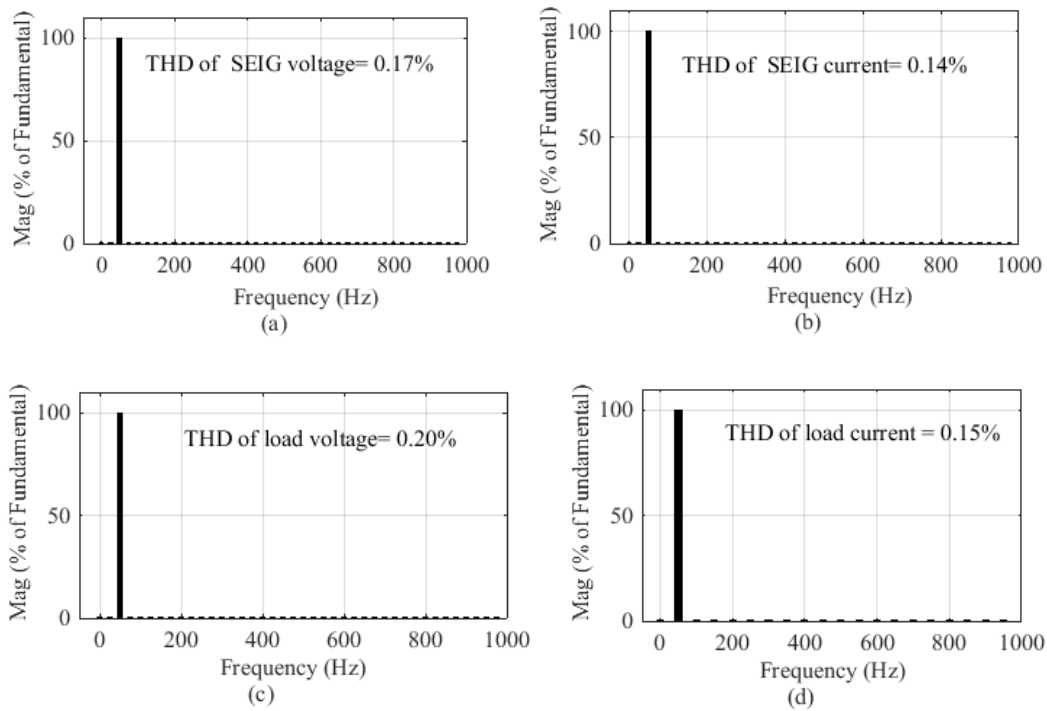


Figure 4.96: FFT analysis of optimized GIC based SEIG system feeding IM load: (a) SEIG stator voltage (b) SEIG stator current (c) IM stator voltage (d) IM stator current

Table 4.4: Total harmonic distortions comparison optimized GIC based SEIG system feeding resistive load with [1]

	SEIG		R load	
	voltage (%)	current (%)	voltage (%)	current (%)
optimized GIC based SEIG	0.12	0.23	0.12	0.12
Chauhan <i>et al</i>	0.79	1.61	2.17	2.17

Table 4.5: Total harmonic distortions comparison optimized GIC based SEIG system feeding IM load with [1]

	SEIG		IM load	
	voltage (%)	current (%)	voltage (%)	current (%)
optimized GIC based SEIG	0.17	0.14	0.2	0.15
Chauhan <i>et al</i>	0.10	0.63	0.82	0.68

## **4.7 Summary of the chapter**

In this chapter parameters of the Generalized Impedance Controller (GIC) based SEIG system are evaluated. SEIG system with GIC is developed by computing optimal values of proportional and integral gains within stable zone using PSO technique. Further, simulation is carried out to study its performance with wind speed variation, resistive and IM load. Performance of optimized GIC based SEIG system is assessed through harmonic analysis. Total Harmonic Distortion (THD) of voltages and currents at generator and load side are achieved within 0.23 %. It is observed that the proposed optimized GIC based SEIG system is able to maintain SEIG voltage and frequency during varied wind speed with resistive and IM load in isolated and remote areas.

# Chapter 5

## GIC based SEIG system using HT and CORDIC

### 5.1 Introduction

Intention of this chapter in the thesis is to develop simple and cost effective voltage controller for SEIG systems to be used in isolated and remote areas. In remote regions, micro- or mini-hydro and wind turbine based SEIG systems are being frequently used in off-grid mode. As described in the previous chapter, a simple voltage control scheme is being used for SEIG using generalized impedance controller (GIC) [35], [16] and [83]. In GIC based SEIG system, a single loop is used to control the voltage. In this scheme, SEIG frequency is controlled in open loop manner and follows GIC frequency which is set at the rated frequency of SEIG. The computation of instantaneous peak voltage plays a significant role in the voltage control scheme of GIC based SEIG system. In the aforesaid voltage controlled GIC based SEIG system conventional technique is used to compute peak where all the three terminal voltages of SEIG are required to be sensed. This conventional approach demands three sensors along with arithmetic functions such as square, sum, and square root. To make controller simple and cost effective a new technique is proposed in this chapter to compute peak voltage using only one sensor along with Hilbert Transform (HT) and CO-ordinate Rotation DIGital Computer (CORDIC). The computed voltage is then processed and employed by the GIC based SEIG system for controlling the SEIG voltage. To study the performance of proposed technique simulation is carried out in MATLAB/Simulink environment. Further, the proposed technique is implemented on commercially available TMS320F2812 Digital Signal Processor to carry out experiment for GIC based SEIG system.

In this chapter voltage control scheme of GIC based SEIG system using the proposed voltage computation technique is described in section 5.2. Section 5.3 describes results and discussion of this chapter followed by chapter summary.

## **5.2 Voltage control scheme of GIC based SEIG system using the proposed voltage computation technique**

As described in previous chapter that the peak voltage of SEIG is one feedback variable to the voltage controller. The computation of instantaneous peak voltage plays an important role in this control scheme which demands three sensors along with arithmetic functions such as square, sum, and square root. To make controller simple and cost effective a new technique is proposed to compute peak voltage using only one sensor along with Hilbert Transform (HT) and COordinate Rotation DIgital Computer (CORDIC) and described in the following subsection.

### **5.2.1 Computation of voltage and frequency of SEIG using HT and CORDIC**

The conventional approach to compute the peak voltage of SEIG [16] using the instantaneous three phase voltages is given as

$$v_m = \sqrt{\frac{2}{3}(v_a^2 + v_b^2 + v_c^2)} \quad (5.1)$$

With reference to Fig. 4.1 of previous chapter and the expression (5.1), the conventional approach demands three voltage sensors to measure three phase voltages and the arithmetic blocks to perform square, addition and square root to compute the peak voltage. A conventional technique given in [84] and shown in Fig. 5.1 is used to compute the peak voltage ( $v_m$ ) using only one voltage sensor by measuring phase voltage  $v_m \sin(\omega t)$  as follows,

$$v_m = \sqrt{(v_m \sin(\omega t))^2 + (v_m \sin(\omega t + 90^\circ))^2} \quad (5.2)$$

However, this technique requires the  $90^\circ$  phase shifter along with arithmetic operators for performing square, addition and square root as well. Hence, as an alternative to the conventional approach the technique proposed here and shown in Fig. 5.2 employs Hilbert transform for shifting phase by  $90^\circ$  along with a single CORDIC to perform the quadratic arithmetic operations mentioned above. Hilbert transform and CORDIC algorithm along

with their use for the computation of peak voltage as given in (5.2) are highlighted in subsequent subsections.

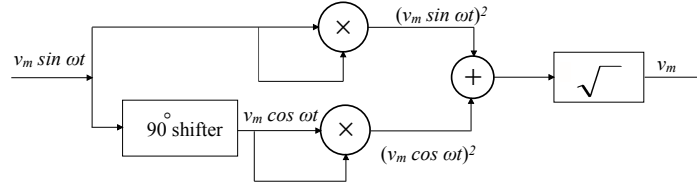


Figure 5.1: Block diagram of the conventional peak voltage computation technique

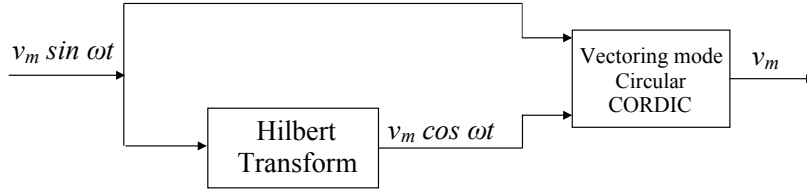


Figure 5.2: Block diagram of the proposed peak voltage computation technique using HT and CORDIC

**(a) Hilbert Transform (HT):** Performing Hilbert transform (HT) [85] is equivalent to passing the signal  $x(t)$  through an all pass filter, *i.e.* the magnitude of the spectral components remains unchanged but their phases are shifted by  $90^\circ$ . This property of HT is used here to shift the phase of the signal by  $90^\circ$ .

For a sinusoidal voltage signal  $x(t) = v_m \sin \omega t$ , corresponding HT of  $x(t)$  is  $y(t) = v_m \cos \omega t$  as presented in the proposed technique shown in Fig. 5.2. Thus, the peak voltage, ( $v_m$ ) can be computed using the input signal  $x(t)$  and its HT, *i.e.*,  $y(t)$  as follows.

$$v_m = \sqrt{[x(t)]^2 + [y(t)]^2} \quad (5.3)$$

For the digital implementation of (5.3), the generalized discrete Hilbert-transform (DHT) [86] is briefly highlighted here for the signal  $x(hT)$ , where  $h = (-q, \dots, -1, 0, 1, \dots, q)$ , where  $q \rightarrow 1024$ . The discrete Hilbert transform,  $y(kT)$  of the signal  $x(hT)$  is computed as follows [86].

$$DHT[x(hT)] = y(kT) = \begin{cases} \frac{2}{\pi} \sum_{h=odd}^q \frac{x(hT)}{k-h}; k \text{ even} \\ \frac{2}{\pi} \sum_{h=even}^q \frac{x(hT)}{k-h}; k \text{ odd} \end{cases} \quad (5.4)$$

Thus,  $x(hT)$  and  $y(kT)$  are used to compute the peak voltage,  $v_m$  using a hardware efficient arithmetic unit, *i.e.*, CORDIC described in the following subsection.

**(b) COordinate Rotation Digital Computer (CORDIC) algorithm:** Real time digital signal processing applications demand the efficient computation of coordinate transformations or vector rotations which are naturally involved with DSP algorithms. Many DSP algorithms require the evaluation of trigonometric functions and multiplications that can not be evaluated efficiently with multiply-accumulate (MAC)-based units. As an alternative, COordinate Rotation Digital Computer (CORDIC) has received renewed attention, as it offers an iterative formulation to evaluate each of these trigonometric functions efficiently. In this chapter CORDIC algorithm is presented starting from the basic philosophy to different modes of operations to compute various trigonometric functions.

The CORDIC algorithm was introduced by Volder [87] for computation of trigonometric functions in navigation problems. Walther [88] realized an unified CORDIC algorithm for computation of various trigonometric functions (such as sine, cosine, tangent and their inverses). CORDIC algorithm is essentially an iterative method to compute rotation of two dimensional vectors. The generalized rotational expression for vectors *i.e.*, initial vector  $(x, y)$  and final rotated vector  $(x', y')$  can be derived for the arbitrary rotation angle of  $\phi$  from the Fig. 5.3 and expressed as follows.

$$\begin{aligned} x' &= V \cos(\phi + \phi_1) \\ y' &= V \sin(\phi + \phi_1) \end{aligned} \quad (5.5)$$

$$\begin{aligned} x' &= V \cos\phi \cos\phi_1 - V \sin\phi \sin\phi_1 \\ y' &= V \sin\phi \cos\phi_1 + V \cos\phi \sin\phi_1 \end{aligned} \quad (5.6)$$

The above expression is further simplified by substituting  $(V \cos\phi_1 = x)$  and  $(V \sin\phi_1 = y)$  and given in (5.7).

$$\begin{aligned} x' &= x \cos\phi - y \sin\phi \\ y' &= x \sin\phi + y \cos\phi \end{aligned} \quad (5.7)$$

In matrix form, the vector rotation can now be expressed by (5.8).

$$\begin{bmatrix} x' \\ y' \end{bmatrix} = \begin{bmatrix} \cos\phi & -\sin\phi \\ \sin\phi & \cos\phi \end{bmatrix} \begin{bmatrix} x \\ y \end{bmatrix} \quad (5.8)$$

Instead of performing the rotation of the vector for arbitrary target angle  $\phi$  (where  $-\frac{\pi}{2} \leq \phi \leq \frac{\pi}{2}$ ) in one step, the desired angle of rotation can be obtained by performing a series of successive  $n$ -rotations [89] by micro-angles as expressed in (5.9).

$$\phi = \pm\alpha_0 \pm \alpha_1 \pm \dots \pm \alpha_i \dots \pm \alpha_{n-1} \quad (5.9)$$

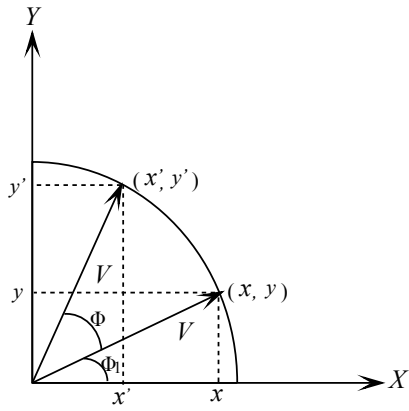


Figure 5.3: Rotation of vector on a two dimensional plane

Expression (5.9) can also be written as

$$\phi = \sum_{i=0}^{n-1} \sigma_i \alpha_i \quad (5.10)$$

where

$$\alpha_i = \tan^{-1}(2^{-i}) \quad (5.11)$$

and

$$\sigma_i \in \{1, -1\} \quad (5.12)$$

$i$  varies from 0 to  $n - 1$  and the number of rotations ( $n$ ) depends on the word length of the processor. The signs  $\sigma_i$  of the elementary angles are chosen such that the total angle will be equal to  $\phi$ . For convenience, values of the elementary angles  $\alpha_i$  for  $i = 0$  to 15 are provided in the Table.5.1.

For better understanding, rotation of vector is presented in Fig. 5.4 and illustrated briefly here.  $\phi$  taken in this figure is  $0 < \phi < 45^\circ$ . At  $i = 0$ ,  $\alpha_i = 45^\circ$  so, in the first step vector is rotated anti clock-wise by  $45^\circ$  to achieve the target angle. Then the residue angle ( $\phi - 45^\circ$ ) is computed which is negative. This makes  $\sigma_i = -1$ . In the second rotation  $i = 1$ ,  $\sigma_i = -1$ ,  $\alpha_i = 26.56^\circ$ . So the vector is rotated clock-wise by  $26.56^\circ$  and residue angle ( $\phi - 45^\circ + 26.56^\circ$ ) is computed. This process continues till target angle  $\phi$  is achieved or residue angle is equal or closely equal to zero.



Table 5.1: Values of the elementary angles  $\alpha_i$  for  $i = 0$  to 15

$i$	$\tan^{-1}(2^{-i})$	$\alpha_i$
0	$\tan^{-1}(1)$	$45^\circ$
1	$\tan^{-1}(1/2)$	$26.56^\circ$
2	$\tan^{-1}(1/4)$	$14.036^\circ$
3	$\tan^{-1}(1/8)$	$7.125^\circ$
4	$\tan^{-1}(1/16)$	$3.576^\circ$
5	$\tan^{-1}(1/32)$	$1.79^\circ$
6	$\tan^{-1}(1/64)$	$0.895^\circ$
7	$\tan^{-1}(1/128)$	$0.448^\circ$
8	$\tan^{-1}(1/256)$	$0.224^\circ$
9	$\tan^{-1}(1/512)$	$0.112^\circ$
10	$\tan^{-1}(1/1024)$	$0.0559^\circ$
11	$\tan^{-1}(1/2048)$	$0.0279^\circ$
12	$\tan^{-1}(1/4096)$	$.01398^\circ$
13	$\tan^{-1}(1/8192)$	$0.0069^\circ$
14	$\tan^{-1}(1/16384)$	$0.0034^\circ$
15	$\tan^{-1}(1/32768)$	$0.0017^\circ$

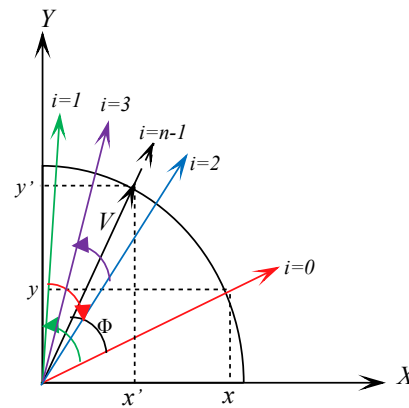


Figure 5.4: Rotation of vector on a two dimensional plane performing a series of successive  $n$ -rotations

Using additive property of rotating matrix presented in Appendix B and equation (5.9), the rotation equation matrix (5.8) is expressed as follows.

$$\begin{aligned} \begin{bmatrix} x' \\ y' \end{bmatrix} &= \begin{bmatrix} \cos\alpha_0 & \mp\sin\alpha_0 \\ \pm\sin\alpha_0 & \cos\alpha_0 \end{bmatrix} \begin{bmatrix} \cos\alpha_1 & \mp\sin\alpha_1 \\ \pm\sin\alpha_1 & \cos\alpha_1 \end{bmatrix} \\ \dots \begin{bmatrix} \cos\alpha_i & \mp\sin\alpha_i \\ \pm\sin\alpha_i & \cos\alpha_i \end{bmatrix} \dots \begin{bmatrix} \cos\alpha_{n-1} & \mp\sin\alpha_{n-1} \\ \pm\sin\alpha_{n-1} & \cos\alpha_{n-1} \end{bmatrix} \begin{bmatrix} x \\ y \end{bmatrix} \end{aligned} \quad (5.13)$$

Factorizing equation(5.13) leads to the following equation:

$$\begin{aligned} \begin{bmatrix} x' \\ y' \end{bmatrix} &= \cos\alpha_0 \cos\alpha_1 \dots \cos\alpha_{n-1} \begin{bmatrix} 1 & \mp\tan\alpha_0 \\ \pm\tan\alpha_0 & 1 \end{bmatrix} \begin{bmatrix} 1 & \mp\tan\alpha_1 \\ \pm\tan\alpha_1 & 1 \end{bmatrix} \\ \dots \begin{bmatrix} 1 & \mp\tan\alpha_i \\ \pm\tan\alpha_i & 1 \end{bmatrix} \dots \begin{bmatrix} 1 & \mp\tan\alpha_{n-1} \\ \pm\tan\alpha_{n-1} & 1 \end{bmatrix} \begin{bmatrix} x \\ y \end{bmatrix} \end{aligned} \quad (5.14)$$

Using equation (5.11), equation (5.14) can be rewritten as

$$\begin{aligned} \begin{bmatrix} x' \\ y' \end{bmatrix} &= \prod_{i=0}^{n-1} \cos\alpha_i \begin{bmatrix} 1 & \mp 2^0 \\ \pm 2^0 & 1 \end{bmatrix} \begin{bmatrix} 1 & \mp 2^{-1} \\ \pm 2^{-1} & 1 \end{bmatrix} \\ \dots \begin{bmatrix} 1 & \mp 2^{-i} \\ \pm 2^{-i} & 1 \end{bmatrix} \dots \begin{bmatrix} 1 & \mp 2^{-(n-1)} \\ \pm 2^{-(n-1)} & 1 \end{bmatrix} \begin{bmatrix} x \\ y \end{bmatrix} \end{aligned} \quad (5.15)$$

In ,  $\prod_{i=0}^{n-1} \cos\alpha_i$  is known as scale factor ( $K_n$ ) and its reciprocal is known as amplification factor ( $A_n$ ). In practice, the matrix operations as depicted in equation (5.2.1) are carried out from left to right (*i.e.*, from  $i = 0$  through  $n - 1$ ). In each step, the sign of the corresponding elementary angle is determined by the sign of the instantaneous error, *i.e.*, residue angle defined as the difference between the desired (target) angle and the already achieved angle given as follows.

$$\text{sign}(\alpha_i) = \text{sign} \left[ \phi - \sum_{rot=0}^{i-1} \alpha_{rot} \right] \quad (5.16)$$

The target angle is reached through the forward and backward motion of the vector. The vector is rotated either clockwise or counterclockwise depending upon the sign of instantaneous error as given by the right-hand side of equation (5.16). From equation (5.16), an equation can be introduced for the residue angle given as follows.

$$z_{i+1} = z_i \mp \alpha_i \quad (5.17)$$

Ignoring the scale factor ( $K_n$ ) from equation (5.2.1) a set of iterative equations using (5.2.1) and (5.17) can be written as follows.

$$\begin{aligned}x_{i+1} &= x_i - \sigma_i y_i 2^{-i} \\y_{i+1} &= y_i + \sigma_i x_i 2^{-i} \\z_{i+1} &= z_i - \sigma_i \alpha_i\end{aligned}\quad (5.18)$$

Thus, the iterative equation (5.18) can be used to compute trigonometric and elementary functions in few iterative steps (equal to word size) using different modes such as rotating and vectoring modes which are described as follows.

**(i) Rotating mode:** In this mode, the desired rotation angle ( $\phi$ ) is given for an input vector  $(x, y)$ , and by setting  $x_0 = x$ ,  $y_0 = y$ ,  $z_0 = \phi$ . After  $n$  iterations, rotating angle variable  $z_n$  becomes

$$z_n = \phi - \sum_{i=0}^{n-1} \sigma_i \alpha_i \quad (5.19)$$

when  $\phi = \sum_{i=0}^{n-1} \sigma_i \alpha_i$ , i.e., the total accumulated rotation angle is equal to  $\phi$ , then  $z_n$  becomes or tends to zero ( $z_n \rightarrow 0$ ). In order to drive  $z_n$  to zero,  $\sigma_i = \text{sign}(z_i)$  is used leading to the following set of equations:

$$\begin{aligned}x_{i+1} &= x_i - \text{sign}(z_i) y_i 2^{-i} \\y_{i+1} &= y_i + \text{sign}(z_i) x_i 2^{-i} \\z_{i+1} &= z_i - \text{sign}(z_i) \alpha_i\end{aligned}\quad (5.20)$$

Here  $i = 0$  to  $n - 1$  and the finally rotated vector is given by  $(x_n, y_n)$ .

To elaborate this rotating mode of CORDIC iterative equation, consider the following example. The initial vector  $(x_0, y_0) = (x, 0)$  rotates to achieve the target angle  $z_0 = \phi$ . The final values after  $n$  iterations becomes as follows.

$$\begin{aligned}x_n &= K_n x \cos \phi \\y_n &= K_n x \sin \phi \\z_n &= 0\end{aligned}\quad (5.21)$$

If  $(x_0, y_0) = (1, 0)$ , then  $x_n = K_n \cos \phi$  and  $y_n = K_n \sin \phi$  and  $z_n = 0$ .  $K_n = \prod_{i=0}^{n-1} \frac{1}{\sqrt{1 + 2^{-2i}}} \approx 0.6073$  (for  $n = 16$  iterations) which is constant and can be used as scale factor. The final

vector can be achieved by pre- or post- multiplication of this constant factor.

**(ii) Vectoring mode:** In this mode, the objective is to rotate the given input vector  $(x, y)$  with magnitude  $\sqrt{x^2 + y^2}$  and angle  $\phi = \tan^{-1} \left( \frac{y}{x} \right)$  towards the  $x$ -axis. Vectoring mode is performed by setting  $x_0 = x$ , and  $y_0 = y$  and  $z_0 = 0$ . Here the rotating scheme is such that, during  $n$ - rotations  $y_n$  is driven to zero with  $\sigma_i = -\text{sign}(y_i)$ . When  $y_n$  results zero,  $z_n$  equal to total accumulated rotation angle after  $n$ - iterations, which is given by the equation (5.22).

$$z_n = \sum_{i=0}^{n-1} \sigma_i \alpha_i \quad (5.22)$$

The final value  $(x_n)$  is the scaled magnitude of the input vector  $(x, y)$ , i.e.,  $x_n = K_n \sqrt{x^2 + y^2}$ . Now the CORDIC iteration driving the  $y_i$  variable to zero is given by the equation (5.23).

$$\begin{aligned} x_{i+1} &= x_i - \text{sign}(y_i) y_i 2^{-i} \\ y_{i+1} &= y_i + \text{sign}(y_i) x_i 2^{-i} \\ z_{i+1} &= z_i - \text{sign}(y_i) \alpha_i \end{aligned} \quad (5.23)$$

Trigonometric and elementary factors computed using two modes (rotating and vectoring) of CORDIC are summarized in the Table .5.2.

Table 5.2: Elementary functions using CORDIC algorithm

mode	Initialization	final output
rotation	$x_0 = x$	$x_n = K_n \cdot (x \cos \phi - y \sin \phi)$
	$y_0 = y$	$y_n = K_n \cdot (y \cos \phi + x \sin \phi)$
	$z_0 = \phi$	$z_n = 0$
vectoring	$x_0 = x$	$x_n = K_n \sqrt{x^2 + y^2}$
	$y_0 = y$	$y_n = 0$
	$z_0 = 0$	$z_n = \phi$

Using obtained  $\theta$  instantaneous frequency ( $f_p$ ) at  $p^{\text{th}}$  instant of time is computed as follows.

$$f_p = \frac{\Delta \phi_p - \Delta \phi_{p-1}}{\Delta t} \quad (5.24)$$

where  $\Delta t$  being the time difference between two consecutive phases (samples) is the sam-

pling time. By putting  $\Delta t = 1$ ,  $f_p = \Delta\phi_p - \Delta\phi_{p-1}$ . Next subsection describes the implementation of proposed computation scheme.

## 5.2.2 Implementation of voltage controller of GIC based SEIG system using proposed voltage computation technique

Fig. 5.5 shows the schematic diagram of proposed GIC based voltage controlled SEIG system using HT and CORDIC algorithm. SEIG voltage is sensed using one sensor as shown in Fig. 5.5. Then, peak voltage of SEIG is computed using the proposed technique employing HT and CORDIC algorithm. Computed peak voltage is compared with the reference peak voltage and the error passed to the *PI* controller. The output of the *PI* is the modulation index ( $m$ ). *PI* is considered for maintaining terminal voltage, because of its simplicity, good performance, fast response and zero steady-state error. The *PI* is described as follows.

$$y(t) = k_p \varepsilon(t) + k_i \int_0^t \varepsilon(t) dt \quad (5.25)$$

where  $y(t) = m$ .  $\varepsilon(t)$  is the voltage error ( $\varepsilon(t) = v_{mref}(t) - v_m(t)$ ).  $v_{mref}(t)$  is the SEIG rated peak voltage.  $v_m(t)$  is the computed peak voltage of SEIG.  $k_p$  and  $k_i$  are the optimized proportional gain and integral gain, respectively of the *PI*. Computation of these gains is already described in the previous chapter. The *PI* maintains the terminal voltage of SEIG at the rated value using the proposed computed peak voltage. The output of *PI* is multiplied with sine wave of unit amplitude and reference frequency, and then compared with carrier wave to obtain switching signals  $S_a, S_b, S_c, \overline{S}_a, \overline{S}_b, \overline{S}_c$  of VSI for providing gate drives to IGBTs. Next section describes the simulation and experimental results and discussion of voltage regulated GIC based SEIG system using the proposed peak computation technique.

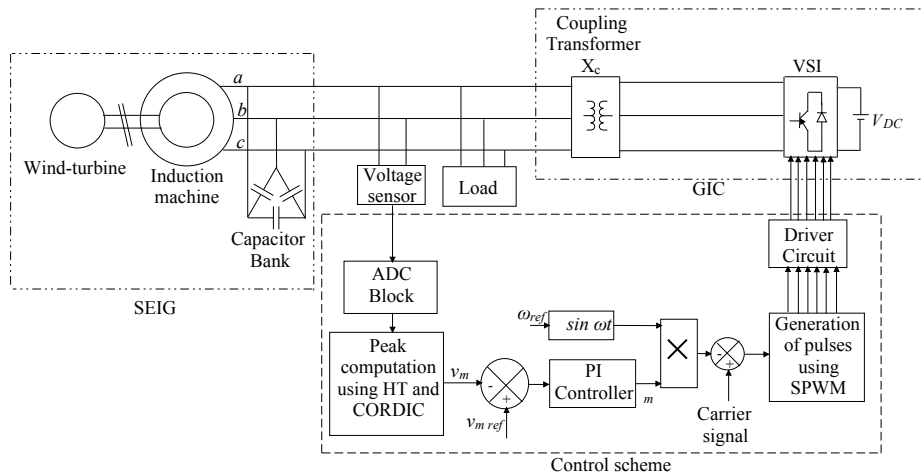


Figure 5.5: Schematic diagram of the proposed GIC based voltage controlled SEIG system using HT and CORDIC algorithm

### 5.3 Results and Discussion

Simulation is carried out in MATLAB/Simulink environment to implement the proposed peak voltage and frequency computation technique using Hilbert transform along with vectoring mode CORDIC algorithm. For this purpose, a time-varying sinusoidal voltage signal is considered as follows.

$$v(t) = v_m \sin \omega t \quad (5.26)$$

where  $v_m$ =peak of the voltage signal,  $\omega = 2 * \pi * f$ . Fig. 5.6 (a) shows a voltage signal with varying amplitude and frequency. The voltage signal consists: (i) peak amplitude of 1 V with frequency 50 Hz from  $t=0$  s to  $t=0.8$  s, (ii) peak amplitude of 0.8 V with 40 Hz from  $t=0.8$  s to  $t=1.6$  s (iii) peak amplitude of 1.5 V with 30 Hz from  $t=1.6$  s to  $t=2.2$  (iv) peak amplitude of 0.8 V with 30 Hz from  $t=2.2$  s to  $t=3.5$  s (v) peak amplitude of 1.2 V with 60 Hz from  $t=3.5$  s to  $t=3.8$  s as seen in Fig. 5.6 (a). HT and CORDIC is applied on the varying voltage signal to compute peak voltage and frequency. Fig. 5.6 (b) and Fig. 5.6 (c) show the computed peak voltage and instantaneous frequency using the proposed technique. Computed peak voltage of the varying voltage as seen in Fig. 5.6 (b) are: 1 V from  $t=0$  s to  $t=0.8$ s, 0.8 V from  $t=0.8$  s to  $t=1.6$  s, 1.5 V from  $t=1.6$  s to  $t=2.2$ , 0.8 V from  $t=2.2$  s to  $t=3.5$  s and 1.2 V from  $t=3.5$  s to  $t=3.8$  s. Similarly, computed instantaneous frequency of varying voltage as seen in Fig. 5.6 (c) are: 50 Hz from  $t=0$  s to  $t=0.8$  s, 40 Hz from  $t=0.8$  s to  $t=1.6$  s, 30 Hz from  $t=1.6$  s to  $t=3.5$ , and 60 Hz from  $t=3.5$  s to  $t=3.8$  s.

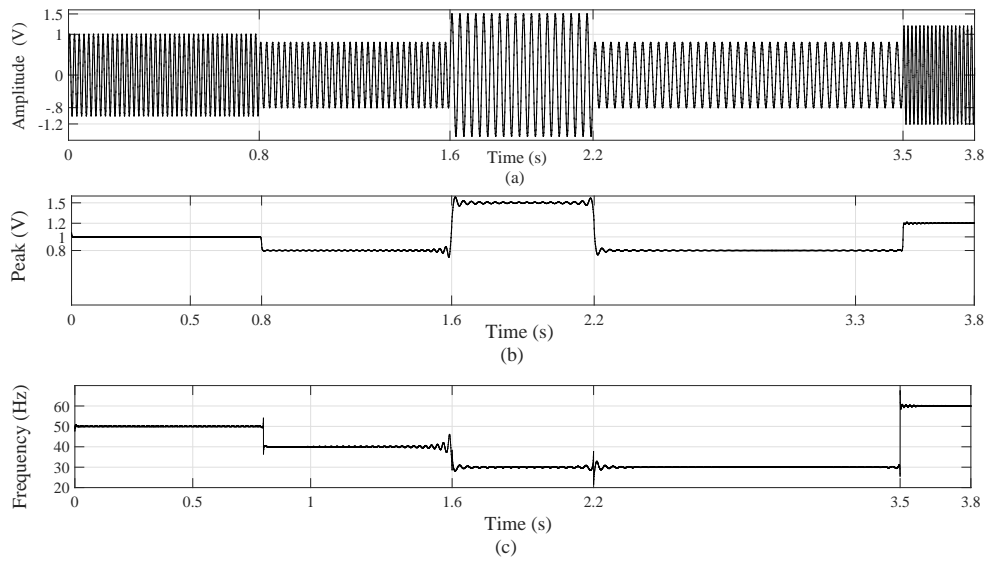


Figure 5.6: Simulation results to test the proposed amplitude and frequency estimation technique: (a) Voltage signal with varying amplitude and frequency (b) Computed voltage amplitude using proposed technique (c) Computed frequency using proposed technique.

The proposed peak voltage computation technique is implemented on SEIG with varied prime mover speed and load. As described in previous chapter GIC is integrated with SEIG to control voltage with varied prime mover speed and load. To maintain rated voltage and frequency of SEIG, GIC is connected at  $t=0.6$  s across the SEIG terminals in such a manner that GIC and SEIG output voltages have the same fundamental frequency and voltage. This condition is set by keeping angle  $\delta$  between both the voltages is  $0.0^\circ$  and by output variable (critical modulation index,  $m$ ) of PI controller. Corresponding to this condition simulation result of the proposed peak voltage computation technique with one voltage sensor and conventional technique with multi sensors is presented in Fig. 5.7. At  $t=0.85$  s prime mover speed is increased from 1500 r.p.m to 1580 r.p.m. For this reason, SEIG terminal frequency is suddenly increased for a moment due to the increase of shaft power. Corresponding to this, the phase angle  $\delta$  is increased in a negative direction as described in previous chapter. Due to this active power is absorbed by GIC from SEIG for matching SEIG frequency with GIC frequency. Due to active power absorbed by the GIC, the SEIG stator voltage is deviated from the rated value of 586.8 V for a moment as seen in Fig. 5.7. But due to voltage feedback in the closed loop, the PI controller changed modulation index,  $m$  and maintained SEIG voltage as presented in Fig. 5.7. At  $t=1.1$  s a balanced resistive load of  $100 \Omega/\text{phase}$  is switched on across the SEIG terminals. SEIG terminal frequency is decreased for a moment due to active power absorbed by the load. As a result, active power is provided by GIC. Finally, active power provided by SEIG is the

sum of active power absorbed by load and GIC. As a result, SEIG frequency matches with GIC frequency. Corresponding to this load switching, the SEIG stator voltage is deviated from the rated value of 586.8 V for a moment as seen in Fig. 5.7 and comes back to rated voltage of 586.8 V as seen in Fig. 5.7. Hence, proposed peak voltage computation is able to maintain SEIG voltage with varied prime mover speed and load switching.

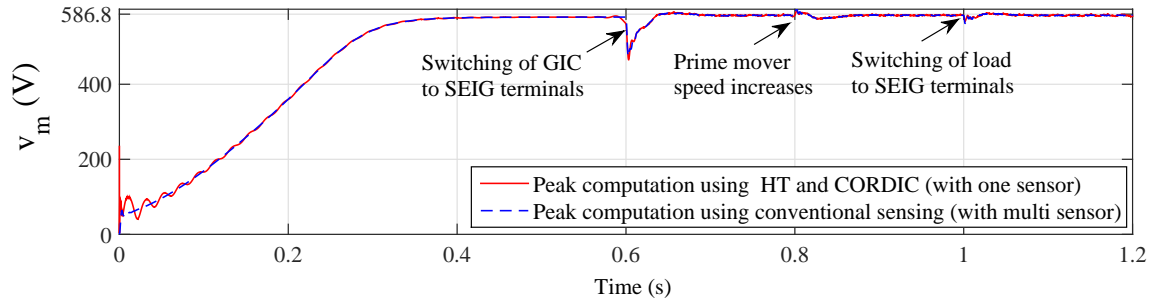


Figure 5.7: Simulation result of peak voltage computation of SEIG during speed and load perturbations in closed loop using two different peak computation techniques.

The proposed technique is implemented on commercially available TMS320F2812 Digital Signal Processor to carry out experiment for GIC based SEIG system. Schematic diagram for the control circuit to implement the proposed control scheme of SEIG system is shown in Fig. 5.8. The clock frequency of the processor is 150 MHz. This processor contains useful peripherals such as ADC, DAC, Timer and PWM generation block. The resolution of sixteen channel on chip ADC is 12-bit. The input voltage range of this ADC is 0 to 3 V with the sampling rate of 0.0001.

Hall effect voltage sensor is used to sense the SEIG terminal voltage and scale it down to the range of 0 to 3 V (*i.e.* the range of ADC input voltage). Voltage sensor output is first processed by ADC interfacing card and further fed as an input to the on-chip ADC of DSP processor as shown in Fig. 5.8. Hardware set up to implement the proposed technique using TMS320F2812 DSP processor is shown in Fig. 5.9.

The peak voltage of SEIG is computed in the processor. The computed peak is compared with reference voltage and error sent to the PI controller.  $k_p$  and  $k_i$  values obtained from PSO are set in the PI controller using 2812 DSP processor. The output of the PI controller is the modulation index ( $m$ ). The  $m$  is multiplied with the unit sin wave whose frequency is set at 50 Hz. Then the modulating signals are sent to PWM block of the processor. The PWM block contains a self-symmetric carrier triangular wave whose frequency is set at 10 kHz. Modulating signals are compared with carrier wave and pulses are generated.



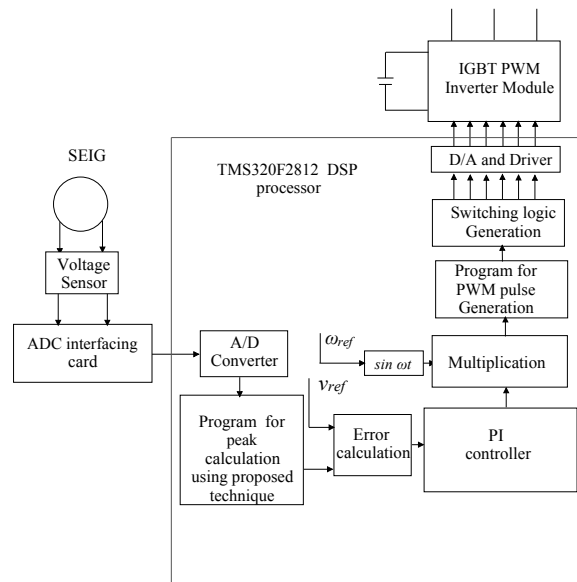


Figure 5.8: Schematic diagram of the control circuit to implement the proposed control scheme.

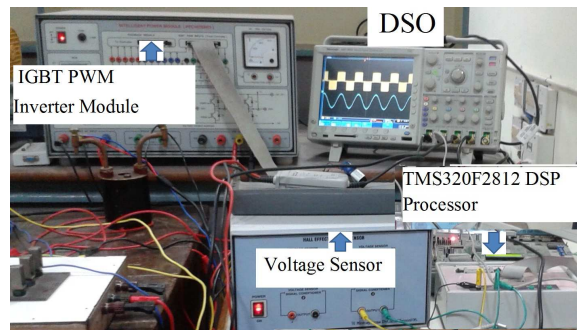


Figure 5.9: Experimental set up to implement the proposed technique using TMS320F2812 DSP processor

Fig. 5.10 (a) shows four gate pulses of PWM block using TMS320F2812 DSP processor with a dead time of  $6 \mu s$ . Scale taken for this figure to represent x-axis and y-axis are  $20 \mu s/div$  and  $2 v/div$ , respectively. Six pulses generated from the PWM block using processor are given to the six IGBT switches of the intelligent power module PEC16DSM01 through the connector provided on the front panel. Fig. 5.10 (b) shows the waveform of the line voltage of GIC and SEIG during synchronization of GIC with SEIG. Scale taken for for this figure to represent x-axis is  $10 ms/div$ . Scale taken to represent y-axis are  $600 V/div$  for GIC and  $5 V/div$  for SEIG, respectively. It is observed from Fig. 5.10 (b) that angle between SEIG and GIC *i.e.*  $\delta = 0^\circ$  to make the exchange of active power flow zero between them.

For matching the SEIG output voltage with GIC at no load,  $m =$  is set at 0.73 to make the exchange of reactive power zero. Fig. 5.10 (c) shows the waveform of the line voltage of GIC (filtered) and SEIG after synchronization of GIC with SEIG.

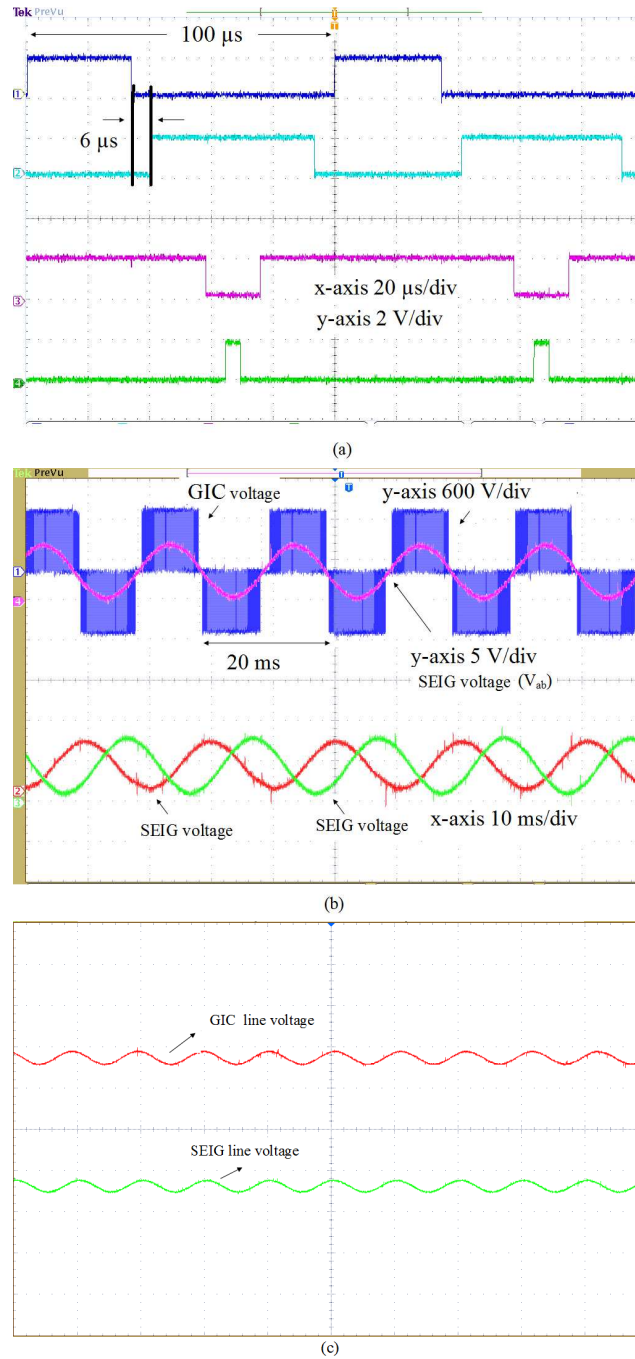


Figure 5.10: Experimental results (a) Generation of pulses (b) Wave form of line voltage of GIC and SEIG during synchronization of GIC with SEIG (c) Wave form of line voltage of GIC (filtered) and SEIG after synchronization of GIC with SEIG

Fig. 5.11 shows the captured experimental photograph of GIC integration with SEIG using DSP processor. After successful integration of GIC with SEIG, a load of  $100 \Omega/\text{phase}$  is connected across it. Fig. 5.12 shows the experimental waveforms of SEIG line voltage, line current and load line current during GIC and load switching in the closed loop using the proposed technique. Fig. 5.12 has two windows *i.e.*, bottom and top where bottom window is the zoomed version of top window. Each window has three waveforms (SEIG line voltage, stator line current and load current). It is observed that when the load connected with GIC based SEIG system SEIG voltage changed for a fraction of a period during the load switching only and comes to the rated voltage in steady state. Load peak line current obtained at steady-state is 3.9 A. It is observed from the open loop experimental results of chapter 3 that SEIG voltage decreases with the load. But it is observed from the closed loop experimental results of Fig. 5.12 that the proposed control technique has the capability to maintain SEIG voltage and frequency during load switching.

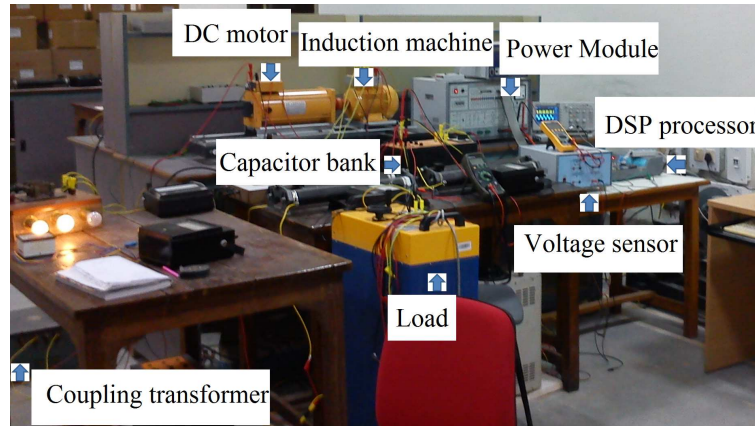


Figure 5.11: Captured experimental photograph of GIC integration with SEIG using TMS320F2812 DSP processor

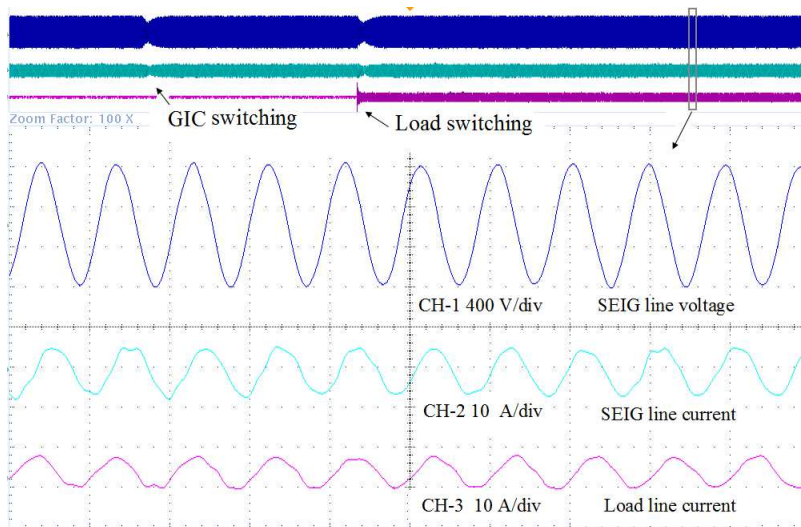


Figure 5.12: Experimental waveforms of SEIG line voltage, line current and load line current during GIC and load switching in closed loop using proposed technique.

## 5.4 Summary of the chapter

A cost effective peak voltage computation technique for SEIG using Hilbert transform and COordinate Rotation DIgital Computer using one voltage sensor is proposed. Simulation is carried out to implement the proposed voltage computation technique in MATLAB/Simulink environment. Closed loop simulation results of SEIG peak voltage of GIC based SEIG system using proposed technique is presented during prime mover speed variations and load switching. Experiment is also carried out for SEIG using the proposed computation technique to control voltage during load switching.

# Chapter 6

## Fault analysis of SEIG system

### 6.1 Introduction

Similar to voltage and frequency control issues fault analysis and detection of SEIG system are also very challenging issues in remote and isolated areas. Voltage collapse and de-excitation occurs in SEIG during three phase short circuit, line-to-line fault, and single phase capacitor opening and these faults develop excessive high torque [12]. Torque pulsation also occurs due to single line opening at SEIG load. Excessive high torque and sustained vibration torque are extremely dangerous for SEIG leading to increased maintenance cost and risk of shaft failure [12]. Time taken to re-excite the SEIG depends upon saturation level, excitation capacitance, discharge time, type of fault and duration of fault [13]. If the fault is detected and cleared before the excitation decays to zero, time takes to re-excite the SEIG reduces. So it is realized that transient analysis of SEIG is essential to know the transient magnitude and duration of voltage, current and torque of SEIG during these fault cases. Fault detection and classification are important to reduce maintenance cost and risk of shaft failure. This chapter first presents the transient performance analysis of SEIG during both balanced and unbalanced faults using stationary frame. Then significance of fault detection and fault classification are also investigated in this chapter. Due to the importance of SEIG fault analysis, to classify them, features of SEIG voltage signals are extracted with the help of Empirical Mode Decomposition (EMD) and Hilbert Transform (HT). The combination of EMD and HT is defined as Hilbert Huang transform (HHT). Extracted features obtained from HHT are then fed to the different classifiers to classify different types of SEIG faults. Different classification techniques such as MultiLayer Perceptron (MLP) neural network, Probabilistic Neural Network (PNN), Support Vector Machine (SVM), and Least Square Support Vector Machine (LS-SVM) are used in this chapter.

Section 6.2 presents transient performance analysis of SEIG during balanced and unbalanced faults. Section 6.3 describes Hilbert Huang Transform (HHT). Section 6.4 presents feature extraction using Hilbert Huang Transform (HHT). Section 6.5 describes fault classification methods using MLP, PNN, SVM and LS-SVM. Results and discussion are presented in section 6.6 followed by chapter summary.

## 6.2 Transient performance analysis of SEIG during balanced and unbalanced faults

In chapter 3 mathematical model of SEIG system is developed and validated through simulation and experimental results. The developed SEIG model is used in this chapter to investigate balanced and unbalanced terminal conditions including different type of faults. Fig. 6.1 shows the schematic diagram of SEIG system with a load connected across it. Different type of faults (balanced and unbalanced) are considered across SEIG and described in following subsection.

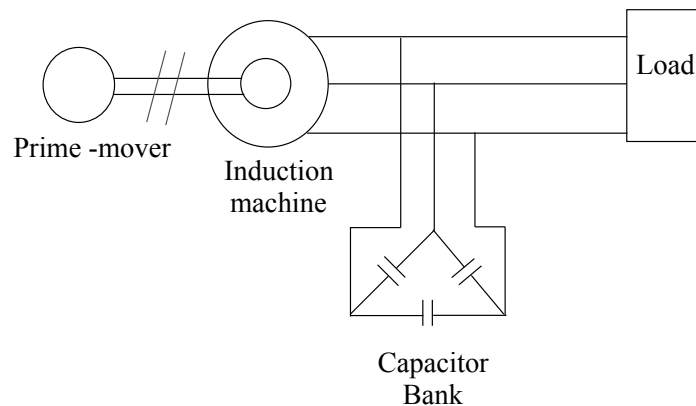


Figure 6.1: Diagram of SEIG system

### 6.2.1 Three phase short circuit across SEIG

Fig. 6.2 shows the diagram of SEIG system with a three phase short circuit across it. Initially, the SEIG is operated with an excitation capacitance of  $21 \mu\text{F}/\text{phase}$  and 1500 r.p.m speed at no load condition. After voltage builds up, a star connected resistive load of  $100 \Omega/\text{phase}$  is connected with SEIG at  $t=1$  s. A three phase short circuit fault is initiated at  $t=1.6$  s across the stator terminals of SEIG. Simulation results of SEIG performance during voltage build-up, loading and three phase short circuit are shown in Fig. 6.3. During build-

up at no load, voltage developed in steady-state is 415 V corresponding to peak voltage of 586.8 V. Corresponding stator peak line current is 6.9 A for no load condition. Fig. 6.3 (a) shows that time taken to attain the steady state rated voltage is 0.55 s. After loading at  $t=1$  s, the peak SEIG line voltage decreases from rated peak of 586.8 V to 469 V and current changes from 6.9 A to 5.8 A. The reason behind this is, active power drawn by load causes increase in impedance drop across stator. This leads to decrease in SEIG stator voltage which causes reduction of reactive power drawn by capacitor. Hence further reduction of SEIG voltage occurs. The effect of short circuit across stator is also shown in Fig. 6.3.

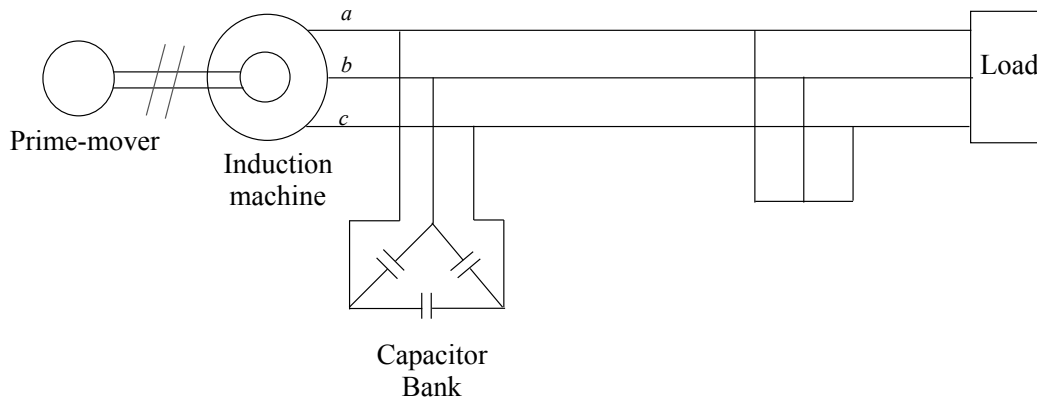


Figure 6.2: Diagram of SEIG system with three phase short circuit fault

As observed from Fig. 6.3 (a) that SEIG could not sustain the three phase short circuit and complete voltage collapse occurred suddenly across the stator terminals. Since the nature of machine impedance is inductive, the current of the machine is opposed to sudden voltage change. A current surge of 25.27 A appears during the first cycle and the current takes 130 ms time to decay completely after the fault initiation as shown in Fig. 6.3 (b). If the fault is not cleared before SEIG loses its residual magnetism, the time taken to re-excite SEIG increases compared to the time taken by the SEIG to build up the voltage in pre-fault condition [12], [13]. The fault is cleared at  $t=2$  s. The load is also subsequently removed. Fig. 6.4 shows the corresponding SEIG re-excitation voltage and current waveforms. Time taken to re-achieve the rated SEIG voltage is 1.22 s. This is more (approximately 0.72 s) than the time taken by SEIG to excite during the pre-fault period. The reason behind this is the residual magnetism of SEIG becomes weak due to the fault.



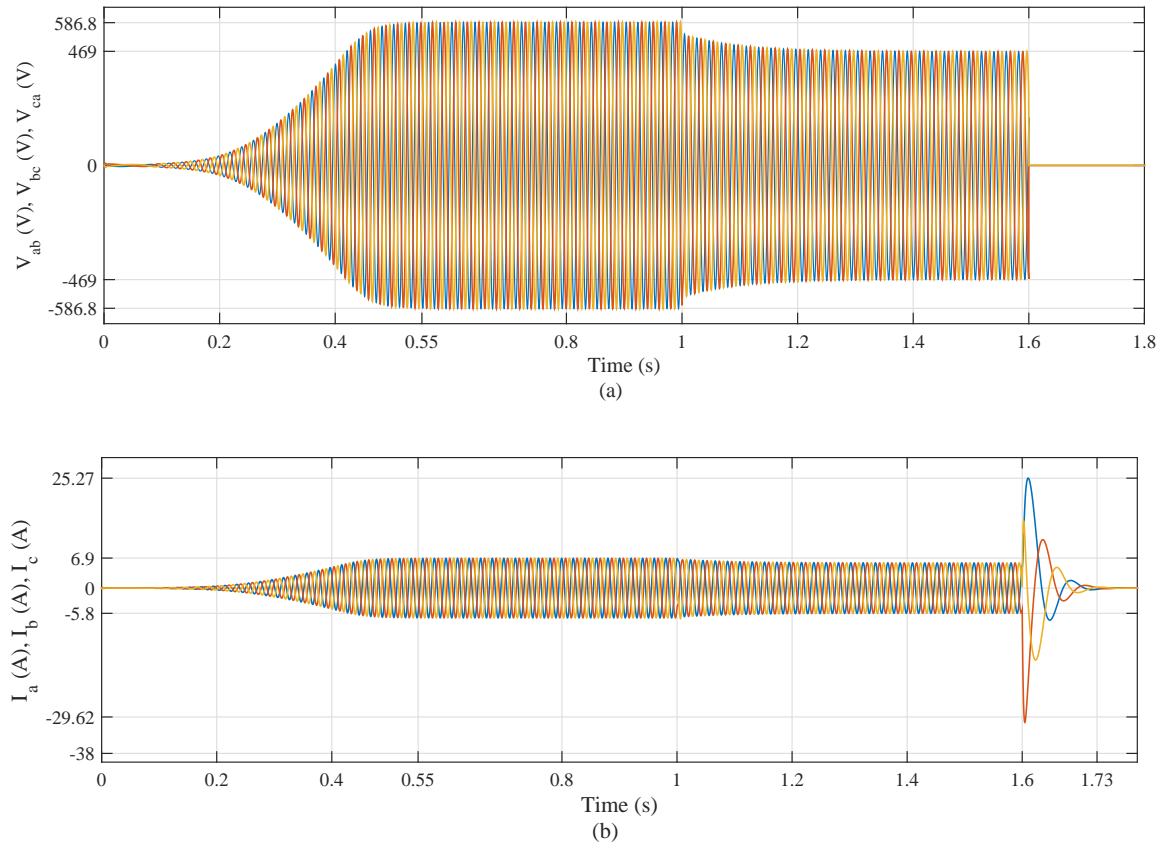


Figure 6.3: Simulation results of SEIG performance for three phase short circuit fault: (a) SEIG voltage waveform (b) SEIG current waveform

## 6.2.2 Line-to-line fault across SEIG

Fig. 6.5 shows the diagram of SEIG system with a short circuit fault initiated between line 'a' and line 'b'. Fig. 6.6 (a) and (b) show the corresponding SEIG voltage and current waveforms before and after the fault. Fig. 6.6 (a) shows the line voltage  $V_{ab}$  between faulty phase 'a' and line 'b'.  $V_{ab}$  reduces instantaneously to zero at  $t = 1.6$  s. However, the healthy line voltages  $V_{bc}$  and  $V_{ca}$  reduce to zero at  $t = 1.67$  s. Fig. 6.6 (b) shows that current surge of approximately 32.6 A appeared in line 'a' and line 'b', during first cycle after the fault initiation. Currents decay to zero at  $t = 1.7$  s. Fault is cleared at  $t = 2$  s and subsequently load gets removed. Fig. 6.7 shows the corresponding SEIG re-excitation voltage and current waveforms. Fig. 6.7 (a) and Fig. 6.7 (b) show that time taken to re-build the rated SEIG voltage is 1.9 s. Time taken for building SEIG voltage, after line-to-line fault clearance is more compared to pre-fault rated SEIG voltage build-up time.



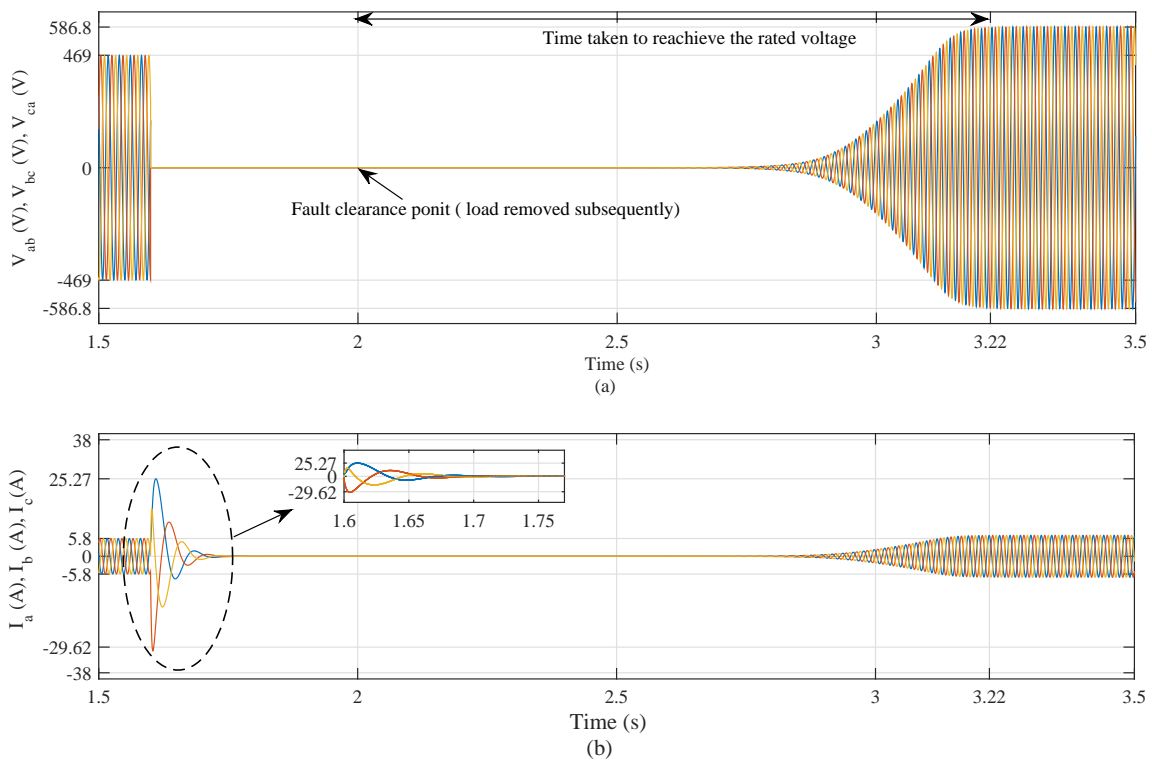


Figure 6.4: SEIG re-excitation voltage and current waveforms after three phase short circuit fault clearing and load removal

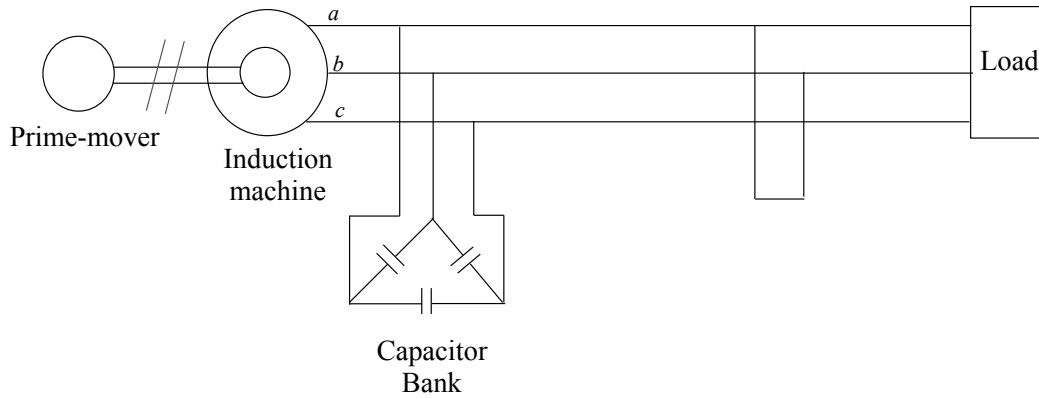


Figure 6.5: Diagram of SEIG system with line-to-line fault

### 6.2.3 Single capacitor opening in capacitor bank

While, SEIG is connected to a balanced three phase load at  $t=1$  s, one capacitor gets opened at  $t=1.6$  s. Corresponding simulation waveforms are shown in Fig. 6.8. It is observed from Fig. 6.8 (a) that voltage collapse occurred but no current surge appeared during opening of capacitor as seen in Fig. 6.8 (b).

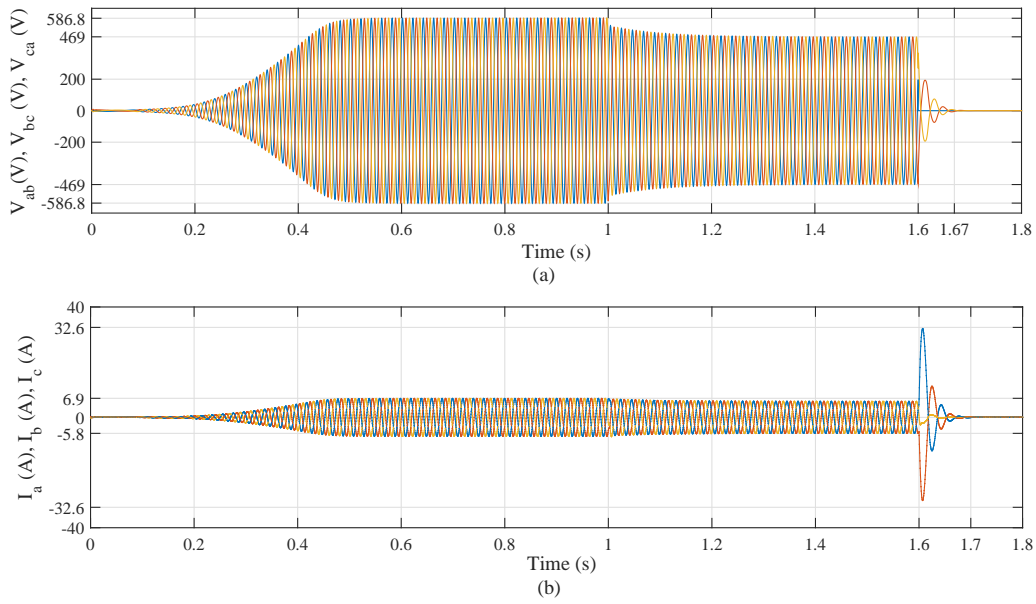


Figure 6.6: Simulation results of SEIG performance for line-to-line fault: (a) SEIG voltage waveform (b) SEIG current waveform

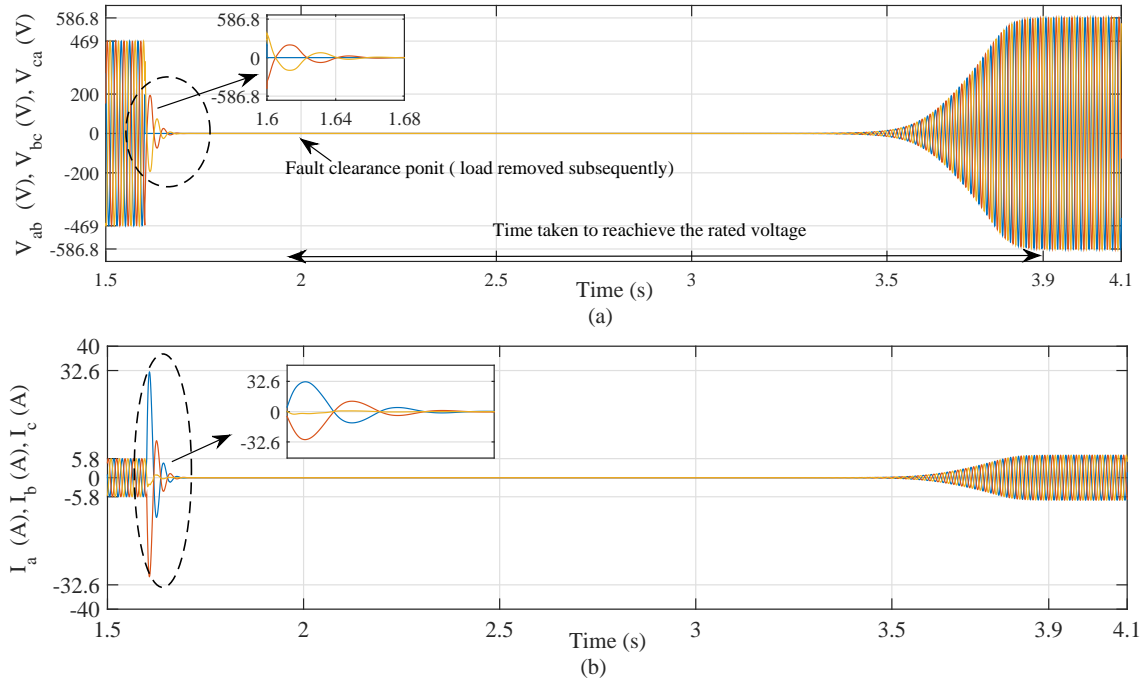


Figure 6.7: SEIG voltage and current waveforms after clearance of line-to-line fault and load removal

### 6.2.4 Single line opening at load

One phase of load connected to SEIG gets opened at  $t = 1.6$  s. Corresponding simulation results are shown in Fig. 6.9. Net load gets reduced and voltage of healthy phases are in-

creased from 469 V to 540 V as seen from Fig. 6.9 (a). As seen from Fig. 6.9 (b), the peak load current increases from 5.8 A to 7.5 A.

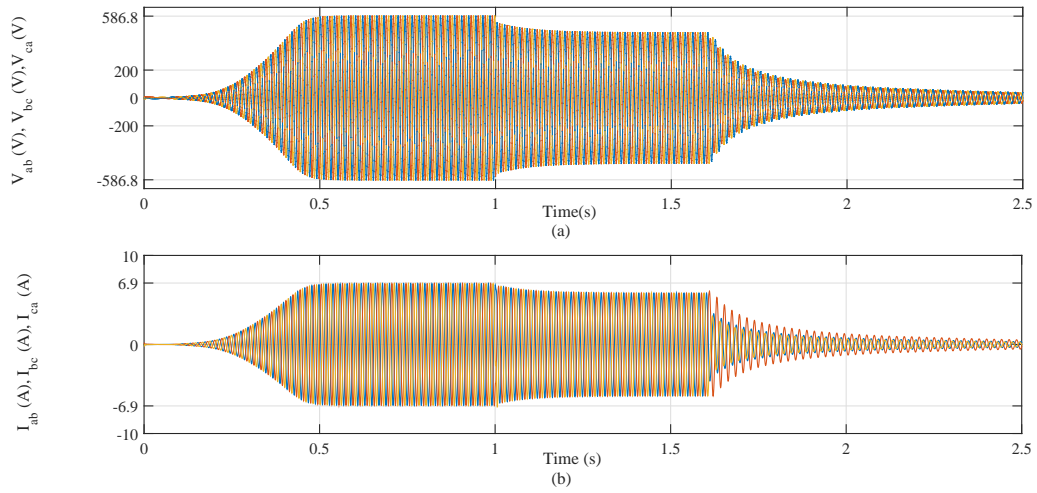


Figure 6.8: SEIG voltage and current waveforms for one capacitor opening

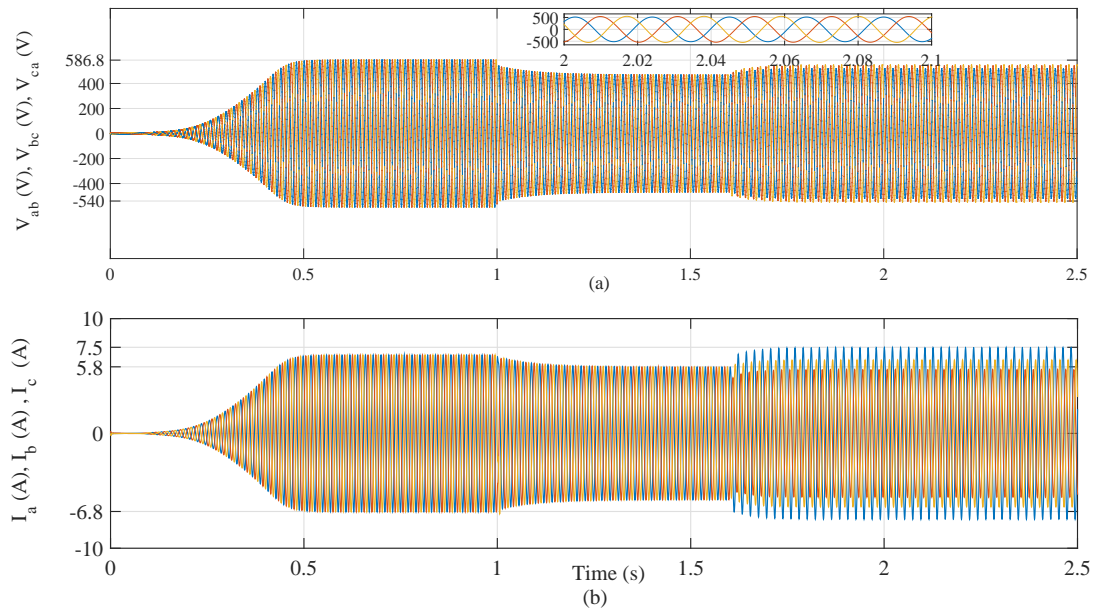


Figure 6.9: SEIG voltage and current waveforms for opening of one phase of load

### 6.2.5 SEIG electromagnetic torque in various faults taken for investigations

Electromagnetic torque ( $T_e$ ) developed by SEIG under different faults considered in the previous subsections are shown in Fig. 6.10. It is observed from Fig. 6.10 (a) and Fig. 6.10 (b) that  $T_e$  increases suddenly to a high value approximately 44 Nm and 47 Nm, respectively for three phase fault and line-to-line fault and decreases to zero as soon as SEIG current decrease to zero within 100 ms. For single capacitor opening, torque also reduces to zero but after 200 ms and corresponding result is shown in Fig. 6.10 (c). The opening of one phase load connected to SEIG, leads to sustained torque pulsation because of unbalanced phase voltage and the consequent result is shown in Fig. 6.10 (d).

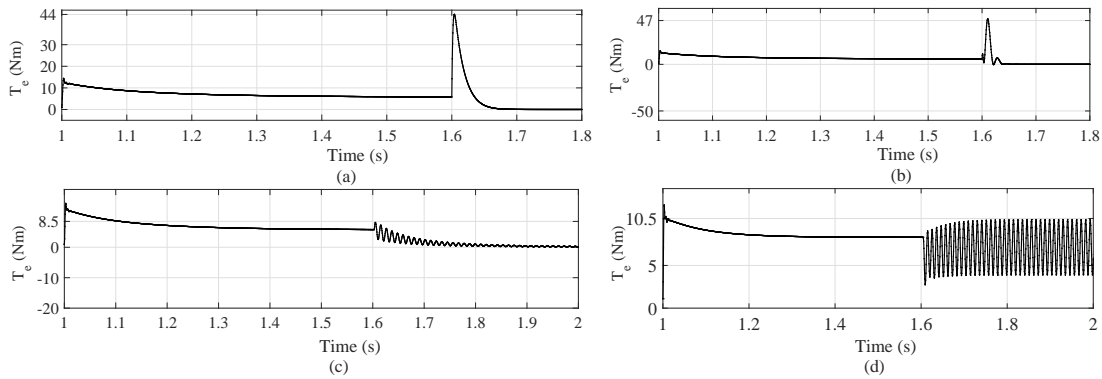


Figure 6.10: Simulation results of electromagnetic torque developed by SEIG during different faults: (a) Three phase short circuit (b) Line-to-line fault (c) Single capacitor opening (d) Single phase load opening

The excessive high torque and sustained vibration torque are extremely dangerous for SEIG leading to increased maintenance cost and risk of shaft failure. So, fault detection and classification in SEIG is very important to mitigate the problems arising due to various faults. Next section describes the Hilbert-Huang Transform used for fault detection in SEIG system.

## 6.3 Hilbert-Huang Transform (HHT)

In 1998, Hilbert proposed Hilbert-Huang Transform (HHT), an empirically based data analysis technique for non-linear and non-stationary processes [90]. HHT consists of two parts: Empirical Mode Decomposition (EMD) and Hilbert Transform (HT).

### 6.3.1 Empirical Mode Decomposition (EMD)

Empirical Mode Decomposition (EMD) decomposes a complex time sequence into many intrinsic mode functions (IMFs) having higher order to lower order frequency. An IMF is a mono-component signal and satisfies the following properties.

- (i) The difference between the number of extrema and the number of zero-crossings must be zero or one.
- (ii) At any point, the mean value of the envelope defined by local maxima and the envelope defined by local minima is zero (for practical applications mean should be less than a threshold value).

EMD algorithm adapts the following steps to extract IMFs from an original signal.

1. All the local maxima and local minima of signal  $s(t)$  denoted by  $M_j$ ,  $j$  belonging to the set of natural numbers  $(1,2,\dots)$  and  $M_k$ ,  $k$  belonging to the set of natural numbers  $(1,2,\dots)$ , respectively are determined.
2. Cubic spline functions are used for connecting, local maxima as the upper envelope and local minima as lower envelope and denoted as  $M_{max}(t)$  and  $M_{min}(t)$  respectively.
3. Mean of the upper and lower envelopes is calculated and defined as  $A(t) = (M_{max}(t) + M_{min}(t))/2$ .
4. Difference of original signal and mean of the envelopes is determined from (6.1)

$$h_1(t) = s(t) - A(t) \quad (6.1)$$

If  $h_1(t)$  follows the properties of an IMF, then  $C_1(t) = h_1(t)$  is the first IMF; otherwise  $h_1(t)$  is not an IMF, and treated as the original signal. Steps from 1 to 3 are repeated to get component  $h_{11}(t)$  as given in (6.2).

$$h_{11}(t) = h_1(t) - A_1(t) \quad (6.2)$$

5. Step 4 is repeated  $k$  times till  $h_{1k}$  becomes an IMF and determined as given in (6.3).

$$h_{1k}(t) = h_{1(k-1)}(t) - A_{1k}(t) \quad (6.3)$$

6. First IMF component is denoted by  $C_1(t)$  and subtract it from the original signal as given in (6.4).

$$s_1(t) = s(t) - C_1(t) \quad (6.4)$$

7. Now,  $s_1(t)$  is considered as original signal. Steps 1 to 6 are repeated to obtain the second IMF.
8. The decomposition procedure is repeated  $p$  times, to determine  $p$  IMFs of signal  $s(t)$ .
9. The iterative process is stopped after obtaining a monotonic IMF pattern from which no more IMF can be extracted.

Thus, EMD process, yields a series of IMFs and a final residual component,  $R(t)$ . The results of signal decomposition using EMD method depends upon the signal disturbance. If EMD apply to a pure sinusoidal component, then only one IMF will come, the signal itself. The obtained IMF satisfies the properties of IMF.

The main focus of this chapter is to identify the fault signal. The first step, towards this identification process, is sensing of SEIG stator voltage signals and determination of negative sequence component. Since, the negative sequence component is retained the information under disturbance condition [91]. The negative sequence component of the SEIG stator voltage,  $V_n$  evaluated using symmetrical component analysis and given by (6.5).

$$V_n = \frac{1}{3} (V_{ab} + A^2 V_{bc} + A V_{ca}) \quad (6.5)$$

where  $V_{ab}, V_{bc}, V_{ca}$  are the three SEIG stator line voltages and  $A = 1 \angle 120^\circ$ . Then next step is the implementation of EMD process as described, on negative sequence voltage component. Fig. 6.11 (a) and (b) show negative sequence voltage component of SEIG during three phase short circuit and line-to-line fault, respectively. Fig. 6.12 shows IMFs obtained for three phase short circuit fault using EMD method. It is observed from the Fig. 6.12 that most frequency content lies in first four IMF components. It is also observed that occurrence of transients at  $t=1.6$  s. Fig. 6.13 shows IMFs obtained for line-to-line fault using EMD method. It is observed from the Fig. 6.13 that most frequency content lies in first six IMF components and identified that transient occurs at  $t=1.6$  s. Next subsection describes the application of Hilbert Transform on IMF.

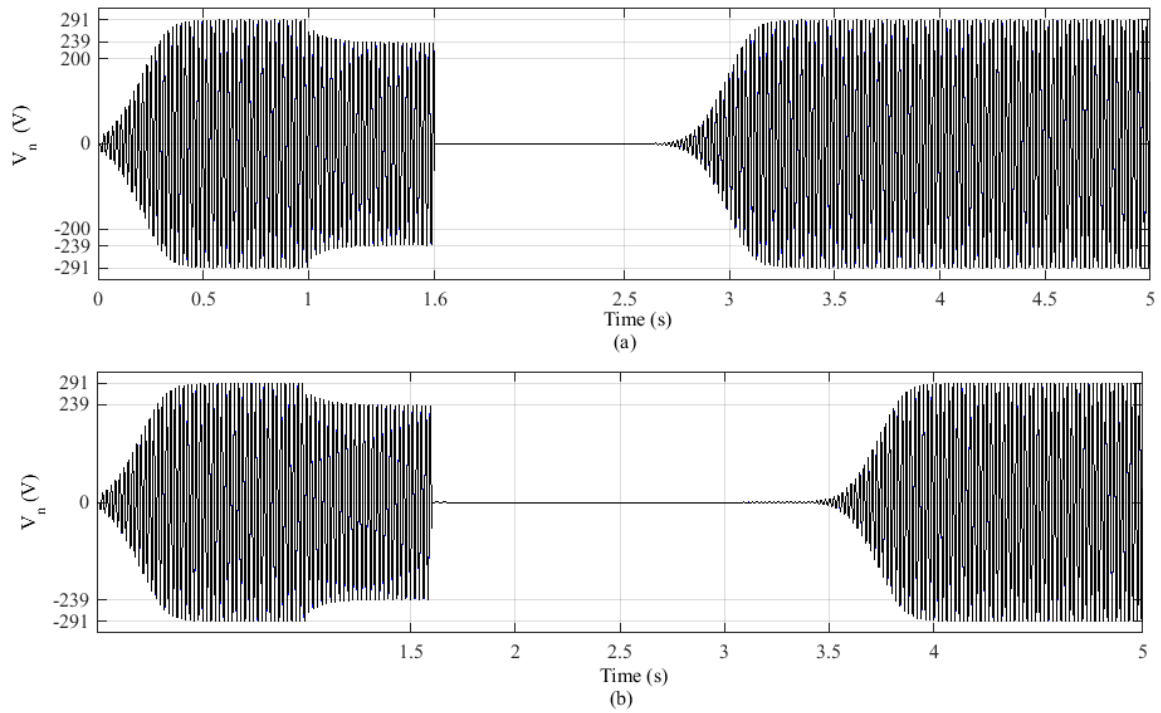


Figure 6.11: Negative sequence component of SEIG stator voltage (before and after) (a) for three phase short circuit fault (b) for line-to-line fault

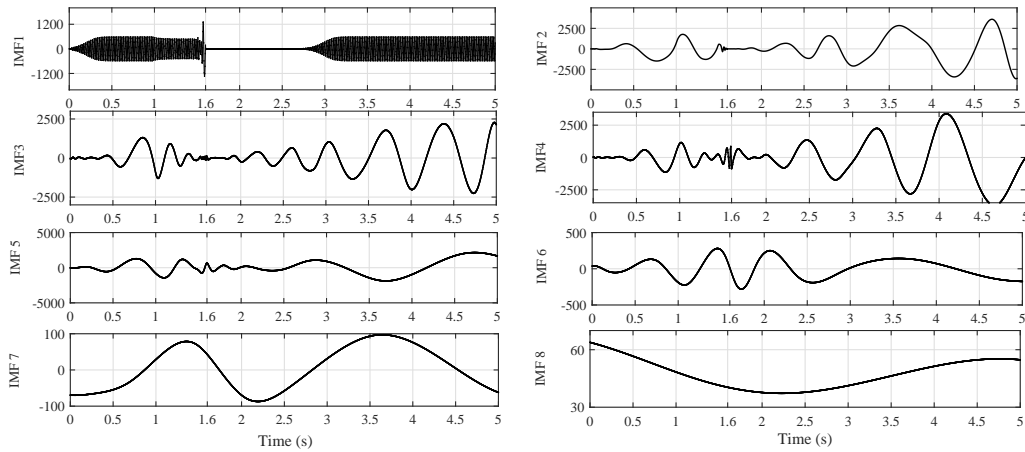


Figure 6.12: IMF components of SEIG stator negative sequence voltage (before and after) for three phase short circuit using EMD method

### 6.3.2 Hilbert Transform (HT)

Basically HT is carried out to determine the instantaneous amplitude, phase and frequency distribution against time. The HT of a real signal  $s(t)$  [92] is computed as

$$\hat{s}(t) = H[s(t)] = \frac{1}{\pi} p.v. \int_{-\infty}^{\infty} \frac{s(\tau)}{t - \tau} d\tau \quad (6.6)$$

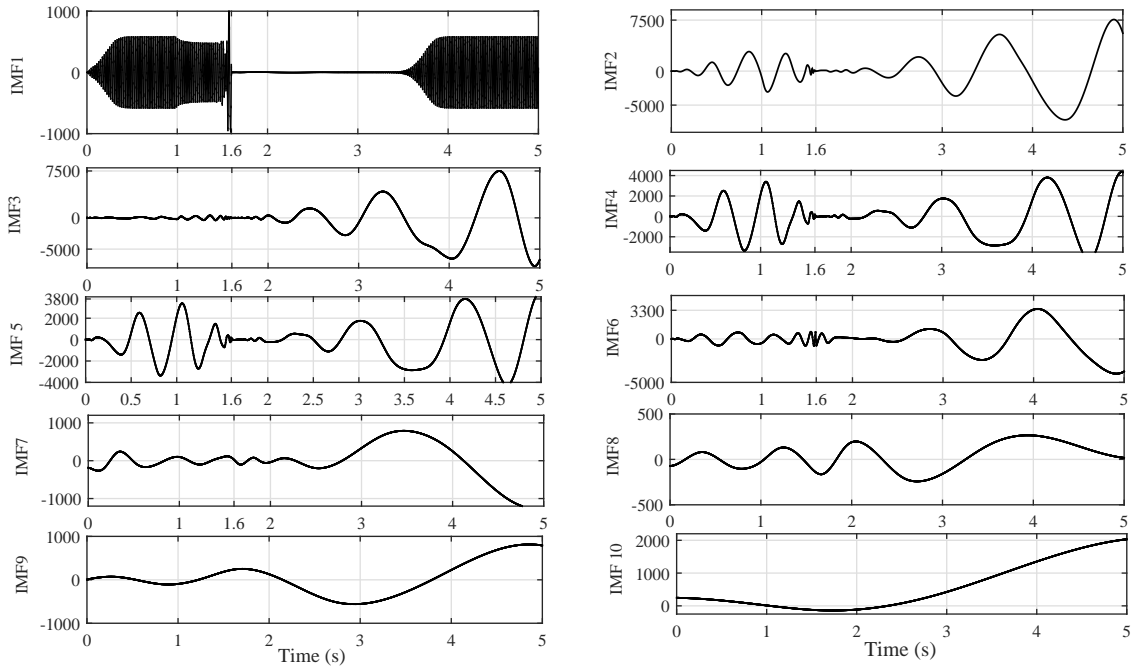


Figure 6.13: IMF components of SEIG stator negative sequence voltage (before and after) for line-to-line fault using EMD method

where  $p.v.$  indicates the principal value of the singular integral,  $\hat{s}(t)$  is the HT of signal  $s(t)$ , being the convolution of signal  $s(t)$  and  $\frac{1}{\pi t}$ . For a sinusoidal signal, frequency is definite but it is not well defined for a non-stationary signal. This leads to the concept of instantaneous frequency and can be determined using HT. Thus, the analytical signal is now determined as:

$$r(t) = s(t) + j\hat{s}(t) = a(t)e^{j\theta(t)} \quad (6.7)$$

The instantaneous amplitude, phase and frequency of signal  $s(t)$  can be determined as

$$a(t) = \sqrt{s(t)^2 + \hat{s}(t)^2} \quad (6.8)$$

$$\theta(t) = \arctan \left[ \frac{\hat{s}(t)}{s(t)} \right] \quad (6.9)$$

$$f_p = \frac{1}{2\pi t} \arctan \left[ \frac{\hat{s}(t)}{s(t)} \right] \quad (6.10)$$

where  $a(t)$  is the instantaneous amplitude,  $\theta(t)$  is the instantaneous phase and  $f_p$  is the instantaneous frequency.  $a(t)$  provides a single value at any time and  $f_p$  provides a single frequency value at any time. In this way, the instantaneous amplitude and frequency



of each IMF described in the previous subsection can be determined and further used to extract some important features. Fig. 6.14 (a) shows the first IMF obtained from negative sequence component during short circuit across SEIG. Instantaneous amplitude and instantaneous frequency of first IMF are shown in Fig. 6.14 (b) and (c) respectively. It is observed from Fig. 6.14 (b) that from  $t=0$  s to  $t=1$  s amplitude is 586.8 V and from  $t=1$  s to  $t=1.6$  s amplitude changed from 586.8 V to 469 V due to load. At  $t=1.6$  s amplitude decreases to zero, identifying that occurrence of some abnormal condition (short circuit). It is observed that at  $t=3.22$  s SEIG attains its rated value of 586.8 V due to clearance of the fault. Similarly, it is observed from Fig. 6.14 (c) that SEIG frequency is 50 Hz up to  $t=1$  s then changed to 47.91 Hz due to load connection. SEIG frequency comes to zero at  $t=1.6$  s, indicating that disturbance occurs. Again SEIG frequency comes from zero to 50 Hz after the clearance of disturbance and SEIG comes to normal condition. Fig. 6.15 (a) shows the first IMF obtained from negative sequence component during line-to-line fault across SEIG. Instantaneous amplitude and instantaneous frequency of first IMF are shown in Fig. 6.15 (b) and (c) respectively. It is observed from Fig. 6.15 (b) that from  $t=0$  s to  $t=1$  s amplitude is 586.8 V and from  $t=1$  s to  $t=1.6$  s amplitude changed from 586.8 V to 469 V due to load. At  $t=1.6$  s, amplitude decreases to zero, identifying that the occurrence of some abnormal condition (line-to-line fault). It is observed that at  $t=3.9$  s, SEIG attains its rated value of 586.8 V due to clearance of the fault. Similarly, it is observed from Fig. 6.15 (c) that SEIG frequency is 50 Hz up to  $t=1$  s, then changed to 47.91 Hz due to load connection. SEIG frequency comes to zero at  $t=1.6$  s, indicating that disturbance occurs. Again SEIG frequency comes from zero to 50 Hz after the clearance of disturbance and SEIG comes to normal condition. Next section describes feature extraction using HHT.

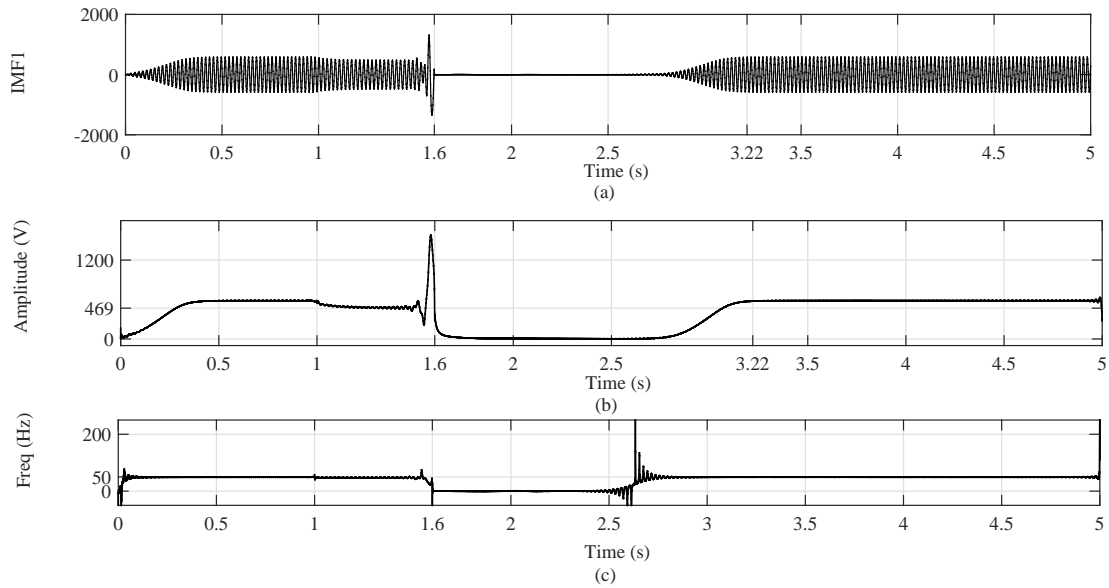


Figure 6.14: Simulation results for SEIG three phase short circuit detection using HT: (a) First IMF obtained from negative sequence voltage during three phase short circuit (b) instantaneous amplitude response of first IMF (c) instantaneous frequency response of first IMF

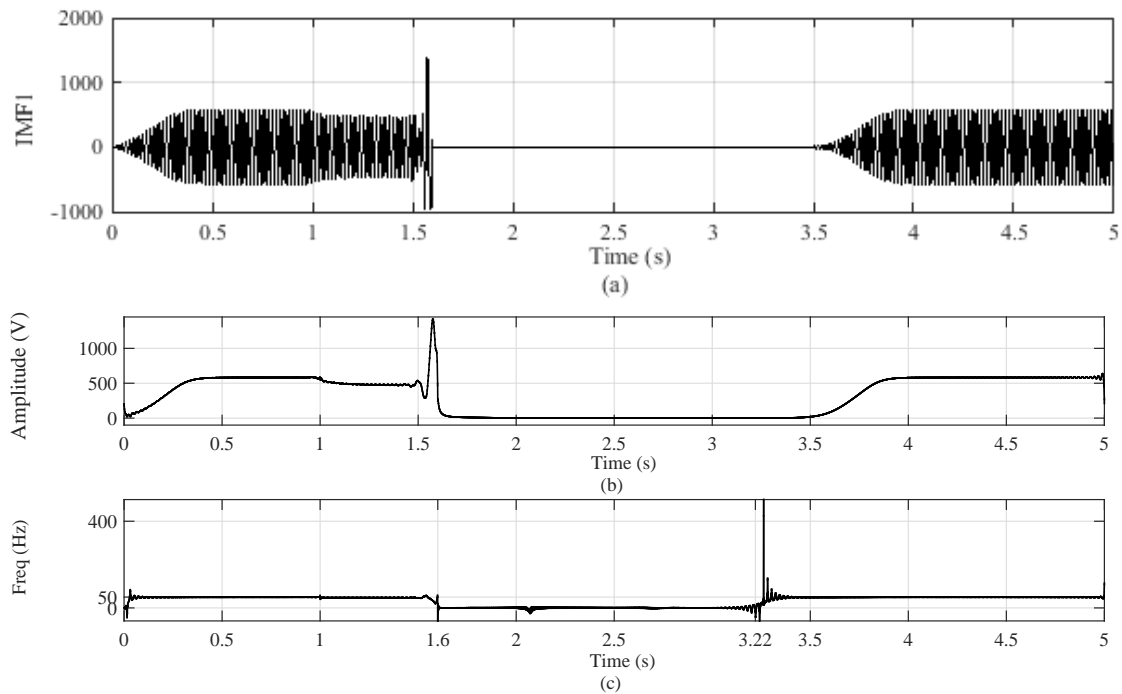


Figure 6.15: Simulation results for SEIG line-to-line fault detection using HT: (a) First IMF obtained from negative sequence voltage during line-to-line fault (b) instantaneous amplitude response of first IMF (c) instantaneous frequency response of first IMF

## 6.4 Feature Extraction using Hilbert-Huang Transform (HHT)

For classification, if the data fed to classifier directly, classification process becomes complicated and computation time also increases. To avoid these problems, data are processed in terms of feature vectors. Hence, selection of feature vectors is very vital and crucial to achieve accurate classification. Selected features vectors are fed to classifier for training and testing. Since the lower-order IMFs capture fast oscillation modes and higher order IMFs capture slow oscillation mode, first six IMFs are considered in this chapter. Hilbert Transform is applied to each of the four IMFs. Following three statistical features are extracted from each of the Hilbert Transformed array.

1. Energy of the elements corresponding to magnitude of the Hilbert-array at each sample.
2. Standard deviation of the amplitude.
3. Standard deviation of the phase contour.

Thus, a total of 18 features are extracted for each faulty signal which is used for classification. Next section describes the different types of classifier.

## 6.5 Classification

Classification is the process to determine a fault or condition from a range of data set. A classifier is a device that takes a number of inputs and based on the pattern of these inputs, decides the most likely condition associated with that pattern. The input fed to the classifier can have any value but the output obtained from the classifier is a discrete value that decides the class. Block diagram of the classification process is shown in Fig. 6.16. The entire input data sets are divided into training sets and testing sets. The training data set is used for updating the free parameters that are associated with each classifier often adaptively to maximize the performance of the classifier. The remaining test data are used for validating the classifier performance. In this study, Least Square Support Vector Machine (LS-SVM) classifier is proposed using the extracted features obtained from HHT, described in the previous subsection. The performance of the proposed LS-SVM classifier is compared with other standards available classifiers, such as MultiLayer Perceptron (MLP) neural network, Probabilistic Neural Network (PNN) and Support Vector Machine (SVM). All the above mentioned classifiers are described in the subsequent subsections.

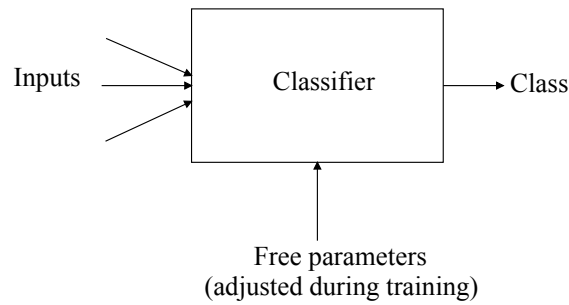


Figure 6.16: Block diagram of a classification process

### 6.5.1 Classification using MultiLayer Perceptron (MLP) neural network

Artificial neural network is made up of a large number of highly interconnected processing elements defined as neurons, working in unison to solve a specific problem. The neurons are organized in layers, each layer consisting of a large number of interconnected nodes. Data from the input layer are processed by one, or more hidden layers through a system of weighted connections. These hidden layers then communicate to an output layer to give the output. The MLP is a special kind of artificial neural network. MLP is a feed-forward multi-layered network consisting of an input layer, and one or more hidden or intermediate layers and one output layer as presented in the Fig. 6.17. The output from every neuron in a layer of the MLP is connected to all inputs of each neuron in the next layer. The input layer processing functions are all linear, but in the hidden layer nonlinear sigmoidal functions such as hyperbolic tangent, logistical function or sigmoid functions are usually used [93]. In MLP the number of neurons in the input and output layers are selected based on the problem to be solved. The net inputs of each neuron of hidden layer and output layer are given as follows [94].

$$net_h = \sum_{i=1}^{NI} w_{ih} o_i \quad h = 1, 2, \dots, NH \quad (6.11)$$

$$net_j = \sum_{h=1}^{NH} w_{hj} o_h \quad j = 1, 2, \dots, NJ \quad (6.12)$$

where  $NI$ ,  $NH$ ,  $NJ$  represent the number of nodes in the input layer, hidden layer, and output layer respectively.  $w_{ih}$  is the connection weight between the input layer  $i$  and hidden layer  $h$ .  $w_{hj}$  is the connection weight between the hidden layer  $h$  and output layer  $j$ .  $o_i$  is the output vector of the input layer.  $o_h$  is the output vector of the hidden layer. After defining the models of the ANNs, training is performed either under the supervision of some teachers (i.e., known input-output responses) or without supervision [95]. Generally, in most of the

classification problems supervised learning methods are used. In supervised learning, the desired output is required in order to learn. In this learning process, a model is created that maps the input data to output data using historical data so that the model can then be used to produce the output when the desired input is unknown. During the training of a MLP network, weights are updated iteratively, to minimize an error function between the actual network output and the corresponding target values. One of the commonly used error functions in MLP is the mean square error (MSE) in MLP. To train MLP back propagation algorithm is a common method of training [96]. The problems with MLP are selection of number of hidden layers, number of nodes per hidden layers, slow convergence and lack of optimality. These problems are solved in some extent using the Probabilistic Neural Network (PNN), described in next subsection.

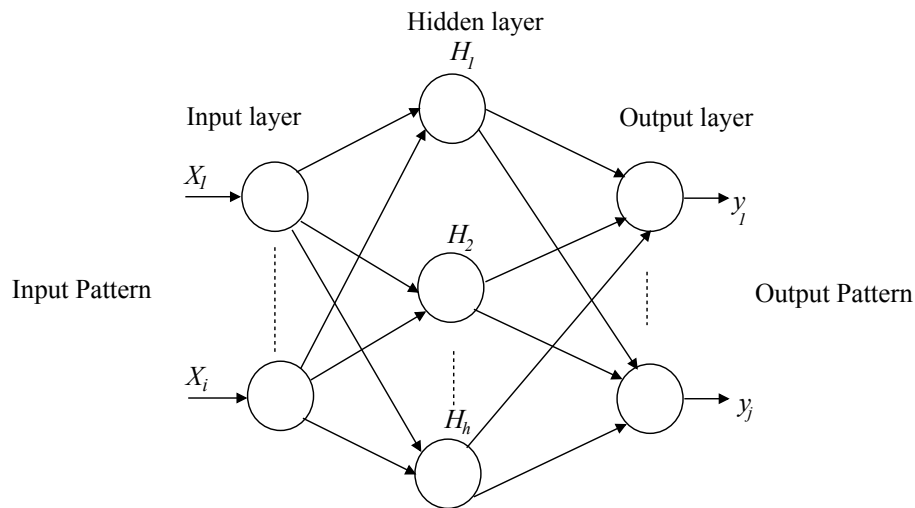


Figure 6.17: A multilayer perceptron neural network.

### 6.5.2 Classification using Probabilistic Neural Network (PNN)

The Probabilistic Neural Network (PNN) is a distinct type of network and effectively used in solving classification problems [97], [98]. In early 1990s, PNN was first introduced by D. F. Specht in [99]. The features of PNN [100] are as follows.

- (i) PNN models using Bayesian classifiers.
- (ii) Learning processes are not required.
- (iii) Initialization of the weights are not required.
- (iv) There is no relation between learning processes and recalling processes.
- (v) To modify the weights, the difference between inference vector and target vector are not used.

(vi) It has fast training process as it requires only a single-pass network training stage without updating the weights.

In the signal classification application, [101] the training examples are classified based on their distribution values of probability density function (pdf). This is the basic requirement of the PNN. A simple pdf is presented by the following expression.

$$f_k(X) = \frac{1}{N_k} \sum_{j=1}^{N_k} \exp\left(-\frac{\|X - X_{kj}\|}{2\sigma^2}\right) \quad (6.13)$$

Block diagram of PNN network as shown in Fig. 6.18, is composed of the radial basis layer

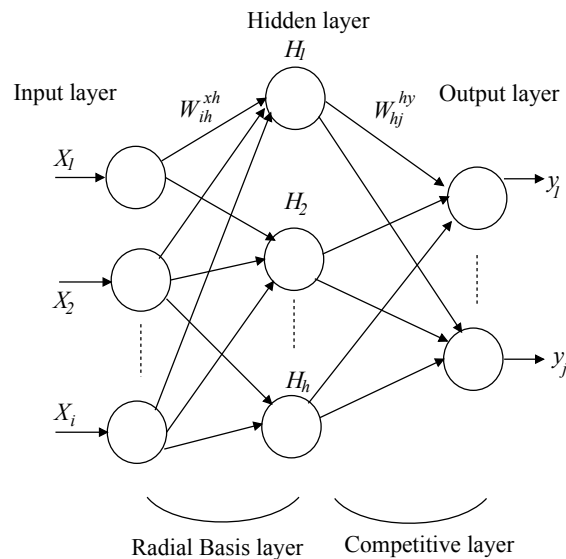


Figure 6.18: A probabilistic neural network.

and competitive layer [102]. Output vector  $H$  of the hidden layer in the PNN is as follows.

$$H_h = \exp\left(\frac{-\sum_i (X_i - W_{ih}^{xh})^2}{2\sigma^2}\right) \quad (6.14)$$

$$\begin{aligned} net_j &= \frac{1}{N_j} \sum_h W_{hj}^{hy} H_h \quad \text{and} \quad N_j = \sum_h W_{hj}^{hy} \\ net_j &= \max_k (net_k) \quad \text{then} \quad y_j = 1, \quad \text{else} \quad y_j = 0 \end{aligned} \quad (6.15)$$

where  $i$  is number of input layers.  $h$  is number of hidden layers.  $j$  is number of output layers.  $k$  is number of training examples.  $N$  is number of classifications.  $\sigma$  is smoothing parameter (standard deviation).  $X$  is input vector.  $\|X - X_j\|$  is the Euclidean distance between vectors  $X$  and  $X_{kj}$ , i.e.,  $\|X - X_j\| = \sum_i (X - X_{kj})^2$ .  $W_{ih}^{xh}$  is the connection weight

between the input layer  $X$  and the hidden layer  $H$ .  $W_{hj}^{hy}$  is the connection weight between the hidden layer  $H$  and the output layer  $Y$ . The problem with PNN is, the requirement of an extensive training and memory [103] (since PNN stores all the training information with its network). Support vector machine is an alternative classifier widely used to overcome the disadvantages associated with MLP and PNN [104] described in next subsection.

### 6.5.3 Classification using Support Vector Machine (SVM)

For classification problems, artificial neural network has been found very effective but it has many disadvantages. These are as follows. The error function of the neural networks is multi modal, which includes many local minima and learning process requires a large number of data for training. SVM has gained importance as a very powerful tool and does not have the above demerits of artificial neural network. Recently, for solving fault classification and section identification of an advanced series compensated transmission line, SVM is employed in [105] and for fault zone detection in a series compensated transmission line SVM is employed in [106]. SVM was first introduced in the late 1960s by Vapnik [107], but in the middle of 1990s, practically used for various applications [96]. SVM is a binary learning machine. SVM uses two important processes: (i) training of data into a higher dimensional feature space through a nonlinear feature mapping function  $\Psi(x)$  and (ii) using an optimization method for finding an optimal hyperplane to separate data points according to their classes and maximize the classification ability. Very large feature spaces can be handled potentially by SVMs to carry out the training, so that the performance of SVM does not affect the dimension of classified vector [108], [109]. In the following paragraphs, detail analysis of different types of SVM is reproduced.

#### (a) Hard-margin linear SVM

A training data set ( $x$ ) consisting of two classes with target ( $y$ ) either the value of  $+1$  or  $-1$  is considered. The SVM creates a line or hyperplane to separate the training data of two classes as shown in Fig. 6.19. In the Fig. 6.19 a series of data points for two different classes are shown by circle (class 1) and square (class 2). The SVM gives the effort to place a linear boundary (solid line) between the two different classes and orient it in such a way that the margin  $D$  is maximized. The data points which are near to this boundary line have a great role to define the margins and are known as support vectors. Support vectors contain all the essential information for the classifier. In Fig. 6.19 support vectors are shown by red circle and green square. Once the support vectors are selected, the rest of the data points have no roles they are simply discarded.

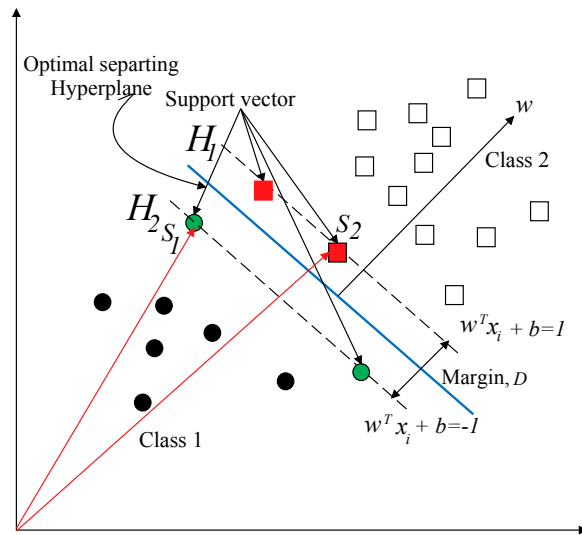


Figure 6.19: SVM classifier (hard-margin)

The hyperplane or decision boundary is represented by [110]

$$w^T x_i + b = 0 \quad (6.16)$$

where  $w$  is the weight vector and  $b$  is the offset or bias term, a scalar. In the lines  $H_2$  and  $H_1$ , where the support vectors are placed, the equations for class 1 and class 2 respectively corresponding to output  $y_i = +1$  and  $y_i = -1$ , are given as,

$$w^T x_i + b = -1 \quad (6.17)$$

and

$$w^T x_i + b = +1 \quad (6.18)$$

Margin  $D$  is determined from the difference between any two support vectors. In Fig. 6.19  $\vec{S}_1$  and  $\vec{S}_2$  are two support vectors, margin is determined as follows:

$$D = (\vec{S}_2 - \vec{S}_1) \quad (6.19)$$

By multiplying unit vector  $\frac{w}{\|w\|}$  (since  $w$  is normal to the plane), to the above expression,

$$D = \frac{w}{\|w\|} (\vec{S}_2 - \vec{S}_1) \quad (6.20)$$



Since  $\vec{S}_1$  and  $\vec{S}_2$  are two points of the lines represented by expressions (6.17) and (6.18) respectively, the expression (6.21) is represented by

$$D = \frac{1 - b + 1 + b}{\|w\|} \quad (6.21)$$

where,  $w\vec{S}_2 = 1 - b$  and  $w\vec{S}_1 = -1 - b$ . Finally the margin,  $D$  is evaluated by

$$\begin{aligned} D &= \frac{2}{\|w\|} \\ &= \frac{2}{\sqrt{w \cdot w}} \end{aligned} \quad (6.22)$$

In SVM, training is performed to find a hyperplane that maximizes the margin,  $D$  (equivalent to minimizing the Euclidean norm of the weight vector  $w$ ). For a training data set of  $N$  points  $(x_i, y_i)$ , where  $i = 1, 2, \dots, N$ , optimum values of the weight vector  $w$  and  $b$  are determined by minimizing the weight vector  $w$  and formulated using the expression (6.22). Corresponding cost function [111] is given as follows.,

$$\begin{aligned} \text{minimize} \quad & F(w) = \frac{1}{2} w^T w \\ \text{subject to} \quad & y_i(w^T x + b) \geq 1; \end{aligned} \quad (6.23)$$

This formulation is called hard-margin SVM. The scaling factor  $\frac{1}{2}$  is included in the expression (6.23) for the mathematical convenience. Since SVM looks for a hyperplane which maximizes the margin,  $D$ , or minimizes the Euclidean norm of the weight vector  $w$ , expression (6.23) is formulated as a constrained optimization problem. Constraints are taken so that no training data falls in the margin,  $D$ . The objective function  $F(w)$  of the optimization problem is quadratic and a convex function of  $w$ . The constraints of the optimization problem are linear in  $w$  and  $b$ . Solving constrained optimization problem will produce the solutions for weight vectors  $w$  and  $b$ , which further provides the maximal margin hyperplane  $w^T x + b = 0$  with the margin,  $D (= \frac{2}{\|w\|})$ . This constrained optimization problem is solved using the method of Lagrange multipliers (1995 Bertsekas) [111]. To solve the optimization problem first, a Lagrangian function is constructed as,

$$J(w, b, \gamma) = \frac{1}{2} w^T w - \sum_{i=1}^N \gamma_i [y_i(w^T x_i + b) - 1] \quad (6.24)$$

where the auxiliary nonnegative variable  $\gamma_i$  are defined as Lagrange multipliers. The solutions of the constrained-optimization problem (6.24) is determined by differentiating

$(Jw, b, \gamma)$  with respect to  $w$  and  $b$  and setting the results equal to zero. Corresponding to this following two conditions of optimality are obtained.

$$\text{condition 1: } \frac{\partial J(w, b, \gamma)}{\partial w} = 0$$

$$\text{condition 2: } \frac{\partial J(w, b, \gamma)}{\partial b} = 0$$

Application of optimality condition 1 to the equation (6.24) provides the following expression (after rearrangement),

$$w = \sum_{i=1}^N \gamma_i y_i x_i \quad (6.25)$$

Similarly, application of optimality condition 2 to the equation (6.24) provides the following expression,

$$\sum_{i=1}^N \gamma_i y_i = 0 \quad (6.26)$$

It is observed from condition that the solution vector  $w$  contains  $N$  training examples. Although the solution  $w$  is unique by virtue of the convexity of the Lagrangian function, the same cannot be said about the Lagrangian multipliers  $\gamma$ . However, Lagrangian multipliers  $\gamma_i$  is a dual variable for each training data point. According to Karush-Kuhn-Tucker (KKT) only those multipliers are assumed nonzero values that exactly satisfy the following condition

$$\gamma_i [y_i (w^T x_i + b) - 1] = 0$$

The primal problem initially started with a convex cost function and linear constraints, but it is also possible to construct another problem called dual problem. This second problem has the same optimal value as the primal problem, but optimal solutions are provided by Lagrangian multipliers. The corresponding dual problem of the primal optimization problem is obtained by expanding the expression (6.24).

$$J(w, b, \gamma) = \frac{1}{2} w^T w - \sum_{i=1}^N \gamma_i y_i w^T x_i - b \sum_{i=1}^N \gamma_i y_i + \sum_{i=1}^N \gamma_i \quad (6.27)$$

Based on the optimality condition of expression (6.26), the third term in right-hand side of equation (6.27) is zero. However, from the expression (6.25), following expression is obtained.

$$w^T w = \sum_{i=1}^N \gamma_i y_i w^T x_i = \sum_{i=1}^N \sum_{j=1}^N \gamma_i \gamma_j y_i y_j x_i^T x_j \quad (6.28)$$

By setting objective function  $J(w, b, \gamma) = Q(\gamma)$ , equation (6.27) is reformulated by

$$Q(\gamma) = \sum_{i=1}^N \gamma_i - \frac{1}{2} \sum_{i=1}^N \sum_{j=1}^N \gamma_i \gamma_j y_i y_j x_i^T x_j \quad (6.29)$$

where the  $\gamma_i$  are all nonnegative. The notation has changed from  $J(w, b, \gamma)$  to  $Q(\gamma)$  to get the dual form of the primal optimization problem. The dual problem is stated as follows.

For a training data set of  $N$  points  $(x_i, y_i)$ , where  $i = 1, 2, \dots, N$ , Lagrangian multipliers  $\gamma_i$  where  $i = 1, 2, \dots, N$ , are evaluated to maximize the objective function

$$Q(\gamma) = \sum_{i=1}^N \gamma_i - \frac{1}{2} \sum_{i=1}^N \sum_{j=1}^N \gamma_i \gamma_j y_i y_j x_i^T x_j \quad (6.30)$$

subject to the constraints

$$\begin{aligned} \sum_{i=1}^N \gamma_i y_i &= 0 \\ \gamma_i &\geq 0 \end{aligned} \quad (6.31)$$

The above dual problem numerically solved (using MATLAB's quadprog function) to get the optimum  $\gamma_i$  values. Obtained optimum  $\gamma_i$  are then used to compute  $w$  by using equation (6.25) and described as

$$w = \sum_{i=1}^N \gamma_i y_i x_i \quad (6.32)$$

For support vectors  $\{x_s, y_s\}$   $\gamma_i > 0$  and  $b$  is computed given as follows.

$$y_s (w^T x_s + b) = 1$$

$b$  is computed using all support vectors which are available in the training sets and their average is taken for the final computation of  $b$ . Because the values of  $\gamma_i$  are computed numerically and have numerical errors. Hence,  $b$  is computed as

$$b = \frac{1}{N_{sv}} \sum_{s=1}^{N_{sv}} \begin{bmatrix} 1 \\ y_s \end{bmatrix} - w^T x_s; \quad N_{sv} \text{ is the total number of support vectors} \quad (6.33)$$

### (b) Soft-margin SVM

The above discussion is not applicable for more difficult case of non-separable patterns. Fig. 6.20 shows that, a training data due to some reason falls on the wrong side of the decision surface. So, to consider this type of case the constraints have to be modified to permit mistakes. To allow errors in training data, slack variables,  $\xi (\geq 0)$ , is introduced in constraints and described as follows.

$$\begin{aligned} w^T x_i + b &\geq 1 - \xi & \text{for } y_i = +1 \\ w^T x_i + b &\leq 1 - \xi & \text{for } y_i = -1 \end{aligned}$$

New constraints is

$$\begin{aligned} y_i (w^T x_i + b) &\geq 1 - \xi \\ \xi &\geq 0 \end{aligned} \quad (6.34)$$

where  $i = 1, \dots, N$ , it is also needed to penalize the errors in the objective function. So,

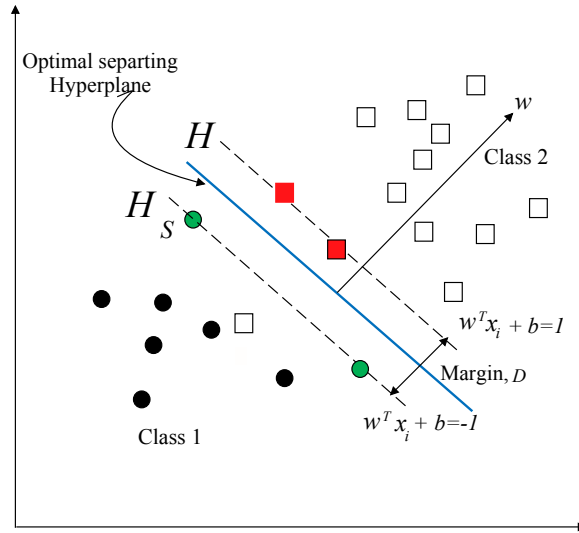


Figure 6.20: SVM classifier (soft-margin)

an extra cost is introduced in the objective functions to represent errors. The new optimization problem becomes as follows.

$$\begin{aligned} & \text{minimize } \frac{1}{2} w^T w + C \sum_{i=1}^N \xi_i \\ & \text{subject to } y_i(w^T x_i + b) \geq 1 - \xi \\ & \quad \quad \quad \xi_i \geq 0 \end{aligned} \quad (6.35)$$

This formulation is called soft-margin SVM, where  $C$  is a user-specified positive parameter. The parameter  $C$  controls the tradeoff between complexity of the machine and the number of non-separable points.  $C$  is also referred as the regularization parameter. When  $C$  is assigned a large value, it implies that the designer of the support vector machine has faith in the quality of training sample. But when  $C$  is assigned a small value, the training sample is considered to be noisy and less emphasis should therefore be placed on it. As discussed, minimizing the first term in equation (6.35) is related to the SVM and the second term  $\sum_i \xi_i$  is an upper bound on the number of test errors. As discussed Lagrangian multipliers are used and the objective function of the dual problem for a training sample  $(\{x_i, y_i\})_{i=1}^N$  (non-separable patterns) is described as follows.

$$Q(\gamma) = \sum_{i=1}^N \gamma_i - \frac{1}{2} \sum_{i=1}^N \sum_{j=1}^N \gamma_i \gamma_j y_i y_j x_i^T x_j \quad (6.36)$$

subject to the constraints

$$\begin{aligned} \sum_{i=1}^N \gamma_i y_i &= 0 \\ 0 &\leq \gamma_i \leq C \end{aligned} \quad (6.37)$$

The slack variables  $\xi_i$  is not appearing in the dual problem. The dual problem for the case of non-separable patterns is almost same as the case of linearly separable patterns. The objective function  $Q(\gamma)$  to be maximized is the same in both cases. But the constraints are  $\gamma_i \geq 0$  for separable patterns and  $0 \leq \gamma_i \leq C$  for non-separable case respectively. The final decision boundary  $w^T x + b = 0$  is computed in the same manner as for Hard-margin case and described as follows.

$$\left[ \sum_i^N \gamma y_i x_i \right]^T x + b = \sum_i^N \sum_j^N \gamma_i y_i x_i^T x_j + \frac{1}{N_{sv}} \sum_{s=1}^{N_{sv}} \left[ \frac{1}{y_s} - w^T x_s \right] \quad (6.38)$$

### (c) Nonlinear SVM

The SVM formulation discussed till now, require that training examples belong to class 1 and class 2 can be linearly represented i.e. the decision boundary must be a hyperplane. But for real life data sets, the decision boundaries are nonlinear. This type of data set which is called input space and solved using nonlinear SVM.

Fig. 6.21 shows that the decision boundary of input space is not linear. Hence to linearly separate, input data are mapped into a high-dimensional feature-space using non-linear transformation  $\Psi(x)$  which is expressed as follows.

$$\Psi(x_i) = \{\Psi(x_1), \Psi(x_2), \Psi(x_3), \dots\}^T, \quad (6.39)$$

where  $\Psi(x_1), \Psi(x_2), \dots$  are nonlinear mapping functions. Fig. 6.22 represents the two mappings occur in SVM (i) nonlinear mapping of an input vector into a high-dimensional feature space that is hidden from both the input and output (ii) construction of an optimal hyperplane for separating the features obtained in step 1. Each  $x_i$  is replaced by  $\Psi(x_i)$ . With the nonlinear transformation, the optimization problem in equation (6.35) becomes as follows.

$$\begin{aligned} \text{minimize } & \frac{1}{2} w^T w + C \sum_{i=1}^N \xi_i \\ \text{subject to } & y_i (w^T \Psi(x_i) + b) \geq 1 - \xi \\ & \xi_i \geq 0 \end{aligned} \quad (6.40)$$

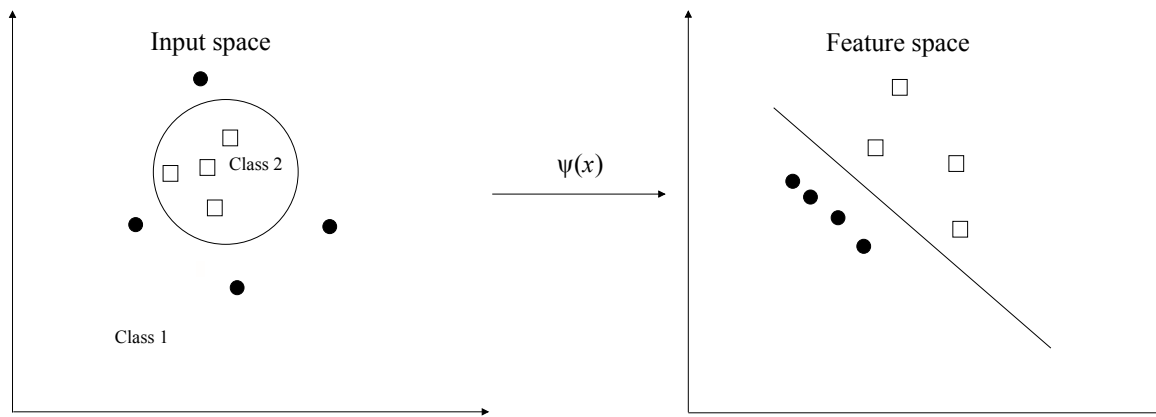


Figure 6.21: Non-linear separation of input and feature space

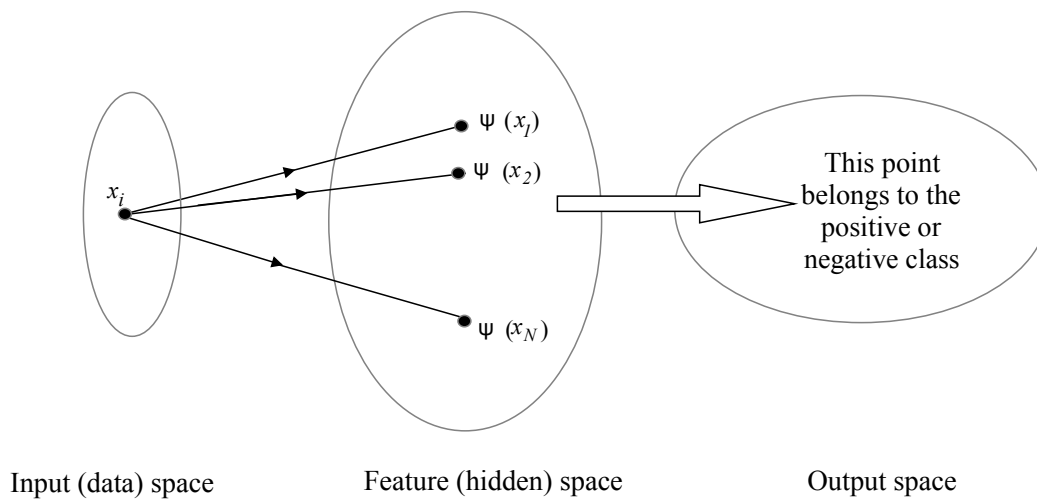


Figure 6.22: Two mappings in a support vector machine (i) nonlinear mapping from the input space to feature space; (ii) linear mapping from the feature space to output space

The corresponding dual form of equation (6.40) is

$$Q(\gamma) = \sum_{i=1}^N \gamma_i - \frac{1}{2} \sum_{i=1}^N \sum_{j=1}^N \gamma_i \gamma_j y_i y_j (\Psi^T(x_i) \Psi(x_j)) \quad (6.41)$$

subject to the constraints

$$\begin{aligned} \sum_{i=1}^N \gamma_i y_i &= 0 \\ 0 &\leq \gamma_i \leq C \end{aligned} \quad (6.42)$$

The problem associated with this approach is, in the feature space lot of dot products  $\Psi(x_i) \cdot \Psi(x_j)$  have to be calculated. But in general, if the feature space is high dimensional,

$\Psi(x_i) \cdot \Psi(x_j)$  will be expensive to compute. Hence  $\Psi(x)$  can be expensive to compute. This type of explicit transformation is avoided, it is observed in equation (6.41) that to construct the decision boundary the evaluation of  $\Psi^T(x_i)\Psi(x_j)$  is required in the feature. By referring (6.38), the decision boundary in feature space (for nonlinear SVM) is described as follows.

$$\sum_{i=1}^N \sum_{j=1}^N \gamma_i y_i \Psi^T(x_i) \Psi(x_j) + b = 0 \quad (6.43)$$

Thus, in feature space  $\Psi^T(x_i)\Psi(x_j)$  is computed directly using the input space vectors  $x_i$  and  $x_j$ . It is not required to know the feature vector  $\Psi(x)$  or even mapping  $\Psi$  itself. A kernel function  $K$  [110] is used to perform this transformation and reduce the computational burden and expressed as follows.

$$K(x_i, x_j) = \Psi(x_i)^T \Psi(x_j) \quad (6.44)$$

There are different kernel functions like polynomial, sigmoid and RBF used in SVM. RBF kernel is expressed as follows.

$$K(x_i, x_j) = \left( -\frac{\|x_i - x_j\|^2}{2\sigma^2} \right) \quad (6.45)$$

where  $\sigma$  is defined as kernel parameter of RBF function. To know whether a kernel is actually an inner product between two points or not Mercer's theorem [111] is used which is described as follows.

Let  $k(x, x')$  be a continuous symmetric kernel that is defined in the closed interval  $p_1 < x < p_2$ , and same for  $x'$ . The kernel  $K(x, x')$  can be expanded in the series as follows.

$$K(x, x') = \sum_{i=1}^{\infty} \Lambda_i \Psi_i(x) \Psi_i(x') \quad (6.46)$$

with positive coefficients  $\Lambda_i > 0$ , for all  $i$ . Necessary and sufficient requires for this expansion to be valid, converge absolutely and uniformly is given as follows.

$$\int_{p_2}^{p_1} \int_{p_2}^{p_1} k(x, x') \Gamma(x) \Gamma(x') dx dx' \geq 0 \quad (6.47)$$

The above expression holds for all  $\Gamma(\cdot)$ , for which

$$\int_{p_2}^{p_1} \Gamma^2(x) dx < \infty \quad (6.48)$$

where  $p_1$  and  $p_2$  are the integration constants. The features  $\Psi_i(x)$  are called eigen functions of the expansion.  $\Lambda_i$  are called eigenvalues. For positive eigenvalues, the kernel  $K(x, x')$  is positive definite. Mercer's theorem is important because it gives information whether a kernel is actually an inner-product kernel in some space and helping to use in SVM. These kernel functions are used in SVM to replace the term  $\Psi^T(x_i)\Psi^T(x_j)$  of equations (6.41) and (6.43). Computation speed depends on training samples. If the training sample increases in number, solution of classical SVM through quadratic programming becomes complex and reduces the computing speed. This problem can be solved using least square support vector machine (LS-SVM) which provides fast implementations without affecting its merits. LS-SVM is described in the next subsection.

### 6.5.4 Classification using Least Square Support Vector Machine (LS-SVM)

In 1999, Suykens and Vandewalle [112] proposed a least square version of SVM classifier. Inequality constraints are used in traditional SVM but LS-SVM uses equality optimization constraints. Hence, to solve a set of linear equations instead of quadratic programming, one can employ least square easily. LS-SVM has proved that computational cost is low for various applications [113]. Based on these advantages in this chapter LS-SVM is selected for SEIG fault classification. First a two class or binary LS-SVM is described, which is then extend to multiclass LS-SVM, described in following part of this subsection.

#### (a) Binary LS-SVM

For a training data set of  $N$  points  $(x_i, y_i)$ ,  $i = 1, 2, \dots, N$ , where  $x_i \in R^N$  is the  $i$ th input data set and  $y_i \in R$  is the  $i$ th output data set. In LS-SVM based classifier, the classification problem can be formulated as follows.

$$\text{Minimize : } F_{LS}(w, b, e) = \frac{1}{2}w^T w + \phi \frac{1}{2} \sum_{i=1}^N e_i^2 \quad (6.49)$$

$$\text{Subject to equality constraint : } y_i[w^T \Psi(x_i) + b] = 1 - e_i, \quad i = 1, 2, \dots, N \quad (6.50)$$

Lagrangian function of expression (6.49) to train LS-SVM classifier [112], is given as:

$$J_{LS}(\gamma) = \frac{1}{2}w^T w + \phi \frac{1}{2} \sum_{i=1}^N e_i^2 - \sum_{i=1}^N \gamma_i (y_i[w^T \Psi(x_i) + b] - 1 + e_i) \quad (6.51)$$

where  $\gamma_i$  are Lagrange multipliers (which are different from those of SVM, since equality constraints are used for LS-SVM). Lagrange multipliers,  $\gamma_i$  of LS-SVM in are either pos-



itive or negative. Based on KKT theorem, the optimality condition of equation (6.51) are expressed as follows.

$$\frac{\partial J_{LS(w,b,e,\gamma)}}{\partial w} = 0 \quad \rightarrow \quad w = \sum_{i=1}^N \gamma_i y_i \Psi(x_i) \quad (6.52a)$$

$$\frac{\partial J_{LS(w,b,e,\gamma)}}{\partial b} = 0 \quad \rightarrow \quad \sum_{i=1}^N \gamma_i y_i \quad (6.52b)$$

$$\frac{\partial J_{LS(w,b,e,\gamma)}}{\partial e_i} = 0 \quad \rightarrow \quad \gamma_i = \varphi e_i \quad (6.52c)$$

$$\frac{\partial J_{LS(w,b,e,\gamma)}}{\partial \gamma_i} = 0 \quad \rightarrow \quad y_i [w^T \Psi(x_i) + b] - 1 + e_i, \quad i = 1, 2, \dots, N \quad (6.52d)$$

By substituting equation (6.52a)-equation (6.52c) into (6.52d), the aforementioned equations can be equivalently written as follows.

$$\begin{bmatrix} 0 & Y^T \\ Y & \frac{1}{\varphi} + ZZ^T \end{bmatrix} \begin{bmatrix} b \\ \gamma \end{bmatrix} = \begin{bmatrix} 0 \\ \vec{1} \end{bmatrix} \quad (6.53)$$

where  $Z = \begin{bmatrix} y_1 \Psi(x_1) \\ y_2 \Psi(x_2) \\ \cdot \\ \cdot \\ y_N \Psi(x_N) \end{bmatrix}$

The feature mapping  $\Psi(x)$  is a row vector,  $Y = [y_1, y_2, \dots, y_N]^T$ ,  $\gamma = [\gamma_1, \gamma_2, \dots, \gamma_N]^T$  and  $\vec{1} = [1, 1, \dots, 1]^T$ . In LS-SVM, as  $\Psi(x)$  is usually unknown. As discussed in non-linear SVM Mercer's condition is applied to get the matrix  $ZZ^T$  which is given as follows.

$$ZZ^T = y_i y_j \Psi(x_i) \Psi(x_j) = y_i y_j K(x_i, x_j) \quad (6.54)$$

The decision function of LS-SVM classifier is expressed using kernel function [113] and expressed as:

$$\left[ \sum_{i=1}^N \gamma_i y_i K(x, x_i) + b \right] \quad (6.55)$$

The Lagrange multipliers  $\gamma_i$ 's are proportional to the training errors  $e_i$  in LS-SVM, while in traditional SVM, many Lagrange multipliers  $\gamma_i$ 's are typically equal to zero. So sparsity is lost in LS-SVM [113]. So far binary classification is discussed. But in this chapter four

different types of faults are considered so how LS-SVM works for multiclass problems described as follows.

### (b) Multiclass LS-SVM

SVM and LS-SVM were originally designed to classify two class problem. To effectively extend this binary classification machine to multiclass classification machines, many researchers are proposed different approaches such as one-versus-all (short of one class versus all the rest) [114] and one-versus-one [115].

To solve  $C$  class problem using one-versus-all method requires  $C$  SVM models [116]. The  $i$ th LS-SVM is trained with all of the training examples in the  $i$ th class with positive labels, and rest of the training examples with negative labels. Hence for a training data set of  $N$  points  $(x_i, y_i)$ ,  $i = 1, 2, \dots, N$ , where  $x_i \in R^N$  is the  $i$ th input data set and  $y_i \in \{1, 2, \dots, l\}$  is the class of  $x_i$ . Here  $i$ th LS-SVM solves the following objective function

$$\text{Minimize : } F_{LS}(w, b, e) = \frac{1}{2}(w^i)^T w^i + \phi \frac{1}{2} \sum_{i=1}^N e_i^2 \quad (6.56)$$

$$\begin{aligned} [(w^i)^T \Psi(x_j) + b^i] &\geq 1 - e_j^i, & \text{if } y_j = i \\ [(w^i)^T \Psi(x_j) + b^i] &\geq -1 + e_j^i, & \text{if } y_j \neq i \end{aligned} \quad (6.57)$$

Equation (6.56) is solved using the procedure discussed in the part (a) of this subsection, finally for  $C$  class problem, there are  $C$  decision functions given as follows.

$$\begin{aligned} &(w^1)^T \Psi(x) + b^1 \\ &(w^2)^T \Psi(x) + b^2 \\ &\quad \cdot \\ &\quad \cdot \\ &\quad \cdot \\ &(w^C)^T \Psi(x) + b^C \end{aligned}$$

$x$  is assigned to the class which has the largest value of the decision function and expressed as

$$\text{class of } x \quad \equiv \quad \operatorname{argmax}_{i=1,2,\dots,C} ((w^i)^T \Psi(x) + b^i) \quad (6.58)$$

Another alternative to solve multiclass classification problem using SVM and LS-SVM is one-over-one method. It was introduced by Knerr in 1990 in [117] that by constructing all possible two-class classifier from a set of  $C$  classes. In this method total number of constructed classifiers are  $\frac{C(C-1)}{2}$  where each one is trained on training examples from two classes. For training data from the  $i$ th and class  $j$ th classes, the following objective

function is solved.

$$\text{Minimize : } F_{LS}(w, b, e) = \frac{1}{2}(w^{ij})^T w^{ij} + \phi \frac{1}{2} \sum_t (e_t^{ij})^2 \quad (6.59)$$

$$\begin{aligned} [(w^{ij})^T \Psi(x_t) + b^{ij}] &\geq 1 - e_t^{ij}, & \text{if } y_t = i \\ [(w^{ij})^T \Psi(x_t) + b^{ij}] &\geq -1 + e_t^{ij}, & \text{if } y_t = j \end{aligned} \quad (6.60)$$

where  $e_t^{ij} \geq 0$ . After all  $\frac{C(C-1)}{2}$  classifiers are constructed, voting strategy is used to determine the class of  $x$  [116]. If  $\text{sign}([(w^{ij})^T \Psi(x_i) + b^{ij}])$  says  $x$  is in the  $i$ th class, then the vote for class  $i$  is added by one. Otherwise, the class  $j$  is added by one. Based on this voting, class is assigned to  $x$ .

Number of classifiers required for One vs All (OVA) method are  $C$  and for One vs One (OVO) are  $\frac{C(C-1)}{2}$ . In the recent literature it is reported that when the number of classes increases OVO performs well [115]. So for SEIG fault classification OVO LS-SVM classifier is selected. Next section presents results and discussion of this chapter.

## 6.6 Results and Discussion

In this chapter, the main objective is to create different types of faults for SEIG system and to classify them using the proposed LS-SVM classifier. In chapter 3 mathematical modeling of SEIG is developed and implemented in MATLAB/Simulink environment. Simulation results of the developed SEIG system are validated through experimental results as described in chapter 3. The same developed model is used in this chapter to study balanced and unbalanced conditions of SEIG. The following four types of faults are considered for the study.

1. C1-Three phase short circuit fault;
2. C2-Line-line fault;
3. C3-Capacitor opening in one phase of capacitor bank;
4. C4-Single line opening at three phase load.

Using the mathematical model of SEIG and MATLAB/Simulink, different types of faults are initiated. For each type of fault, SEIG stator voltage signals are sensed and negative sequence component computed as it retains the information under disturbance condition. The Empirical Mode Decomposition (EMD) method is then applied to each negative sequence component for obtaining the intrinsic mode functions (IMFs). First 6 IMFs are selected

and then, Hilbert Transform is applied on these IMFs. Further, the features of each IMF such as energy, standard deviation of the amplitude and phase contour are obtained. So, eighteen number of features are selected for each faulty signal. These features are used to study and classify faults of SEIG system by using various classifier methodologies such as MultiLayer Perceptron (MLP) neural network, Probabilistic Neural Network (PNN), Support Vector Machine (SVM), and Least Square Support Vector Machine (LS-SVM). In this study 140 different cases of each type of fault are taken where 40 and 100 cases selected randomly for training and testing of these classifiers methods. Final size of the matrix is  $560 \times 18$  which used as input to each classifier. Fig. 6.23 shows a flowchart which describes the steps required to classify the four different types of SEIG fault.

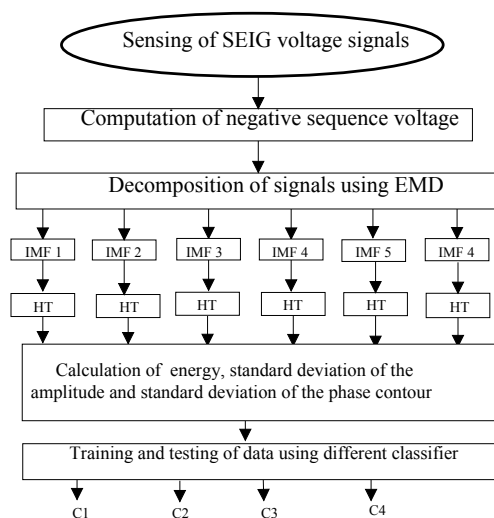


Figure 6.23: Flowchart of the proposed technique to classify SEIG faults.

The performance of each class is analyzed by computing the classifier accuracy defined below.

$$\eta = \frac{(\text{Total number of cases} - \text{Total number of misclassified cases})}{\text{Total number of cases}} \quad (6.61)$$

Table 6.1 shows the results obtained using LS-SVM classifier and the average accuracy obtained is 99.5 % for one fold. The diagonal elements of Table 6.1 represent correctly classified faulty signals and off-diagonal elements represent misclassification cases. As observed from Table 6.1 that out of 400 testing sets only two cases of class C2 are misclassified and other 398 cases are correctly classified.

To show the effectiveness of the LS-SVM classifier, classification accuracy obtained by LS-SVM is compared with other three classifiers. For each classifier, features are ex-

tracted using HHT. The comparison result is presented in Table 6.2. To have a correct evaluation, the input matrix is reshuffled and given to each classifier and average accuracy obtained. Four-fold cross-validation is considered for training/testing data partitioning. Average classification performance in terms of accuracy using LS-SVM, SVM and PNN classifier is presented in the Table 6.3 and the overall average accuracy obtained using classifiers MLP, PNN, SVM and LS-SVM are 92.75 %, 97 %, 98.25 % and 99.25 %. From the obtained results it is observed that LS-SVM performs well to classify the faulty signal into a distinct class. As already described to avoid the de-excitation stage of SEIG and transient pulsations detection and classification of faults are essential. Hence, HHT with LS-SVM classifier is suitable to detect and classify different types of SEIG faults.

Table 6.1: SEIG fault classification results obtained using HHT with LS-SVM for 1st fold.

Cases	C1	C2	C3	C4
C1	100	0	0	0
C2	2	98	0	0
C3	0	0	100	0
C4	0	0	0	100
Classification efficiency in %	100	98	100	100
Misclassification efficiency in %	0	2	0	0
Overall efficiency	99.5 %			

Table 6.2: Comparison of fault classification results using different classifiers

Classifier	MLP				PNN				SVM				LS-SVM			
	C1	C2	C3	C4	C1	C2	C3	C4	C1	C2	C3	C4	C1	C2	C3	C4
C1	92	4	2	2	98	2	0	0	99	1	0	0	100	0	0	0
C2	4	94	1	1	4	96	0	0	3	97	0	0	2	98	0	0
C3	3	2	93	2	1	0	98	1	0	0	100	0	0	0	100	0
C4	3	2	3	92	0	1	1	98	0	0	0	100	0	0	0	100
Classifier $\eta$ (%)	100	98	100	100	99	97	100	100	98	96	98	98	92	94	93	92
Overall $\eta$ (%)	92.75				97.5				99				99.5			

Table 6.3: Average classification accuracy obtained over four-fold using four different classifier

Fold/Classifier	MLP	PNN	SVM	LS-SVM
1	92.75	97.5	99	99.5
2	90.75	97	98.5	99
3	90.75	97.5	98.5	99.5
4	88.5	96	97	99
Average accuracy in %	90.6	97	98.25	99.25

## 6.7 Summary of the chapter

In this chapter, transient analysis for SEIG system is presented taking different types of faults such as three phase short circuit, line-to-line fault, single line opening at load and single phase capacitor opening. During three phase short circuit fault and line-to-line fault SEIG re-excitation time is more compared to the pre-fault excitation time for building rated voltage. Single line opening at load leads to sustained pulsation torque which may damage the induction machine if the fault is not cleared quickly. As concluded, the fault detection and classification are mandatory to avoid de-excitation of SEIG and torque pulsations. Due to non-linear and non-stationary nature of SEIG stator voltage, Hilbert-Huang transform (HHT) is selected for analysis of the fault voltage signal and its statistical features extraction. Extracted statistical features are processed using different classifiers such as MultiLayer Perceptron (MLP) neural network, Probabilistic Neural Network (PNN), Support Vector Machine (SVM), and Least Square Support Vector Machine (LS-SVM). To have a correct evaluation, the input size of the matrix is reshuffled and given to each classifier. The overall average accuracy obtained using classifiers MLP, PNN, SVM and LS-SVM are 92.75 %, 97 %, 98.25 % and 99.25 %. In this study, it is observed that LS-SVM among above classifiers provides higher classification accuracy.

# Chapter 7

## Conclusions and future scope

In this thesis, various aspects such as voltage control and fault detection schemes of SEIG stand-alone system along with proposed new schemes are studied using simulation and laboratory experiment. Finally, This chapter presents following concluding points along with the future scope of this research work presented in this thesis.

### 7.1 Conclusions of the thesis

- An analytical expression for the minimum value of capacitance required to develop SEIG rated voltage and frequency is derived.
- Mathematical model of wind turbine driven SEIG system is reviewed.
- Simulation of the wind turbine driven SEIG system is carried out in MATLAB/Simulink environment. The performances of wind turbine driven SEIG system taking different types of load such as resistive load,  $R - L$  load, induction motor (IM) load are discussed.
- Laboratory experiments are carried on SEIG system with resistive and IM load to verify its performance without using any controller. It is observed that SEIG excitation fails with overload and IM load.
- Simulation results of SEIG system with wind variations are also discussed and presented.
- Voltage can be compensated to some extent by increasing the excitation capacitance value.
- Simulation and experimental results of SEIG system with capacitance variation are presented, discussed and compared.
- SEIG system with Generalized Impedance Controller (GIC) is developed to control voltage and frequency during wind speed variations and load switching by computing optimal values of proportional and integral gains within stable zone using PSO technique. Further, simulation is carried out to study its performance with wind speed variations, resistive and

IM load.

■ Performance of GIC based SEIG system (with computed optimal proportional and integral gains) is assessed through harmonic analysis. Total Harmonic Distortion (THD) of voltages and currents at generator and load side are within 0.23 %.

■ A new technique is proposed to compute SEIG peak voltage using Hilbert transform and COordinate Rotation DIgital Computer. Simulation is carried out by taking a varying sinusoidal voltage signal to implement the proposed peak voltage computation technique in MATLAB/Simulink environment.

■ Further, simulation is carried out to study the performance of GIC based SEIG system using the proposed peak voltage computation technique during prime mover speed variations and load switching.

■ To implement the proposed control technique experimental setup is developed using a commercially available TMS320F2812 DSP processor. Further, laboratory experiments are carried for GIC based SEIG system to maintain rated voltage during load switching.

■ Transient analysis for SEIG system is presented taking different types of faults such as three phase short circuit, line-to-line fault, single line opening at load and single phase capacitor opening.

■ As observed from transient analysis of SEIG system, during three phase short circuit fault and line-to-line fault SEIG re-excitation time is more compared to the pre-fault excitation time for building rated voltage. It is also observed that single line opening at load leads to sustained pulsation torque which may damage the induction machine if the fault is not cleared quickly.

■ Hence, fault detection and classification are mandatory to avoid de-excitation of SEIG and torque pulsations.

■ Hilbert-Huang transform (HHT) is selected for analysis of the fault voltage signal and its statistical features extraction. Extracted statistical features are processed using different classifiers such as Multi-Layer Perceptron (MLP) neural network, Probabilistic Neural Network (PNN), Support Vector Machine (SVM), and Least Square Support Vector Machine (LS-SVM).

■ To have a correct evaluation, the input size of the matrix is reshuffled and given to each classifier. The overall average classification accuracies are computed for all these four classifiers to study their performance. The overall average accuracy obtained using MLP, PNN, SVM and LS-SVM classifiers are 92.75 %, 97 %, 98.25 % and 99.25 %, in that order.

■ In this study, the accuracy obtained by using LS-SVM (99.25 %) is higher compared to the other three classifiers.



## 7.2 Scope for future work

As discussed the limitations of this research work, the scope of the thesis can be extended as follows.

- The proposed technique for peak voltage computation is studied for balanced resistive,  $R - L$  and IM load. However, suitable technique for peak voltage computation in case of unbalanced load can be exploited.
- Fault analysis is done here using Hilbert-Huang transform (HHT) in simulation level, however real time implementation of HHT for SEIG fault signals on hardware can be considered as the future scope of this work.
- Integration of fault detection unit with GIC based SEIG system is also an attractive future research scope.

# References

- [1] Y. K. Chauhan, S. K. Jain, and B. Singh, "Operating performance of static series compensated three-phase self-excited induction generator," *Int. Jour. of Electric Power and Energy Syst.*, vol. 49, pp. 137–148, July 2013.
- [2] B. V. Perumal, "An investigation on some operational aspects of a generalized impedance controller based self excited induction generator," *Ph.D thesis, IIT Delhi*, Aug. 2006.
- [3] G. K. Kasal, "Analysis, design and development of voltage and frequency controllers for asynchronous generators in isolated power generation," *Ph.D thesis, IIT Delhi*, Dec. 2008.
- [4] K. Idjdarene, D. Rekioua, T. Rekioua, and A. Tounzi, "Performance of an isolated induction generator under unbalanced loads," *IEEE Trans. Energy Convers.*, vol. 25, no. 2, pp. 303–311, 2010.
- [5] Y. K. Chauhan, S. K. Jain, and B. Singh, "A prospective on voltage regulation of self-excited induction generators for industry applications," *IEEE Trans. Ind. Appl.*, vol. 46, no. 2, pp. 720–730, Mar./Apr. 2010.
- [6] "<http://www.indianwindpower.com>."
- [7] S. S. Kumar, N. Kumaresan, M. Subbiah, and M. Rageeru, "Modelling, analysis and control of stand-alone self-excited induction generator-pulse width modulation rectifier systems feeding constant DC voltage applications," *IET Gener. Transm. and Distrib.*, vol. 8, no. 6, pp. 1140–1155, 2014.
- [8] D. Palwalia and S. Singh, "Digital Signal Processor Based Fuzzy Voltage and Frequency Regulator for Self-excited Induction Generator," *Electric Power Compo. and Syst.*, vol. 38, no. 3, pp. 309–324, 2010.
- [9] K. H. Youssef, M. A. Wahba, H. A. Yousef, and O. A. Sebakhy, "A new method for voltage and frequency control of stand-alone self-excited induction generator using pulse width modulation converter with variable DC-link voltage," *Electric Power Compo. and Syst.*, vol. 38, no. 5, pp. 491–513, 2010.
- [10] B. Singh, S. S. Murthy, R. R. Chilipi, S. Madishetti, and G. Bhuvaneshwari, "Static synchronous compensator-variable frequency drive for voltage and frequency control of small-hydro driven self-excited induction generators system," *IET Gener. Transm. and Distrib.*, vol. 8, no. 9, pp. 1528–1538, 2014.
- [11] D. Seyoum, C. Grantham, and M. F. Rahman, "The dynamic characteristics of an isolated self-excited induction generator driven by a wind turbine," *IEEE Trans. Ind. Appl.*, vol. 39, no. 4, pp. 936–944, July/Aug. 2003.

- 
- [12] S. K. Jain, J. D. Sharma, and S. P. Singh, "Transient performance of three-phase self-excited induction generator during balanced and unbalanced faults," *IEE Proc. Gener. Transm. and Distrib.*, vol. 149. no. 1, pp. 50–57, Jan. 2002.
- [13] K. L. V. Iyer, X. Lu, Y. Usama, V. Ramakrishnan, and N. C. Kar, "A twofold Daubechies-wavelet-based module for fault detection and voltage regulation in **SEIGs** for distributed wind power generation," *IEEE Trans. Ind. Appl.*, vol. 60. no. 4, pp. 1638–1651, Apr. 2013.
- [14] B. Singh, S. S. Murthy, and S. Gupta, "Analysis and design of **STATCOM**-based voltage regulator for self-excited induction generators," *IEE Proc. Gener. Transm. and Distrib.*, vol. 19. no. 14, pp. 783–790, Dec. 2004.
- [15] B. Singh and V. Rajagopal, "Neural-network-based integrated electronic load controller for isolated asynchronous generators in small hydro generation," *IEEE Trans. Ind. Electro.*, vol. 58, no. 9, pp. 4264–4274, Sept. 2011.
- [16] B. V. Perumal and J. K. Chatterjee, "Voltage and frequency control of a stand alone brushless wind electric generation using generalized impedance controller," *IEEE Trans. Energy Convers.*, vol. 23. no. 2, pp. 632–641, June 2008.
- [17] G. J. Silva, A. Datta, and S. P. Bhattacharyya, "New results on the synthesis of **PID** controllers," *IEEE Trans. Autom. Control*, vol. 47, no. 2, pp. 241–252, 2002.
- [18] G. J. Silva, S. P. Bhattacharyya, and A. Datta, "**PID** controllers for time delay systems," *Control Engineering*, pp. 135–148, 2004.
- [19] S. Murthy, O. Malik, and A. Tandon, "Analysis of self-excited induction generators," *IEE Proc. C Gener. Transm. and Distrib.*, vol. 129, no. 6, pp. 260–265, 1982.
- [20] A.K.Tondon, S.S.Murthy, and G.J.Berg, "Steady state analysis of capacitor self-excited induction generator," *IEEE Trans. Power Appa. and Syst.*, vol. 3, no. PAS-103.
- [21] S. P. Singh, B. Singh, and M. P. Jain, "Performance characteristics and optimal utilization of a cage machine as capacitor excited induction generator," *IEEE Trans. Energy Convers.*, vol. 5, no. 4, pp. 679–685, 1990.
- [22] S. Murthy, B. P. Singh, C. Nagamani, and K. Satyanarayana, "Studies on the use of conventional induction motors as self-excited induction generators," *IEEE Trans. Energy Convers.*, vol. 3, no. 4, pp. 842–848, 1988.
- [23] S. Singh, B. Singh, and M. Jain, "Comparative study on the performance of a commercially designed induction generator with induction motors operating as self excited induction generators," *IEE Proc. C Gener. Transm. and Distrib.*, vol. 140, no. 5, pp. 374–380, 1993.
- [24] L. Ouazene and G. McPherson, "Analysis of the isolated induction generator," *IEEE Trans. Power Appa. and Syst.*, vol. 8, no. PAS-102, pp. 2793–2798, 1983.
- [25] T. Chan, "Analysis of self-excited induction generators using an iterative method," *IEEE Trans. Energy Convers.*, vol. 10, no. 3, pp. 502–507, 1995.
- [26] A. L. Alolah and M. A. Alkanhal, "Optimization-based steady state analysis of three phase self-excited induction generator," *IEEE Trans. Energy Convers.*, vol. 15, no. 1, pp. 61–65, 2000.

- 
- [27] M. Haque, "A novel method of evaluating performance characteristics of a self-excited induction generator," *IEEE Trans. Energy Convers.*, vol. 24, no. 2, pp. 358–365, June 2009.
- [28] A. Kheldoun, L. Refoufi, and D. E. Khodja, "Analysis of the self-excited induction generator steady state performance using a new efficient algorithm," *Electric Power Syst. Res.*, vol. 86, pp. 61–67, May 2012.
- [29] D. Joshi, K. S. Sandhu, and M. K. Soni, "Constant voltage constant frequency operation for a self-excited induction generator," *IEEE Trans. Energy Convers.*, vol. 21, no. 1, pp. 228–234, 2006.
- [30] J. Elder, J. T. Boys, and J. Woodward, "Self-excited induction machine as a small low-cost generator," vol. 131, no. 2, pp. 33–41, 1984.
- [31] C. Grantham, D. Sutanto, and B. Mismail, "Steady-state and transient analysis of self-excited induction generators," *IEE Proc. B Electric Power Appl.*, vol. 136, no. 2, pp. 61–68, 1989.
- [32] K. Natarajan, A. Sharaf, S. Sivakumar, and S. Naganathan, "Modeling and control design for wind energy power conversion scheme using self-excited induction generator," Dept. of Electrical Engineering, Univ. of New Brunswick, Fredericton, Tech. Rep., 1987.
- [33] L. Shridhar, B. Singh, and C. Jha, "Transient performance of the self regulated short shunt self excited induction generator," *IEEE Trans. Energy Convers.*, vol. 10, no. 2, pp. 261–267, 1995.
- [34] L. Wang and C.-H. Lee, "A novel analysis on the performance of an isolated self-excited induction generator," *IEEE Trans. Energy Convers.*, vol. 12, no. 2, pp. 109–117, 1997.
- [35] J. K. Chatterjee, B. V. Perumal, and N. R. Gopu, "Analysis of operation of a self-excited induction generator with generalized impedance controller," *IEEE Trans. Energy Convers.*, vol. 22, no. 2, pp. 307–315, 2007.
- [36] K. Idjdarene, D. Rekioua, T. Rekioua, and A. Tounzi, "Vector control of autonomous induction generator taking saturation effect into account," *Energy Convers. and Management*, vol. 49, no. 10, pp. 2609–2617, 2008.
- [37] B. Ooi and R. David, "Induction-generator/synchronous condenser system for wind-turbine power," *IEE Proc. C Gener. Transm. and Distrib.*, vol. 126, no. 1, pp. 69–74, 1979.
- [38] M. B. Brennen and A. Abbondanti, "Static exciters for induction generators," *IEEE Trans. Ind. Appl.*, no. 5, pp. 422–428, 1977.
- [39] N. Malik and S. Haque, "Steady state analysis and performance of an isolated self-excited induction generator," *IEEE Trans. Energy Convers.*, no. 3, pp. 134–140, 1986.
- [40] T. Maguire and A. Gole, "Apparatus for supplying an isolated DC load from a variable-speed self-excited induction generator," *IEEE Trans. Energy Convers.*, vol. 8, no. 3, pp. 468–475, 1993.
- [41] N. H. Malik and A. A. Mazi, "Capacitance requirements for isolated self excited induction generators," *IEEE Trans. Energy Convers.*, no. 1, pp. 62–69, 1987.
- [42] R. Mishra, B. Singh, and M. Vasantha, "Voltage regulator for an isolated self-excited cage induction generator," *Electric Power Syst. Res.*, vol. 24, no. 2, pp. 75–83, 1992.

- 
- [43] T. Ahmed, E. Hiraki, M. Nakaoka, and O. Noro, "Three-phase self-excited induction generator driven by variable-speed prime mover for clean renewable energy utilizations and its terminal voltage regulation characteristics by static var compensator," *Proc. Industry Appl. Conf. 38th IAS Annual Meeting*, vol. 2, pp. 693–700, Oct. 2003.
- [44] G. Raina and O. Malik, "Wind energy conversion using a self-excited induction generator," *IEEE Trans. Power Appa. and Syst.*, no. 12, pp. 3933–3936, 1983.
- [45] E. Muljadi, T. Lipo *et al.*, "Series compensated pwm inverter with battery supply applied to an isolated induction generator," *IEEE Trans. Ind. Appl.*, vol. 30, no. 4, pp. 1073–1082, 1994.
- [46] P. K. S. Khan, "Performance evaluation of a solid-state lead-lag var compensator and its application in stand-alone self-excited induction generation," *Ph.D thesis, IIT Delhi*, Aug. 1999.
- [47] H. R. Karshenas and A. Abdolahi, "Analysis of a voltage regulator for self-excited induction generator employing current-type static compensator," *IEEE Conf. Electrical and Computer Eng. Canadian*, vol. 2, pp. 1053–1058, 2001.
- [48] B. Singh and L. Shilpakar, "Analysis of a novel solid state voltage regulator for a self-excited induction generator," *IEE Proc. Gener. Transm. and Distri.*, vol. 145, no. 6, pp. 647–655, 1998.
- [49] E. G. Marra and J. A. Pomilio, "Self-excited induction generator controlled by a **VS-PWM** bidirectional converter for rural applications," *IEEE Trans. Ind. Appl.*, vol. 35, no. 4, pp. 877–883, 1999.
- [50] L. Wang and C. H. Lee, "Long-shunt and short-shunt connections on dynamic performance of a **SEIG** feeding an induction motor load," *IEEE Trans. Energy Convers.*, vol. 15, no. 1, pp. 1–7, Mar. 2000.
- [51] S. Singh, S. K. Jain, and J. Sharma, "Voltage regulation optimization of compensated self-excited induction generator with dynamic load," *IEEE Trans. Energy Convers.*, vol. 19, no. 4, pp. 724–732, Dec. 2004.
- [52] B. Singh, M. Singh, and A. K. Tandon, "Transient performance of series-compensated three-phase self-excited induction generator feeding dynamic loads," *IEEE Trans. Ind. Appl.*, vol. 46, no. 4, pp. 1271–1280, 2010.
- [53] S. Wekhande and V. Agarwal, "A new variable speed constant voltage controller for self-excited induction generator," *Electric Power Syst. Res.*, vol. 59, no. 3, pp. 157–164, 2001.
- [54] S. Kuo and L. Wang, "Analysis of voltage control for a self-excited induction generator using a current-controlled voltage source inverter (**CC-VSD**)," *IEE Proc. Gener. Transm. and Distri.*, vol. 148, no. 5, pp. 431–438, 2001.
- [55] L. A. Lopes and R. G. Almeida, "Wind-driven self-excited induction generator with voltage and frequency regulated by a reduced-rating voltage source inverter," *IEEE Trans. Energy Convers.*, vol. 21, no. 2, pp. 297–304, June 2006.
- [56] B. Singh, S. Murthy, and S. Gupta, "Analysis and design of electronic load controller for self-excited induction generators," *IEEE Trans. Energy Convers.*, vol. 21, no. 1, pp. 285–293, 2006.
- [57] B. Singh and G. K. Kasal, "Solid state voltage and frequency controller for a stand alone wind power generating system," *IEEE Trans. Power Electro.*, vol. 23, no. 3, pp. 1170–1177, 2008.

- 
- [58] G. K. Kasal and B. Singh, "DSP based voltage controller for an isolated asynchronous generator feeding induction motor loads," *Electric Power Compo. and Syst.*, vol. 37, no. 8, pp. 914–935, 2009.
- [59] D. Palwalia and S. Singh, "Digital signal processor based fuzzy voltage and frequency regulator for self-excited induction generator," *Electric Power Compo. and Syst.*, vol. 38, no. 3, pp. 309–324, 2010.
- [60] H. Geng, D. Xu, B. Wu, and W. Huang, "Direct voltage control for a stand-alone wind-driven self-excited induction generator with improved power quality," *IEEE Trans. Power Electro.*, vol. 26, no. 7-8, pp. 2358–2368, Aug. 2011.
- [61] X. Lu, K. L. V. Iyer, K. Mukherjee, and N. C. Kar, "A Wavelet/PSO based voltage regulation scheme and suitability analysis of copper and aluminum rotor induction machines for distributed wind power generation," *IEEE Trans. Smart Grid.*, vol. 3, no. 4, pp. 1923–1934, Dec. 2012.
- [62] S. Deraz and F. A. Kader, "A new control strategy for a stand-alone self-excited induction generator driven by a variable speed wind turbine," *Renewable Energy*, vol. 51, pp. 263–273, 2013.
- [63] S. Shukla, S. Mishra, and B. Singh, "Empirical-mode decomposition with Hilbert transform for power-quality assessment," *IEEE Trans. Power Del.*, vol. 24, no. 4, pp. 2159–2165, 2009.
- [64] Y. Gu and M. H. Bollen, "Time-frequency and time-scale domain analysis of voltage disturbances," *IEEE Trans. Power Del.*, vol. 15, no. 4, pp. 1279–1284, 2000.
- [65] P. K. Ray, N. Kishor, and S. R. Mohanty, "Islanding and power quality disturbance detection in grid-connected hybrid power system using Wavelet and S-Transform," *IEEE Trans. Energy Convers.*, vol. 3, no. 3, pp. 1082–1094, 2012.
- [66] Y.-Y. Hong and Y.-Q. Bao, "FPGA implementation for real-time empirical mode decomposition," *IEEE Trans. Instr. and Meas.*, vol. 61, no. 12, pp. 3175–3184, 2012.
- [67] N. C. Tse, J. Y. Chan, W.-H. Lau, and L. L. Lai, "Hybrid wavelet and hilbert transform with frequency-shifting decomposition for power quality analysis," *IEEE Trans. Instr. and Meas.*, vol. 61, no. 12, pp. 3225–3233, 2012.
- [68] Y. Lei, J. Lin, Z. He, and M. J. Zuo, "A review on empirical mode decomposition in fault diagnosis of rotating machinery," *Mechanical Syst. and Signal Proces.*, vol. 35, no. 1, pp. 108–126, 2013.
- [69] B. Sawetsakulanond and V. Kinnares, "Design, analysis, and construction of a small scale self-excited induction generator for a wind energy application," *Energy*, vol. 35, no. 12, pp. 4975–4985, 2010.
- [70] M. G. Simões, S. Chakraborty, and R. Wood, "Induction generators for small wind energy systems," *IEEE Power Electro. Society Newsletter*, vol. 18, no. 3, pp. 19–23, 2006.
- [71] F. Martinez, L. C. Herrero, and S. de Pablo, "Open loop wind turbine emulator," *Renewable Energy*, vol. 63, pp. 212–221, Oct. 2014.
- [72] J. Zaragoza, J. Pou, A. Arias, C. Spiteri, E. Robles, and S. Ceballos, "Study and experimental verification of control tuning strategies in a variable speed wind energy conversion system," *Renewable Energy*, vol. 36, no. 5, pp. 1421–1430, 2011.
- [73] P. C. Kruse, O. Wasynczuk, and S. Suudhoff, "Analsis of electric machinery," *Piscataway, NZ*, IEEE Press 1995.

- 
- [74] C. J. B. Singh, L. Shridhar, "Transient analysis of self-excited induction generator supplying dynamic load," *Electric Machines and Power Syst.*, vol. 27, no. 9, pp. 941–954, 1999.
- [75] <http://www.windcare.com>.
- [76] B. Singh, M. Singh, and A. K. Tandon, "Transient performance of series-compensated three-phase self-excited induction generator feeding dynamic loads," *IEEE Trans. Ind. Appl.*, vol. 46, no. 4, pp. 1271–1280, 2010.
- [77] J. Chauhan, J. Chatterjee, H. Bhare, B. Perumal, and D. Sarakar, "Synchronized Operation of **DSP** based **Generalized Impedance Controller With Variable-Speed Isolated SEIG** for **Novel Voltage and Frequency Control**," *IEEE Trans. Ind. Appl.*, vol. 51, no. 2, pp. 1845–1854, 2015.
- [78] Y. Del Valle, G. K. Venayagamoorthy, S. Mohagheghi, J.-C. Hernandez, and R. G. Harley, "Particle swarm optimization: basic concepts, variants and applications in power systems," *IEEE Trans. Evolutionary Computation*, vol. 12, no. 2, pp. 171–195, 2008.
- [79] Z. L. Gaing, "A particle swarm optimization approach for optimum design of **PID** controller in **AVR** system," *IEEE Trans. Energ. Convers.*, vol. 19, no. 2, pp. 384–391, 2004.
- [80] H. M. Hasanien and S. M. Muyeen, "A taguchi approach for optimum design of proportional-integral controllers in cascaded control scheme," *IEEE Trans. Power Syst.*, vol. 28, no. 2, pp. 1636–1643, 2013.
- [81] B. Mehta, P. Bhatt, and V. Pandya, "Small signal stability enhancement of **DFIG** based wind power system using optimized controller parameters," *Electric Power and Energy Syst.*, vol. 70, pp. 70–82, 2015.
- [82] C. H. Liu and Y. Y. Hsu, "Design of a self-tuning **PI** controller for a **STATCOM** using particle swarm optimization," *IEEE Trans. Ind. Electro.*, vol. 57, no. 2, pp. 702–715, 2010.
- [83] J. K. chatterjee and P. J. Chauhan, "A novel non-fragile single-loop voltage and frequency controller for induction generator based isolated renewable energy conversion system," *Proc. of IEEE IECON 36th Annual Conf.*, pp. 303–308, Nov. 2010.
- [84] C. Bhende, S. Mishra, and S. G. Malla, "Permanent magnet synchronous generator-based standalone wind energy supply system," *IEEE Trans. Sust. Energy*, vol. 2, no. 4, pp. 361–373, 2011.
- [85] M. Feldman, "Hilbert transform in vibration analysis," *Mechanical Syst. and Signal Proces.*, vol. 25, no. 3, pp. 735–802, 2011.
- [86] S. Kak, "The discrete finite **Hilbert** transform," *Indian Jour. Pure and Appl. Math.*, vol. 8, pp. 1385–1390, 1977.
- [87] J. E. Volder, "The birth of cordic," *Jour. of VLSI Signal Proces. Syst.*, vol. 25, no. 2, pp. 101–105, 2000.
- [88] J. S. Walther, "The story of unified cordic," *Jour. of VLSI Signal Proces. Syst.*, vol. 25, no. 2, pp. 107–112, 2000.
- [89] P. K. Meher, J. Valls, T.-B. Juang, K. Sridharan, and K. Maharatna, "50 years of cordic: Algorithms, architectures, and applications," *IEEE Trans. Circuits and Syst. I: Regular Papers*, vol. 56, no. 9, pp. 1893–1907, 2009.



- 
- [90] N. E. Huang, Z. Shen, S. R. Long, M. C. Wu, H. H. Shih, Q. Zheng, N. C. Yen, C. C. Tung, and H. H. Liu, "The empirical mode decomposition and the Hilbert spectrum for nonlinear and non-stationary time series analysis," *Proc. of the Royal Society of London A: Math., Physical and Eng. Sciences*, vol. 454, no. 1971, pp. 903–995, 1998.
- [91] P. K. Ray, S. R. Mohanty, and N. Kishor, "Disturbance detection in grid-connected distributed generation system using wavelet and S-transform," *Electric Power Syst. Res.*, vol. 81, no. 3, pp. 805–819, 2011.
- [92] D. Lauria and C. Pisani, "On Hilbert transform methods for low frequency oscillations detection," *IET Gener. Transm. and Distri.*, vol. 8, no. 6, pp. 1061–1074, 2014.
- [93] J. zarei, "Induction motors bearing fault detection using pattern recognition techniques," *Expert Syst. with Appl.*, vol. 39, pp. 68–73, 2012.
- [94] M. Rukonuzzaman, H. Shaibon, and K. L. Lo, "Neural network approach of harmonics detection," *Proc. of EMPD Energy Management and Power Del.*, vol. 2, pp. 467–472, 1998.
- [95] N. Das, B. Das, R. Sarakar, S. Basu, M. Kundu, and M. Nasipuri, "Handwritten bangla basic and compound character recognition using mlp and svm classifier," *Jour. of Computing*, vol. 2, no. 2, pp. 109–115, Feb. 2010.
- [96] B. Samanta, "Gear fault detection using artificial neural networks and support vector machines with genetic algorithms," *Mechanical Syst. and Signal Proces.*, vol. 18, no. 3, pp. 625–644, 2004.
- [97] K. Z. Mao, K. C. Tan, and W. Ser, "Probabilistic neural-network structure determination for pattern classification," *IEEE Trans. Neural Net.*, vol. 11, no. 4, pp. 1009–1015, 2000.
- [98] N. Perera and A. D. Rajapakse, "Recognition of fault transients using a probabilistic neural-network classifier," *IEEE Trans. Power Del.*, vol. 26, no. 1, 2011.
- [99] D. F. Specht, "Probanilistic neural network," *Neural Net.*, vol. 3, no. 1, pp. 109–118, 1990.
- [100] Z. L. Gaing, "Wavelet-based neural network for power disturbance recognition and classification," *IEEE Trans. Power Del.*, vol. 19, no. 4, pp. 1560–1568.
- [101] S. Mishra, C. N. Bhende, and B. K. Panigrahi, "Detection and classification of power quality disturbances using S-transform and probabilistic neural network," *IEEE Trans. Power Del.*, vol. 23, no. 1, pp. 280–287, 2008.
- [102] S. R. Samantaray and P. K. Dash, "Pattern recognition based digital relaying for advanced series compensated line," *Int. Jour. of Electric Power and Energy Syst.*, vol. 30, no. 2, pp. 102–112, 2008.
- [103] V. Bhargav, R. P. Maheshwari, and B. Das, "Protection of series compensated transmission line: Issues and state of art," *Electric Power Syst. Res.*, vol. 107, pp. 93–108, 2014.
- [104] A. Foroughi, E. Mohammadi, and S. Esmaeili, "Application of hilbert–huang transform and support vector machine for detection and classification of voltage sag sources," *Turk. Jour. of Electrical Eng. and Computer Sci.*, vol. 22, no. 5, pp. 1116–1129, 2014.
- [105] P. K. Dash, S. R. Samantaray, and G. Panda, "Fault classification and section identification of an advanced series-compensated transmission line using support vector machine," *IEEE Trans. Power Del.*, vol. 22, no. 1, pp. 67–73, 2007.



- 
- [106] U. B. Parikh, B. Das, and R. Prakash, "Combined wavelet-svm technique for fault zone detection in a series compensated transmission line," *IEEE Trans. Power Del.*, vol. 23, no. 4, pp. 1789–1794, 2008.
- [107] V. N. Vapnik, "The nature of statistical learning theory," *2nd edition*, Springer-Verlag, New York, 2000.
- [108] P. K. Ray, S. R. Mohanty, and N. Kishor, "Classification of power quality disturbances due to environmental characteristics in distributed generation system," *IEEE Trans. Sust. Energy*, vol. 4, no. 2, pp. 302–313, 2013.
- [109] S. Ekici, "Classification of power system disturbances using support vector machines," *Expert Syst. with Appl.*, vol. 36, no. 6, pp. 9859–9868, 2009.
- [110] V. Bhargav, R. P. Maheshwari, and B. Das, "Investigation for improved artificial intelligence techniques for thyristor-controlled series-compensated transmission line fault classification with discrete wavelet packet entropy measures," *Electric Power Compo. and Syst.*, vol. 42, no. 6, pp. 554–566, 2014.
- [111] S. Haykin, "Neural networks and learning machines," *3rd edition*, Pearson Education, New Jersey, USA, 2009.
- [112] J. A. K. Suykens and J. Vandewalle, "Least squares support vector machine classifiers," *Neural proces. letters*, vol. 9, no. 3, pp. 293–300, 1999.
- [113] G. B. Huang, H. Zhou, X. Ding, and R. Zhang, "Extreme learning machine for regression and multiclass classification," *IEEE Trans. Syst. Man and Cybernetics, Part B*, vol. 42, no. 2, pp. 513–529, 2012.
- [114] R. Rifkin and A. Klautau, "In defense of one-vs-all classification," *The Jour. of Mach. Learning Res.*, vol. 5, pp. 101–141, 2004.
- [115] E. G. M. Galar, A. Fernández, E. Barrenechea, H. Bustince, and F. Herrera, "An overview of ensemble methods for binary classifiers in multi-class problems: Experimental study on one-vs-one and one-vs-all schemes," *Pattern Recognition*, vol. 44, no. 8, pp. 1761–1776, 2011.
- [116] C. H. Hsu and C. Lin, "A comparison of methods for multiclass support vector machines," *IEEE Trans. Neural Net.*, vol. 13, no. 2, pp. 415–425, 2002.
- [117] L. P. S. Knerr and G. Dreyfus, "Single-layer learning revisited: a stepwise procedure for building and training a neural network," *Neurocomputing*, pp. 41–50, 1990.

# Thesis Dissemination

## Journal Publications

- [1] J. Dalei, and K. B. Mohanty, "Performance improvement of three-phase self-excited induction generator feeding induction motor load," *Turk. Jour. of Electrical Eng. and Computer Sci.*, vol. 23, no. 6., pp.1660–1672, Nov. 2015.
- [2] J. Dalei, and K. B. Mohanty, "Fault classification in SEIG system using Hilbert-Huang transform and least square support vector machine," *Int. Jour. of Electrical Power and Energy Syst.*, (Elsevier), vol. 76, pp.11–22, Mar. 2016.
- [3] J. Dalei, and K. B. Mohanty, "An approach to estimate and control SEIG voltage and frequency using CORDIC algorithm," *Transaction of the Institute of Measurement and Control*, (Sage), on line available (DOI:10.1177/0142331215621374).
- [4] J. Dalei, and K. B. Mohanty, "An approach to improve performance of three-phase SEIG feeding induction motor load using Hilbert transform and Coordinate Rotation Digital Computer," *Electric Power Components and Systems*, (Taylor and Francis), (accepted).

## Conference Publications

- [1] J. Dalei, and K. B. Mohanty, "A novel method to determine minimum capacitance of the self-excited induction generator," *Proc. of IEEE Int. Conf. Technical Symposium*, Kharagpur, India, pp. 408–413, 2014.
- [2] J. Dalei, and K. B. Mohanty, "Application of Second Generation Wavelet Transform for SEIG load transient detection," *Proc. of IEEE Int. Conf. Power Electronics, Drives and Energy Systems (PEDES)*, Mumbai, India, pp.1–5, Dec. 2014.
- [3] J. Dalei, and K. B. Mohanty, "Fault detection of Self excited induction generator," *Proc. of IEEE Conf. Energy, Power and Environment (ICEPE)*, Meghalaya, India, June 2015.
- [4] J. Dalei, and K. B. Mohanty, "Fuzzy PI controller for improved voltage regulation in STATCOM based SEIG," *Proc. of IEEE India Conf. (INDICON)*, New Delhi, India, Dec. 2015.

# Author's Biography

Jyotirmayee Dalei was born on June 12th, 1979 in Rourkela (Odisha). After finishing her schooling from N.A.C High School, Nayagarah in 1994, she completed her +2 Science from Sashi Bhusan Rath Government Women's College in 1996. She obtained B. Tech (Electrical Engg.) and M. Tech (Power System) from University College of Engineering, Burla (presently, Veer Surendra Sai University of Technology) in 2001 and 2004 respectively. Then she joined as an Asst. Professor at Roland Institute of Technology, Berhampur in the year 2004. She took admission for Ph.D at National Institute of Technology, Rourkela in 2011. She has four journals and four conferences publications out of her doctoral research work. Her area of interest is Power Electronics and Drives, Distributed generation system. She is a life member of Indian Society for Technical Education.

# Appendix A

In subsection 4.5.2 Theorem 5.5 and Theorem 5.6 (Chapter 5 [18]) are used and presented in this Appendix. Characteristic equation of time-delay system is known as quasi-polynomials. Pontryagin first studied these quasi-polynomials and derived necessary and sufficient conditions for the roots of these polynomials to have negative real parts.

## Theorem 5.5

Let  $C^*(s)$  a quasi-polynomial, and by substituting  $s = j\omega$  rewrite as

$C^*(j\omega) = C_r(\omega) + jC_i(\omega)$  where  $C_r(\omega)$  and  $C_i(\omega)$  represent, respectively, the real and imaginary parts of  $C^*(j\omega)$ .  $C^*(s)$  is stable if and only if

- (i)  $C_r(\omega)$  and  $C_i(\omega)$  have only simple, real roots and these interlace.
- (ii)  $C'_i(\omega_o)C_r(\omega_o) - C_i(\omega_o)C'_r(\omega_o) > 0$ , for some  $\omega_o$  in the range  $(-\infty, \infty)$ .

where  $C'_r(\omega_o)$  and  $C'_i(\omega_o)$  represent the first derivative with respect to  $\omega$  of  $C_r(\omega_o)$  and  $C_i(\omega_o)$ , respectively. Time-delay system is stable for only the real roots of  $C_r(\omega)$  and  $C_i(\omega)$ . In this context, Theorem 5.6 (Chapter 5 [18]) is presented here to know the nature of roots of  $C_r(\omega)$  and  $C_i(\omega)$

## Theorem 5.6

Let  $M_1$  and  $N_1$  represent the highest powers of  $s$  and  $e^s$ , respectively, in  $C^*(s)$ . Let  $\eta_1$  be an appropriate constant such that the coefficients of terms of highest degree in  $C_r(\omega_o)$  and  $C_i(\omega_o)$  do not vanish at  $\omega = \eta_1$ . Then for the equations  $C_r(\omega) = 0$  or  $C_i(\omega) = 0$  to have only real roots, it is necessary and sufficient that in each of the intervals

$$-2l_1\pi + \eta_1 \leq \omega \leq 2l_1\pi + \eta_1, l_1 = l_o, l_{o+1}, l_{o+2}, \dots$$

$C_r(\omega_o)$  or  $C_i(\omega_o)$  have exactly  $4l_1N_1 + M_1$  real roots for a sufficiently large  $l_o$ . Description of how this theorem is used to know the nature of the roots of  $C_r(\omega)$  or  $C_i(\omega)$  presented here taking a first order time-delay system.

Let a first-order time delay system with delay time of 10 s is represented by,

$$G(s) = \frac{1}{2s+1}e^{-10s}$$

Let value of  $k_p=1.8$  and  $k_i=0.2$ . Now the characteristic equation of the closed-loop becomes

$$C(s) = 2s^2 + s + (1.8s + 0.2)e^{-10s}$$

Quasi-polynomial of the above characteristic equation becomes

$$C^*(s) = e^{10s}C(s) = 0.2 + 1.8s + (2s^2 + s)e^{\tau s}$$

Expression  $C^*(s)$  is rewritten by changing variables  $s = \frac{\hat{s}}{10}$ . Then the expression for  $C^*(s)$  is rewritten as

$$\widehat{C}^*(\hat{s}) = (0.02\hat{s}^2 + 0.1\hat{s})e^{\hat{s}} + 0.18\hat{s} + 0.2$$

For this new quasi-polynomial,  $M_1 = 2$  and  $N_1 = 1$ . The real and imaginary parts of  $\widehat{C}^*(\hat{s})$  after substituting  $\hat{s} = j\hat{\omega}$  are presented as follows.

$$\begin{aligned}\widehat{C}_r(\hat{\omega}) &= 0.2 - 0.1\hat{\omega}\sin\hat{\omega} - 0.02\hat{\omega}^2\cos(\hat{\omega}) \\ \widehat{C}_i(\hat{\omega}) &= \hat{\omega}[0.18 + 0.1\cos(\hat{\omega}) - 0.02\hat{\omega}\sin(\hat{\omega})]\end{aligned}$$

From the right hand side of imaginary part following two expressions are obtained

$$\begin{aligned}\hat{\omega} &= 0, \text{ or} \\ 0.18 + 0.1\cos(\hat{\omega}) - 0.02\hat{\omega}\sin(\hat{\omega}) &= 0\end{aligned}$$

It is observed from the first expression that one root of the imaginary part is  $\hat{\omega}_0 = 0$ . The positive real roots obtained from second expressions are  $\hat{\omega}_1 = 8.0812$ ,  $\hat{\omega}_2 = 8.8519$ ,  $\hat{\omega}_3 = 13.5896$ ,  $\hat{\omega}_4 = 15.4332$ ,  $\hat{\omega}_5 = 19.5618$ ,  $\hat{\omega}_6 = 21.8025$  .....

Next  $\eta = \frac{\pi}{4}$  is selected so that  $\sin(\eta) \neq 0$  to check the conditions mentioned by Theorem 5.6. Root distributions of  $\widehat{C}_i(\hat{\omega})$  is presented in Fig. 7.1 which will help to apply the Theorem.

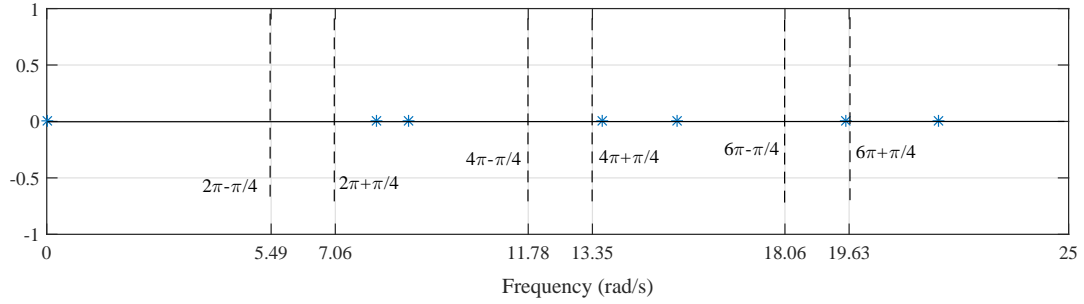


Figure 7.1: Root distribution of  $\widehat{C}_i(\hat{\omega})$

From the figure it is observed that  $\widehat{C}_i(\hat{\omega})$  has only one root in the interval  $[0, 2\pi - \frac{\pi}{4}] = [0, \frac{7\pi}{4}]$  i.e., root at the origin. Since  $\widehat{C}_i(\hat{\omega})$  is an odd function of  $\hat{\omega}$ , it follows that in the interval  $[-\frac{7\pi}{4}, \frac{7\pi}{4}]$ ,  $\widehat{C}_i(\hat{\omega})$  will have only one real root. As seen in the same figure that  $\widehat{C}_i(\hat{\omega})$  has no real roots in the interval  $[\frac{7\pi}{4}, \frac{9\pi}{4}]$ . Hence,  $\widehat{C}_i(\hat{\omega})$  has only one real root in the interval

$$[-2\pi + \frac{\pi}{4}, 2\pi + \frac{\pi}{4}],$$

which not satisfy the condition  $4N_1 + M_1 = 6$  for  $l_o = 1$ .

Further, take  $l_o = 2$ , so now the number of real roots must be  $8N_1 + M_1 = 10$ . As seen in the figure in the interval,

$$[-4\pi + \frac{\pi}{4}, 4\pi + \frac{\pi}{4}],$$

the function  $\widehat{C}_i(\hat{\omega})$  has only five real roots. With the same procedure for  $l_1 = 3, 4, \dots$  it is concluded that the number of real roots of  $\widehat{C}_i(\hat{\omega})$  in the interval

$$[-2l_1\pi + \frac{\pi}{4}, 2l_1\pi + \frac{\pi}{4}],$$

is always less than  $4l_1N_1 + M_1 = 4l_1 + 2$ . So based on the Theorem 5.6 it is concluded that the roots of  $\widehat{C}_i(\hat{\omega})$  are not all real, hence the gains are considered are not within the stable zone.

# Appendix B

The generalized rotational expression for vectors is given as follows:

$$\begin{bmatrix} x' \\ y' \end{bmatrix} = Rot(\theta) \begin{bmatrix} x \\ y \end{bmatrix} \quad (7.1)$$

where  $(x,y)$  and  $(x',y')$  are input and output vectors respectively for rotation. where

$$Rot(\phi) = \begin{bmatrix} \cos\phi & -\sin\phi \\ \sin\phi & \cos\phi \end{bmatrix} \quad (7.2)$$

Applying two successive *Rots* on a vector, that is rotating a vector through two different angles  $\phi_1$  and  $\phi_2$  in succession is equivalent to rotating the vector once, i.e applying *Rot* once, through an angle equal to the sum of the two angles  $\phi_1 + \phi_2$ . We can write the trigonometric equation as follows:

$$\begin{bmatrix} \cos(\phi_1 + \phi_2) & -\sin(\phi_1 + \phi_2) \\ \sin(\phi_1 + \phi_2) & \cos(\phi_1 + \phi_2) \end{bmatrix} = \begin{bmatrix} \cos\phi_2 & -\sin\phi_2 \\ \sin\phi_2 & \cos\phi_2 \end{bmatrix} \begin{bmatrix} \cos\phi_1 & -\sin\phi_1 \\ \sin\phi_1 & \cos\phi_1 \end{bmatrix} \quad (7.3)$$

This equation may be written as in the following expression

$$Rot(\phi_1 + \phi_2) = Rot(\phi_2)Rot(\phi_1) \quad (7.4)$$